FLOW LOSS IN SUPERPLASTICIZED CEMENT PASTES

A thesis submitted to attain the degree of

DOCTOR OF SCIENCES of ETH ZURICH

(Dr. sc. ETH Zurich)

presented by

SARA MANTELLATO

Laurea Specialistica in Chimica Industriale, Università degli Studi di Padova

born on 14.08.1982

citizen of Italy

accepted on the recommendation of

Prof Dr Robert J. Flatt, examiner

Prof Dr Phillip F. G. Banfill, co-examiner

Dr Mohsen Ben Haha, co-examiner

Prof Dr Paul Bowen, co-examiner

2017

Acknowledgements

I would like to thank the committee members for reviewing this dissertation: Prof Dr Robert J. Flatt from ETH Zurich, Prof Dr Phillip F. G. Banfill from Heriot-Watt University, Dr. Mohsen Ben Haha from Heidelberg Cement and Prof Dr Paul Bowen from EPFL. I am also thankful to Prof Dr Irena Hajnsek from ETH Zurich who was the Chairwoman of the committee. I also want to thank them for letting my defense be an enjoyable moment and for the brilliant comments and suggestions.

I would like to express my special appreciation and thanks to my supervisor Prof Dr Robert J. Flatt. I would like to thank you for trusting me and encouraging my research with enthusiasm and constructive criticisms. You were always able to give the right motivations sharing your immense knowledge.

I was particularly fortunate to work and/or spend my time with the current and previous members of PCBM: Dr Yurena Segui Femenias, Dr Giulia Gelardi, Paula Bran, Dr Delphine Marchon, Prof Dr Prannoy Suraneni, Dr Marta Palacios, Dr Tim Wangler, Ass Prof Dr Francesco Caruso, Dr Thibault Demoulin, Ylenia Praticò, Matteo Stefanoni, Lex Reiter, Kornel Kovacs, Marc Schultheiss, Heinz Richner, Ana Vallejo Vitaller, Andrea Louys, Nicolas Ruffray, Dr Ena Lloret, Dr Elizaveta Pustovgar, Denise Altermatt, Gaby Peschke, Asel Maria Aguilar Sanchez, Carolina Boschmann, Federica Boscaro, Luigi D'Avico, Federico Martinelli, Lucas Michel, Anne Weckwerth, Patrick Pfändler, Dr Wei Shi, Dr Zhidong Zhang, Abhishek Jain, Weiqing Xu, Prof Dr Ueli Angst, Oliver Glauser, Dr Ratan Mishra, Dr Daniel Sanz, Dr Wei Cai, Andi Reusser, Köbi Scherrer, Prof Dr Nicolas Roussel and Prof Dr Bernhard Elsener.

In addition, I would like to thank the post-docs who worked with me for their valuable guidance and collaboration. I especially want to thank Marta for her support decoding Robert's ideas and fruitful meetings. She was always thoughtful and supporting with her smiles during conferences and presentations. My thanks

experiences. I thank my little boy Saverio for the patience he showed during the writing. You fill my life with joy, love and passion. Words would never say how grateful I am to both of you.

Zusammenfassung

Verflüssiger, welche auch unter dem Englischen Begriff "Superplasticizers" bekannt sind, sind polymere Dispergatoren welche häufig in der Betontechnologie eingesetzt werden. Bei der neuesten Generation handelt es sich um Polycarboxylatether basierte Copolymere (*PCEs*). Diese sind die effizientesten Verflüssiger, welche sowohl exzellente Dispergierung, als auch verbesserte Verarbeitbarkeit, Dauerhaftigkeit und Festigkeitsentwicklung bewirken. Eines der grössten Probleme im Zusammenhang mit dem Einsatz von Verflüssigern, ist die Tatsache, dass diese dazu führen, dass das Fliessverhalten des Betons mit der Zeit abnimmt (flow loss). In der Praxis kann eine Verschlechterung des Fliessverhaltens zu gravierenden Problemen bei Verarbeitung und Fertigstellung von Beton führen. Derartige Probleme werden auf der Baustelle häufig unzureichend gelöst, indem nachträglich PCE- oder im schlimmsten Falle sogar Wasser hinzugegeben wird. Das Ausmass, in welchem die Fliesseigenschaften abnehmen hängt von mehreren Faktoren, wie dem Typ und der Dosierung des Zusatzmittels ab.

Die Abnahme der Fliesseigenschaften wurde im Laufe der letzten Jahre hauptsächlich durch qualitative und vergleichende Ansätze erklärt. Dies ist auf die Komplexität zurückzuführen, welche die zu Grunde liegenden Mechanismen mit sich bringen. Zu diesen Mechanismen zählt beispielsweise die Veränderung des Agglomerationsgrades, welcher eine Folge des Reaktionsfortschritts der Zementhydratation darstellt. Es wird angenommen, dass sich insbesondere die Zunahme an spezifischer Oberfläche auf den Grad der Dispergierung auswirkt. Der Grad der Dispergierung steht in Bezug zu den PCEs. Es gilt zu beachten, dass die PCEs darüber hinaus auch Einfluss auf die Hydratationskinetik nehmen. Von einem experimentellen Standpunkt aus gesehen hinderte der Mangel an verlässlichen Methoden zur Messung der spezifischen Oberfläche Wissenschaftler daran, das Phänomen der Abnahme der Fliesseigenschaften zu quantifizieren.

Folglich liegt der Fokus zu Beginn dieser Arbeit auf der Etablierung verlässlicher analytischer Methoden zur Charakterisierung frischen Zementleims. Die daraus

ermittelten Daten können verwendet werden, um die Fragestellung bezüglich der Abnahme der Fliesseigenschaften in Angriff zu nehmen.

Die Entwicklung der Fliesseigenschaften wurde anhand von Zementleim, welcher PCEs beinhaltet untersucht. Insbesondere wurde dabei erforscht, inwiefern die Abnahme der Fliesseigenschaften in Bezug zum molekularen Aufbau der Polymere steht. Die Dosierung wurde variiert, um eine große Bandbreite an ursprünglicher Fliessgrenze (*yield stress*) abzudecken. Somit war es möglich Veränderungen in Partikelgrösse, spezifischer Oberfläche und adsorbiertem Polymer zu erfassen, um dadurch die Entwicklung der Fliessgrenze genau nachzuvollziehen.

Eine deutliche Abhängigkeit der Entwicklung der Fliessgrenze und Hydratationskinetik von der Wärmeentwicklung (*heat rate*) nach dem Startpunkt (*onset*) wurde postuliert. Der Startpunkt markiert hierbei den deutlichen Übergang von der Induktionsperiode (*induction period*) zur Beschleunigungsperiode (*acceleration period*), nach welcher die Fliessgrenze exponentiell ansteigt. Zum ersten Mal war es möglich aufzuzeigen, dass zwei verschiedene Prozesse – einer reversibel, der andere irreversibel- vor und nach dem Startpunkt ablaufen. Diese zeigen unterschiedliche Abhängigkeiten von der Hydratationskinetik. Als Folge dessen kann diese nicht durch eine einzelne Gleichung beschrieben werden.

Die Zunahme der Fliessgrenze nach dem Startpunkt hängt sowohl vom molekularen Aufbau, als auch von der Dosierung der PCEs und der Zunahme der Wärmeentwicklung ab. Nach dem Startpunkt verhalten sich die Hydratationsgeschwindigkeit und Veränderungen der spezifischen Oberfläche proportional zueinander. Dies deutet an, dass der mechanistische Ursprung der Abnahme an Fliesseigenschaften durch die Bildung zusätzlicher spezifischer Oberfläche der Hydrate während der frühen Nukleierungs- und Wachstumsphase begründet werden kann, und nicht durch die Wärmeentwicklung per se. Mit der Einführung eines Zusammenhangs zwischen Fliessgrenze und spezifischer Oberfläche war es möglich, die exponentielle Zunahme der Fliessgrenze quantitativ zu beschreiben. Hierbei wurden zwei wesentliche Faktoren berücksichtigt: Die Veränderung der Partikelgrösse und der Bedeckungsgrad. Beide Faktoren werden

durch die Polymere induziert. Ein wesentlicher Aspekt der Ergebnisse ist die Beschreibung der exponentiellen Beziehung zwischen Fliessgrenze und der adsorbierten Menge an Polymer pro Einheitsfläche Zement.

Die physikalische Interpretation der Abnahme der Fliesseigenschaften als Funktion der molekularen Parameter der PCEs und der Zusammensetzung des Zements, welche im Zuge dieser Arbeit postuliert wurden, können als eine Art „heiliger Gral" der Forschung und Entwicklung an chemischen Zusatzmitteln für Zement betrachtet werden. Die Möglichkeit die Fliessfähigkeit von Beton in Abhängigkeit von der Zeit genau einstellen zu können, ist von höchster praktischer Relevanz, da es die Einführung neuer Generationen an Kompositzement und die Entwicklung robuster Formulierungen für Zusatzmittel wesentlich vereinfacht.

Abstract

Superplasticizers are polymeric dispersants widely used in concrete technology. Their last generation, polycarboxylate ethers-based comb copolymers (PCEs), are the most efficient ones providing excellent dispersion as well as enhanced workability, durability, and strength development. One of the most relevant problems of superplasticized concrete is the flow loss over time. In practice, an unexpected flow loss could lead to serious problems of placement and finishing of concrete. Such problems are usually improperly solved by re-dosing the PCE or – even worse – by adding water on the job site. The extent to which flow loss occurs depends – among several factors – on the type and dosage of the admixture.

Flow loss in superplasticized systems has been mainly explained in qualitative and comparative ways over the past years. This is due to the intrinsic complexity of the underlying mechanism that must involve a change in the agglomeration degree as a result of minor advancements of the cement hydration. Specifically, increasing specific surfaces are expected to modify over time the dispersion degrees given by PCEs that themselves modify hydration kinetics. From an experimental point of view, the lack of a reliable methodology for measuring specific surfaces must have additionally discouraged researchers from attempting to understand the phenomena of flow loss in quantitative terms.

A main initial focus of this thesis has therefore been to establish an ensemble of reliable analytical methods to study fresh cement pastes to obtain the data that has been missing in the literature to confidently attack the question of flow loss mechanisms.

The evolution of the flow properties was investigated on cement pastes with PCEs, specifically examining how flow loss is modified in relation to the molecular structure of polymers. The dosages were also varied to cover a broad range of initial yield stress values. This allowed to properly account for changes in particle size,

specific surface area, and adsorbed polymer over time, making possible an accurate rationalization of the yield stress evolution.

A strong correlation between yield stress evolution and hydration kinetics expressed as heat rate after the onset was established. The onset time marks the clear transition from the induction to the acceleration period after which the yield stress grows exponentially. For the first time, it was possible to demonstrate that two distinct processes – reversible and irreversible – occur before and after the onset, showing different dependencies on hydration kinetics that cannot be described by a single expression.

The increase of the yield stress after the onset depends on the molecular structure and dosage of PCEs and the increase of the heat rate. After the onset, hydration rate and specific surface changes are proportional one to the other. This implies that the mechanistic origin of flow loss lies in the formation of additional specific surface at the early stages of hydrates nucleation and growth rather than in the heat rate per se. Introducing the relation between yield stress and specific surface, it was possible to quantitatively account for the exponential increase of the yield stress through a combination of two main factors: a change in particle size and a change in surface coverage, both induced by the polymers. An essential and original aspect of this result involves having established the exponential dependence of yield stress on the amount of adsorbed polymer per surface unit of cement.

The physical interpretation of the flow loss in relation to the molecular parameters of PCEs and cement composition reached in this thesis can be considered as one of the *holy grails* of research and development on chemical admixtures. The ability to properly tune concrete fluidity over time is of major practical relevance, facilitating the implementation of new generations of blended cements and the development of robust admixtures formulations.

Riassunto

Gli additivi superfluidificanti sono largamente usati nel campo del calcestruzzo come disperdenti polimerici. I superfluidificanti di ultima generazione, policarbossilati eteri (PCEs), sono i più efficienti in quanto forniscono un'eccellente dispersione, migliori performances in termini di lavorabilità, durabilità e sviluppo di resistenze meccaniche.

Uno dei problemi più rilevanti in calcestruzzi in presenza di PCEs è la perdita di fluidità nel tempo. In particolare, un'inaspettata perdita di fluidità può portare a seri problemi durante la messa in opera e rifinitura del calcestruzzo. Questi problemi sono solitamente risolti in modo inadeguato ridosando l'additivo o – nel caso peggiore – aggiungendo acqua in cantiere. L'entità con la quale avviene la perdita di fluidità dipende, tra vari fattori, sia dal tipo che dal dosaggio dell'additivo.

Negli anni passati, la perdita di lavorabilità in sistemi additivati è stato per lo più spiegato in modo qualitativo e comparativo. Questo è dovuto all'intrinseca complessità del meccanismo di fondo che comporta un cambiamento del grado di agglomerazione come risultato dell'idratazione del cemento. Più nello specifico, ci si aspetta che un aumento dell'area superficiale specifica modifichi il grado di dispersione nel tempo dato dai PCEs, che al loro volta, modificano la cinetica di idratazione. Dal punto di vista sperimentale, la mancanza di metodologie affidabili per la misurazione della superficie specifica ha scoraggiato i ricercatori dal cercare di capire i fenomeni relativi alla perdita di lavorabilità in modo quantitativo.

L'obiettivo principale di questa tesi è quindi stato quello di stabilire un insieme di metodi analitici affidabili per lo studio di paste di cemento fresche al fine di ottenere dei dati ancora mancanti in letteratura che permettano di approfondire il problema della perdita di lavorabilità.

L'evoluzione della fluidità è stata investigata in paste di cemento con PCEs, esaminando nello specifico come la perdita di fluidità viene modificata in relazione alla struttura molecolare dei polimeri. Questo ha permesso di spiegare in modo

appropriato i cambiamenti delle dimensioni delle particelle, della superficie specifica e del polimero adsorbito nel tempo, rendendo possibile un'accurata razionalizzazione del cambiamento nel *yield stress*.

È stata stabilita un'importante correlazione tra i cambiamenti di *yield stress* e la cinetica di idratazione espressi in termini di *heat rate* dopo l'*onset*. Il tempo di *onset* delimita una transizione chiara tra il periodo di induzione e quello di accelerazione dopo il quale *yield stress* cresce in modo esponenziale. Per la prima volta, è stato possibile dimostrare che avvengono due processi diversi – reversibile e irreversibile – prima e dopo l'*onset*, mostrando diverse dipendenze sulla cinetica di idratazione che non possono essere descritte da una sola singola espressione.

L'aumento di *yield stress* dopo l'*onset* dipende dalla strutta molecolare e dal dosaggio dei PCEs e dall'aumento di *heat rate*. Dopo l'*onset*, i cambiamenti della velocità di idratazione e della superficie specifica sono proporzionali gli uni agli altri. Questo implica che l'origine meccanicistica della perdita di fluidità stia nella formazione di una superfice specifica aggiuntiva durante i primi stadi di nucleazione e crescita degli idrati piuttosto che nei cambiamenti di *heat rate* in sé. Dall'introduzione della relazione tra *yield stress* e superficie specifica, è stato possibile spiegare in modo quantitativo la crescita esponenziale del *yield stress* attraverso la combinazione di due fattori principali: i cambiamenti della dimensione delle particelle della copertura della superficie (*surface coverage*), entrambi causati dalla presenza dei polimeri. Un aspetto originale ed essenziale di questo risultato comporta l'aver stabilito la dipendenza del *yield stress* con la quantità di polimero adsorbito per unità di superficie di cemento.

L'interpretazione fisica della perdita di lavorabilità in relazione ai parametri strutturali dei PCEs e la composizione del cemento raggiunta in questa tesi può essere considerata alla stregua del *Sacro Gral* nella ricerca e sviluppo nel campo degli additivi superfluidificanti. La capacità di variare in modo appropriato la fluidità del calcestruzzo nel tempo è un tema di grande importanza pratica, in quanto facilita l'impiego di cementi miscelati (*blended cements*) di nuova generazione e lo sviluppo di versatili formulazioni di additivi.

Contents

List of figures

List of tables

Glossary

Cement notation

C	Calcium oxide, CaO
S	Silicon dioxide, SiO_2
A	Aluminium oxide, Al_2O_3
F	Iron oxide, Fe_2O_3
$	Sulfur trioxide, SO_3
H	Water, H_2O
C_3S	Tricalcium silicate
C_2S	Dicalcium silicate
C_3A	Tricalcium aluminate
C_4AF	Calcium alumino-ferrite
C-S-H	Calcium-silicate hydrates
CH	Portlandite / calcium hydroxide $Ca(OH)_2$
AFt	Ettringite / trisulfo aluminoferrite
AFm	Monosulfoalumino ferrite
DH	Gypsum

Acronyms

OPC	Ordinary Portland cement
SCM	Supplementary cementitious material
PCE	Polycarboxylate ether
LS	Lignosulfonate
PNS	Polynaphtalene sulfonate
PEG	Polyethylene glycol
FBW	Flexible backbone worm
SC	Side chain
BB	Backbone
C/E	Carboxylate to ester ratio
P	Side chain length
N	Number of monomers in BB for one SC
n	Number of SCs for one molecule
w/c, w/s	Water to cement or solid ratio
UPW	Ultrapure water
APS	Artificial pore solution
IPA	Isopropanol
DEE	Diethyl ether

ICP-OES   Inductively Coupled Plasma - Optical Emission Spectrometry
PSD   Particle Size Distribution
SEM   Scanning Electron Microscopy
TGA   Thermogravimetric analysis
XRD   X-ray diffraction
XRF   X-ray fluorescence
TOC   Total Organic Carbon
SEC   Size Exclusion Chromatography

Rheology and flow loss notation

τ_0 Yield stress
μ_p Plastic viscosity
ϕ Volume fraction
θ Surface coverage
u   Yield stress gain coefficient
ν Rate of flow loss coefficient
ν^* Revised rate of flow loss coefficient
α Degree of hydration
OS   Onset
τ_0^* Normalized yield stress

Chapter 1
Introduction

1.1 General introduction

One of the essential problems of superplasticized concrete is the loss of fluidity over time. The extent to which this happens depends – among several factors – on the type and dosage of the admixture.

Flow loss is an issue of practical relevance since the required fluidity retention of concrete depends on each intended application. In ready-mix concretes, the main requirement is a good slump retention until the concrete is placed on site. This period of time might be quite long: namely because of traffic jams or long distances from the concrete plants to the job sites. On the other hand, precast concretes require a higher water reduction, whereas the fluidity must only be retained during the first 30 minutes after mixing. On the job sites, the ease with which concrete is processed is an extremely important aspect to ensure fast placing, thus reducing the labour costs.

In all these cases, a premature flow loss generally can lead to:

- poor consolidation with negative consequences on strength and durability;
- disposal of the concrete;
- adding water (legally or not) to recover the necessary workability for the casting, detrimentally compromising long-term performance and durability;
- re-dosing of the superplasticizer, which, if overdosed, can lead to segregation.

The addition of high range water reducers, also called superplasticizers (SPs), provides excellent dispersion, which makes it possible to produce high quality concrete with enhanced workability, durability, strength and/or reduced environmental impact. These admixtures have therefore become an essential ingredient of modern concrete. In particular, polycarboxylate ethers (PCEs) are now the most important type of superplasticizers on the market and are the ones studied in this thesis.

The molecular structure of PCEs is that of comb copolymers with variable molecular architecture. They are used either alone or in combination with other compounds in commercial products [1], accounting for an annual production of about two million tonnes in the construction field [2].

The working mechanism of superplasticizers involves first the adsorption on cement particles. Adsorbed PCEs then play a key role at the solid/liquid interface acting as dispersants thanks to the steric repulsion associated with their non-adsorbing polyether side chains [3–5]. By doing so, they control the state of flocculation that, in turn, has a strong effect on the rheological properties.

Several factors could affect this fundamental mechanism of action. Among them, the adsorption of PCEs on cement particles can be compromised by either a competition with other ions present in the pore solution or a possible sequestration by aluminates hydrates, reducing their dispersing action [5–8].

The latter case has been proposed to involve either an intercalation in AFm [5,6] or an increase in the specific surface area due to an enhanced formation of aluminate hydrates [9]. Both cases involve an effective increase in specific surface with negative consequences on fluidity [10]. However, the mechanisms and, therefore, the remedies to them are different. Most recent results point more to the creation of additional surface and it has been the objective of this thesis to examine this question critically and quantitatively.

In practice and to some extent, these perturbing phenomena can be tuned by varying the admixture dosage to reach the desired initial fluidity. However, the subsequent evolution is much more problematic to manage. Furthermore, the

transient nature of the bonds forming among hydrating cementitious phases complicates the evaluation of the rheological properties. Due to the complexity of both of these processes and of cementitious systems themselves, flow loss phenomena in superplasticized systems have been mainly explained in qualitative and comparative ways over the past years [11–13].

A physical interpretation of the flow loss in relation to the molecular parameters of PCEs and cement composition can be considered as one of the *holy grails* of research and development on chemical admixtures. The ability to properly anticipate and regulate concrete fluidity over time would be a tremendous practical benefit [14]. In particular, it would facilitate the use of new generations of blended cements with reduced environmental impact, in addition to paving the way for robust admixtures combinations.

This PhD tackles fundamental scientific questions relating to this ambitious goal. Specifically, it focusses on the conditions causing flow loss of cement pastes. To generate truly novel and quantitative insight into this question required the development of reliable analytical methods to study fresh cement pastes in terms of specific surface and aqueous phase composition. A quantitative relation is obtained explaining changes of yield stress after the onset in relation to changes in particle size and polymer adsorption per unit surface. This detailed understanding should pave the way to a knowledge-based design of concrete formulations having both a reduced environmental impact and predictable performance.

1.2 Objective of the thesis

The main aim of this work is to study how comb-shaped copolymers induce and affect the flow loss of cement pastes. The evolution of the flow properties is investigated on cement pastes with PCEs, specifically examining how it is modified in relation to the molecular structure of polymers. The dosages are also varied to cover a broad range of initial fluidity values.

A fundamental question is to determine if and to what extent this phenomenon is related to the increase of cement surface area caused by hydration. Indeed, with a higher specific surface, the number of contact points between particles and the average force at these points should increase. While conceptually simple, this view point required a quantitative experimental approach able to incorporate considerations on the molecular structure and dosage of PCEs.

From this perspective, the impact of PCEs on early hydration kinetics should play an important role. This has allowed us to capitalize on recent results regarding the retardation induced by PCEs [15,16]. Similarly, to those studies, this thesis has made it possible to rationalise all results in terms of a master curve, whereby flow loss can be expressed as a function of molecular structure, dosage and hydration kinetics.

1.3 Structure of the manuscript

The manuscript is structured as follows:

Chapter 2 presents the state of the art of the research. It is divided in 5 parts dealing with comb-shaped polycarboxylate superplasticizers (PCEs), cement hydration with and without PCEs, adsorption of superplasticizers and rheology of cementitious systems. Parts of these sections include the personal contribution published as three chapters of the book *Science and Technology of Concrete Admixtures* [10,14,17].

Chapter 3 establishes and describes a reliable method to measure the specific surface area of cementitious materials by nitrogen adsorption adopting the BET model for the data analysis. This was initially developed on anhydrous cement and synthetic ettringite and validated on early-aged superplasticized cement pastes. Part of the chapter is dedicated to the stop of hydration by solvent replacement. The presented protocols, providing robust experimental results, overcome previously known issues in the sample preparation of delicate hydrating cementitious systems. This chapter has been published as two journal and one conference papers [18–20].

Chapter 4 reports the development of an ICP-OES method for the characterization of cementitious pore solutions from superplasticized early-aged cement pastes. The

main challenge was the quantification of ultratrace elements in pore solutions, the latter being very concentrated matrices. Besides, it was evidenced how the addition of PCEs cause major changes in cement pore solutions, from the alteration of both dissolution and nucleation of cement phases. A robust characterization of pore solutions is therefore crucial for a detailed understanding of the working mechanisms of chemical admixtures. This chapter consists of a journal paper recently published in *Cement and Concrete Research* [21]. It has been featured as "Highlight of Analytical Sciences in Switzerland" in a recent issue of *CHIMIA*, the Official Membership Journal of the Swiss Chemical Society (SCS) and its Divisions [22].

Chapter 5 analyses the effect of PCEs on the evolution of the fluidity in cement paste showing the relation between increase of yield stress and heat rate. Part of this chapter includes the detailed description of the principle we use to define correctly the onset time, after which the yield stress shows an exponential growth. Based on this, it was possible to identify an authentic master curve showing the dependence of the flow loss on the molecular structure and dosage of PCEs. Results in this chapter are not yet published.

Chapter 6 introduces a clear distinction between the induction and the acceleration period through a clear and quantitative approach. It also establishes a novel approach to express the dependence of yield stress on surface coverage. This proves to be essential in the analysis of the master curve on which this chapter focusses. The essential result is that changes in yield stress can be quantitatively related to changes of particle size and surface coverage. This is the main and most original result of this thesis, which heavily relies on the methods developed in the previous chapters. Results in this chapter are not yet published.

Chapter 7 presents the general conclusions and the outlook of this thesis.

The graphical depiction of the manuscript structure is reported below, where the circles are the chapter numbers.
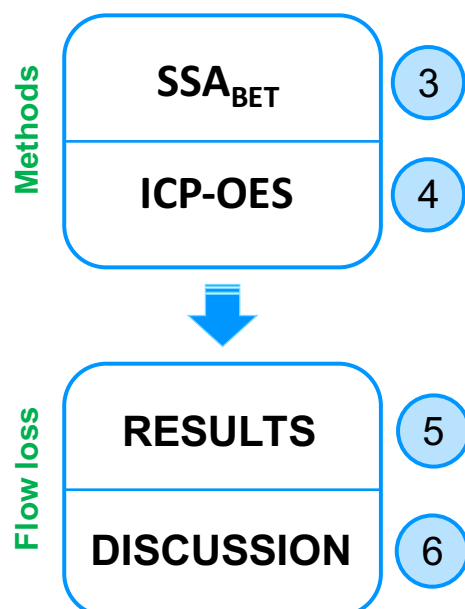
Chapter 2
State of the art

Part of this chapter is based on the personal contributions to three chapters written as second author by Sara Mantellato for the book *Science and Technology of Concrete Admixtures* [10,14,17]:

- Section 2.3.1 of the present chapter is based on section 10.2 in *Chapter 10 – Adsorption of chemical admixture* [10];
- Sections 2.3.4 and 2.4.4 of the present chapter are based on sections 16.4.1 and 16.3, respectively, in *Chapter 16 – Superplasticizers in practice* [14];
- Sections 2.4.1-3 of the present chapter are based on sections 7.2-4 in *Chapter 7 - Concrete rheology: a basis for understanding chemical admixtures* [17]

2.1 Cement hydration

Clinker is the main component of Portland cement and it consists of four main phases: alite, an impure form of C_3S, belite, an impure form of C_2S, and an interstitial phase composed of two phases based on tricalcium aluminate (C_3A) and tetracalcium aluminoferrite (C_4AF). During the grinding of clinker, a sulfate carrier, either gypsum or one of its dehydrated forms, is added to the clinker to form Ordinary Portland Cement (OPC).

The OPC hydration involves the dissolution of these phases in solution and the precipitation of new hydrates. The hydration products from silicates hydration include a calcium silicate hydrate (C-S-H), sometimes referred to as a gel because of its lack of long-range order, and a crystalline phase called portlandite (calcium hydroxide). The hydration of aluminates in presence of calcium sulfate leads to the formation of two different families of phases: trisulfoaluminoferrite hydrates (AFt) and monosulfoaluminate hydrates (AFm).

2.1.1 Hydration of aluminates

C_3A accounts for about 5-15% of the total mass of OPC. C_3A plays a major role in the first hours of hydration, impacting mainly the rheological performance, with minor effects on the mechanical properties. In absence of sulfates, C_3A reacts quickly with water leading to the formation of meta-stable calcium aluminate phases having a double layered structure with hexagonal symmetry, C_4AH_{19} or C_4AH_{13} and C_2AH_8 [23]. With time, they finally transform to a stable hydrogarnet product, C_3AH_6. This process leads to a rapid and inexpedient setting, called *flash set*, that limits the workability timeframe, but also silicates hydration [24].

The addition of calcium sulfates (typically about 5 wt % with respect to the overall content of the cement) during the grinding of clinker enables slowing down the setting. In presence of sulfates, the hydration of C_3A leads to the formation of ettringite (AFt):

$$C_3A + 3C\$H_2 + 26H \rightarrow C_6A\$_3H_{32} \qquad\qquad \textbf{(2.1)}$$
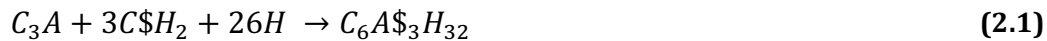
Ettringite presents different morphologies that can vary from short hexagonal prisms to long needles, depending on the degree of supersaturation [25]. Ettringite is stable as long as the concentration of sulfates in solution is high enough, which can generally be related to whether calcium sulfates are still available in the system.

As the calcium sulfate content decreases, monosulfoaluminate (AFm) forms from the reaction of the previously formed AFt with the remaining C$_3$A.

$$2C_3A + C_6A\$_3H_{32} + 4H \rightarrow 3C_4A\$H_{12} \qquad\qquad \textbf{(2.2)}$$

As shown in Figure 2.1, the heat rate evolution of the C$_3$A hydration in presence of gypsum shows different steps [26]. C$_3$A hydration is a dissolution/precipitation process in which the key factor is the sulfates content in solution. Just after the first seconds of mixing with water, C$_3$A dissolves quickly in presence of gypsum releasing a high amount of heat that is reflected by an intense exothermic peak in the calorimetry curve (stage a in Figure 2.1a). After this initial period of rapid reaction, a deceleration of the hydration occurs while the presence of sulfates still ensures the formation of ettringite from aluminates released by the continued C$_3$A dissolution (Figure 2.1b), as shown during the stages b and c in Figure 2.1a.

Pratt and Scrivener [28] questioned the possibility that ettringite needles, in the form of hexagonal rods, could form an effective coating as proposed previously [23,24], suggesting, in turn, the formation of disorganized gel-like layer. Years later, the composition of this layer was identified as small needles of ettringite with a massive presence of AFm sheets in C$_3$A-gypsum system. However, it was also clearly shown that C$_3$A surface is coated even without gypsum [25,26,29]. The fact that only the system with gypsum shows a deceleration therefore discredits the theory of the diffusion barrier. Minard et al. [26] observed that the duration of the slow reaction linearly extends as the gypsum content increases and the C$_3$A surface area decreases. The formation of ettringite and the gypsum dissolution occur at the same

rate, implying that the hydration reaction is controlled by the C$_3$A dissolution which is slowed down by the adsorption of sulfate ions on reactive sites.
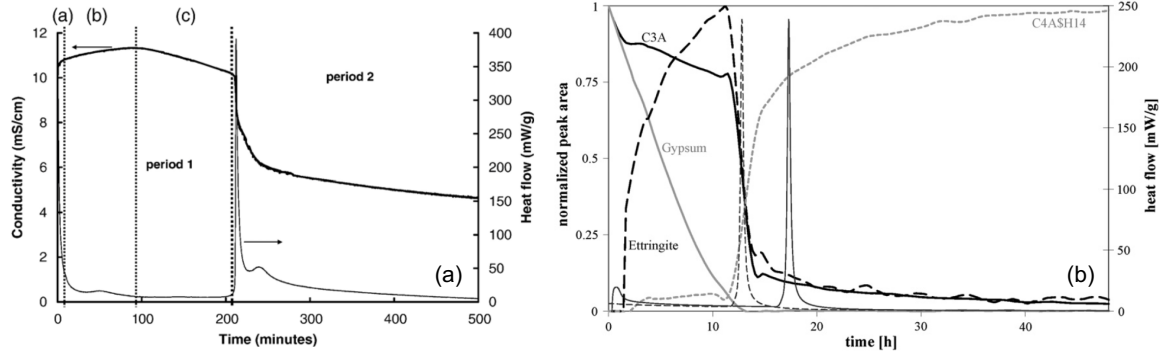
Figure 2.1: (a) Heat rate and conductivity measurements during C$_3$A hydration with gypsum in saturated solution with respect to portlandite from Minard et al. [26]; (b) Evolution of the phase assemblage monitored by in-situ XRD combined with heat flow measurements for a pure C$_3$A-gypsum system (35% gypsum) from Quennoz and Scrivener [27].

When all the calcium sulfate is consumed, an acceleration of the C$_3$A dissolution rate is observed corresponding to the second sharp exothermic peak followed by an exponential decay (Period 2 in Figure 2.1a). At this stage, AFm platelets start forming (Figure 2.1b). However, AFm formation might be hindered in favour of ettringite precipitation by replacing gypsum with a more soluble hemihydrate [30]. This heat rate evolution has been recently explained from the nucleation and growth of AFm phases on dissolving C$_3$A surface. The acceleration is related to the formation of AFm nuclei on the free C$_3$A surface. This, in turn, depends on the initial gypsum content, that limits the dissolution of C$_3$A, as explained previously. When the growing hydrates start impinging, a deceleration is observed [27].

2.1.2 Hydration of alite

The C$_3$S, referred to alite, constitutes about 50-70% of the total mass of OPC. Alite is a form of tricalcium silicate with impurities of aluminium, magnesium, iron, or sodium. From its hydration, C-S-H and portlandite (CH) precipitate.

$$C_3S + (3 - x - n)H_2O \rightarrow C_x - S - H_n + (3 - x)CH \qquad \textbf{(2.3)}$$
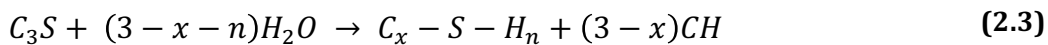
where *n* represents the water to silicate ratio in C-S-H.

The hydration of alite can be divided in five periods according to the calorimetry curve, as shown in Figure 2.2. These stages, discussed in the following subsections, are interpreted in relation to different rate limiting mechanisms.
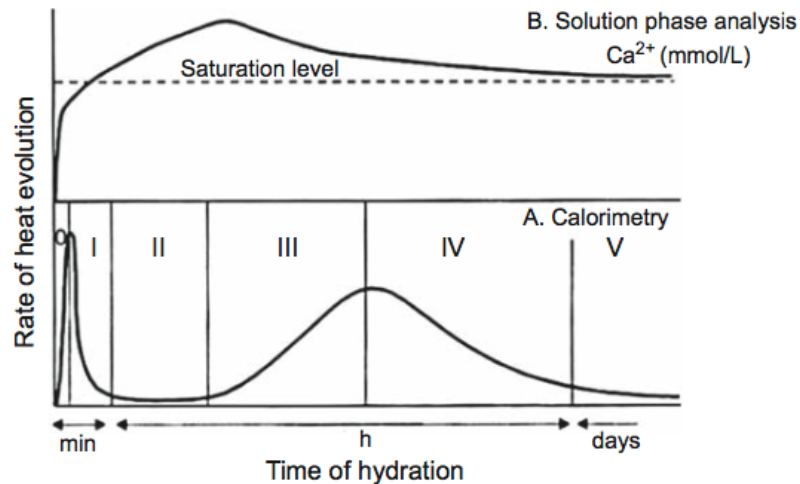
Figure 2.2: Illustration of the different stages of alite hydration following the Ca²⁺ concentration evolution and the associated heat flow measured by isothermal calorimetry [31].

2.1.2.1   Initial dissolution and induction period (Stages I and II)

The initial dissolution of alite is represented by the first exothermic peak in the heat rate curve (stage I in Figure 2.2). This stage is followed by a rapid decrease of the heat rate in the first minutes of hydration. As alite is a very soluble phase, a high supersaturation is reached in the aqueous phase with respect to C-S-H and portlandite with the consequent rapid precipitation of these phases. Therefore, both the first deceleration step and the induction period (stage II in Figure 2.2) are theoretically not expected and their occurrence is still a matter of debate [32]. Three main theories have been proposed in the past years for explaining the transition between these two hydration stages.

The former theory involves the formation of an impermeable protective layer made of a metastable form of C-S-H that covers alite particles preventing its further dissolution [33]. The breakage of this layer due to either the formation of a more stable and soluble C-S-H [33,34] or a change in osmotic pressure [35] could explain

the end of the induction period. However, no clear evidences experimentally confirmed such insoluble layer [36,37].

The geochemical theory, in which the dissolution rate is dependent on the undersaturation of the solution with respect to the dissolving phases, is then favoured to explain this mechanism [38–40]. As long as the system undersaturation is high, a fast dissolution occurs through the simultaneous formation of etch pits on the surface defects combined with step retreat. However, approaching a threshold degree of undersaturation, in correspondence to the portlandite saturation, the dissolution rate substantially slows down [38,41]. By decreasing the undersaturation, the dissolution process is governed by step retreat of the pre-existing etch pits [38]. This slow dissolution might be explained adducing either the hydroxylation of the C_3S surface [38,39], that reduces its solubility, or passivation of etch pits opening. This view is supported by recent findings showing that the C_3S surface is hydroxylated even before the contact with water and that the number of hydroxylated silicates remain roughly constant until the end of the acceleration period [42].

The latter theory considers the formation of C-S-H nuclei just after few minutes from the initial contact with water [43,44]. This is supported by analyses of solution compositions showing a drop of the silicon concentration at the end of the induction period [45]. In addition, the promoted nucleation induced by the addition of C-S-H seeds in cementitious systems leads to a faster C_3S hydration, eliminating, at extreme cases, the induction period [46]. This suggests that the induction and the acceleration period are controlled by the nucleation and the growth of hydrates, coupled with the first dissolution stage. This theory, however, fails to clarify the first rapid deceleration step.

2.1.2.2   Acceleration period (stage III)

The beginning of the acceleration period is represented by the massive increase of the heat rate measured due to an increased C_3S dissolution (stage III in Figure 2.2). At this stage, both C-S-H and Portlandite start growing rapidly. The formation of C-S-H is responsible for the hardening and the strength development of hydrating

cementitious matrices. It is a poorly crystalline phase with a variable stoichiometry, whose Ca/Si ratio is approximately 1.7.

Portlandite nucleation and precipitation, very often observed as small bump at the end of the induction period [47,48], has been suggested as a possible trigger for the accelerated hydration rate [49]. This is inferred from a change of the solution composition with the drop of calcium concentration leading to a renewed C_3S dissolution [47,50], rather than a mere presence of portlandite nuclei. However, this theory remains still controversial because the resulting interpretation is influenced by the theory used to explain the induction period [49].

The acceleration period is widely believed to be due to the growth of C-S-H, that lowers the ionic concentration towards a new undersaturation state promoting alite dissolution. However, it remains unclear whether the growth rate is affected by a critical size and amount of small nuclei [45,46], changes in morphology and/or composition of the C-S-H – in form of aggregates of nanoscale particles [51–54], defective sheets of silicate layers [55,56] or polymerized silicates [42]–, or changes in the distribution and orientation of C-S-H in the pores [57].

2.1.2.3   Deceleration period (Stages IV and V)

The deceleration period (stage IV in Figure 2.2) has been explained by different theories: from the densification of the loosely packed C-S-H due to space restriction [58] to the impingement among growing hydrates [58,59], and the slower diffusion of ions through the hydrates [43–45,50].

The view that densification of C-S-H plays a dominant role is supported by μic (an open-source three-dimensional microstructural modelling platform) simulation and ESEM observations [57,58]. Specifically, C-S-H grows as needles with a well-defined shape outside the grains until the surface is covered and a new densified C-S-H starts growing. However, this cannot explain alone the lower rate of hydration at this stage.

Another interpretation was proposed by Garrault et al. [43–45]. It states that water access to the surface of hydrating C_3S becomes limited because of the formation of a

hydrated shell around the grains. In this case, the hydrated layer thickness is much larger than the layer that some researchers advocate to control the initial hydration phase. Specifically, Garrault and co-authors propose that the onset of the deceleration depends on a balance between growth rates parallel and perpendicular to the surface.

In contrast, Bazzoni [57] evidenced that the densified C-S-H preferentially grows at the interface between anhydrous grains and the previously formed needles. In other words, these observations tend to rule out the presence of an impermeable layer to account for the deceleration period. The argument about C-S-H densification might be linked to the formation of polymerized C-S-H having longer chains that Pustovgar et al. [42] showed to start forming at the onset of the deceleration. Such a process would slow down the dissolution process reducing the C-S-H growth rate. A similar conclusion was proposed by Bullard et al. [40], who indicated that a decrease in the fraction of C_3S surface that can dissolve (i.e. that is not covered by C-S-H) should be considered as an explanation for the deceleration period. This interpretation differs from the one by Garrault et al., since the surface is not considered to be homogeneously covered.

2.1.3 Hydration of OPC

For a better understanding the hydration of OPC, it is important to take into consideration the synergic interactions among the different phases, involving mainly the balance between silicates, aluminates and sulfates. Without sulfates, the presence of aluminates in solution inhibits the silicate hydration [24,60–62]. At low content of gypsum, the extent of the silicate hydration increases and the sulfate depletion point is delayed. Beyond about 4% of gypsum by the total mass of cement, the sulfate depletion point appears right after the silicate peak (Figure 2.3) [24,63].

As for alite, the hydration kinetics measured by isothermal calorimetry can be divided in five similar steps. The main differences come from the initial precipitation of ettringite, the secondary precipitation of ettringite after the main dissolution peak of C_3S and the formation of AFm phases at the last stage, as shown in Figure 2.3.
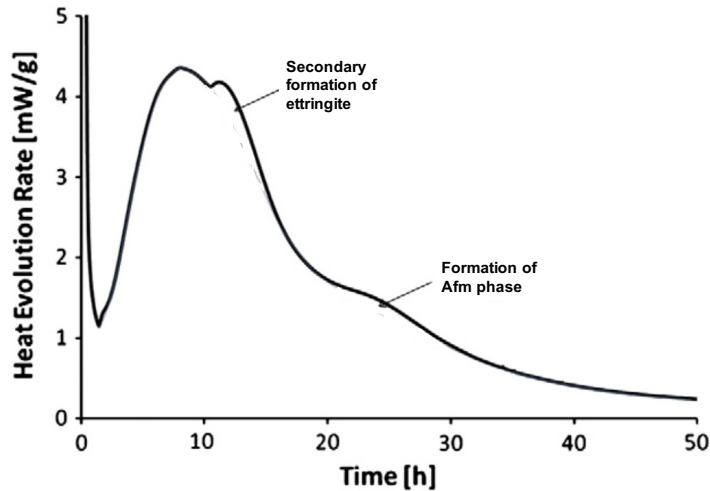
Figure 2.3: Schematic heat rate evolution during ordinary Portland cement hydration.

Many studies demonstrated that the C_3S dissolution is slowed down by the presence of aluminium ions in solutions [60–64]. In particular, a longer induction period was observed either by direct addition of aluminium [62] or release of aluminium from alite [60,63].

Explanations for this behaviour include a surface poisoning through either the adsorption of aluminium ions on pre-existing etch pits [61] or the formation of covalent bonds between Al and silicates (Si–O–Al) stabilized by Ca^{2+} ions [64] that reduce the C_3S dissolution rate. It has been demonstrated that this process is strongly dependent on the pH and aluminium concentration. At mildly alkaline conditions (8 < pH < 12), the C_3S dissolution rate is reduced even at very low aluminium concentrations [61,62,64], whereas the passivation seems to disappear at pH higher than 13 [61]. Recent MD simulations has shown that Al ions desorbs in presence of calcium, sodium and hydroxide ions at pH > 13 [62], confirming the ineffective action of aluminium on the C_3S dissolution rate at any concentration [61].

Furthermore, Begarin et al. [60] indicated that calcium aluminate silicate hydrates (C-A-S-H) formed during the hydration of alite do not act as nuclei to C-S-H growth with the consequent delay of alite hydration. Finally, Quennoz and Scrivener [63] concluded that the presence of aluminate hydrates in the space for the nucleation and growth of C-S-H could be the responsible for the extension of the induction period.

In properly sulfated C_3S-C_3A systems, sulfates cancel the retarding effect of the aluminates causing an early appearance of the main silicate hydration peak and a shorter induction period with respect to the unsulfated system. The presence of sulfates, independently of their addition time [62], results in the consumption of free aluminium ions through the precipitation of poorly soluble ettringite. The aluminium concentration in pore solution is then reduced preventing its negative effect on C_3S hydration [62,63].

2.2 PCE superplasticizers

The latest generation of superplasticizers (SPs) are polycarboxylate-ethers (PCEs). They were developed in the mid-1980 in Japan, but they overwhelmingly entered the market only about fifteen years later, replacing the old-generation polymers based on PNS (Polynaphtalene Sulfonates) and LS (Lignosulfonates). Versatile chemical structures and excellent water reduction capability (up to 40%), showing a good workability retention at low water to cement ratio even at very low dosages, are the main qualities responsible for their massive use.

PCEs are comb-shaped copolymers. The polymeric backbones consist of monomers bearing carboxylic acid groups, typically acrylic or methacrylic acid, to which non-ionic polyether side chains are attached. In alkaline media, the carboxylic groups dissociate conferring a negative charge to the backbone. The anionic backbone of the polymer is responsible for the adsorption of the PCE onto the positively charged cement particles. The dispersing ability is due to the steric hindrance induced by the non-adsorbing side chains. While the adsorption depends strongly on the number of free carboxylic groups, the steric stabilization depends on the amount and length of the side chains of the adsorbed polymer [2,65,66].

Two main synthetic paths are commonly used for the PCEs production in the industry (Figure 2.4): one is the free-radical polymerization of a monomer bearing carboxylic groups and a monomer bearing the side chain; the other approach

consists of the esterification of a pre-formed backbone, bearing carboxylic groups, with monofunctional PEG (polyethylene glycol monomer).
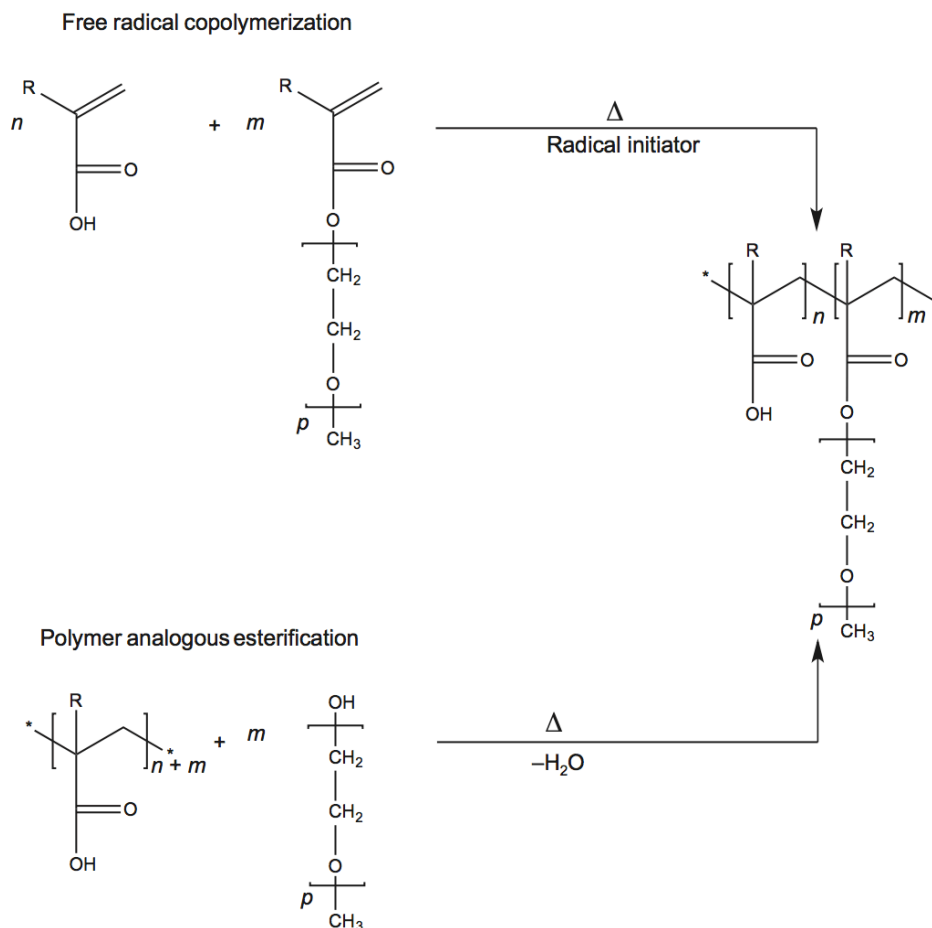
Figure 2.4: Schematic representation of the two main routes for synthetizing an acrylic or a methacrylic-based PCE (R = H, CH$_3$) [2].

The main peculiarities are summarized in Table 2.1. Besides these, controlled radical polymerization techniques have been recently developed, such as Reversible Addition-Fragmentation chain-Transfer (RAFT) polymerization, enabling the production of relatively monodisperse PCEs having a well-controlled architecture [67,68]. The combination of specific monomers in favour of other ones for both backbone and side chain is intentionally studied to change the adsorption capability, and therefore, the rheological properties of PCEs as well as their tolerance against sulfates and clays.

Table 2.1: Main features for free-radical polymerization and esterification

Free-radical polymerization	Polymer esterification
Cheaper and faster due to easy accessibility to monomers	Pre-formed backbone needed (in principle, one more synthetic step)
Gradient distribution of the side chains due to the different monomeric reactivities after activation	Random distribution of the side chains along the backbone
Easy incorporation in the backbone of monomers with different chemical structure	Controlled length of the backbone
High polydispersity	Low polydispersity

2.3 Adsorption

The working mechanisms of numerous chemical admixtures involve the adsorption of water-soluble compounds at a solid-liquid interface. For a given dispersant, its impact on fluidity increases with dosage, provided that the admixture continues to adsorb on the surface of the solid particles to disperse. On the basis of the synthetic nature of PCEs, one can target specific performances by changing the chemistry of the backbone and its length, the number of ionic groups with respect to the side chains (expressed as C/E ratio or grafting density), the length of the side chains, etc. All of these factors affect the adsorption, which in turn affects the rheological properties, as evidenced in numerous papers [11,12,69–73].

2.3.1 Adsorption and fluidity

2.3.1.1   Initial fluidity

The adsorption increases with polymer dosage until the surface of the solid particles is completely covered. At the same time, the fluidity increases and approaches a maximum level that is dictated by the adsorbed conformation of the polymer and the saturation of the surface [12,74] (Figure 2.5).

The polymer affinity for the surface has a critical effect on the amount of polymer that must be added before the surface is covered. For example, a polymer with a low affinity for the surface will have to be dosed in large amounts because a substantial part of it remains in solution rather than being adsorbed. This has led authors to define the so-called saturation dosage, above which a further addition of polymer does not much affect the fluidity.
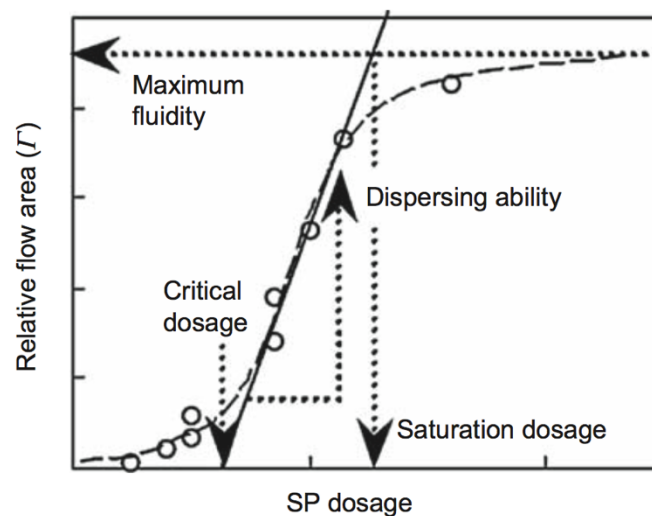
Figure 2.5: Critical and saturation dosages with respect to the dispersing ability. Adapted from Hanehara and Yamada [74].

Another concept that is found in the literature with regard to polymer efficiency is the critical dosage. This is defined as the dosage above which a dispersion effect is noticed. However, values of this dosage are extremely dependent on the experimental conditions, such as the water-to-cement ratio (w/c) or volume fraction, the type of cement, and the type and the chemical structure of the polymer.

2.3.1.2   Fluidity retention

Vickers et al. demonstrated that the loss of fluidity depends on the amount of polymer remaining in solution [13]. This might be explained by considering that a reserve of polymer is available in solution to adsorb on newly formed hydrates [8]. The question of why some polymers that do not adsorb initially would adsorb later in time has two possible answers.

The first is that if there is equilibrium between the solid particles surface and the solution, then the distribution of polymers between both depends on the ratio of the surface area to the solution volume. Consequently, if more surface is created, at least one part of the non-adsorbed polymers will move onto the newly created surface, even if the original surface is not fully covered.

The second reason is that during the initial couple of hours of hydration, most of the hydrates formed are aluminates for which the polymers have a higher affinity. Therefore, we could consider that aluminates may initially be at full surface coverage, but not silicates. As long as polymers are available in solution, they would extensively adsorb on the aluminates while remaining in equilibrium with partially covered silicate surfaces (see section 2.4.3.4).

Apart from this, another general consideration is that the workability is lost much faster in cases of partial surface coverage than of full surface coverage [11]. The explanation lies in the ability of adsorbed admixtures to modify the chemical kinetics of cement hydration and the associated creation of new surfaces that are detrimental to workability. Additionally, partially covered particles more easily let polymers rearrange themselves on their surfaces, which means that contacts between uncoated parts of cement surfaces are more likely. Since these have stronger cohesive forces it is highly detrimental to fluidity.

2.3.2 Adsorption isotherms

The adsorption measurements are typically carried out by solution depletion. In this approach, adsorption is determined by measuring the difference between the amount of admixture added and its fraction remaining in solution after a given time.

Adsorption results are usually reported in terms of surface coverage (θ). In this case, the surface coverage is obtained by dividing the adsorbed polymer by the adsorption at full coverage. The limitation here is that the full coverage does not necessarily correspond to the value at the plateau, mainly in the case of competitive

adsorption. The choice of an appropriate reference material for which the plateau has been reached could overcome this problem.

A valid alternative is to express the adsorption as the ratio between the amount of adsorbed polymer and the surface of the solid, provided reliable surface area measurements can be made. The most common choice, although with the poorest physical meaning, remains the adsorption with respect to the initial mass of solid.

Several models have been proposed to adequately represent the adsorption behaviour of polydispersed and grafted polymers, as in the case of PCEs. The most popular model is the Langmuir adsorption isotherm, where the adsorbed amount is supposed to be proportional to the concentration in solution. This is valid at low polymer concentration and the slope of the linear range gives the adsorption equilibrium constant. However, at higher dosages, the distribution of the polymer between surface and solution is altered and the change in conformation to maximize the adsorption depends on the adsorption energy. At the plateau, the interaction between polymer and cement is dynamic and the equilibrium is a balance between adsorption and desorption. Indeed, it has been demonstrated that polymers are not immobilized on the surface and are more likely to be displaced by water [75] or other ions [7,76].

Adsorption isotherms of superplasticizers show two distinct regimes depending on the concentration of polymer added in solution (Figure 2.6). At low concentrations, adsorption isotherms show a linear range in which the adsorbed amount is proportional to the solution concentrations. In spite of the high affinity observed for LSs in the linear range [77], the adsorption of PCEs is relatively limited and very differentiated depending on the molecular architecture [78]. The linear range can be explained adducing a preferential adsorption of some fractions of polydispersed PCEs with respect to others [69,79]. In contrast, only a constant and small portion of polymer is adsorbed on the free surface, so that the equilibrium between the number of sites occupied and the amount of polymer has to be established. Increasing the solution concentration, polymers tend to rearrange their conformation to minimize the system free energy – enhancing the adsorption

process – until a plateau is reached and the adsorbed amount is independent of the solution concentration [80,81].
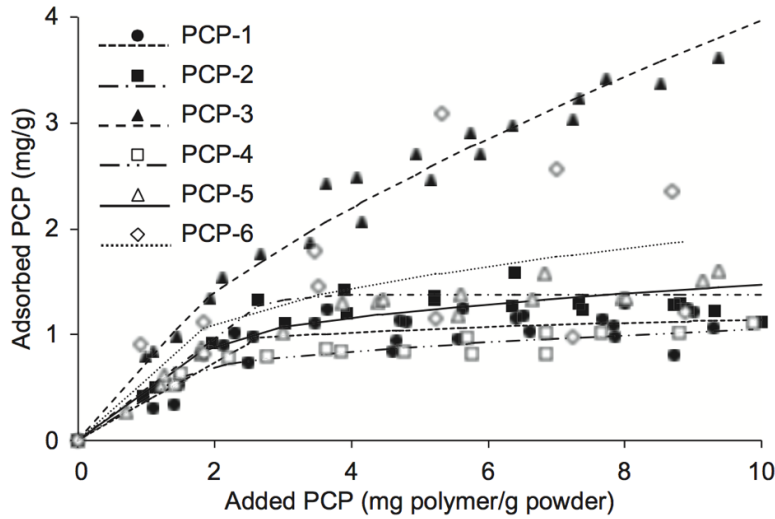
Figure 2.6: Adsorption data of different polycarboxylate polymers plotted as a function of the added polymer amount from Houst et al. [77].

The equilibrium constant provided by Marchon et al. [7], resulting from the ratio between the adsorption (k_A^a) and desorption (k_A^d) rate constants, links the structural parameters of a polymer to its adsorption capability. It considers that the adsorption kinetics is linked to the surface charge density of the adsorbed molecules $z(N-1)/(P^{9/10}N^{3/10})$ and the number of repeating units (n) leading to:

$$K_A = \frac{k_A^a}{k_A^d} = \frac{z^2 (N-1)^2}{nP^{9/5}N^{3/5}}$$
(2.4)

where z is the number of charges carried by each monomer in the backbone, N corresponds to the monomers in the backbone and P the monomers in the side chain (Figure 2.7).

However, it is worth noticing that in cementitious systems the cement surface evolves over time limiting the contact time for the interaction with the PCE and the reaching of a true equilibrium is questionable. Furthermore, PCEs do not adsorb uniformly on the different cementitious phases, rather preferably on aluminates than silicates [82–84].

2.3.3 Adsorption of superplasticizers

Comb-copolymers can be described as the assemblage of n repeating structural units, each containing N or C/E +1 monomers (as C/E = carboxylic to ester ratio) in the backbone and one side chain of P monomers as indicated in Figure 2.7.
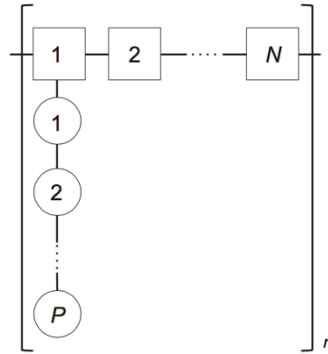
Figure 2.7: Schematic notation of the structure of a comb-shaped copolymer or homopolymer made of n repeat units each carrying one side chain made of P monomers and a backbone segment of N monomers.

Gay and Raphaël proposed various possible chain conformations in good solvent [85]. Based on the structural parameters listed above, five groups can be identified (Figure 2.8). Among them, FBW (Flexible Backbone Worm) conformation can represent common PCEs in a good solvent (as water), having side chains significantly shorter than the backbone.

In solution, the hydrodynamic radius of these polymers (R_c) follows a scaling law of its molecular structure parameters [65,85]:

$$R_C = \left(\left(\frac{a_N}{a_P} \right)^2 \frac{(1 - 2\chi)}{2} \right)^{1/5} a_P P^{2/5} N^{1/5} n^{3/5} \qquad \textbf{(2.5)}$$

This relation was recently confirmed by Gelardi et al. using a combination of methods (SEC, DLS, SANS) [86]. However, some uncertainty on the exact value of the pre-factors was highlighted.

The conformation of such comb-shaped copolymers when adsorbed through their backbones can be derived in a similar way assuming a 2D self-excluding chain of adsorbed cores of which the radius of gyration is:

$$R_{AC} = \left(2\sqrt{2}(1-2\chi)\frac{a_P}{a_N}\right)^{1/5} a_P P^{7/10} N^{-1/10} \tag{2.6}$$

where a_N and a_P are the size of the backbone and side-chain monomers respectively
[65]. For methacrylic acid monomer, a_N = 0.25 nm and for PEG a_P = 0.36 nm. χ is the
Flory parameter and is equal to 0.37 for PEG.
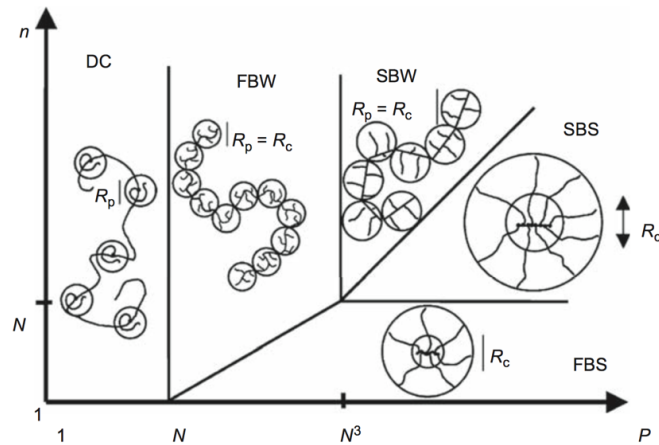
**Figure 2.8: Phase diagram for comb-shaped homopolymers with the structure defined in
Figure 2.7. Reproduced from Gay and Raphaël [85].**

R_{AC} defines the adsorbed layer thickness which plays an important role in steric
hindrance. Additionally, the surface S_A occupied by each molecule on a particle,
expressed in nm^2 per molecule of polymer, can be calculated from:

$$S_A = \frac{\pi}{\sqrt{2}} a_N a_P \left(2\sqrt{2}(1-2\chi)\frac{a_P}{a_N}\right)^{2/5} P^{9/10} N^{3/10} n \tag{2.7}$$

Molecular mass plays an important role in superplasticizer adsorption, regardless of
their molecular nature. Reports about this can be found for sulfonate naphtalene
formaldehydes polycondensates (SNFCs) [87], LSs [88,89], vinyl copolymers [79],
and PCEs [69,71,90]. Also, the adsorption of PCEs is affected by their specific
polydispersity in size and structure [69,79].

The density of ionic groups in the backbone is the most important parameter during
adsorption. Indeed, PCE adsorption increases with the density of ionic groups on the
backbone [12,91]. Interestingly, independent studies from Regnaud et al. [91] and

Winnefeld et al. [69] suggest that adsorption drops strongly below a C/E ratio of 2, regardless of the length of the side chains [92].

2.3.4 Ineffective adsorption

The effectiveness of superplasticizers depends on the number of adsorbed molecules (surface coverage) and on the conformation in their adsorbed state. Any factor affecting them may perturb the performance in the cement fluid state. In particular, various processes can reduce the amount of superplasticizers available per unit surface of fine particles in suspension. These can be summarized as follows:

- Competitive adsorption by which the preferential adsorption of a compound, namely sulfates [76,93], hydroxides [7,94], and retarders [95] prevents the superplasticizer from adsorbing. This depends on the relative affinity of the competing compounds for surfaces as well as on their relative concentrations;

- Formation of organo-aluminate phases [6,96], that sequestrate admixtures in the internal layers of AFm phase [5];

- Adsorption of PCEs onto clay minerals due to the strong affinity of their PEG-based side chains for clay minerals, mainly smectites [97–100];

- Increased specific surface area due to the modification of the surface on which admixtures adsorb. This occurs by the interaction of PCEs with hydration products, mainly ettringite, having higher specific surface area than anhydrous phases [9,101–103].

Due to the limitations of the solution depletion method used for adsorption measurements, an apparent increase of the adsorption degree might be observed in combination with a marked fluidity reduction. This is likely to occur when PCEs are either precipitated or intercalated. It is also expected to occur for adsorption measurements performed over time when additional surfaces are created by hydration, so that the polymer initially remaining in solution is somehow consumed and the yield stress increases. While often discussed in qualitative terms, this

question has never been systematically addressed and it is an important objective of this thesis to do so.

2.4 Concrete rheology

Concrete can be considered as a multiscale material in which solid particles (coarse aggregate) are suspended in a mortar matrix, while the mortar matrix can be viewed as a suspension of sand particles in a finer matrix (cement paste). Concrete can also be seen as a biphasic material, in which rigid sand and coarse aggregate particles are suspended in a cement paste matrix. It is important to mention that the action of chemical admixtures takes place at the paste level and that their effects are felt right up to the concrete level.

The rheology of concrete changes with time, due to reversible physical phenomena (flocculation of its fine particles) and irreversible chemical reactions due to cement hydration. In addition to mix design, concrete rheology is strongly influenced by the concurrent effect of several parameters. Among them, the effect of superplasticizers will be discussed in detail below.

2.4.1 Different rheological behaviour

Rheology is defined as the science of deformation and flow of matter under the influence of stresses [104,105]. It is a science at the intersection of solid and fluid mechanics dealing more specifically with the relationship between shear stress, shear rate and time.

Several rheological models have been proposed to describe the flow curve of materials. These models are identified according to the macroscopic response of the material subjected to various shear rates. The most common models are shown in Figure 2.9.

Unlike the Newtonian model, the Bingham curve does not pass through the origin, although above the yield stress τ_0 [Pa] the increment in shear stress is proportional

to the increment in shear rate and the proportionality factor is called plastic viscosity μ_p [Pa $\cdot$ s] (Figure 2.9).
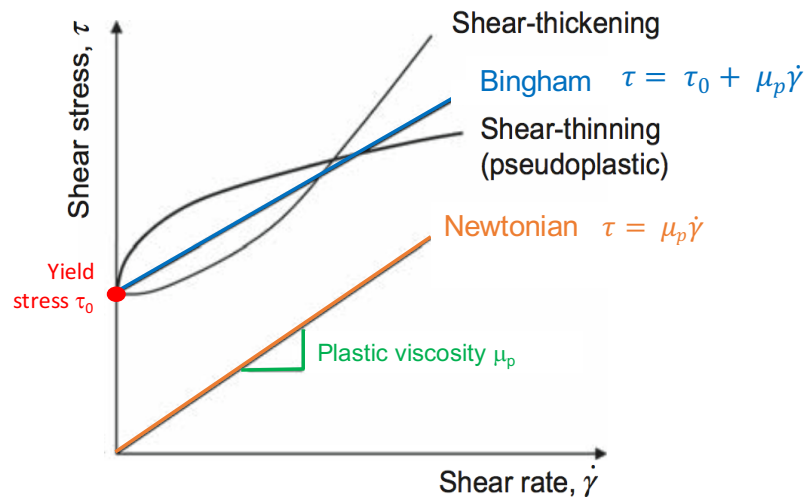
Figure 2.9: Illustration of different rheological behaviours – the cases of shear thinning and shear thickening shown include a yield stress, which is not necessarily always the case.

The Bingham model can be expressed as:

$$\tau = \tau_0 + \mu_p\dot{\gamma} \tag{2.8}$$

Among the non-Newtonian fluids whose viscosity depends on shear rate or shear rate history, two different behaviours can be observed: shear thinning and shear thickening. Shear-thinning fluids are characterized by a decrease in the apparent viscosity when shear rate increases, where the apparent viscosity is defined as the ration $\tau/\dot{\gamma}$ at the value of $\dot{\gamma}$ under consideration. On the other hand, shear-thickening fluids correspond to materials for which the viscosity increases as the shear rate increases. The most commonly used model to describe the rheological behaviour of these fluids is the Herschel-Bulkley model given in Equation (2.9):

$$\tau = \tau_0 + K\dot{\gamma}^n \tag{2.9}$$

where K is the consistency factor and n is the shear-thinning index (shear thinning if $n < 1$, shear thickening if $n > 1$). We note however that with $n > 1$, because of yield stress, the behaviour will be shear thinning initially and then turn to shear thickening at higher shear rates.

Below the yield stress, the mixture does not flow and behaves as an elastic material. A number of other materials apparently do not flow under gravity, and are thus referred to as yield stress materials. The statement that a material does not flow is of course associated with the time of observation. In suspensions such as cementitious materials, yield stress is a consequence of the attractive interparticle forces between cement grains and other fine particles that may or not be in the mix [106,107]. This yield stress is then amplified by the presence of inclusions such as sand and coarse aggregates.

The existence of a yield stress has long been debated [108–110], mainly because of the inherent difficulty in measuring it. Indeed, yield stress is most often determined by the extrapolation of the flow curve to zero shear rate. The accuracy in determining yield stress, therefore, mainly relies on the choice of the rheological models used to describe shear stress/ shear rate flow curves, rheometer geometries [111,112] and material behaviour [113].

Yield stress can be defined as the limit stress below which the material stops flowing and it depends on the applied stress or shear rate. It is therefore the property that controls the casting process [114]. Indeed, a theoretical correlation has been established between yield stress and the shape of the concrete at stoppage measured by slump tests [115–117] or minicone spread tests [93,118,119].

2.4.2 Micromechanical behaviour of suspensions

The rheological behaviour of concrete is profoundly affected by the properties of the paste, and it is at this level that chemical admixtures act. This is influenced by various forces acting in the system, the most important of which can be summarized as follows:

- *Hydrodynamic forces* arise from the relative motion of particles to the surrounding fluid, but dominate for particles larger than 10 μm [120];

- *Colloidal forces* exist between suspended particles and can be attractive or repulsive. Van-der-Waals, electrostatic and steric forces belong to this category;

- *Brownian motion* arises from thermal randomizing forces causing constant translational and rotational movements. However, this is of only secondary importance for the micrometre- size particles found in cementitious systems;

- *Inertial forces* become important as shear rates increase. They can play a role in shear thickening of cementitious systems, even at relatively lower shear rates when the solids volume fraction is high;

- *Gravitational forces* cause segregation of the suspensions unless the particle size and density are balanced by adequate opposing forces (e.g. colloidal, browning or viscous).

2.4.3 Effect of superplasticizers on cement rheology

2.4.3.1   Yield stress

The yield stress originates from the attractive interparticle forces at stake between particles in flocculated systems above the percolation threshold (ϕ_{perc}). Electrostatic forces are also present, but at high ionic strengths they are not sufficiently strong to prevent the particles from agglomerating [121–123]. Hence, a flow is observed when the applied stress is sufficient to break down particle networks.

In a broader context, Zhou et al. [124,125] found that the yield stress increases when increasing the volume fraction and decreasing the particle size for spherical monodispersed alumina powders. They calculated that, without dispersant, the minimum distance between adjacent particles is about 2 nm, independent of the particle size. Compared to conventional vibrated concrete, self-consolidating concrete, which is proportioned with a relatively higher volume of powders to lower friction between aggregates, has a relatively lower yield stress.

Establishing a quantitative relationship for all these parametric dependences is one of the challenges in proposing a model for yield stress. The yield stress model

[126,127] deals with such challenges. It correctly accounts for interparticle forces, the volume fraction of solids, particle sizes and their distribution, and can also be extended to polydispersed powder mixes. It discriminates three main contributions affecting the yield stress (Equation (2.10)). The first accounts for the powder characteristics as the particle size distribution (pre-factor m, particle average diameter d, and radius of curvature a* among particles at contact points) and the Hamaker constant A_0. The second contribution is *h* the interparticle distance, on which superplasticizers play a major role. The third contribution accounts for the impact of volume fraction ϕ, which is affected by, ϕ_m, the maximum packing fraction and the percolation threshold ϕ_{perc}:

$$\tau_0 \cong m \frac{A_0 a^*}{d^2 h^2} \frac{\phi^2 (\phi - \phi_{\mathrm{perc}})}{\phi_m (\phi_m - \phi)} \tag{2.10}$$

The strength of the flocculated network increases with the number of particle contacts, and therefore decreases with particle size. This contribution to yield stress can only be changed by modifying the concentration of the solids. The adsorption of superplasticizers on cement surfaces increases the average separation distance *h*, consequently reducing the maximum attractive interparticle forces, the yield stress and the degree of flocculation.

Yield stress decreases with increasing superplasticizer dosage. Once the surface coverage is completed, the interparticle distance can be estimated based on twice the coiled size of the side chains of PCEs [122]. This approximation is valid as long as the van der Waals forces are not large enough to cause substantial compression of the adsorbed polymers and the side chains start overlapping [92,128]. For a common side chain, molar mass of 1000 g/mol, this interparticle distance is in the range of 5 nm. This average separation distance varies with the conformation and surface coverage achieved by adsorbed admixtures. Both of these relate to the molecular structure of admixtures in different ways. The relationship between yield stress, the polymer structure, and dosage has been confirmed by consolidation experiments [128,129]. Generally, at full coverage, side chains play a key role in terms of dispersions, whereas the grafting ratio is fundamental for the initial

adsorption on particles. At low surface coverage, the situation is more complex and also of greater practical relevance: additional attractive forces become important in those areas where the polymer is not adsorbed and the scaling law, valid at full coverage, cannot be extended at surface coverages lower than 0.6 [123]. A reliable prediction of the performance at low surface coverage, therefore, remains an important and challenging subject that is addressed in this PhD. As a practical consideration, this means that at a very low w/c ratio, PCE polymers with long side chains and high carboxylic to ester (C/E) ratio can counteract more efficiently the attractive forces than polymers with low C/E ratio and short side chains [69]. The effect of superplasticizers on the rheological properties of cementitious materials is strongly linked to the amount of polymer adsorbed onto the surface of cement particles [11,130] (Figure 2.10).
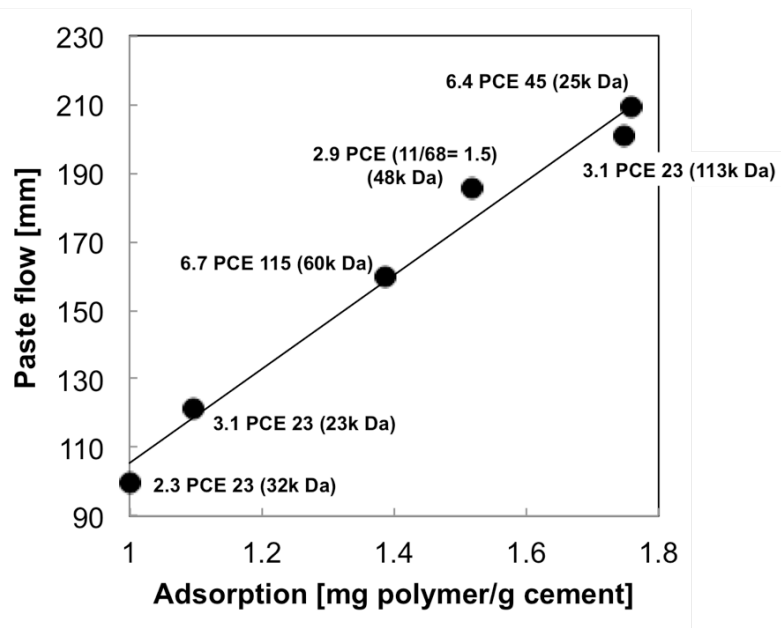
Figure 2.10: Correlation between adsorbed polymer and flow of cement pastes prepared with different PCE polymers having a polymethacrylic-based backbone. Polymer notation indicates the C/E ratio as the first number, the side chain length expressed by the number of PEO monomeric units as the second number, and the molecular weight (Mw) in brackets. The characteristic data of the polymers were obtained combining the data reported in Schöber and Flatt [11] and Houst et al. [77].

It is worth keeping in mind, however, that this simple relationship can be altered by the incompatibility of superplasticizers with cements, observed in the case of sulfate competition [76] and formation of organo-aluminate phases [6].

When the polymer dosage decreases below the saturation dosage, the surface is only partially covered by the polymer and particles tend to stick together in those areas where the polymer is not adsorbed. On the contrary, the plateau at a high dosage corresponds to a complete surface coverage, where particles are well dispersed and the yield stress reaches a minimum value [128].

Saturation and critical dosages can be derived by adsorption isotherms as well as by using flow spread measurements [12], which are related to yield stress. Regarding the saturation dosage, earlier works have proposed to also obtain those by Marsh cone test. However, for low yield stress fluids, this test provides information mainly on the plastic viscosity [131]. Therefore, the Marsh cone cannot reliably be used to detect differences between well-dispersed pastes, although it detects differences between poorly fluid ones.

The identification of critical dosage is not as trivial as for the saturation dosage because it is extremely dependent on the experimental conditions. In a spread flow test, flow initiation occurs if the yield stress of the paste is lower than the gravitational load on the sample, which depends on the sample height [118,132]. Hence, for each and every different mold height, a different critical yield stress should be obtained. Moreover, for specific cementitious systems, this mold-specific limiting yield stress will be reached by the right combination between volume fraction and interparticle forces. The result should therefore also strongly depend on w/c. Provided such limitations are recognized and understood, the critical dosage may nevertheless be some useful comparison criterion between superplasticizers.

2.4.3.2   Viscosity

Concretes with (very) low w/c ratios can have very low yield stresses if enough superplasticizers are added, but they are nevertheless defined as sticky. This is most probably related either to plastic viscosity or to shear thickening. In both cases, the excess of energy needed to increase the shear rate above the yield stress increases with the packing fraction of solids, as when w/c is decreased.

A shear thinning behaviour in superplasticized systems is generally reported in the literature [70,133–135] and results from the yield stress. Above the yield stress, a linear dependence of shear stress on shear rate is often observed, which is why the Bingham model is often used. The slope of this linear regime is referred to the plastic viscosity. However, the range over which the linear regime can be assumed is still under debate.

An answer to this question can be found in the work of Hot et al. [136] who introduced the concept of residual viscosity. This isolates the hydrodynamic contribution from the yield stress by defining the residual viscosity as follows:

$$\mu_{res} = \left(\mu_{app} - \tau_0 / \dot{\gamma} \right) \tag{2.11}$$

where μ_{app} is the apparent viscosity. Using this procedure and testing different polymers at different dosages, these authors found that at low shear rate viscous dissipation decreases with increasing polymer adsorption. This implies that plastic viscosity is also affected by superplasticizers, as for the yield stress [137]. In first order, this effect on plastic viscosity is attributed to a flow resistance of the interstitial fluid between cement particles and is therefore impacted by the separation distance imposed by the steric layer of the adsorbed polymers. A second order effect at equivalent dispersion degree is however also observed, and its extent relates to the conformation of either adsorbed or non-adsorbed polymer [136,137].

Beyond a critical shear rate, the residual viscosity increases, revealing the onset of a shear thickening regime often observed in the presence of superplasticizers [138]. This is mostly detrimental, since more energy is needed to increase the material flow rate, impacting mainly mixing, pumping and extrusion processes [117]. The origin of this phenomenon is still debated, but two main theories are considered here.

The first theory states that the hydrodynamic viscous forces promoting the formation of hydro-clusters overcome Brownian motions, tending to distribute particles evenly in the fluid. This relation is expressed by the Peclet number defined

as $Pe_{\dot{\gamma}} = \mu_0 d^3 \dot{\gamma}/k_B T$, where μ_0 is the viscosity of the suspending liquid, d the particle radius, k_B the Boltzmann constant and T the absolute temperature.

It is worth noting here that Brownian motions are negligible when compared to attractive forces of particles in the size range of 10-50 µm in flocculated systems [138]. In turn, this contribution becomes important when decreasing the particle size, and might compete with reduced colloidal forces [139]. To examine this transition in cement pastes, Roussel et al. [138] calculated that the critical shear rate at which shear thickening occurs should be in the order of 10^{-3} s^{-1}, far below realistic conditions. This theory seems to contradict results showing a decrease in the critical shear rate and an increase of shear-thickening intensity when the dosage of the polymer is increased [136,140].

The alternative theory proposes the dominance of particle inertia over the viscous contributions [138,140]. The critical shear rate decreases with increasing particle size, as implied by the Reynold number $Re = \rho_0 d^2 \dot{\gamma}/\mu_0$, where ρ_0 is the density of the suspending fluid, μ_0 the viscosity of the suspending liquid and d the particle radius.

Comparing results from the literature [141–143], the shear rate at which shear thickening occurs is observed to decrease with the increase of volume fraction ϕ, where the gap between particles becomes smaller. Also, if one considers the residual viscosity discussed above, at a given volume fraction the intensity of the shear thickening is independent on the dosage of polymers, and seems to be promoted only by either collisions or sustained frictional contacts between particles under vigorous agitation [136].

This observation would tend to exclude a possible reduction in surface coverage at high shear rates, earlier proposed by Cyr et al. [144]. Such a surface coverage reduction might occur if polymers cannot disentangle fast enough, so part of the polymer is pulled out of the surface, leading to higher interparticle forces. However, with increasing polymer dosage these sites would be very rapidly reoccupied.

From this point of view, shear thickening should not directly depend on the nature of the superplasticizers, but appears more in highly dispersed systems because of lower volume fractions that can be accessed.

Additionally, it should be mentioned that shear thickening may take place progressively as the shear rate is increased (continuous shear thickening) or discontinuously (discontinuous shear thickening) [145]. Recently, the transition between both modes has been related to a change in the lubrication regimes at particle contacts [146].

2.4.3.3   Thixotropy

Thixotropy is a phenomenon by which the structure of a fluid is broken down under shear and rebuilt at rest [106,107,117]. Thixotropy is therefore a reversible process, and a schematic representation of this can be seen in Figure 2.11.
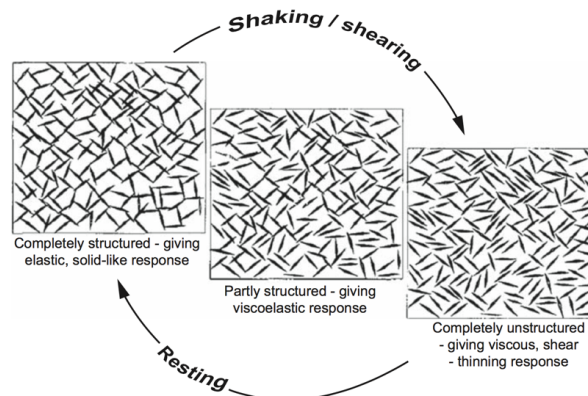
Figure 2.11: Breakdown and build-up of a 3D thixotropic structure. Reproduced from Barnes [106].

In cementitious materials, thixotropy can be present in addition to irreversible structural breakdown. Thus, these materials can exhibit a combination of both reversible and irreversible structural breakdown, only the first of which is associated with thixotropy.

It is worth emphasizing that thixotropy is time-dependent. Immediately after mixing, cement particles are dispersed. At rest, cement particles flocculate due to the colloidal attractive forces and form a percolated network of interacting particles,

causing an increase of the apparent (or static) yield stress. When flowing, the steady state shear stress increases proportionally to the applied shear rate [114,117,147]. At a given shear rate, the viscosity evolves towards a steady-state value and takes a certain time to do so. A non- thixotropic shear-thinning fluid, in contrast, would (almost) immediately reach its steady-state viscosity in response to a change in shear rate.

2.4.3.4   Fluidity loss

Cementitious materials are rather complex, and lend themselves to easy mislabelling of their properties. Indeed, they combine both thixotropy and irreversible structural breakdown. The latter term was introduced by Tattersall and Banfill [104] to emphasize the fact that cementitious materials exhibit shear-dependent behaviour. In particular, when exposed to high shear, as in a concrete mixer, they do not fully recover their previous yield stress. However, the 'residual' yield stress is associated with a microstructure that can be broken down under shear and recovered at rest (or at lower shear rates), which corresponds to true thixotropy.

While thixotropy dominates over short timescales, the irreversible breakdown becomes significant at later times. Kovler et al. [148] defined that, after mixing, the effect of thixotropy dominates rheological changes during about 30 minutes. After that, the role of irreversible chemical reactions cannot be neglected. However, the respective extent of these two phases might be altered by several factors, such as W/C ratio, cement composition and, more importantly, the addition of PCEs.

In the case of non-admixed cementitious systems, Roussel et al. [107] showed that cementitious systems not only have a critical deformation at strains on the order of 10^{-3}, but also one at about 10^{-1}. The first and smallest is attributed to the flocculation between nanoscopic hydrates, suggesting specifically the nucleation of C-S-H bridging particles. The second strain is attributed to the cohesion at the interparticles level, whose magnitude depends on the separation distance among particles. At this stage, the number and the size of C-S-H increase with the formation of stronger and more rigid bonds at the contact points between particles, requiring higher shear to break them. Therefore, hydration is believed to be at the origin of

the fluidity loss when the mixing energy becomes insufficient to break these interparticle connections [107,149,150]. From a macroscopic prospective, the setting process is viewed as the transformation of a cement paste from a viscous suspension to a rigid load-bearing one [149,151]. This corresponds to the start of an exponential increase of the yield stress and is often identified as the end of the induction period in isothermal calorimetry measurements [152–156].

Superplasticized fresh concretes are also well known to lose their workability over time at rates that can be problematic for some applications. The extent to which this happens depends, among several factors, on the type and dosage of the admixture and the mixing procedure. It was demonstrated that non-adsorbed polymer fraction in solution can impact the fluidity over time [8]. This might be explained by assuming either that the reserve of polymer in solution can interact with newly created surfaces or preferential interaction of polymers with aluminates hydrating faster than silicates in the first hours of hydration. Whatever the nature of these surfaces, high surface coverages – and therefore high fluidity – are maintained longer (Figure 2.12).

In terms of molecular structure, in practice, polymers having a lower amount of charges on the backbone (lower initial adsorption) and short side chains should be preferred if extended workability time is desired [12,13]. This would more likely be the case in ready-mix applications. In precast applications, where workability retention requirements are of minor interest, more ionic polymers are generally preferred.

The addition time of chemical admixtures is a very important factor in rheology of cementitious systems. If they are added at the beginning with the mixing water, the hydrating aluminate phase can sequestrate them from the solution either by forming organo-mineral phases [5,6,157] or by adsorption on ettringite, of which the specific surface can be increased in presence of admixtures [9,16]. Consequently, a part of the polymer is not available for dispersing the cement and the fluidity is reduced, although the polymer seems to be adsorbed more extensively. In this case, PCEs depletion takes longer, causing a longer workability [158,159]. However, this may

also impact the initial fluidity that in many cases would be increased. Higher levels of dispersion may be reached and possible segregation may occur. As a result, in most cases, the superplasticizer dosage should be reduced. This, in turn, would reduce the workability time, so that the final benefits are not obvious.
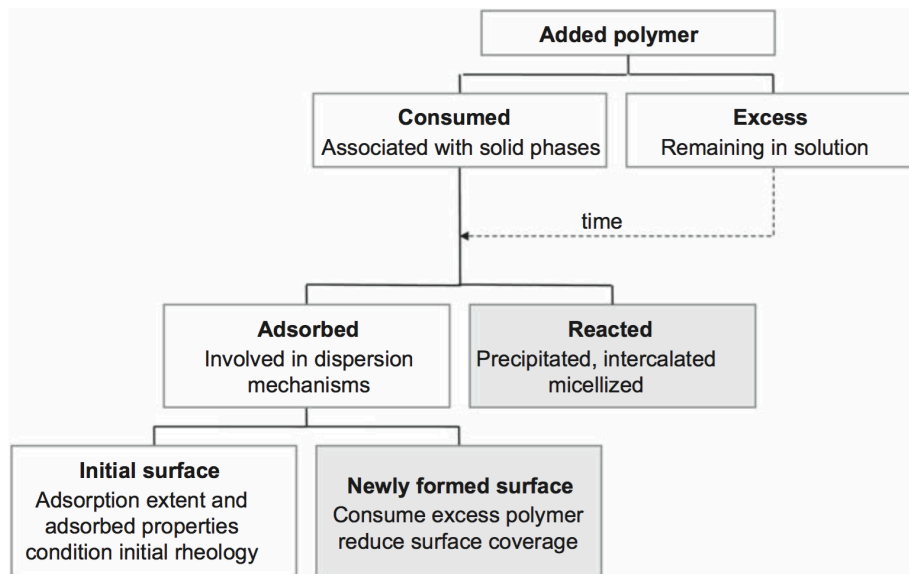
Figure 2.12: Schematic presentation differentiating the polymer that is usually identified as adsorbed (consumed) and the polymer that is actually effective in the dispersion mechanisms. Reproduced from Flatt et al. [8].

The mixing process affects the initial fluidity of concrete as well as its evolution in time [13,160]. Vickers et al. [13] found out that the consumption of the polymer is much higher in concretes than in cement pastes mixed at 700 rpm at the same conditions of w/c ratio, mixing time, and polymer dosage. This is attributed to the fact that the high energy applied on the cement paste in concrete might lead to the formation of precipitates with higher surface area and therefore a higher polymer adsorption capacity [119,160]. The origin of these additional surfaces may result from a more efficient solution exchange on particle surfaces through higher shear, leading to more extensive formation of etch pits and globally faster hydration kinetics [38,160,161]. The important macroscopic observation remains, however, that a faster fluidity loss is generally observed when high shear rates are applied during initial mixing. Ultimately, these effects most likely result from different rates of specific surface generation through hydration reactions and their modification by shear and/or chemical admixtures [160].

Such basic principles involving surface area formation, surface coverage as well as hydration evolution lay the foundations for the understanding of the fluidity loss in presence of PCEs. However, detailed studies about the direct impact of PCEs with different molecular structures and dosages on the evolution of the rheological properties of fresh cementitious systems have been barely reported in literature. In this PhD, we have examined such questions and establish general trends common to a wide range of PCEs.

2.5 Cement hydration with PCEs

As a general observation, superplasticizers delay cement hydration. The retardation does not depend only on their dosage, chemical nature, molecular architecture, and the time of admixture addition, but also on the characteristics of the cement, such as its mineralogical composition, fineness, and sulfate availability. As shown in the calorimetric curves in Figure 2.13, retardation induces a prolonged induction period coupled with a delay of both the onset of the acceleration period and the main silicate peak. In addition, the slope of the acceleration period, the maximum heat release and/or the sulfate depletion point may be affected by the addition of superplasticizers.
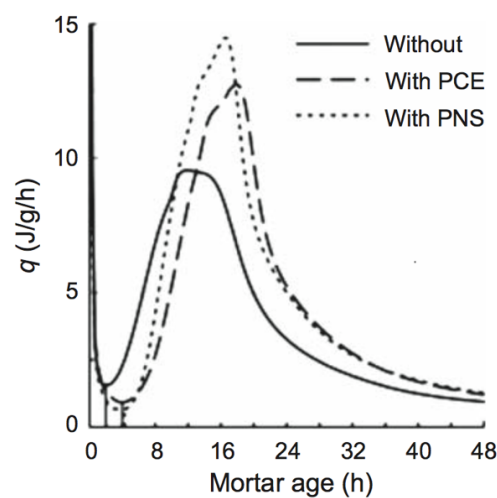
Figure 2.13: Example of isothermal calorimetry showing the effect of a PCE and polynaphtalene sulfonate (PNS) superplasticizer on a mortar with OPC [162].

2.5.1 Effect of PCEs on the formation of ettringite

The nucleation and growth of aluminate hydrates are mostly affected by the presence of superplasticizers [6]. The influence of superplasticizers on the crystal growth and morphology of the hydrates – mainly ettringite – presents a key factor for the macroscopic properties of cement pastes including workability, setting behaviour and development of the microstructure [9,102,163,164].

In sulfonated melamine-formaldehyde (MFS) and polycondensate naphthalene (PNS)-based mixes, thicker and shorter ettringite clusters were found than in plain mixes [165–167]. A detailed ESEM images analysis concluded that both the length (L) and the diameter (D) of the ettringite decrease proportionally one to the other – down to 1.5 µm in diameter – while the amount of added anionic charges is increased [103]. PNS-based polymers inhibit the ettringite growth as long as the polymer sufficiently covers its surface. Later, when the polymer is consumed, the AFt growth – in the form of long needles – is recovered [167].

More interestingly in the context of this thesis, PCEs strongly promote the nucleation of the ettringite, whereas they slow down its growth rate [9,103,168]. It has been recently demonstrated on model cementitious systems that the amount and the specific surface area of the forming ettringite are affected by the dosage, the type as well as the polymer addition mode [9,16,103]. Specifically, highly-charged PCEs promote the formation of small particles of ettringite with higher surface area within the first 30 minutes from the beginning of the hydration [9]. It was evidenced by cryo-microscopy that these particles have a size smaller than 500 nm [169]. Such changes of the specific surface of early-aged cementitious systems might be responsible for a different demand in admixture to achieve a given surface coverage and therefore a given rheological behaviour. However, the importance given to the polymer adsorption on the surface of newly formed hydrates and the resulting effect on hydrates formation is still poorly documented and often studied with questionable methodologies to measure reliably the specific surface area of early-aged cementitious pastes. This is another topic that the present PhD thesis has systematically strived to improve.

In absence of PCEs, AFt particles precipitate on the grains of the anhydrous clinker leading to the formation of agglomerates that are inferred to be responsible for the fast setting of plain cement pastes. After the addition of PCEs, however, a significant fraction of these nanoparticles remains in the interstitial fluid delaying the formation of agglomerates [169]. This aspect has not only practical implications in the macroscopic rheological properties, but also on the preparation, measurements and data interpretation of superplasticized cementitious pore solutions.

2.5.2 Mechanisms of retardation by PCEs

As shown in Figure 2.13, complex interactions between chemical admixtures and cement take place during cement hydration. Several mechanisms, summarized as follows, have been proposed to explain how PCEs can modify the rates of the dissolution, nucleation and/or growth of various phases inducing retardation:

- *Ca^{2+} ions complexation*. This might occur either by ion-dipole interaction with the ether oxygen atoms [170–172] or chelation by the carboxylic groups along the backbone [173,174]. In practice, however, the amount of PCEs is commonly too low to justify a significant immobilization of calcium. In support of this, sugars, having a lower complexation capability than PCEs, evidence a much longer retardation [175];

- *Inhibition of dissolution*. Either the adsorption of PCEs on anhydrous phases [176] or the slowdown of the etch pits opening [61,177,178], lead to the inhibition of the C_3S dissolution. Similar conclusions were drawn with other organic compounds bearing carboxylic groups [179];

- *Inhibition of nucleation/growth of hydrates*. PCEs limit the ordered agglomeration of silicates due to the preferential bridging between Ca^{2+} ions and polymers, penalizing C-S-H nucleation [174]. Also, the inhibition of the precipitation observed for portlandite and calcite has been explained by the poisoning of the growing nuclei on which superplasticizers and sugars adsorb [175,180–182]. Specifically, PCEs can modify the growth, size, and morphology of the calcite crystals [181,183].

- *Disturbance of silicate-aluminate-sulfate balance.* This mechanism is the most unpredictable one due to its intrinsic complexity. Besides the delay of the C_3S hydration, PCEs can also alter the interaction between aluminates and sulfates through various mechanisms. Among them, many authors proposed that the promoted ettringite formation and/or precipitation of monosulfoaluminates, that can respectively adsorb or intercalate polymers will modify the aluminate-silicate-sulfate balance [6,96,102,184]. This typically modifies the shape of the main hydration peak, mainly because of a shift in the occurrence of the sulfate depletion peak [185]. If aluminates freely react too early, C_3S hydration can be strongly inhibited (see section 2.1.3). One theory states that this can occur because of PCEs hinder the dissolution of calcium sulfate [186]. In contrast, other studies propose that a faster depletion of sulfates, which would also allow C_3A hydration to revive and negatively impact that of C_3S. This would be caused by a favoured nucleation of ettringite having higher specific surface area [176]. An advanced phase quantification based on XRD and Rietveld refinement with an external standard coupled to isothermal calorimetry has recently confirmed the greater ettringite precipitation in model clinker in presence of PCEs leading to a faster sulfates depletion [15,178].

2.5.3 Effect of the molecular structure on hydration retardation

Most studies about the impact of polymers on cement hydration compare retardation at equivalent polymer dosages expressed as polymer mass with respect to the cement mass. This is somewhat misleading because the main effect is expected to come from the number of charges introduced [15,178].

One implication of this study is that polymers with the same C/E and P values but different molar masses would be expected to have a similar impact on retardation. Marchon et al. also show that, in delayed addition, two polymers with the same C/E but different P values induced the same retardation if the dosage is adjusted to introduce the same number of charges. If the comparison is done on a mass basis,

then, the polymer with the longer side chains will introduce fewer charges and cause a lower retardation.

While the importance of charges and C/E on retardation is clear, Marchon et al. could for the first time quantitatively account for retardation in relation to molecular structure. In particular, their results resolve the ambiguities related to comparing retardation of polymers dosed equally on a mass basis. Having said this, it is worth to recall most observations reported in the literature.

A regularly quoted study by Winnefeld et al. [69,187] showed that polymers with higher charge density lead to a better adsorption, that, in turn, leads to on a better dispersion of cement pastes. Also, at constant dosage (0.3% by weight of cement), the same structural variation (increase of the C/E ratio) causes a longer induction period (Figure 2.14). It is therefore tempting to relate this impact on hydration to the modification of adsorption.

The initial PCEs adsorption increases by increasing C_3A content [185,187] and by decreasing alkali amount [76]. Polymethacrylate-based PCEs (PMA-PCEs) are more sensitive to these two parameters than polyacrylate-based PCEs (PAA-PCEs) [188]. This difference probably originates from the hydrolysis of side chains from PAA-PCEs at high pH.
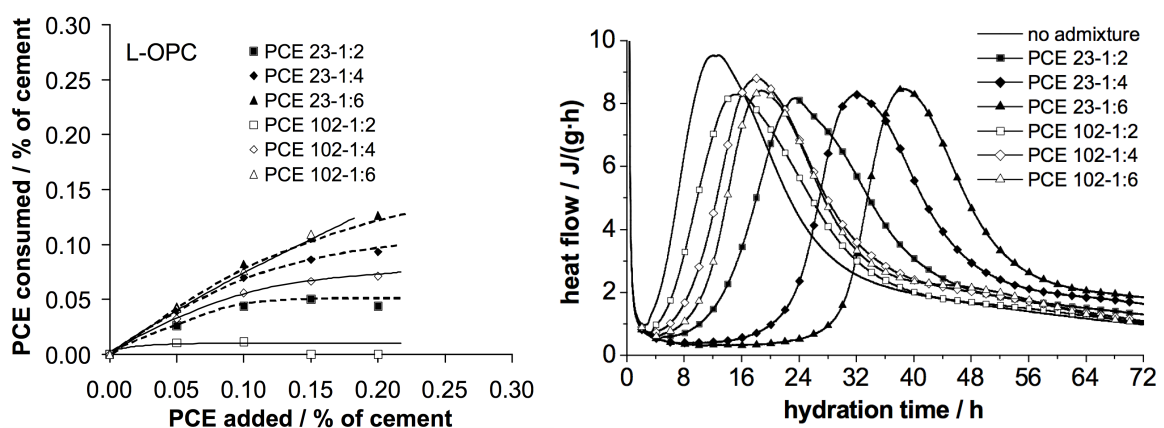
Figure 2.14: Impact of polymethacrylate molecular structure on adsorption (left) and isothermal calorimetry (right). Reproduced from Winnefeld et al. [187].

Beside the effect of the polymer dosage and structure on the hydration, a more detailed insight has been recently provided accounting also for the polymer addition

mode [15]. For this purpose, a model cement (80% C_3S, 18% C_3A and 5% $CaSO_4.1/2H_2O$) was used to assess the effect of PCEs on the simultaneous hydration of different phases.

When the polymer is added few minutes after the mixing water (*delayed addition mode*), the retardation is proportional to the number of repeat units $\frac{c_{PCE}}{M_{RU}}$, where c_{PCE} is the PCE dosage by mass and M_{RU} is the molar mass of a repeat unit. In turn, the number of repeat units is linked to the number of charges introduced and the dosage (Figure 2.15a). The slopes γ_{SP} varies with the C/E ratio, more specifically as $\frac{(C/E)^{1/2}}{(C/E+1)^{3/2}}$. Therefore, the master curve in Figure 2.15b can be derived by accounting for this, showing that the retardation is proportional to the polymer structure function $\left(\frac{C/E}{C/E+1}\right)^{3/2}$ and to the number of repeat units. This model was validated on both model cement and OPC.
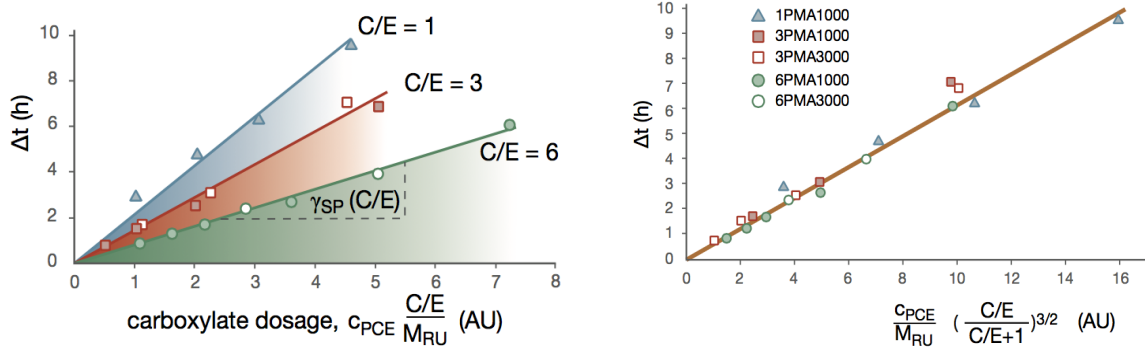
Figure 2.15: Effect of PCEs on the hydration of model cement when the polymer is added in delayed mode. (left) linear relation between the retardation of the main silicate peak with the number of repeat units introduced; (right) linear proportionality between retardation and polymer structure. Reproduced from Marchon (2016) [15,16].

On the other hand, when the polymer is added with the mixing water (*direct addition mode*), three main retardation zones are identified according to two critical polymer concentrations: at c* the onset of the retardation takes place and at c**, which represents the end of the transition of the balanced to the unbalanced system, most of the sulfates have been already consumed and AFm phases preferentially form (Figure 2.16).
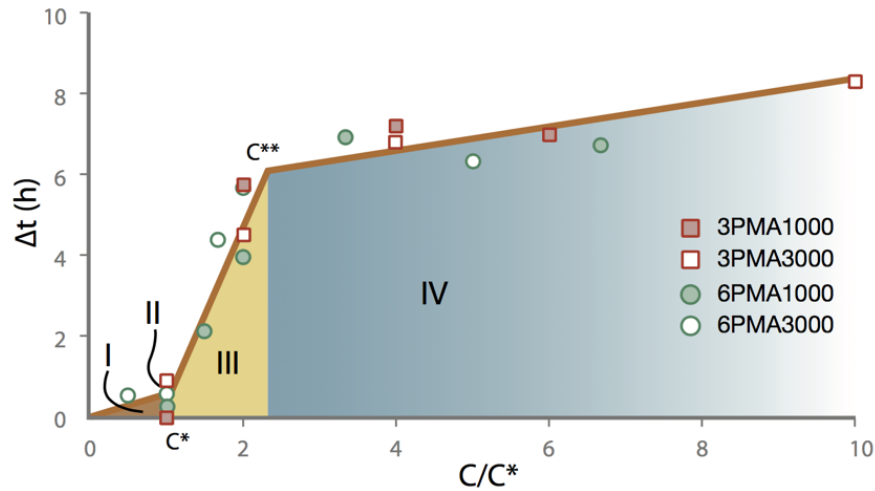
Figure 2.16: Retardation in case of direct addition of PCEs. From Marchon (2016) [15]

At c < c* (zone I), the hydration retardation is barely noticeable because polymers are preferentially immobilized on the ettringite [9]. In contrast, in delayed addition, neither the nucleation or growth of ettringite are modified because this hydrate precipitates before the addition of the polymer and this zone is not observed.

A rapid increase of the retardation is noticed by increasing the polymer dosage at concentration between c* and c** (zone III), showing the same dependency to polymer structure as in delayed addition. The increase of surface area of the hydrating model cement depends on both polymer dosage and structure due to a favoured nucleation of ettringite [9,101–103]. However, the formed ettringite surface is not sufficient to adsorb all the polymer, so that PCEs start adsorbing on silicates inducing a longer retardation. This might be explained referring to the inhibition of the silicates dissolution in presence of PCEs, as observed with other organic compounds bearing carboxylate groups [179]. Indeed, they preferentially block highly reactive surfaces, characterized by defects in form of kinks and etch pits, limiting the step retreat process.

At higher concentrations (c > c** in zone IV), an unbalanced or undersulfated system is caused by the promoted formation of ettringite, that leads to a massive consumption of sulfates and aluminium. This, in turn, accelerates the dissolution of aluminates and the concentration of aluminium ions in solution increases again [63], leading to the formation of AFm phases. Consequently, PCEs strongly adsorb/intercalate on the newly formed hydrates [5,6,157] and the retardation

could be caused only by the detrimental impact of free aluminium ions on silicates [61,63,64]. The fact that an undersulfated model cement without PCE give roughly the same retardation plateau as above c** in Figure 2.16 very strongly supports this.

Chapter 3

Reliable specific surface area measurements of cementitious systems

This chapter consists of two journal papers, a conference paper and part of book chapter. All experimental work, data analysis and paper writing was done by Sara Mantellato under the supervision of Dr. Marta Palacios and Prof. Dr. Robert Flatt:

- Sara Mantellato, Marta Palacios, Robert J. Flatt, Impact of Sample Preparation on the Specific Surface Area of Synthetic Ettringite, *Cement and Concrete Research* 86 (2016): 20–28 [20];

- Palacios, Marta, H. Kazemi-Kamyab, Sara Mantellato, and Paul Bowen. 2016. "Laser Diffraction and Gas Adsorption Techniques." In *A Practical Guide to Microstructural Analysis of Cementitious Materials.* Taylor & Francis [189]

- Sara Mantellato, Marta Palacios, Robert J. Flatt, Reliable specific surface area measurements on anhydrous cements, *Cement and Concrete Research* 67 (2015) 286–291 [19];

- Sara Mantellato, Marta Palacios, Robert J. Flatt, Reliable Specific Surface Area Measurements of Fresh Cement Pastes, In Monographie Bd. 45, (2012):29–34. Dübendorf (Switzerland) [18].

3.1 Introduction

3.1.1 General considerations

The specific surface area (SSA) of cement is broadly recognized to impact its reactivity as well as physical and mechanical properties of fresh and hardened concrete, such as rheology [101], hydration kinetics [190,191] and strength development [192]. Because of this, SSA is commonly included as quality control measurement in cement production, in addition to the particle size distribution [126,127] and the phase composition [82]. The specific surface area (SSA) of the anhydrous cement has a direct influence on the initial fluidity of superplasticized cementitious materials. Furthermore, the evolution of the SSA in the first hours of hydration is believed to have direct implications in their flow loss [9,10,14]. Additionally, superplasticizers are reported to impact the specific surface of ettringite [9]. This can change the availability of these molecules to modify the kinetics of cement hydration [193] and similar effects may be expected for other chemical admixtures, which cover a wide range of chemical structures [2]. There is, therefore, a clear interest and need for reliable measurements of the specific surface of cementitious materials, also at early age. This is in fact of central importance for the underlying hypothesis guiding this PhD thesis. However, the quantification of specific surface changes is non-trivial because SSA measurements on fresh [101] and hydrated cement paste [194–196] are delicate due to the possible dehydration of hydrated phases. The fact that such problems are also highly relevant for anhydrous cement is barely documented.

There are three major methods to measure the specific surface area of anhydrous cement: Blaine air permeability, laser diffraction (calculating SSA from the particle size distribution) and gas adsorption. The cement industry largely relies on Blaine measurements, often arguing that results are more consistent than nitrogen adsorption measurements, which additionally are more time consuming. In contrast, academics tend to prefer nitrogen adsorption measurements because of their more

fundamental basis and mostly look down on Blaine measurements because of their semi-empirical nature.

The Blaine test [197] is based on measuring the resistance encountered by air passing through a well-packed but still porous powder bed under a given air pressure gradient. In its most common use, both the pressure gradient and the flow rate of air vary during the test. This greatly simplifies the measurement, but prevents the use of basic equations (Kozeny–Carman equation) for the steady-state flow of air through a bed of packed particles [198–200]. The main contribution of R.L. Blaine was to propose semi-empirical equations to overcome this problem [197], involving a calibration procedure now defined in ASTM C204-11 [201]. Nevertheless, this semi-empirical procedure can compromise the reliability of results and their comparison between laboratories.

Laser diffraction (LD) is the most common technique to determine the particle size distribution of powders, from which the SSA can be calculated assuming a specific shape (most often spherical). Because of the irregular shape of cement particles [202–204], their real size will be smaller than the one determined by LD and consequently, the SSA will be underestimated [205]. In addition, it is necessary to know the refractive index of the measured powder in the dispersive media. In the case of Portland cement, this value has been measured but it needs to be determined for cements containing supplementary cementitious materials [206].

The nitrogen adsorption method is based on quantifying the volume of nitrogen molecules needed to cover the sample surface. The SSA is calculated using the BET (Brunauer–Emmett–Teller) model [207]. In contrast with the two methods described above, nitrogen adsorption can be used to measure hydrated cement paste. Also, in terms of working principle, it does not postulate the particle shape or include semi-empirical equations, which is why it is considered more reliable. In contrast to Blaine and LD tests, samples measured by nitrogen adsorption must be degassed before the measurement. This is required to remove physisorbed molecules so that the adsorptive gas may interact directly with the sample along its small cavities. Degassing is normally performed by heating the samples, by purging

them with an inert gas (N_2) or by applying vacuum. While extremely important, degassing conditions are not always reported in the literature, in particular for anhydrous cements.

3.1.2 SSA measurements on anhydrous cements

Although relatively high degassing temperatures do not affect the clinker phases of anhydrous cement, it is known that gypsum ($CaSO_4 \cdot 2H_2O$) is thermodynamically stable at temperatures lower than 42 °C and at relative humidity higher than 50% [208,209]. At higher temperature or lower relative humidity, it partially or totally dehydrates [210] to hemihydrate or anhydrite, which has a direct effect on its SSA [211,212]. Therefore, the degassing conditions should be carefully chosen to prevent gypsum dehydration from compromising SSA measurements of cement. Previous studies [101,194,213] have confirmed that the sample preparation, involving stopping of hydration and degassing, can introduce artefacts due to possible structural modifications of hydrated phases with consequent biased and misleading final SSA_{BET} values. Such studies are mainly focused on hardened pastes. However, studies conducted on early age cementitious pastes (up to 5 h) are still limited [9]. Indeed, achieving reliable SSA of fresh cement pastes is viewed as a challenge due to the presence of highly sensitive components, mainly ettringite ($Ca_6Al_2(SO_4)_3(OH)_{12} \cdot 26H_2O$) [101]. Hence, a significant variability of surface area values in fresh cement pastes might arise from a morphological and/or chemical alteration of these components occurring throughout the sample preparation.

3.1.3 SSA measurements on hydrated cements

When dealing with hydrating cement, the removal of capillary water is a critical step to arrest cement hydration. It should be fast and efficient, as well as inert to cement phases. Zhang and Scherer compared the effect of different drying methods on cement pastes [213]. They concluded that oven drying at temperatures typically between 60 and 105 °C and vacuum drying damage the micro-structure of hydrates such as C–S–H and ettringite, whereas D-drying does not stop the hydration in a

short time. Solvent exchange, involving the use of isopropanol, is widely accepted to be the most effective method, although the structure of ettringite in hardened pastes could be partially damaged after a prolonged contact with the solvent [214]. However, these severe conditions used on hardened cement pastes – long exposure to high amount of solvent – are not mandatory on the fresh cement pastes studied in this thesis and for which the cementitious matrix shows a low cohesion and the diffusion of the solvent is fast [213].

The degassing becomes even more crucial when it is necessary to remove adsorbed organic solvents, previously used to stop cement hydration. Indeed, this requires more radical conditions, but it is widely known that the structure and/or morphology of ettringite is altered by temperatures higher than 60 °C [101,215,216] or under high vacuum conditions [216–220].

From the above, we conclude that both stopping hydration and degassing treatment can cause structural changes on anhydrous cement and ettringite, the main hydrated phase in early aged cementitious systems. However, the connection between these structural modifications and the SSA_{BET} is still unclear. The main objective of this chapter is therefore to determine an adequate protocol to measure the SSA of anhydrous cement and hydrated cement pastes, in particular ettringite. Based on the presented outcomes, it was possible to figure out the limiting conditions under which reliable SSA_{BET} values of cementitious materials can be obtained.

3.2 Materials and methods

3.2.1 Materials

3.2.1.1   Anhydrous cement, clinker and gypsum

A commercial cement CEM I 52.5 R and a clinker supplied by Holcim (Switzerland) were used in the present work. The clinker was milled in the Vibratory Disk Mill (Retsch) for 45 s at 700 rpm and, afterwards, in the planetary mill (Pulverisette 5) for 4 min at 400 rpm to reach a similar particle size distribution to the commercial

cement. The ground clinker was homogenized in Turbula for 2 h. The gypsum (Acros Organics, 98%, extra pure) was sieved under 20 μm in order to reach a similar PSD as the clinker. A model cement was produced by mixing the clinker and 5% of sieved gypsum (by mass of clinker) in a Turbula for 16 h. In commercial cements, where clinker and gypsum are ground together, PSD of gypsum could be smaller than that of clinker due to its lower hardness.

Mineralogical composition of the used materials (Table 3.1) was determined by Rietveld analysis of the X-ray diffraction (XRD) patterns and expressed in values normalized to 100% of crystalline phases (further details about XRD are given in 3.2.2.3). Characteristic particle diameters (volume based) of cement, clinker and gypsum are reported in Table 3.2 and were measured by laser diffraction (Mastersizer, Malvern Instruments) after dispersion in isopropanol.

Table 3.1: Mineralogical composition of Portland cement, clinker and gypsum determined by Rietveld analysis of the XRD patterns.

	Cement % (w/w)	Clinker % (w/w)	Gypsum % (w/w)
C_3S	66.3	72.6	-
C_2S	6.7	8.6	-
C_3A	5.9	5.9	-
C_4AF	10.8	12.9	-
Quartz	0.4	-	-
Calcite	3.9	-	-
Gypsum	4.3	-	93.5
Hemihydrate	1.7	-	5.9
Anhydrite II	-	-	0.6

Table 3.2: Characteristic particle diameters of the powders determined by laser diffraction.

	d_{10} (μm)	d_{50} (μm)	d_{90} (μm)
Cement	1.12	8.47	26.80
Clinker	0.66	6.95	29.19
Gypsum	3.19	8.99	22.40
Model cement	0.78	7.82	25.59

3.2.1.2   Synthetic ettringite

Calcium oxide (CaO) and aluminum sulfate octadecahydrate $Al_2(SO_4)_3 \cdot 18H_2O$ (ACS reagent, ≥98%, Sigma-Aldrich Chemie GmbH) were used as starting materials to synthesize pure ettringite. Calcium oxide was obtained by the calcination of calcium hydroxide (≥ 96%, Sigma-Aldrich Chemie GmbH) in an oven at 1000 °C overnight.

The Ca/Al molar ratio of 3.2 and the ultrapure water (ρ = 18.2 MΩ cm, TOC around 1–2 ppb) content of 1500 g were kept constant in all the syntheses. CaO was dissolved in 1400 g of ultrapure water and mixed in a three-neck round-bottom flask with a EUROSTAR power control visc overhead stirrer IKA equipped with PTFE half-moon impeller at 400 rpm for 2 h at room temperature. The $Al_2(SO_4)_3 \cdot 18H_2O$ was dissolved in the remaining 100 g of ultrapure water and added to the CaO solution, stirring continuously for further 3 h. The synthesis was conducted under N_2 atmosphere to prevent CO_2 contamination. Table 3.3 reports the experimental conditions of the synthesized ettringites varying its concentration in suspension.

Table 3.3: Concentration of ettringite in suspension

Sample name	AFt concentration in suspension % (w/w)	Water/AFt	pH at 22 °C
AFt_0.39	0.39	258	11.40
AFt_0.67	0.67	150	11.25
AFt_3.89	3.89	25	11.15

The ettringite suspension was filtered by a membrane filter connected to a vacuum pump (ultimate vacuum ≈ 100 mbar). A polyamide membrane filter with a pore size of 0.45 µm (Sartolon Polyamid) was used. The solid ettringite, in the form of a thin cake, was placed in a petri dish and stored in desiccator with $CaCl_2$ saturated solution (32% RH) at 20 °C under N_2 atmosphere until constant mass. The drying lasted 1 month on average. Previous studies [221] have confirmed the preservation of ettringite structure under these conditions, contradicting thermodynamic expectations probably because of kinetic constraints. The final amount of dry AFt was insufficient at the first two concentrations, AFt_0.39 and 0.67, for an entire set of SSA measurements. Therefore, several batches of dry ettringite produced under

the same conditions were prepared and then mixed and homogenized together by hand in an agate mortar. Only one batch of AFt_3.89 was synthesized, its yield being sufficient for all the analyses.

Inductively Coupled Plasma Optical Emission Spectroscopy (ICP-OES) Thermo iCAP 6300 was used to quantify the concentration of the remaining Al in the water solution after filtration. From these values, the yield of the reaction was then calculated. The ettringite solutions were diluted 5 times with a 2% (w/w) HNO_3 ultrapure water solution. The yield of reaction was calculated assuming the absence of nano-sized particles of ettringite that might pass through the pores of the filter and increase the content of aluminium in solution (Table 3.4).

Table 3.4: Yield of reaction calculated for the ettringite syntheses.

Sample name	Yield of reaction (%)
AFt_0.39	84 ± 1
AFt_0.67	90.1 ± 0.8
AFt_3.89	98.7

3.2.2 Methods

3.2.2.1   Stopping of hydration of fresh cement pastes

In this section, we present an assessment of the protocols for stopping cement hydration monitored by SSA_{BET}. For such protocols, AFt_3.89_DH0.5 (Table 3.3) was used. Three different protocols to stop cement hydration were studied: 1. solvent-exchange method using isopropanol (IPA) at different temperatures; 2. treatment with diethyl ether after initial solvent exchange with isopropanol; 3. freeze-drying method. We underline that we examined the effect of these conditions on pre-formed ettringite to decouple this question from cement hydration kinetics.

In the first set of experiments, ettringite was mixed in a beaker with a constant amount of isopropanol (IPA, ACS reagent ≥99.5%, Scharlau) 50 g of solvent per gram of powder. The solvent was previously stored at different temperatures, −18 °C, 5 °C and 22 °C. Ettringite was gently mixed with IPA for 1 min, filtered for 4 min with a

0.45 µm polyamide membrane filter and dried under inert atmosphere in desiccator at 20 °C until constant mass.

The second set of experiments was inspired by previous evidence in literature [222] that a less polar solvent removes possibly adsorbed isopropanol. For such a reason, the effect of diethyl ether (DEE, ACS Reagent >99%, Sigma-Aldrich Chemie GmbH, 1 mL per gram of powder, 1 min mixing) on the SSA of the ettringite previously in contact with IPA (1:50 powder to solvent ratio) at 5 °C was also explored.

The freeze-drying protocol consisted in the immersion of the sample in liquid nitrogen for 15 min and quickly transferring it to the Alpha I/6 Christ freeze dryer, of which the temperature and vacuum were at 23 °C and 0.1 Pa, respectively, for 24 h.

The different steps for the sample preparation before the SSA_{BET} measurements are shown in Figure 3.1. The simulation of the stopping hydration is carried out on ettringite powders after drying in desiccator. In particular, a second drying in desiccator is required after the use of IPA to remove the excess of solvent. Degassing is always conducted before SSA_{BET} measurements regardless of previous treatments on the samples.
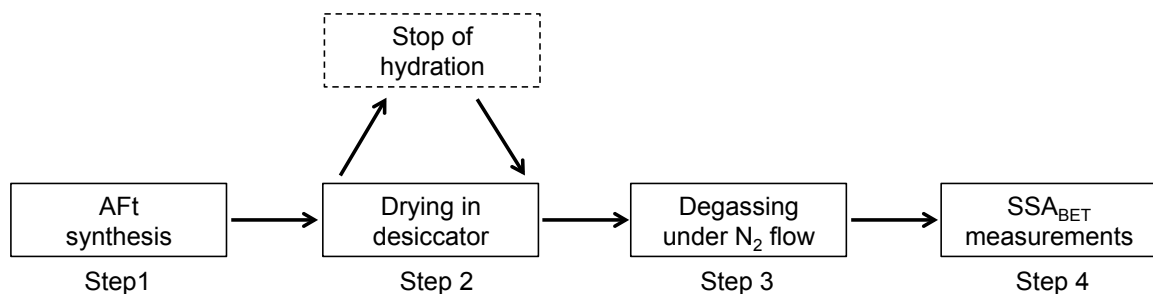
Figure 3.1: Summary of the different steps used for the sample preparation before SSA_{BET} measurements.

The impact of the protocol used for stopping cement hydration was also studied on early-aged hydrating cement paste with and without superplasticizers. Cement pastes were prepared in PP containers by mixing 200 g of cement Holcim Normo 5R (Table 3.1) and 60 g of UPW (Ultrapure Water) (w/c ratio = 0.3). The powder was put in the liquid and the resulting suspension was stirred at 200 rpm for 30 s and then at 800 rpm for 4 min with a EUROSTAR power control visc overhead stirrer

equipped with a 4-bladed propeller stirrer, both by IKA. PCEs having different grafting degree and side chains length, namely 2.5PMA1000, 4.0PMA1000 and 2.5PMA2000 (for further information about the characteristics of these polymers, see section II.1), were added to the mixing UPW (direct addition). The solvent exchange was carried out by using about 10 g of cold (5 °C) pure IPA (Sigma-Aldrich, puriss. p.a., ACS reagent > 99.8%) per g of paste. The drying step was applied on about 7-8 g of fresh cement paste.

Following the procedure here defined as "single-step filtration" (SF), IPA/paste suspensions are mixed together for 1 minute, poured into a stainless-steel pressure filter holder through a nylon 0.45 μm membrane filter under air pressure. The powder is, finally, stored in a desiccator with a calcium chloride saturated solution (32% RH at 20 °C) until constant mass. Dried powders were, then, gently homogenized in an agate mortar before the different measurements.

3.2.2.2   SSA measurements

The surface area measurements were carried out using a BET multi-point nitrogen physisorption apparatus (Micromeritics Tristar II 3020). The nitrogen adsorption was measured from an eleven-points isotherm in a relative pressure P/P_0 range of 0.05 to 0.30 at 77.3 K. The SSA measurements were repeated three times for each sample. Anhydrous cement samples were degassed in an external degassing station (VacPrep 061 from Micromeritics) in the range of temperature between 40 and 150 °C, under vacuum (2.67 Pa) and N_2 flow (with a flux of about 3×10^{-3} m^3/h) for 16 h. These long degassing times are required to eliminate the physisorbed contaminants at low temperatures. Longer degassing processes (24 and 48 h) were also considered. Ettringite samples were degassed in an external degassing station (VacPrep 061 from Micromeritics) between 30 and 120 °C, under N_2 flow for 16 h.

The temperature of the degassing station was calibrated by measurements in and out of the sample chamber. For the first case, a sensor Sensirion SHT21 was inserted into the glass tubes under N_2 flow and both temperature and relative humidity were measured over time. In the second case, a mercury thermometer with a precision of 0.05 °C was installed in the degassing station between the glass tube and the heating

mantle. As shown in Figure 3.2, a linear correlation exists between set temperature and measured temperature. The difference between the set temperature and the effective one is confirmed both by the sensor and the thermometer. At all temperatures, the relative humidity measured in the glass tubes under N_2 flow approached zero.
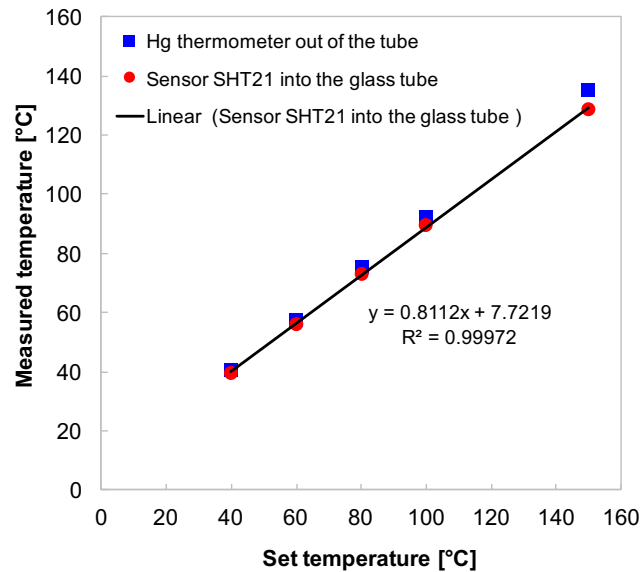
Figure 3.2: Linear calibration of the degassing station VacPrep 061 between 40 and 150 °C.

The Blaine surface area of the above-mentioned samples was measured according to ASTM C204-11 standard [201]. The density of each sample was measured by the pycnometer Micromeritics AccuPyc II 1340 using helium as inert gas.

3.2.2.3   X-Ray Diffraction (XRD)

The XRD patterns were obtained using a Bruker AXS D8 ADVANCE diffractometer. The X-Rays are generated by the impact of high-energy electrons with the metal target of Cobalt anode (λ = 1.7902 Å). The sample is stationary, placed in horizontal position, while the source and the detector arms are synchronized to realize the θ-θ condition. A solid-state detector was used. The angles range between 3 and 80 °2θ with a step size of 0.02 °2θ and a resolution defined as time per step of 5 s. The qualitative analysis of powders was conducted using the DiFFPlus EVA software and AutoQuan software was used for Rietveld analyses. All the samples were sieved under 20 μm and the same sample mass (0.1 g) was used for the XRD measurements.

3.2.2.4   Thermal analysis

TGA analyses for the cement anhydrous phases were performed using the TGA/SDTA 851e (Mettler Toledo). About 40 mg of dry sample was heated in an open crucible from 25 to 1000 °C using a heating rate of 10 °C/min under pure N_2 flow of 50 mL/min. In the case of the ettringite synthetic samples, the TGA analyses were performed using the Q50 TGA (TA Instrument). About 15 mg of dry sample was heated in an open platinum crucible from 25 to 1000 °C using a heating rate of 10 °C/min under a N_2 flow of 40 mL/min. Specifically, for AFt samples XRD and TGA were used to characterize the materials after contact with the solvent or freezing procedure, after the degassing process and after the SSA_{BET} measurements. All the samples were degassed at 40 °C under N_2 flow for 16 h and the SSA_{BET} measurements were repeated three times for each sample.

3.2.2.5   ESEM

Gypsum and synthetic ettringite samples were studied by Scanning Electron Microscopy (SEM) by using a FEI Quanta 200 3D microscope (FEI, North America NanoPort, Hillsboro, OR, USA). Backscattered-electron (BSE) images were taken in low vacuum mode.

3.3 SSA of anhydrous cement and gypsum

3.3.1 Results on SSA of anhydrous cement and gypsum

3.3.1.1   Influence of the degassing conditions

Figure 3.3 shows the SSA_{BET} of the anhydrous cement after degassing either under vacuum or N_2 flow at temperature between 40 and 150 °C.

Higher temperatures cause an increase of the SSA of the anhydrous cement from about 1.2 m^2/g at 40 °C to 1.8 m^2/g at 150 °C, corresponding to a SSA increase of about 35%. Furthermore, at 40 °C Figure 3.3 shows that increasing the degassing time from 16 h to 48 h induces an increase of 25% of the SSA. The derivative of

thermogravimetric measurement (DTG) in Figure 3.4 shows that, before degassing under vacuum, anhydrous cement has three main peaks associated respectively with the dehydration of gypsum (between 80 and 120 °C), the dehydration of portlandite (around 450 °C) and the decarbonation of calcite (between 600 and 700 °C).
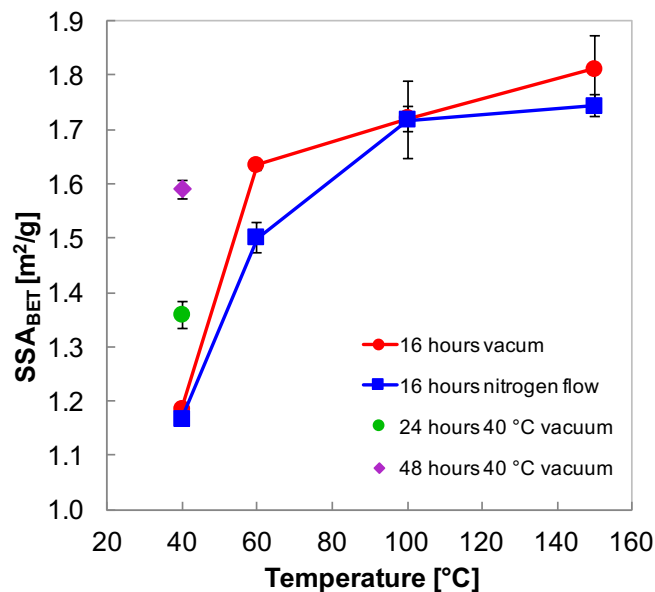
Figure 3.3: SSA of anhydrous cement at different degassing conditions. The error bars correspond to the standard deviation on the measurements.

The presence of portlandite indicates that the initial cement was partially pre-hydrated, which is known to occur depending on the relative humidity that cement has been exposed to [223,224]. As the degassing temperature increases, the intensity of the gypsum dehydration peak decreases and it is not observed in gypsum degassed at temperatures higher than 40 °C under vacuum. Samples degassed over 40 °C show a small weight loss between 75 and 100 °C which could be due to water adsorbed on bassanite or condensed in the pores created during gypsum dehydration. This confirms that the gypsum in anhydrous cement dehydrates during the degassing, whereas portlandite and calcite are unchanged as expected.
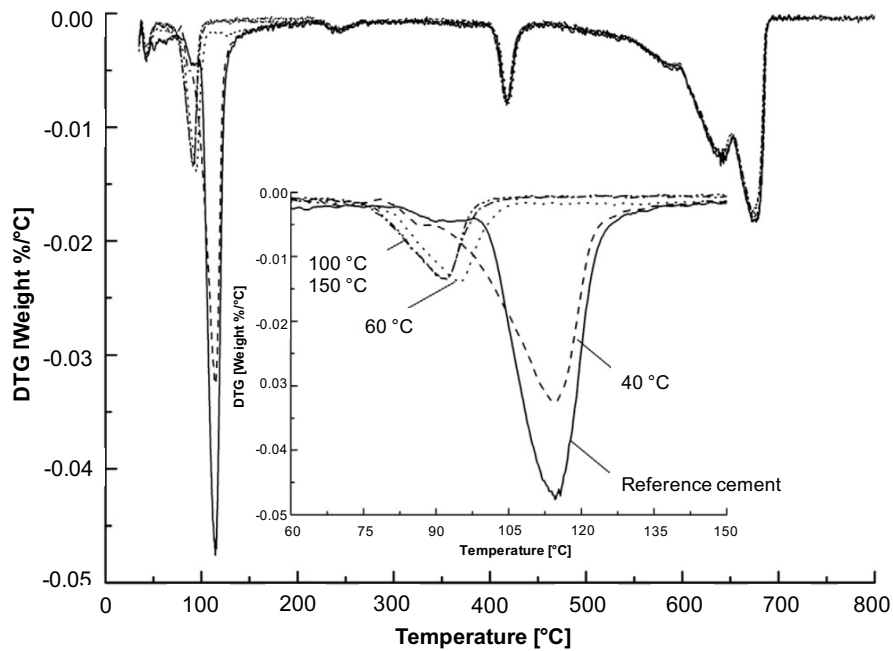
Figure 3.4: DTG of anhydrous cement degassed at different temperatures under vacuum. The insert shows the peaks where the major modifications occur.

3.3.1.2   Effect of the dehydration of gypsum on the SSA

For a better understanding of the relationship between the change of the SSA and the dehydration of gypsum, the same set of measurements was performed on gypsum as on Portland cement. As shown in Figure 3.5, degassing conditions also have an important impact on the SSA of pure gypsum. For example, degassing at 100 °C for 16 h under vacuum leads to SSA_{BET} about 11 times larger than at 40 °C. Beyond 100 °C, SSA values reach a plateau, the value of which depends on whether vacuum or N_2 flow is used.

In comparison to the cement samples, the degassing conditions have a more significant effect on the SSA of gypsum, mainly at high temperatures. Additionally, SSA_{BET} values at 40 °C for gypsum differ by about 17% between degassing under N_2 or vacuum. This is significant as the experimental error between samples prepared under same conditions was generally lower than 3%.

Mass reductions of the gypsum samples measured immediately after degassing are reported in Table 3.5.
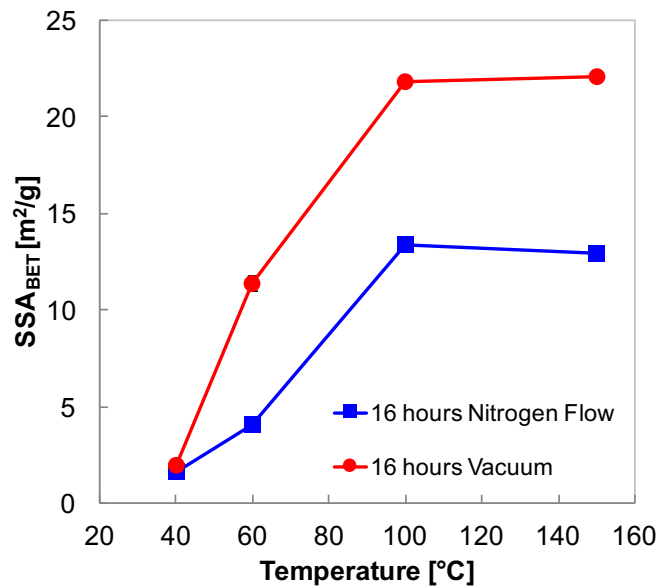
Figure 3.5: SSA measurements of gypsum at different degassing conditions. Error bars corresponding to one standard deviation (three measurements) are included but not visible because of being smaller than the symbols.

Table 3.5: Mass loss of the gypsum sample after the degassing at different temperatures, under N_2 and vacuum.

Temperature (°C)	Mass reduction after degassing (%)	
	N_2 flow	Vacuum
40	0.7 ± 0.5	1.4 ± 0.2
60	2.9 ± 0.1	10.8 ± 0.6
150	19.7 ± 0.4	20.7± 0.3

The mass loss of our gypsum (containing small amounts of hemihydrate and anhydrite) determined by TGA was 20.38%. In our tests, we measured very similar values (about 20%) at the highest temperatures, indicating that a complete dehydration takes place whether the samples are degassed under vacuum or N_2 flow.

After degassing, samples were studied by XRD and Rietveld analysis (Figure 3.6). Results show that degassing at 40 °C under N_2 flow for 16 h preserves the phase composition, whereas vacuum causes a slight dehydration (about 2%). At 60 °C, dehydration to β-hemihydrate is promoted, but more under vacuum than N_2 flow. At 100 °C and above, the conversion was total and the amount of the anhydrite II slightly increased. The reason why mass loss measurements suggest full conversion

to anhydrite, whereas XRD identify β-hemihydrate is considered in the discussion in section 3.3.2.
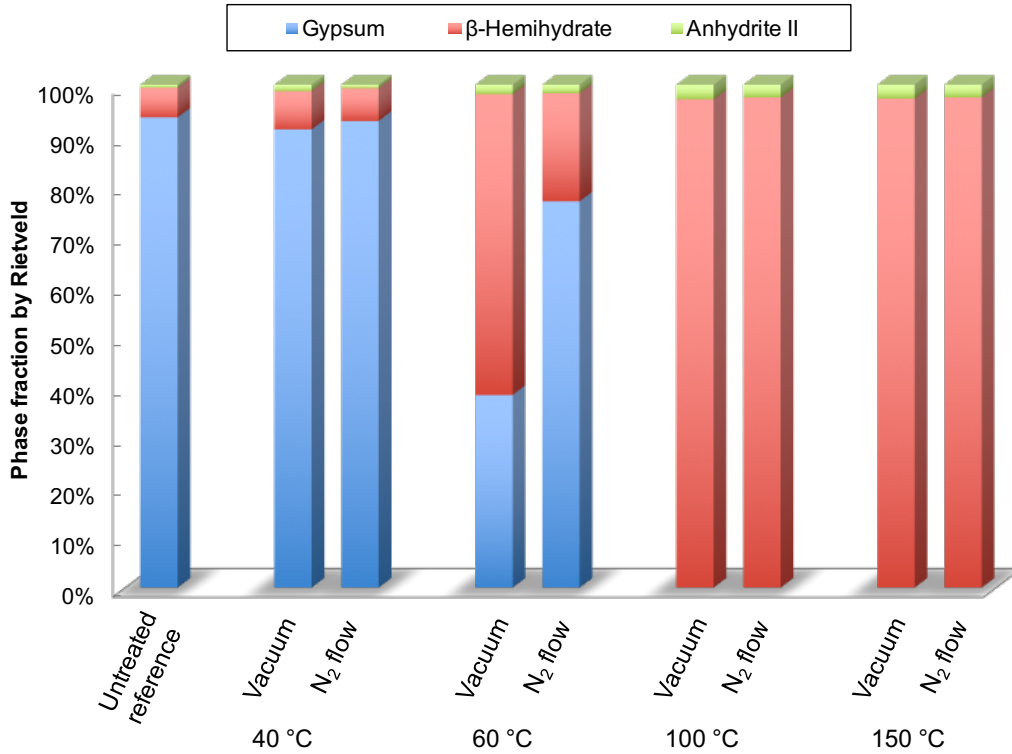
Figure 3.6: Mass percentage of mineralogical phases in gypsum samples degassed at different temperatures and environment conditions determined by Rietveld analysis.

After degassing and prior to nitrogen adsorption measurements, vacuum must be briefly applied to purge the helium and to calculate the free space in the sample cell. On the basis of the above results, the vacuum applied in this purging stage might also modify the specific surface of cementitious materials. Therefore, the effect of evacuation time during purging was also investigated on gypsum samples degassed under gentle conditions (40 °C under N_2 flow for 16 h). Fortunately, it was found that short evacuation times ranging from 25 to 75 min do not affect the measured SSA values.

3.3.1.3   SSA of clinker and model cement

SSA_{BET} was also determined on ground clinker and on a model cement composed of the same ground clinker mixed with 5% (w/w) of gypsum. As shown in Figure 3.7, degassing conditions do not influence the SSA_{BET} of clinker, but increase it on the

model cement by about 60% at 100 °C.
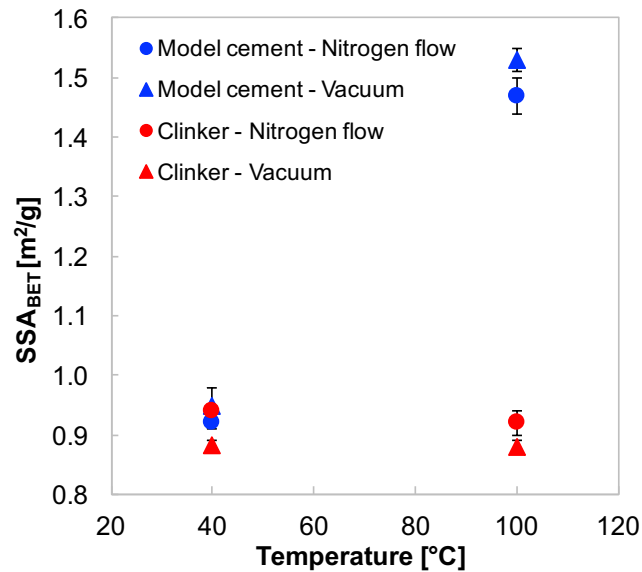
Figure 3.7 SSA measurements of clinker and model cement at different degassing conditions. The error bars correspond to the standard deviation on the measurements.

This confirms that the SSA increase observed on the commercial cement is only due to the gypsum dehydration depending on the degassing conditions used. For both the clinker and the model cement, degassing at 40 °C shows only a slight SSA change depending on whether vacuum or N_2 flow is used. Clinker samples degassed under N_2 show a slightly higher SSA than those degassed under vacuum, while model cement samples show the opposite behaviour.

3.3.1.4   Comparison between Blaine and N_2 adsorption techniques

In this section, the SSA obtained from nitrogen adsorption and Blaine tests is compared. Figure 3.8a shows that both on the model and the commercial cement the SSA_{BET} varies independently of the Blaine fineness. These changes result strictly from different degassing conditions and emphasize that nitrogen adsorption is highly sensitive to them. Because Blaine measurements do not require degassing they are not influenced by them. This is however not the case for the pure gypsum samples as shown in Figure 3.8b. However, the increase in Blaine values is much smaller than those in SSA_{BET}.
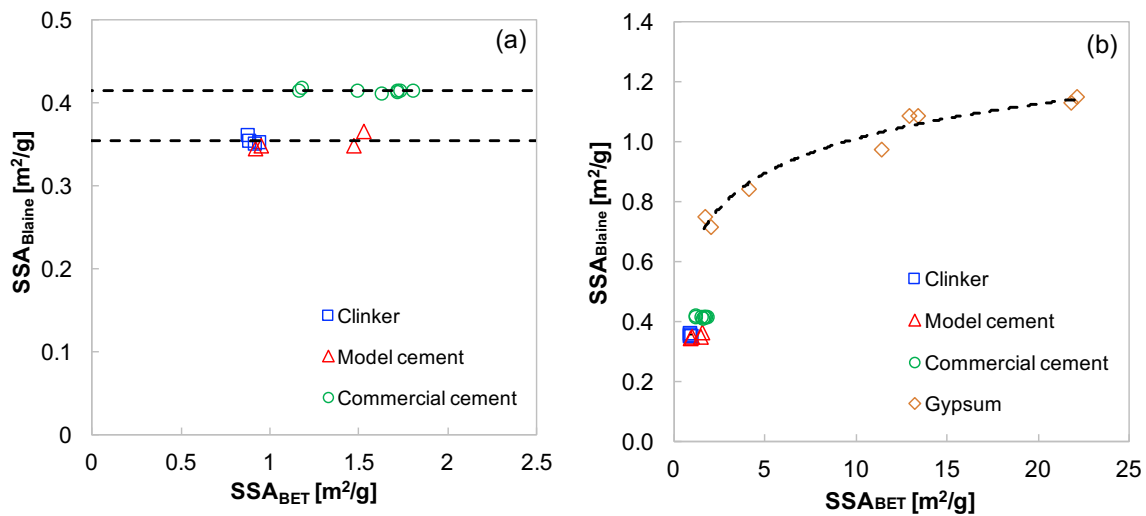
Figure 3.8: Correlation between SSA values measured by Blaine and BET nitrogen adsorption. (a) clinker, model cement and commercial cement. Discontinuous lines show the average Blaine value on the commercial and model cements. (b) same as (a) but with gypsum. The discontinuous line is a logarithmic fit serving as guide for the eye. In both figures, the error bars correspond to the standard deviation on the three measurements. When not visible, they are smaller than the symbols. No physical meaning is proposed to the observed logarithmic relation between Blaine and BET for gypsum. As explained in the text degassing of gypsum not only leads to dehydration but also to a complex particle fragmentation.

3.3.2 Discussion on SSA of anhydrous cement and gypsum

The present study shows that degassing conditions previous to SSA_{BET} measurements (temperature, pressure and time) significantly influence results on anhydrous Portland cement because of the dehydration of the gypsum it contains. Inadequate degassing conditions lead to misleading results. The extent of this error will depend not only on the amount of gypsum in the cement, but also on the degassing conditions.

The reason for the specific surface changes is supported by measurements of mass loss, XRD and TGA. However, we found that mass losses after degassing at 150 °C (Table 3.5) suggest a total dehydration to anhydrite, while XRD identifies β-hemihydrate (Figure 3.6). This might be due to a transition from gypsum to soluble anhydrite ($CaSO_4$ III or γ-$CaSO_4$), occurring under reduced vapour pressure [225,226] even at moderate temperatures [227]. Being strongly hygroscopic, this phase will rapidly rehydrate to β-hemihydrate during sample preparation before the XRD measurement. This quick rehydration has been deeply discussed in the

literature [228–230]. However, as this is only of marginal relevance to the main scope of this work, we do not examine it in further detail.

In regard to the selection of adequate degassing conditions, our XRD results show that gypsum dehydration can take place even at 40 °C if vacuum is applied. However, at that temperature the extent of degassing is strongly time dependent (Figure 3.3). The dehydration of gypsum is a topotactic solid-state reaction and as observed in Figure 3.9, it involves significant structural changes at the level of particles.
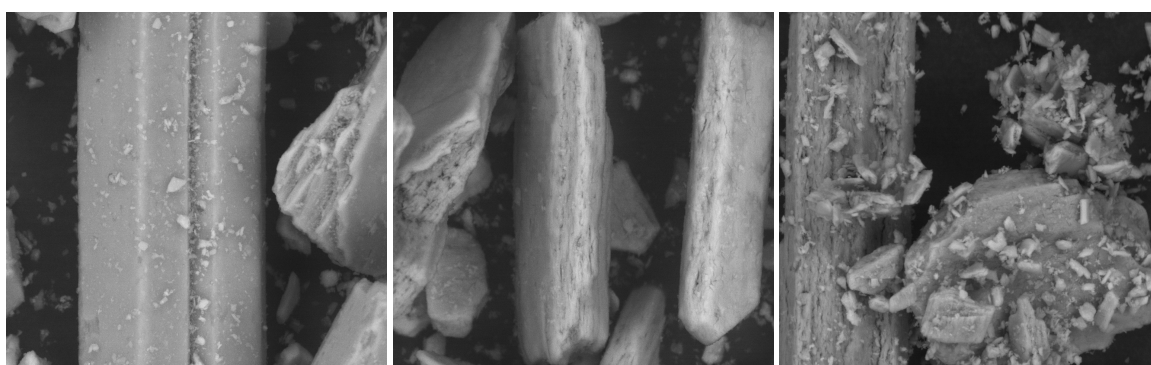
Figure 3.9: Scanning electron microscopy images of gypsum (a) untreated, (b) degassed at 150 °C under N$_2$ flow, (c) degassed at 150 °C under vacuum.

The SEM image of the untreated gypsum (Figure 3.9a) shows a smooth and regular surface of the needle-like crystals. On the other hand, gypsum degassed at 150 °C exhibits large cavities on the particles, which is in agreement with the porous structure of anhydrite and hemihydrates produced by thermal decomposition [231,232]. The structures of β-hemihydrate and anhydrite III are very similar. They are both hexagonal with structural channels of 0.4 nm diameter filled with water molecules for the former and empty for the latter [230,233]. In the case of gypsum degassed under vacuum, the formation of small particles is also observed (Figure 3.9c). This might result from a lowering of the boiling point of water, which together with the water released by the dehydration of gypsum would produce an overpressure in the particles that would strongly damage them [232,234]. This interpretation is supported by the absence of these small particles in the sample dried under N$_2$ (Figure 3.9b). In the latter case, the particles are characteristic of a pseudomorphism keeping the initial particle shape but creating porosity within them.

Comparing SSA$_{BET}$ with Blaine fineness of the four powders studied, the Blaine test always gives lower values. As explained above, this is due to the fact that in nitrogen adsorption technique, nitrogen can access to cracks, crevices and pores that Blaine test is not able to distinguish. This is in agreement with previous studies in the literature [23,206].

An essential result is shown in Figure 3.8a. The Blaine values remain constant while SSA$_{BET}$ changes substantially both for the commercial and the model cement. This shows that Blaine values are not affected by changes in the hydration state of the sulfate carrier, in contrast to SSA$_{BET}$. In practice, this hydration state depends not only on the humidity to which the cement has been exposed, but also on the grinding and storage temperature. This – together with a possible variation of the gypsum content in the small samples used for BET measurements – probably explains why the cement industry has experienced Blaine measurements to be much more constant than BET. Much of this variability may disappear with proper degassing conditions at 40 °C under N$_2$ flow for 16 h. Using such conditions, it would be possible to re-evaluate the relative benefits of BET and Blaine specific surfaces in the cement industry.

However, we must emphasize that this protocol provides a measurement in which a part of the surface comes from the hemihydrate initially present in the sample. Although its amount can be quantified by XRD, its surface is not known. As this results from thermal decomposition, one might expect that its SSA might be similar to the SSA increase obtained when gypsum present in the cement is thermally decomposed. In our specific cement, 0.55 m^2/g is created by 4.3% gypsum for decomposition at 100 °C under N$_2$, a more realistic condition than vacuum used in this study. This means that the 1.7% hemihydrate also contained in our cement (~2% gypsum equivalent) might account for about 0.22 m^2/g in our measurement, and that the SSA of our cement without the gypsum is probably in the range of 0.97 rather than 1.17 m^2/g. It is beyond the scope of this study to examine this issue in further detail. However, we would like to point to the fact that this clinker surface might be the most adequate one to use when considering the kinetics of cement hydration.

3.4 SSA of ettringite

3.4.1 Results on SSA of ettringite

3.4.1.1 Characterization of synthetic ettringite

The mineralogical composition of the used materials (Table 3.6) was determined by Rietveld analysis of the X-ray diffraction (XRD) patterns and expressed in values normalized to 100% of crystalline phases.

Table 3.6: Mineralogical composition of ettringites determined by Rietveld refinement of the XRD patterns. The ICDD-PDF nos. are reported in brackets for each phase. Note for reviewers: The table has been slightly modified.

Sample name	Ettringite (41-1451) % (w/w)	Gypsum (DH) (36-0432) % (w/w)	Calcite (5-0586) % (w/w)
AFt_0.39_DH1.2	98.0	1.2	0.8
AFt_0.39_DH5.5	92.6	5.5	1.9
AFt_0.67_DH3.4	95.2	3.4	1.4
AFt_3.89_DH0.5	99.3	0.5	0.2

The ettringite (AFt) notation indicates the solid concentration in suspension as first number, and the percentage of gypsum (DH) as second number. It is not clear if the small amounts of gypsum were formed during the synthesis of ettringite or during its drying.

Table 3.7 reports the structural parameters refined by Rietveld analyses for the studied synthetic ettringite samples. Ettringite is trigonal with a = 1.1229 nm and c = 2.1478 nm [235] and crystallizes in the space group P31c. The microstrain was not considered in the refinement and the amount of the non-crystalline phase was not determined. As shown in Table 3.7, the structural parameters of our synthetic ettringite samples match those ones reported in the literature, with a slight expansion of the a-axis.

Table 3.7: Structure parameters of synthetic ettringite samples refined by Rietveld. Standard uncertainties are reported in parentheses.

Sample name	Lattice parameters		Crystallite size [nm]	Rwp [%]
	a [nm]	c [nm]		
AFt_0.39_DH1.2	1.1239(8)	2.1473(2)	86.39 ± 2.19	8.67
AFt_0.39_DH5.5	1.1239(3)	2.1477(5)	97.33 ± 2.52	7.97
AFt_0.67_DH3.4	1.1236(7)	2.1470(7)	93.05 ± 2.28	8.89
AFt_3.89_DH0.5	1.1237(2)	2.1478(1)	94.00	6.55

The size of the needles was qualitatively estimated by ESEM image analysis of solid pieces of around 10 mm^2 (Figure 3.10). At the lowest concentration (Figure 3.10a), the needles appear approximately 0.5 µm thin and 20 µm long. In contrast, the matrix becomes denser and a significant reduction of the needles length is observed by increasing the concentration of the suspension (Figure 3.10c).
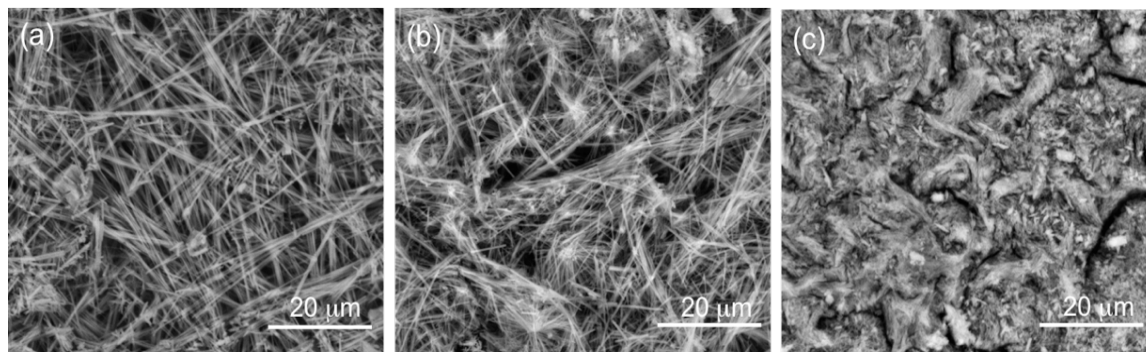
Figure 3.10: Scanning electron microscopy images of solid piece of ettringite (a) AFt_0.39_DH1.2, (b) AFt_0.67_DH3.4, and (c) AFt_3.89_DH0.5.

3.4.1.2   Thermal stability of ettringite

Figure 3.11 shows a gradual mass loss (%) after degassing when a higher temperature is used. The reported mass loss corresponds to the water loss calculated in the temperature range between 25 and 550 °C, without assignment to the different mineralogical phases, namely AFt and gypsum.

For the four synthetic ettringites, the removal of water follows the same evolution with temperature, regardless of the different content of gypsum. The initial content of water is not preserved even at the very moderate temperature of 30 °C, whereas almost 25% of the total mass is lost at 50 °C.
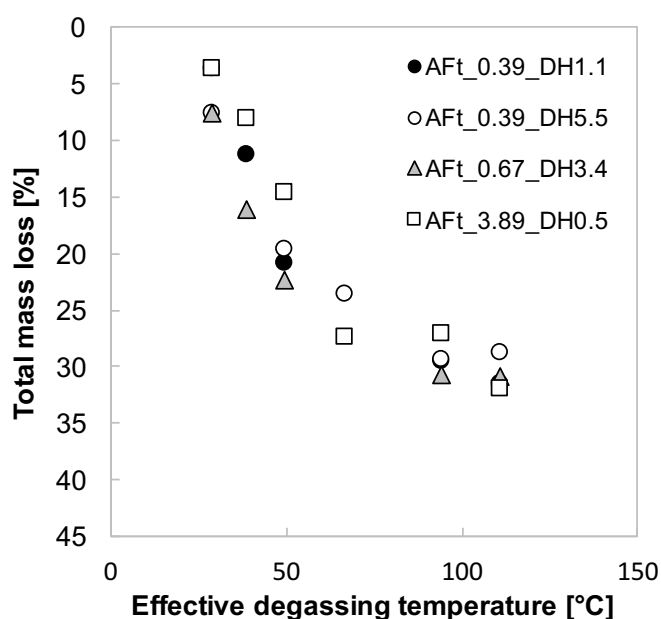
Figure 3.11: Mass loss (%) measured by TGA after degassing at different temperatures under N₂ flow for 16 h. The effective temperatures are plotted in the x-axis and refers to that one calculated from the calibration of the degassing station according to Figure 3.2.

The effect of the evacuation required at the beginning of the SSA_{BET} measurement on the ettringite was also investigated by TGA measuring the mass loss of the samples after degassing and SSA_{BET} measurements, corresponding to steps 3 and 4 in Figure 3.1, respectively. In the specific case of the AFt_3.89 degassed at 40 °C under N_2 flow for 16 h, for example, around 5 molecules of water are lost after the SSA_{BET} measurements. However, only about 2% of the total mass – corresponding to 1.4 molecules of water – was lost during the evacuation, meaning that the major contribution to the sample decomposition occurs in the degassing step.

The dehydration induced by thermal degassing causes a structural disorder of ettringite, as shown in Figure 3.12. The degassed samples were compared to the untreated AFt, whose pattern evidences well-defined reflections despite the gentle milling and sieving steps necessary for the XRD sample preparation.

The comparison of the XRD patterns obtained after degassing with the one of the reference material indicates a significant collapse of the peak intensity even for samples degassed at moderate temperatures (50 °C) for 16 h. Under these conditions, furthermore, the gypsum present in the ettringite is converted into

calcium sulfate hemihydrate. The number of water molecules was calculated considering the mass loss measured by TGA between 25 and 550 °C.
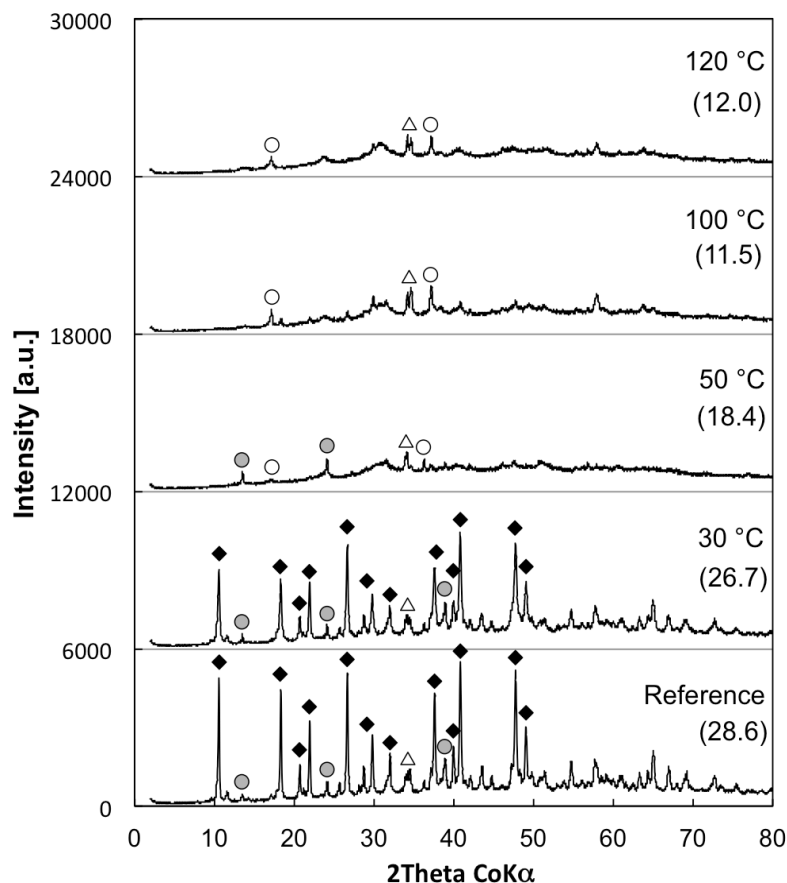
Figure 3.12: Structural changes in AFt_0.39_DH5.5 XRD patterns observed after degassing under N$_2$ flow for 16 h at different temperatures. The number of water molecules in the ettringite is reported in brackets taking into account the contribution of gypsum. The same scale length was plotted in the y-axis keeping the original intensity for each XRD pattern. The black diamonds indicate the reflections of ettringite, the grey circle gypsum, the white circles calcium sulfate hemihydrate, and the white triangle calcite.

3.4.1.3   Effect of temperature on the SSA of ettringite

Figure 3.13 on the top shows the normalized SSA$_{BET}$ values plotted against the lost water molecules calculated from the TGA results in the temperature range between 25 and 550 °C on the samples after the SSA$_{BET}$ measurements. The content of gypsum was quantified by XRD-Rietveld and the corresponding water molecules were subtracted. The SSA$_{BET}$ values were normalized by the SSA$_{BET}$ values measured after degassing at 30 °C under a N$_2$ flow for 16 h. This facilitates the comparison of

the results on ettringites having different particle size distribution and primary needle sizes due to different synthesis conditions.

The amorphization of the samples prepared at high temperatures made the Rietveld quantification of the dehydration products from gypsum very difficult. Therefore, the number of water molecules lost was estimated from the TGA measurements considering the water loss from the constant gypsum content in each reference ettringite. For this reason, the calculation results are exact only up to 40 °C. Above this temperature, the loss of water molecules is slightly overestimated, since gypsum partially dehydrates to calcium sulfate hemihydrate. However, the evolution of the normalized SSA_{BET} still includes the contribution of both gypsum and its dehydration products.

Figure 3.13 (top) can be divided in two distinct areas, of constant and increasing normalized SSA_{BET}. In the latter, the evolution of the normalized SSA_{BET} is strongly dependent on the lost water molecules, which are directly linked to the degassing temperature (Figure 3.13, bottom), type of ettringite (concentration of starting suspension) as well as the gypsum content. In contrast, the ettringite composition does not influence the normalized SSA_{BET} values when less than 12 molecules of water are thermally removed from the structure.

Furthermore, on samples having a gypsum content lower than 2%, the increase of the normalized SSA_{BET} starts above 50 °C (Figure 3.13, bottom), with an associated loss of 14 or more molecules of water. For these samples, the increase is higher for the more concentrated ettringite suspensions, which also corresponds to powders with a shorter needle size. At higher content of gypsum, the normalized SSA_{BET} increases up to 50% once 12 or more molecules of water are lost starting from temperatures higher than 40 °C (Figure 3.13, bottom). At 110 °C, a systematic drop of the SSA_{BET} is observed.
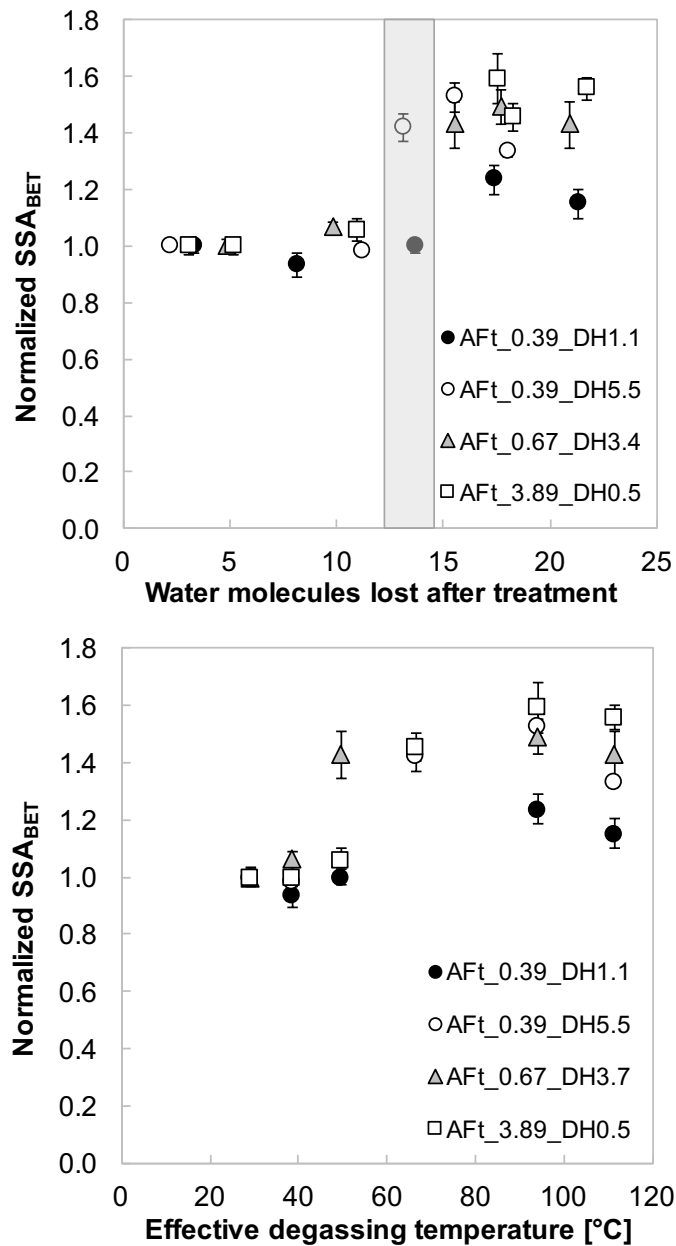
Figure 3.13: Evolution of the normalized SSA$_{BET}$ with the number of water molecules lost (top) and the degassing temperature (bottom) after thermal treatments. The grey-shaded band in the plot on the top indicates the threshold (12-14 water molecules lost) below which the SSA$_{BET}$ remains constant. The error bars correspond to the standard deviation on the SSA$_{BET}$ measurements.

3.4.1.4   Effect of stopping hydration protocol on the early-aged cement pastes

Figure 3.14 shows the XRD patterns of the synthetic ettringite after contact with IPA. No new crystalline reaction products were detected by XRD. The patterns of the samples treated with the organic solvent are characterized by a systematic decrease

of the intensity of all the peaks in comparison to the initial one of ettringite, while the width of the peaks remains unchanged.

When ettringite is in contact with IPA at 22 °C, its structural order is partially altered showing a significant decrease of the overall peak intensity of about 55%. However, when IPA at 5 °C and − 18 °C is used, the structural changes induced on the ettringite are substantially reduced.
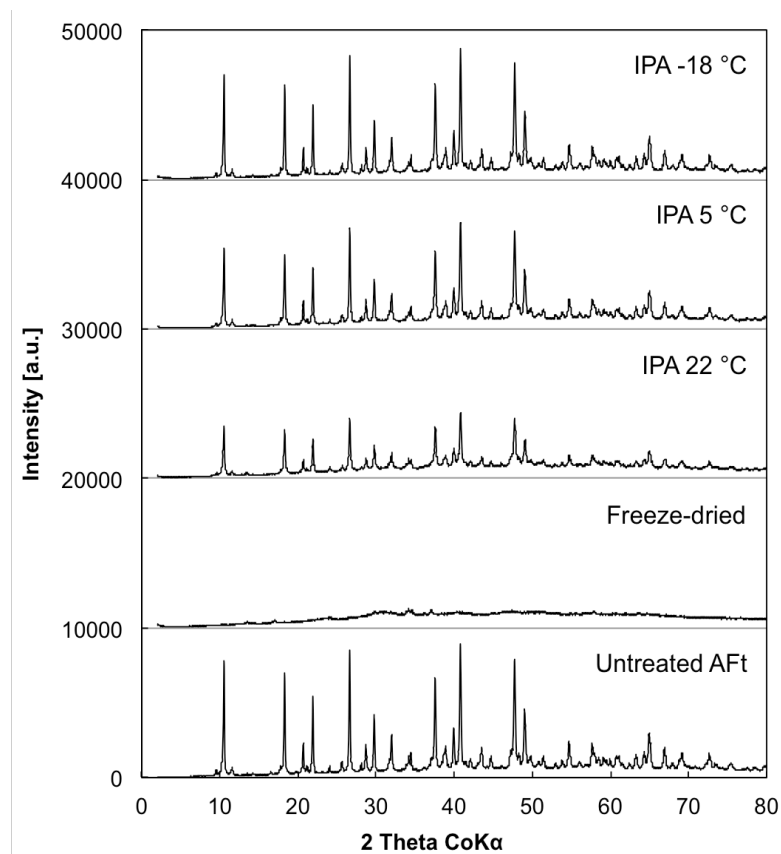
Figure 3.14: XRD patterns of AFt after treatment with isopropanol (IPA) at powder to solvent ratio 1:50 at different solvent temperatures and after freeze-drying. The same scale length was plotted in the y-axis keeping the original intensity for each XRD pattern.

Table 3.8 shows an increase of the loss of water molecules with the temperature of the isopropanol. This increase is higher when DEE is used afterward.

The SSA$_{BET}$ measurements in the same table confirm that the partial dehydration induced by the solvents does not involve any change in the SSA$_{BET}$ of the ettringite. The freeze-dried sample shows a much more important mass loss. This implies an almost complete amorphization of the sample, as shown in Figure 3.14. Surprisingly, the change of the SSA$_{BET}$ measured is minimal and barely even significant.

Table 3.8: Effect of the protocol used to stop of hydration on the SSA$_{BET}$ and water molecules loss of the ettringite AFt_3.89_DH0.5. For the solvent replacement, the powder to solvent ratio was 1:50.

Sample	SSA$_{BET}$ (m²/g)	Water molecules lost	
		After stop of hydration	After SSA$_{BET}$ measurements
Reference	8.8 ± 0.2	--	5.1
AFt/IPA (22 °C)	8.8 ± 0.2	1.9	6.6
AFt/IPA (5 °C)	8.8 ± 0.3	1.4	6.6
AFt/IPA (-18 °C)	8.8 ± 0.3	0.9	6.7
AFt/IPA (5 °C) + DEE	8.6 ± 0.3	7.0	11.7
Freeze-drying	9.3 ± 0.3	16.5	17.1

We examined whether the presence of adsorbed polymer could affect the SSA$_{BET}$ of a substrate, for example by modifying the adsorption of N_2 (surface occupied). For this we used an inert powder of $CaCO_3$ (Sigma-Aldrich, ACS reagent, 99.95-100.05% dry basis).

As first step, the powder was put in UPW at a water-to-solid ratio of 5 at 23 °C for 24 hours to mimic the formation of a hydrated shell on the surface, then it was filtered by a membrane filter (polyamide membrane filter with a pore size of 0.45 µm (Sartolon Polyamid)) connected to a vacuum pump (ultimate vacuum ≈ 100 mbar) and dried in a desiccator at 23 °C with a $CaCl_2$ saturated solution until constant weight. In a similar experiment, 0.4% active by weight of solid of 4PMA1000 (for further details, see Table 5.3 in session 5.2) was added to the hydrated $CaCO_3$ in UPW and mixed for further 2 hours: part of the suspension was then directly filtered, whereas the rest was put in contact with IPA (ACS reagent ≥99.5%, Scharlau) at 23 °C to mimic the stopping of hydration by solvent replacement. Prior to this, we had verified that the polymer dosage used was sufficient to fully cover the powder surface. Both obtained samples were dried under $CaCl_2$ saturated solution environment.

Table 3.9 reports similar values for the three situations examined, evidencing the negligible modification of the overall SSA$_{BET}$ of hydrated $CaCO_3$ induced by the adsorbed polymer. It is worth emphasizing that the PCE addition occurred on a pre-formed crystalline phase. On the other hand, PCE addition during the nucleation of

the same phase is likely to affect its morphology with some consequent changes of the SSA_{BET}. Those would relate to impact on the phase formation process, but not from a modification of the SSA_{BET} measurement itself, in particular the surface occupied by each adsorbed molecule of N_2.

Table 3.9: Effect of the adsorbed PCE on the SSA_{BET} of $CaCO_3$ powder.

Samples	SSA_{BET} [m^2/g]
Hydrated $CaCO_3$	5.1 ± 0.2
Hydrated $CaCO_3$ + PCE	5.3 ± 0.1
Hydrated $CaCO_3$ + PCE + solvent	5.26 ± 0.06

It has been shown how to properly prepare samples before SSA_{BET} measurements, involving the degassing and the stop of hydration using cold IPA. These procedures have been mostly validated on anhydrous cementitious phases and synthetic ettringite. The proposed methodologies have been applied on fresh cement pastes and the main challenges with this complex matrix come from stopping hydration with cold isopropanol. Indeed, this step should be performed in a very short time to enable the collection of many solid samples over the workability timeframe of hydrating cement pastes. The latter might last from one to several hours, depending on both polymer dosage and structure.

The initial contact time between IPA and cement in the beaker is only 1 minute. Nevertheless, the total contact with IPA could be far longer (more than 40 minutes) during the filtration of the solvent, mainly for highly dispersed cement pastes, as indicated in Figure 3.15 (single-step filtration SF as filled symbols). The extension of the filtration time appears to be strongly dependent on both polymer structure and dosage.

The alternative proposed methodology – defined as "double-step filtration" (DF) – consists of the initial filtration of fresh pastes alone under pressure, allowing the removal of superplasticized interstitial liquid. Then, the moist paste is put in contact with the solvent and mixed in a beaker, keeping the solvent/powder ratio of 10 and mixing for 1 minute. The suspension is poured and filtered into a stainless-steel

pressure filter holder as before. The powder is stored in a desiccator with a calcium chloride saturated solution (32% RH at 20 °C) until constant mass. Dried powders were, then, gently homogenized in an agate mortar before the different measurements. The proposed double-step filtration drastically reduces the filtration time – down to a maximum of 5 minutes –, regardless of either the polymer structure or its dosage (Figure 3.15, empty symbols).
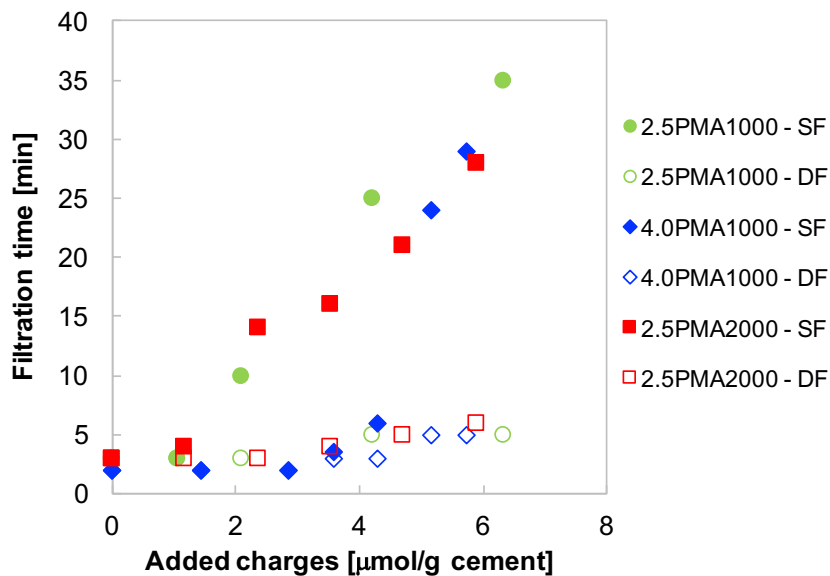
Figure 3.15 Effect of the polymer structure and dosed charges on the time necessary to remove the solvent after solvent exchange by comparing single-step filtration (SF, filled symbols) and double-step filtration (DF, empty symbols).

It is worth noticing that the proposed filtration time is only based on qualitative observations, as the amount of initial paste. Therefore, the amount of solvent was comparable, but not exactly the same. Nevertheless, the difference in terms of filtration time between both procedures is quite remarkable. Besides the effect of the contact time, it is important to remember that the solvent temperature increases over time, leading to possible damage.

Without polymer, the time required for the removal of the solvent is very short applying both methods. However, the mixing of the moist paste in the DF is difficult and many lumps form, limiting the contact between the paste and the solvent.

As observed in Figure 3.16, the SSA_{BET} values measured on cement pastes using the two different procedures are statistically comparable when the hydration is stopped

after 7 minutes of hydration (according to *t*-test with *P* = 0.05 [236]). However, this comparison is not valid for samples without polymer.
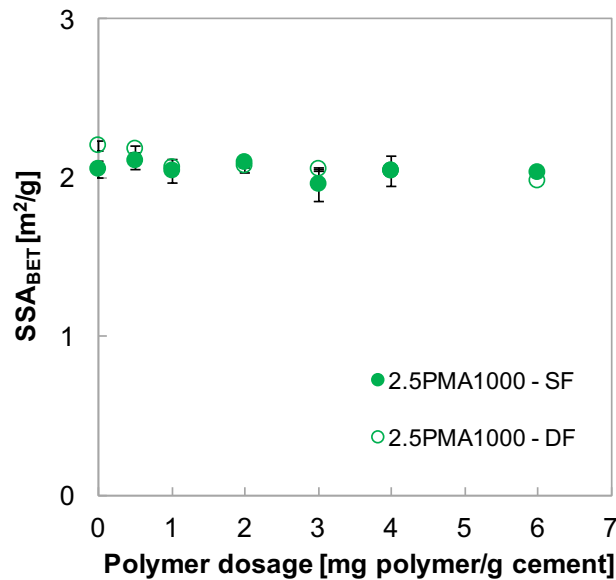
Figure 3.16: Comparison of SSA$_{BET}$ values from pastes obtained from single filtration (full symbols) and double filtration (empty symbols) used to stop the hydration.

3.4.2 Discussion on SSA of ettringite

The systematic study of the thermal effect on synthetic ettringite crystals (Figure 3.11) has confirmed that under the applied degassing conditions (16 h under N$_2$ flow), partial dehydration occurs even at moderate temperatures. Specifically, at 40 °C a loss of around 12 molecules of water has been measured. Such dehydration involves a decrease of the crystallinity of the ettringite (Figure 3.12). However, this does not imply a change of its SSA$_{BET}$. In contrast, when ettringite is exposed to higher temperatures and more than 14 molecules of water are lost, a substantial increase of the SSA$_{BET}$ is observed.

Studies conducted in the past years showed the strong correlation between temperature and partial pressure on the AFt decomposition, confirming that AFt starts decomposing with no chance to re-hydrate at 40 °C and 0% RH [216,218]. In the specific conditions applied during the degassing for SSA$_{BET}$ measurements, Dalas [237] examined also the degassing time, observing that the AFt decomposition occurs even at 25 °C but for longer times than at higher temperatures. He also

showed that different partial pressures induced by the use of both nitrogen and air at different temperatures affect the AFt decomposition. However, this author failed to mention the systematic effect on the SSA_{BET}.

Here, the degassing time was kept constant at 16 hours. Only a degassing under N_2 flow was considered for all the samples and the measured RH in the tube at the height of the powder sample approached zero. Therefore, the effects reported can confidently be attributed to the temperature rather than changes in partial pressure.

Ettringite crystals are hexagonal prisms that consist of columns and channels parallel to c-axis (Figure 3.17). The composition of the columns is $[Ca_6(Al(OH)_6)_2 \cdot 24H_2O]^{6+}$. Each $[Al(OH)_6]^{3-}$ ion at the corners of the unit cell is linked to three Ca^{2+} that are octa-coordinated by hydroxyl groups and four water molecules. Three sulfate groups and two molecules of water occupy the inter-column channels [219,235,238].

During dehydration, ettringite initially loses the two molecules of water from the inter-column channels. This does not involve a noticeable change of unit cell size or crystallinity, as confirmed by our results (Figure 3.12) [215,217,219,239].

Afterward, the removal of 12 additional water molecules bonded to Ca^{2+} in apices 3 and 4, as well as the partial loss of the bridging OH groups occurs. This reduces the cell dimension a, the inter-column space, and causes a small contraction of the cell dimension *c* [219,220,239], but it also leads to a loss of crystallinity as shown in Figure 3.12. According to Skoblinkskaya and Krasilnikov [219], this water removal happens in individual and consecutive steps. On the other hand, Young and Shimada [215] – on the basis of their NMR experiments – concluded that the loss of water molecules from apex 3 and from the bridging OH occur simultaneously. According to our XRD results, the loss of 10 molecules of water already implies a significant decrease of the crystallinity, in contrast with the results in the literature showing a structure retention up to a loss of 14 water molecules [215,220]. However, in this range of water loss, the SSA_{BET} of synthetic ettringites remains constant, as shown in Figure 3.13 (top).
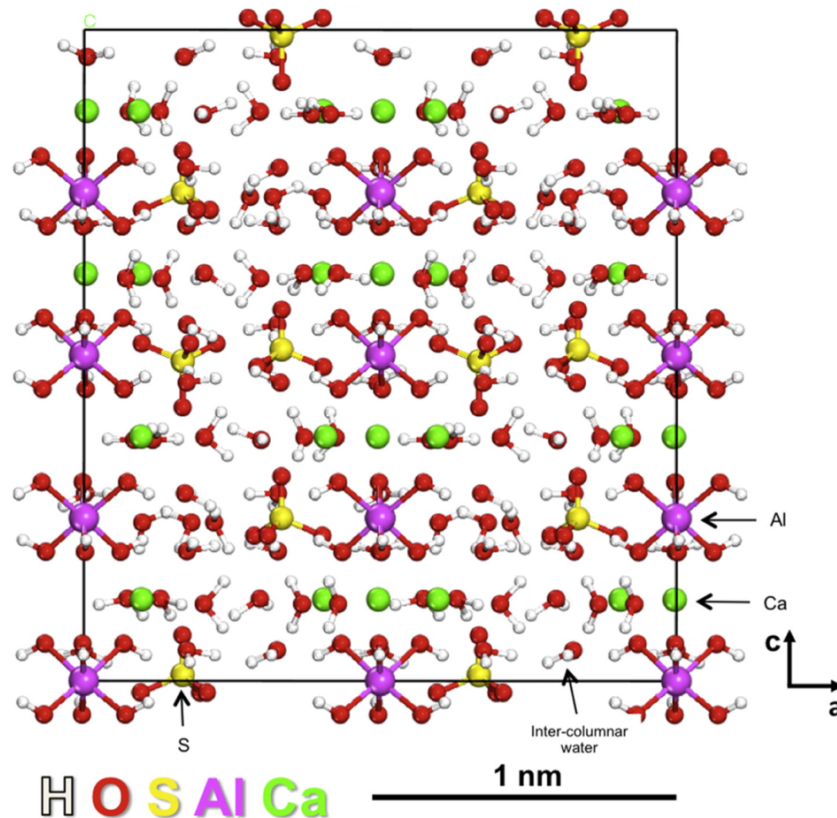
Figure 3.17: Crystal structure of ettringite. The atomistic view is projected perpendicularly to the b axis onto the horizontal ac plane. The crystallographic structural data are from [238]. Image is courtesy of Dr R.K. Mishra (IfB-ETHZ).

Ettringite is well known to exchange as well its sulfate group with other anions, (as OH^-, CO_3^{2-}, $B(OH)_4^-$ and CrO_4^-) as Al^{3+} with other cations (as Fe^{3+}, Cr^{3+} and Si^{4+}) [240–243]. Among the substituted AFts, thaumasite $(Ca_3Si(OH)_6(SO_4)(CO_3) \cdot 12H_2O)$ originates in concrete from sulfate attack at low temperatures involving the reaction of calcium silicate hydrate (C–S–H) with dissolved carbonate and sulfate ions [192]. It shows no water loss up to 40 °C, even for a prolonged heating time [244] because its structure is stabilized by the presence of carbonate ions that hinder the dehydration process [245]. In thaumasite, the presence of carbonate groups prevents the shrinkage along the *a*- and *c*-axes of its hexagonal structure (space group *P6₃*) while dehydrating. In contrast, the pure CO_3-ettringite, with a trigonal symmetry, behaves more similarly to the pure ettringite, showing a halving of *c*-axis [245]. From a qualitative point of view, we conclude that our sample conditioning protocol for SSA_{BET} measurements should be also adequate for other forms of ettringite because all the above-mentioned minerals have a better thermal stability

than the pure ettringite studied in this paper. Nevertheless, partial pressure and heating time also play a role in dehydration, so that this expectation ought to be checked experimentally in future research.

3.4.2.1   Region of constant specific surface area

The initial loss of water without modification of the SSA_{BET} implies that individual ettringite particles must increase their density when a maximum of 12 molecules of water are removed. This has been confirmed experimentally, but the reason why this should lead to a constant specific surface deserves to be discussed in further detail.

In what follows we examine how various properties are affected by water loss. As we are interested only in this dependency we use proportionality relations, using the ≈ sign and removing all multiplication terms that are constant. Let us assume that, in pure ettringite, the density of the water that gets initially lost is the same as that of bulk water. In such a situation, the density of ettringite after partial water loss (ρ_2) would be:

$$\rho_2 = \frac{m_1 - m_{lost}}{V_{initial} - V_{water\ lost}} = \frac{m_1 - m_{lost}}{m_1/\rho_1 - m_{lost}/\rho_w} \approx \frac{1 - x_m}{1 - \rho_1^r x_m} \qquad \textbf{(3.1)}$$

where m_1 and ρ_1 are the initial mass and the initial density of an ettringite particle (considered constant parameters), m_{lost} is the mass of water lost from this particle, x_m is the water lost expressed as a fraction of the initial particle mass, $V_{initial}$ and V_{lost} water are the volumes of the initial ettringite particle and of the lost water, respectively, ρ_w the density of water, while ρ_1^r is the relative density of the starting ettringite with respect to that of water equal to 1.9.

As shown in Figure 3.18, this relation agrees perfectly with the measured densities, up to the point where more than 12 water molecules are lost (grey zone in Figure 3.18). The increase in density implies that the ettringite particles must shrink and the question is whether this occurs similarly in all directions or not. Because of the crystal structure, it appears more probable that this shrinkage would take place in the directions perpendicular to the c-axis [239].
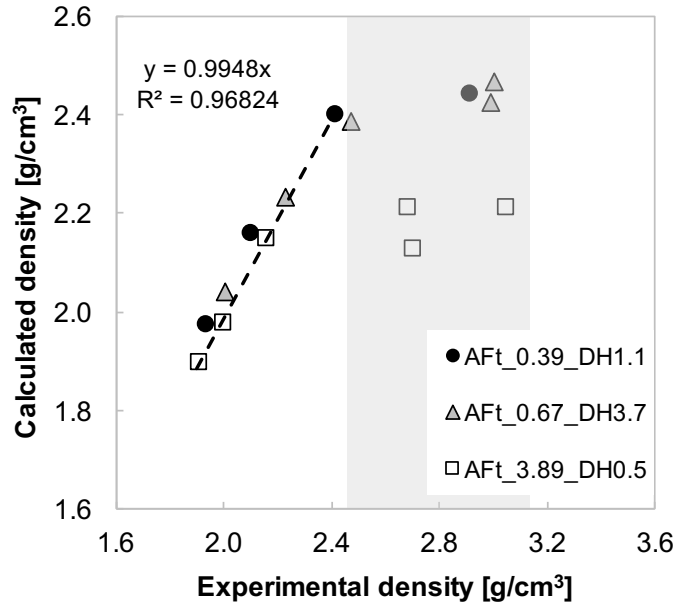
Figure 3.18: Correlation between calculated and experimental densities. The linear relation corresponds to the region where the SSA$_{BET}$ of the ettringite is constant despite the water lost (up to 12 molecules of water). The grey-shaded band indicates the samples losing more than 12 molecules of water.

Thus, the volume V_2 of a reference ettringite particle after partial water loss can be expressed as a function of the characteristic lateral dimension a_2 and of the fractional weight loss x_m as:

$$V_2 \approx a_2^2\, h \approx \frac{m_2}{\rho_2} \approx \frac{1-x_m}{\rho_2} \tag{3.2}$$

where h is its length being unchanged by the water loss. Together with Equation (3.1), this gives the following expression for a_2 as a function of the water loss:

$$a_2 \approx \sqrt{1 - \rho_1^r x_m} \tag{3.3}$$

Considering the fact that our ettringite crystalized as long needles, their surface comes mainly from the long sides. Therefore, considering shrinkage only perpendicular to the c-axis and the same shrinkage in the two directions of the cross section, the specific surface area for a prism with a square cross section after a partial water loss SSA_2 can be written as:

$$SSA_2 = \frac{S_2}{m_2} = \frac{2a_2^2 + 4a_2h}{m_2} \qquad\qquad \textbf{(3.4)}$$

where a_2 is the lateral dimension of the needle and h the unchanged length of the prism. Because of its significantly lower value, $2a_2^2$ can be neglected. Moreover, the above relation can be generalized for any cross-sectional area, simply by considering a characteristic dimension a_2 of this area, so that:

$$SSA_2 \approx \frac{a_2}{m_2} \approx \frac{a_2}{\rho_2\, a_2^2} \approx \frac{1}{\rho_2\, a_2} \qquad\qquad \textbf{(3.5)}$$

Substitution of Equations (3.1) and (3.3) gives:

$$SSA_2 \approx \frac{\sqrt{1 - \rho_1^r x_m}}{1 - x_m} \qquad\qquad \textbf{(3.6)}$$

Although this equation shows a certain dependence of the specific surface area as a function of the water lost, this remains very small because the value of the relative density of ettringite is close to two, which cancels the first order dependence on x_m in a Taylor expansion. It is worth noting that a stronger dependence on x_m is recovered if the particle is assumed to shrink similarly in all three dimensions. In that case, the numerator of Equation (3.6) would have a power of $^3/_2$ instead of $^1/_2$.

Consequently, we conclude that when ettringite loses its first 12 water molecules, it shrinks only in the directions perpendicular to the *c*-axis. This, together with their needle shape and starting density, explains the zone of constant specific surface reported in Figure 3.18. This simple calculation matches the macroscopic measurements of specific surface area of our samples. However, a more detailed investigation of the pertinence of the underlying hypothesis concerning crystal deformations would deserve further attention, using quantitative XRD measurements, but this is beyond the scope of the present study.

Also, as suggested by Zhou et al. [239], this transformation may be considered as topotactic, namely the atom groups would largely maintain their relative positions and orientations. The loss of crystallinity would result from a lack of alignment of the columns after this transformation. It is worth mentioning that the specific

surface should also remain constant if particles split (break) in their length, but that their summed length in the *c* direction remains unchanged.

3.4.2.2   Region of varying specific surface area

Above 50 °C, the additional loss of water causes an increase in the SSA$_{BET}$ as shown in Figure 3.13. In this region, it also appears that the increase in specific surface is more important for the samples with the smallest needle size (Figure 3.11) [219]. Additionally, for a constant particle size, the SSA$_{BET}$ increases more for the sample with the largest gypsum content, probably because of the surface created by the additional dehydration of this calcium sulfate phase [19].

In terms of structural modification, the thermal dehydration of the ettringite in this region leads to the formation of meta-ettringite (m-AFt) having a number of water molecules ranging between 9 and 13 [216,237,239]. According to the literature [220,246], the decrease of the number of molecules retained in the structure from 18 to 6 involves the decrease of the coordination number of Ca and Al. It would also induce the breakdown of ettringite columns and the introduction of defects and cracks [220,239] with the consequent increase of the SSA$_{BET}$ evidenced at temperatures higher than 60 °C (Figure 3.13, bottom). Zhou et al. [239] conclude that the collapse of ettringite to meta-ettringite cannot occur without scissoring and possible rotation of individual columns with the consequent loss of crystalline structure as demonstrated in the XRD patterns (Figure 3.12).

3.5 Effect of different stopping hydration protocols on SSA

3.5.1 Synthetic ettringite

With respect to the protocols for stopping hydration, we have confirmed that both organic solvents and freeze-drying can partially extract water from the crystal structure of ettringite, as previously reported by other authors [214,247–250].

However, if the solvent is applied at low temperature, this effect can be *de facto* eliminated.

After freeze-drying, a loss of up to 17 molecules of water as well as a complete loss of crystallinity are observed (Figure 3.12). Therefore, this method is not suitable to stop cement hydration, if an XRD-based quantification of the ettringite is intended [251]. Despite the slight increase of the ettringite SSA_{BET}, in practice, freeze-drying is inappropriate because the use of high vacuum can alter the free gypsum present in early-aged cement pastes.

In the case of the solvent replacement method, all the conditions reported in .

Table 3.8 lead to the same SSA values. This is because the number of water molecules lost remains below 12 and, therefore, in the region of constant SSA_{BET}. This also holds for the samples after the additional treatment with DEE, which increases the number of water molecules lost without altering the SSA_{BET}. Moreover, as also indicated in .

Table 3.8, all these values are identical to the untreated powder ettringite surface. This indicates that the applied drying procedure is sufficient to remove the solvent from the ettringite surface (degassing over 16 h under N_2 flow, after an adequate drying in the desiccator).

However, the partial removal of water from the structure of ettringite using solvents results in a partial loss of crystallinity. This problem can be reduced or even eliminated by using cold isopropanol (5 °C or −18 °C), as shown in Figure 3.14. Therefore, we conclude that the use of cold isopropanol is an effective way to preserve the crystallinity of ettringite when stopping hydration, which makes quantitative phase analysis possible.

3.5.2 Early-aged cement pastes with and without PCEs

Increasing the polymer dosage, the filtration of the solvent from the hydrating cement paste extends up to 40 minutes (Figure 3.15). This is not acceptable for the purpose of the present work, where the hydration has to be stopped frequently in a

short time. The filtration time can be substantially reduced by applying the proposed DF, limiting possible damage of the hydrates due to longer exposure with the solvent. According to the author's opinion, the hydration is already mostly stopped after the first filtration step, as the interstitial fluid is removed, thus reducing the hydration rate.

The mixing of the moist cementitious matrix with the solvent is eased by the presence of the remaining polymer that disperses the paste. In absence of PCE, the paste tends to agglomerate, making the contact with the solvent inhomogeneous. This might be the reason for the major difference from the sample of which the hydration was stopped by DF (Figure 3.16). Therefore, the single-step filtration is preferred in absence of polymer.

A longer filtration time might be due to the interaction of the organic solvent with the finest superplasticized particles, causing the blockage of the filter pores. For this purpose, the interaction of an Artificial Pore Solution (APS), containing elements at very high concentrations, namely calcium, sodium, potassium, sulfur, with a PCE has been qualitatively studied by using a different organic solvent. This APS mimics the composition of the cement pore solution obtained from the cement Holcim Normo 5R used in this study at w/c of 0.3 (Table 3.1). A non-commercial polycarboxylate ether-based comb polymer obtained by copolymerization with poly(methacrylic acid) based-backbone, C/E ratio of 2.5 and PO side chains length of 1000 Da was dosed at 0.2% active by weight of cement (bwc). Admixed synthetic pore solutions with the most common polar solvents used for stopping cement hydration, such as isopropanol, ethanol acetone and methanol, produced flocculated and turbid systems as shown in Figure 3.19. This effect occurs at room temperature as well as at 5 °C, independently of the solvent used together with the synthetic pore solution. From this can be inferred the beneficial effect of the removal of most of the interstitial fluid before the contact with the solvent on the filtration time.

The main concern coming from a prolonged exposure to the organic solvent is a possible structural dehydration of the ettringite. Synthetic ettringite was then mixed with cold IPA for one minute in a beaker and left to rest for 5, 30 and 120 minutes.

The solvent was filtered away in the stainless filtration system mounted with a nylon 0.45 μm membrane filter (Sartorius) under a pressure of 4 bar. It was confirmed that, despite a long contact with a *warming* solvent, the SSA_{BET} of synthetic ettringite is not altered, since less than 12 molecules of water were lost, as shown in Table 3.10.
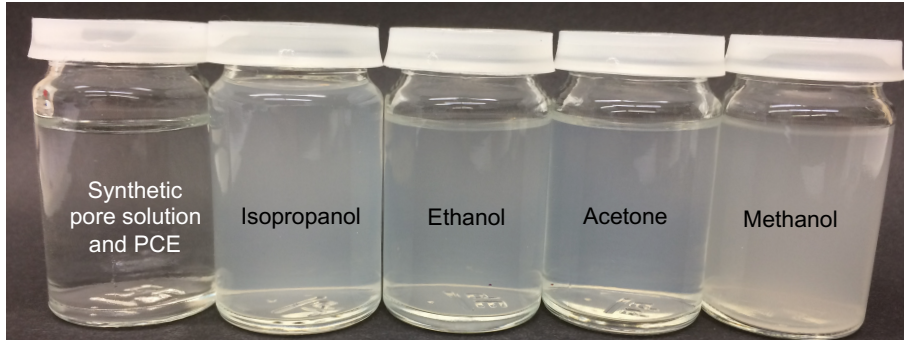
Figure 3.19: Flocculated systems produced at room temperature by the interaction between PCE, artificial pore solution (APS) and four common organic solvents used to stop the cement hydration (isopropanol, ethanol, acetone, and methanol).

Table 3.10: SSA_{BET} of synthetic ettringite and water molecules lost after prolonged exposure times with IPA at 5 °C.

Time [min]	SSA_{BET} [m²/g]	Water molecules lost	
		After stop of hydration	After SSA_{BET} measurements
No solvent	8.8 ± 0.2	--	--
5	8.9 ± 0.2	1.4	6.6
30	8.8 ± 0.2	2.9	8.3
120	8.7 ± 0.2	3.8	9.3

This validates the analogous results in early hydrated cement pastes obtained with the prolonged single-step filtration at the same PCE dosage. However, a shorter contact with cold IPA is recommended if a reliable quantification of cement hydrates is necessary.

A slight decrease of SSA_{BET} values are measured by increasing the polymer dosage at the beginning of the hydration (Figure 3.15). This might be explained by a preferential adsorption of the PCE on the reactive sites of the cement surface that leads to a decreased number of steps able to retreat [15]. However, recent studies

[9,15] showed that PCEs significantly increase the SSA$_{BET}$ on the basis of their structure and dosage just after few minutes after the contact with water due a massive formation of ettringite. In those studies, model systems having high contents of aluminates were used to amplify the effect of PCEs. In commercial cements, in contrast, the content of aluminates is typically much lower and the lower amount of forming ettringite has a less evident impact on the overall SSA$_{BET}$.

3.6 Conclusions

We demonstrated that the selection of the degassing conditions (temperature, pressure and time) becomes crucial for reliable SSA measurements of anhydrous cements by nitrogen adsorption. This is because of the dehydration of the gypsum it contains, which involves an increase of the SSA.

At temperatures higher than 100 °C, the gypsum dehydration is complete and SSA$_{BET}$ values reach a plateau, the value of which depends on whether vacuum or N$_2$ flow is used. XRD results show that gypsum partially dehydrates even at 40 °C under vacuum. At this condition, the dehydration process is strongly time dependent. The thermal dehydration of gypsum involves the formation of cracks and crevices. As the adsorptive N$_2$ can access them, the SSA$_{BET}$ increases significantly, whereas Blaine values remain nearly constant. This confirms the poor sensitivity of Blaine test to the This confirms the poor sensitivity of Blaine test to the different hydration conditions and structural modifications of the calcium sulfate carrier.

It was also demonstrated that the dehydration of ettringite occurs even at moderate temperatures under N$_2$ flow (0% RH). However, this partial dehydration up to 12 molecules of water does not modify the SSA$_{BET}$. At high temperatures, ettringite dehydration involves a significant modification of its crystalline structure and increase of the SSA$_{BET}$.

Mild conditions involving the degassing at 40 °C under N$_2$ flow for 16 h are mainly recommended to preserve the chemical composition and morphology of calcium sulfate carrier.

We have also confirmed that both solvent exchange and freeze-drying, which are typically used to stop cement hydration, lead to a slightly larger water removal from the AFt structure, but a moderate increase in specific surface area is observed only on the freeze-dried samples. Both protocols were also shown to reduce the crystallinity of ettringite, but freeze-drying was much more drastic, leading to a complete amorphization of this mineral. More importantly, it was shown that stopping hydration with cold isopropanol makes possible to retain the crystallinity of ettringite, thus enabling quantitative phase analysis of samples whose hydration would be stopped in this way.

In fresh cement pastes, the contact with the cold solvent to stop the hydration is generally longer than 5 minutes due to the solvent interaction with of the pore solution containing PCEs. This leads to some nano-precipitate or micelle that slows down the removal of the solvent probably by blocking the filter. A prolonged exposure to the solvent does not affect the overall SSA_{BET}. Nevertheless, this limits the number of samples that can be possibly collected in a short time. The proposed Double Filtration (DF) shortens the filtration time down to 5 minutes regardless of the dosage and the structure of the PCE used.

These findings and methodologies represent an essential development to address the main scientific question in this work concerning the flow loss of superplasticized cement pastes and their possible link to specific surface modifications by PCEs.

Chapter 4

Characterization of cement pore solutions by ICP-OES

This chapter consists of the paper "ICP-OES method for the characterization of cement pore solutions and their modification by polycarboxylate-based superplasticizers", Francesco Caruso, Sara Mantellato, Marta Palacios, Robert J. Flatt, published in *Cement and Concrete Research* 91, 52–60 [21]. This work has been also featured as "Highlight of Analytical Sciences in Switzerland" in a recent issue of *CHIMIA*, the Official Membership Journal of the Swiss Chemical Society (SCS) and its Divisions [22].

Ms Mantellato, in collaboration with Francesco Caruso, developed from scratch the ICP-OES method for the characterization of cementitious pore solutions, being missing for this application in the literature. Specifically, Ms Mantellato shares the first co-authorship with Francesco Caruso. Under the light of her main project, this method has been also applied for the study of pore solutions from superplasticized cement pastes. Ms Mantellato with Marta Palacios and under the supervision of Prof. Flatt identified major changes in cement pore solutions with PCEs, posing the basis for a detailed understanding of working mechanisms of chemical admixtures.

The effect of the polymer structure and dosage on the cement pore solution composition has been investigated by ICP-OES and preliminary results are reported in Appendix I. Limitations coming from the sample preparations as well as the evolution of the elemental concentrations over time are also presented.

4.1 Introduction

Hydration of cement is a dissolution-precipitation process. Therefore, the quantification of the elements in cement pore solutions gives relevant information about the assemblage of solid phases and their levels of saturation [23,38,252,253]. Besides, the analysis of pore solution is a powerful tool to predict concrete durability [254]. It can also provide insight into understanding how chemical admixtures, which cover a broad range of chemical structures [2], can modify cement hydration by acting on one of the involved mechanistic steps [193,255].

Pore solution composition has been extensively combined in the literature with thermodynamic modelling to understand the impact of different factors on cement hydration such as temperature [222], supplementary cementitious materials (SCMs) [222,256] and chemical admixtures [257,258]. Among different analytical techniques such as ion chromatography, atomic absorption spectroscopy and inductively coupled plasma – optical emission spectrometry (ICP-OES), the latter is the most powerful to analyse trace elements in complex matrices, such as cement pore solutions. ICP-OES can simultaneously measure the concentration of up to 70 elements, considering the matrix interferences [259].

However, although several studies have been performed on the thermodynamics and speciation aspects of cement pore solutions [33,253,260–263], very little has comparatively been done to define an appropriate experimental ICP-OES protocol, including sample preparation, to provide highly reliable starting analytical data. In particular, this method hosts the main challenge of the characterization of a complex matrix with elements at very high concentration and other ones at very low concentration, something barely ever mentioned in the cement literature. With regard to the elements at very low concentrations, the quantification of aluminium at microtrace levels is particularly challenging, considering the absence of any reference operating condition in the existing literature. Furthermore, the analysis of aluminium is of particular relevance in admixed cement samples, as a dramatic increase of its concentration has been reported in their pore solutions [258,264], although the cause of such an increase still remains unclear.

For the first time, we present here an easy and reliable ICP-OES method suitably developed to quantify calcium, potassium, sodium, sulfur, aluminium, iron, magnesium and silicon in cement pore solutions with high accuracy. This study provides researchers and operators working in the field of cement with some clear guidelines for characterizing their cement pore solutions. In particular, we show that this approach leads to the improvement of the level of quantification of aluminium by at least a factor 3.4 (when keeping into account the dilution factor), with respect to the best case found in the literature [265]. In more extreme cases, the improvement of the level of quantification reaches a factor 34 [253,256,262].

Finally, the use of this method is also illustrated by demonstrating the effect that polycarboxylate-based superplasticizers (SPs) have on the chemical composition of the pore solution, highlighting features that have not been previously reported. For this purpose, the method presented here has been developed on pore solutions extracted from fresh cement pastes, but the approach can directly be extended to solutions extracted at later stages.

4.2 Essential analytical chemistry background

4.2.1 ICP-OES

ICP-OES is an instrumental analytical technique that allows the quantification of elemental traces (down to 10 ng/L for some selected elements [266]) in liquid solutions. It is one of the variations of atomic emission spectroscopy with an atomization and excitation means consisting of an inductively coupled plasma torch. Considering that plasmas – typically, argon-based – operate at much higher temperatures than flames and graphite furnaces, the efficiency of the atomization/excitation process is much higher, thus providing highly populated excited states and, therefore, improved detection limits, high precision and an extended linear response range (namely, the range of signal values for which there is a linear correspondence with the analyte concentration) of the resulting signals [267,268].

Depending on the position of the observation zone (the direction where the emission radiation of the plasma is collected, collimated, filtered and detected), radial and axial views are possible in an ICP-OES instrument [269,270]. The radial case is a lateral (90°) view of the plasma plume, whereas the axial one is a top view. The axial view guarantees improved sensitivity, but also shows increased interferences, especially when complex matrices are analysed [271].

After the atomization-excitation by the plasma, the grating separates the analytes complex emission radiation into its fundamental wavelengths (spectral lines). After achieving wavelength separation, the detector allows "viewing" the spectral information [272]. The choice of the spectral lines suitable for the analysis is dictated by the sensitivity and the absence of interferences [267].

A schematic diagram of a typical ICP-OES instrument with the detection system in radial mode is shown in Figure 4.1.
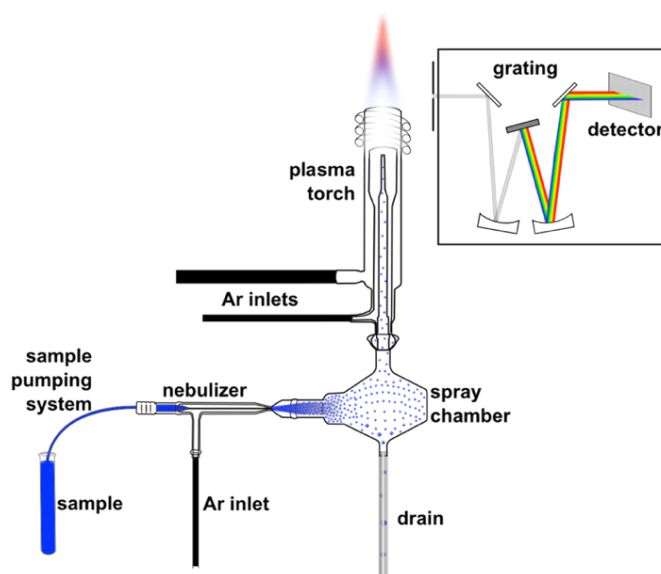
Figure 4.1: Diagram of a typical ICP-OES instrument with radial configuration of the detection system, highlighting the most important parts.

Due to the above-mentioned extended linear range of the resulting signals, a single-point calibration is usually sufficient [273]. However, when it is necessary to analyse samples containing elements at very high concentration (in the order of g/L) and others at very low concentration (in the order of μg/L) – such as cement pore

solutions –, two sample dilutions and two multi-elements calibration solutions might be needed. Furthermore, when such complex matrices are at stake, two or more spectral lines have to be used to meet the sensitivity requirements and avoid possible spectral interferences during the measurement.

The main shortcomings of the technique are the high running costs, the necessity of a constant gas source (for the plasma and the nebulization of the sample), the spectral clutter (due to the abundance of spectral features in the emission radiation generated by a high-energy excitation-atomization source, such as plasma), which can give rise to interferences, and a relatively high background noise [274]. The presence of the above-mentioned spectral clutter calls for a careful selection of the spectral lines depending on the matrix of the sample to be analysed. Aqueous phases of cementitious systems therefore require specific procedures for a reliable analysis of their composition by ICP-OES.

When designing a proper ICP-OES method, matrix effects must be kept into account. This is because the mass transport properties in the nebuliser spray chamber of an ICP instrument partly depend on the sample characteristics (viscosity, surface tension, vapour pressure, density). Standards, therefore, must be matrix-matched to exhibit similar transport characteristics [266].

This implies for example, that when analysing cement pore solutions, a first indication about their composition is needed to prepare representative calibration solutions and blanks. Blank solutions contain all the chemicals used for the analysis but the analyte [268]. This first estimate of the composition can come from experience with similar samples or data from the literature.

4.2.2 Main figures of merit of an analytical method

The *trueness* of an analytical method is defined as the agreement between the measured value of an analyte in a reference material and a reference one [236,275]. Trueness is not a quantity and cannot be expressed numerically. However, measures of closeness of agreement are possible [276]. The *precision* is a measure of the

variability between different measurements on the same analyte [275]. A measure of precision is the *standard deviation* [277]. Both trueness and precision contribute to the *accuracy* of a method, as shown in Figure 4.2.
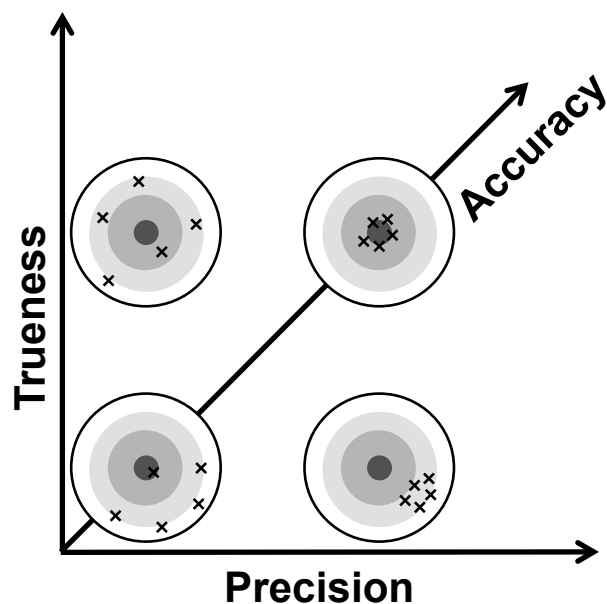
Figure 4.2: A depiction of the trueness, precision and accuracy concepts, according to the current ISO definitions [275]. The crosses represent single independent measurements. The true values are at the centre of the targets.

The *limit of detection* (LOD) is the quantity or the concentration of an analyte that can be *detected* with a given level of confidence for an analytical method [278]. An additional important quantity is the *limit of quantification* (LOQ), which is the quantity or the concentration of an analyte that can be *quantified* with a given level of confidence for an analytical method [279].

4.3 Materials and methods

4.3.1 Materials

Two 25 kg-bags of fresh CEM I 52.5R OPC were provided by Holcim (Holcim Group Services Ltd/Holcim Technology Ltd, Zurich, Switzerland) (C1) and Jura (Jura-Cement-Fabriken AG, Wildegg, Switzerland) (C2). When arrived, the content of the cement bags was transferred into two PE screw cap barrels to limit possible changes

in composition due to hydration and carbonation reactions. Table 4.1 shows the chemical and mineralogical composition of these cements.

Table 4.1: Chemical and mineralogical composition of C1 and C2 cements. The chemical composition was obtained by X-ray fluorescence, whereas the mineralogical composition was obtained by X-ray diffraction and Rietveld refinement. LOI = loss on ignition. IR = insoluble residue. SO_3 and IR contents were determined by gravimetric analysis, as reported in [280].

Chemical composition (% (w/w))	C1	C2	Mineralogical composition (% (w/w))	C1	C2
CaO	62.6	63.5	C_3S	70.6	64.7
SiO_2	19.7	20.0	C_2S	8.5	14.5
Al_2O_3	5.1	4.9	C_3A cubic	4.7	5.4
MgO	2.3	1.8	C_3A orthorhombic	1.2	0.5
MnO	0.0	0.1	C_4AF	8.7	8.5
SO_3	3.8	3.2	Gypsum	1.4	3.0
Fe_2O_3	3.1	3.3	Bassanite	1.8	0.6
Na_2O	0.1	0.2	Anhydrite	0.6	0.1
K_2O	1.1	0.7	Quartz	0.1	0.4
TiO_2	0.4	0.3	Periclase	0.5	0.3
P_2O_5	0.2	0.2	Calcite	2.0	1.8
LOI	1.8	2.0	Dolomite	0.1	0.2
IR	0.3	0.5			
Sum	100	101	Sum	100	100

Characteristic particle diameters (volume-based) of C1 and C2 cements (in isopropanol suspensions) were measured by laser diffraction with a Malvern Mastersizer 5 instrument (Malvern Instruments Ltd, Malvern, UK) and are reported in Table 4.2. The same also shows the specific surface area (SSA_{BET}) of both commercial cements determined by nitrogen adsorption with a Tristar II instrument by Micromeritics (Micromeritics GmbH, Aachen, Germany). For this purpose, the samples were degassed in an external degassing station (VacPrep 061, also by Micromeritics) at 40 °C under nitrogen flow for 16 h (see Chapter 3).

Table 4.2: Characteristic particle diameters (volume based) and SSA of C1 and C2 cements. The results of the SSA are expressed as the mean value and the standard error of the mean at the 95% confidence limit ($n_{samples}$ = 3).

Cement	D_{v10} (µm)	D_{v50} (µm)	D_{v90} (µm)	SSA (m²/g)
C1	1.63	11.28	32.02	1.04 ± 0.01
C2	1.48	9.76	30.44	1.0 ± 0.1

A non-commercial polycarboxylate ether-based comb polymer was used as SP in the present study. This was previously obtained by copolymerization and, eventually, ultrafiltered to remove possible residues. The backbone of the used SP is based on poly(methacrylic acid). The polyethylene oxide side chains molecular weight was 1000 Da. The molar mass of the SP (M_n = 22600 g/mol, M_w = 39500 g/mol) was determined by size exclusion chromatography (SEC). SEC analysis was carried out on an Agilent 1260 Infinity system (Agilent Technologies, Santa Clara, CA, USA) equipped with a refractive index detector, also by Agilent. The eluent for SEC was Na_2HPO_4 0.067 mol/L at a flow rate of 1 mL/min. The system was previously calibrated with PEO/PEG molar mass standards. The carboxylate to ester ratio (C/E = 2.7) was determined by ultra-high performance liquid chromatography. The hydrodynamic radius of the SP (9.5 ± 0.2 nm) in synthetic pore solution [77] was determined by dynamic light scattering (DLS) using a Malvern Zetasizer Nano ZS equipment.

The used ultrapure water (UPW, ρ = 18.2 MΩ·cm, TOC around 1-2 ppb) was dispensed by a Milli-Q A+ water purification system from MilliPore (Merck & Cie, Schaffhausen, Switzerland). The nitric acid (TraceSELECT, ≥69%) for the preparation of the samples was purchased from Fluka (Sigma-Aldrich Chemie GmbH, Buchs, Switzerland). 1000 mg/L aluminium, calcium, iron, magnesium, potassium, silicon, sodium, and sulfur standard solutions for ICP (TraceCERT) were also purchased from Fluka.

4.3.2 Samples preparation

Around 2 kg of OPC were sampled from the PE barrel at different heights, after that this was swirled and turned upside down several times, to ensure homogeneity.

Samples with and without SP were prepared. In the first case, two different dosages and two times of addition of the SP were studied.

In all the cases, the resulting liquid was filtered in a plastic syringe connected to one of the following disposable syringe filters (depending on the needed filtration dimensions): 0.1 μm Puradisc 25 TF by Whatman (GE Healthcare Europe GmbH, Glattbrugg, Switzerland) and 0.45 μm CHROMAFIL Xtra H-PTFE-45/35 by Macherey-Nagel (Macherey-Nagel AG, Oensingen, Switzerland).

As will be clearer in the presentation of the results and the discussion, the sample preparation involves two dilutions. After filtration, the pore solution is immediately diluted 1:10 by mass with HNO_3 2% (w/w) in UPW and a portion of this is further diluted 1:20 by mass – for a final dilution of 1:200 – with HNO_3 2% (w/w) in UPW for quantifying low- (Al, Fe, Mg, Si) and high-concentration elements (Ca, K, Na, S), respectively. The resulting diluted solutions are put in screw cap PP containers, sealed with Parafilm and stored in the fridge at 4 °C.

The ICP analyses were carried out within one week of the extraction.

4.3.2.1   Preparation of pore solutions from cement pastes without SP

Cement pastes were prepared in PP containers by mixing 200 g of cement and 60 g of UPW (w/c ratio = 0.3). The powder was put in the liquid and the resulting suspension was stirred at 200 rpm for 30 s and then at 800 rpm for 4 min with a EUROSTAR power control visc overhead stirrer equipped with a 4-bladed propeller stirrer, both by IKA (IKA-Werke GmbH & Co. KG, Staufen, Germany). Afterwards, the cement paste (around 180 g) was put in the barrel (V_{max} = 200 mL) of a stainless-steel pressure filter holder (no. 16249) previously mounted with a nylon 0.45 μm membrane filter (no. 25006), both by Sartorius (Sartorius Stedim Biotech GmbH, Göttingen, Germany). The stainless-steel pressure filter holder was then connected to a high-pressure air circuit (4 bar) to let the system filter the cement paste for 10 min. The total sample preparation time was therefore around 15 min.

4.3.2.2   Preparation of pore solutions from cement pastes with SP

Cement pastes from cements C1 and C2 were prepared as described in the previous paragraph. SP at two different dosages, 0.2 and 0.4% active by weight of cement (bwc), was added. The amount of water included in the SP was subtracted to maintain a constant w/c = 0.30. The SP was added at two different times. In the first case, the SP was added to the mixing UPW (direct addition). In the latter, the SP was added after 15 minutes of initial contact between cement and UPW (delayed addition). This is the time when the initial aluminates hydrates are formed and the reactivity of tricalcium aluminate is significantly reduced. Furthermore, this time corresponds to the end of the first peak in isothermal calorimetry tests. In all the cases, the filtration of the pore solution started after 20 min of hydration and finished after 40 minutes. Cement pastes without SP and filtered at the same times were also prepared for comparison.

4.3.3 High-speed centrifugation

Other pore solutions from C2 cement with SP 0.4% active bwc were centrifuged for 1 h at 41000 g with a 3-30KS instrument from Sigma (SciQuip Ltd, Newtown, UK) and filtered with a 0.45-μm filter for comparing both direct and delayed additions.

4.3.4 ICP-OES

A Thermo Scientific iCAP 6300 Dual View ICP-OES (Thermo Fisher Scientific Inc., Waltham, MA, USA) with a CETAC ASX-260 autosampler (CETAC, Omaha, NE, USA) was used for the analyses. Its operating conditions are reported in Table 4.3. In this paper, we took the values provided by Kauppi et al. [281] as starting composition for calibration solutions. Then with the results of the first series of analysis, the composition of the calibration solutions was adjusted to ensure that they cover the whole range of concentrations measured in this study.

Table 4.3: Operating conditions for the ICP-OES measurements with the iCAP 6300 Dual View.

Operating condition/Instrument part	Value/Type
Effective focal length	383 mm
Spectral range	166-847 nm
Detector	CID86 chip (charge injection device)
RF generator	27.12 MHz solid state
Plasma viewing	Dual
Plasma and shear gas	Argon
Nebulizer	Concentric glass
Spray chamber	Glass cyclone
Plasma torch	Enhanced matrix tolerance (EMT) semi-demountable
RF power	1150 W
Pump rate	50 rpm
Auxiliary gas flow	0.5 L/min
Nebulizing gas flow	0.5 L/min
Number of replicates per sample	3
Maximum integration time for low WL range	15 s (both axial and radial)
Maximum integration time for high WL range	10 s (axial) and 5 s (radial)
Flush time	45 s

Table 4.4: Composition of the calibration solutions used in this study. CS refers to the calibration solution used for quantifying both high- and low-concentration elements in the cement pore solutions without SPs. CS-SP-L and CS-SP-H refer – respectively – to the calibration solutions used for quantifying low- and high-concentration elements in the cement pore solutions with SP. The high concentrations of calcium, potassium, sodium and sulfur in CS and CS-SP-L solutions provide matrix-matched standards.

	CS	CS-SP-L	CS-SP-H
Solvent/blank	HNO_3 2% (w/w) in UPW	SP 0.2%/0.4% act. bwc 1:10 in HNO_3 2% (w/w) in UPW	SP 0.2%/0.4% act. bwc 1:200 in HNO_3 2% (w/w) in UPW
c_{Ca} (mg/L)	10	10	10
c_K (mg/L)	200	200	200
c_{Na} (mg/L)	20	20	20
c_S (mg/L)	100	100	100
c_{Al} (µg/L)	20	200	---
c_{Fe} (µg/L)	200	500	---
c_{Mg} (µg/L)	20	500	---
c_{Si} (µg/L)	400.4	1001	---

This procedure must be conducted every time different types of samples are used but is something that does not seem to be done in the cement literature (or at least that is not reported). It can be noted that when this procedure is properly applied, the values are obtained by interpolation (namely, inside the calibration range) and never by extrapolation [272]. The composition of the calibration solutions used in this study is reported in Table 4.4.

4.3.5 Dynamic light scattering and total organic carbon

A Malvern Zetasizer Nano ZS was used to determine the presence of nanoparticles in the filtered pore solutions. Measurements were conducted at 25 °C. The wavelength of the incident laser was 633 nm and the scattered light was detected at a constant angle of 173°. DLS measurements were carried out on solutions extracted from pastes prepared in section 4.3.2.2, with SP 0.4% active bwc (direct and delayed additions). For reference purposes, DLS measurements were also carried out on the pure SP in a synthetic pore solution (prepared as in [77]).

A Shimadzu TOC-V CSH total organic carbon (TOC) analyser (Shimadzu Schweiz GmbH, Reinach, Switzerland) was used to quantify the amount of SP in the cement pore solutions.

DLS and TOC analyses, together with ICP-OES, were carried out on filtered cement pore solutions before and after high-speed centrifugation.

4.4 Results

4.4.1 Analytical figures of merit of method

4.4.1.1   Trueness

The trueness of our method was evaluated by calculating of the closeness of agreement, taken as the mean percentage deviation of three measurements from the expected value of an independently prepared reference solution. The procedure was

carried out for both the low- and the high-concentration elements. The composition of the reference solution for the low-concentration elements was: 10 μg/L of Al, 100 μg/L of Fe, 10 μg/L of Mg, 200.2 μg/L of Si and 100 mg/L of Na, K and S and 50 mg/L of Ca – as interferences – in HNO_3 2% (w/w) in UPW. The composition of the reference solution for the high-concentration elements was: 5 mg/L of Ca, 100 mg/L of K, 10 mg/L of Na and 50 mg/L of S in HNO_3 2% (w/w) in UPW. The measures of closeness of agreement are shown in Table 4.5. Data are reported for the different spectral lines. Such data emphasize the importance of choosing an adequate line to enhance measurement accuracy. This also is something that has never been reported in the cement literature.

Table 4.5: Measures of closeness of agreement obtained with our method. The value was computed as the mean (the measurement of the reference solution was repeated three times) percentage deviation from the expected value of an independently prepared reference solution. The selected spectral lines in nm and the corresponding closeness values they provide for our samples are also shown. The selected spectral lines allow covering the range of concentrations of the samples in this work. The plasma viewing for potassium and sodium lines is radial, whereas the plasma viewing for all the other lines is axial.

Element	Selected spectral line (nm)	Closeness of agreement
Al	167.079	0.5%
	396.152	5%
Ca	315.887	1.8%
	317.993	1.7%
	318.128	0.9%
Fe	259.940	0.7%
K	766.490	2%
	769.896	2%
Mg	279.079	6%
	279.553	4%
Na	589.592	2%
S	182.034	0.3%
	182.624	2%
Si	251.611	0.5%
	288.158	0.1%

4.4.1.2   Limits of detection and quantification

The LOD and the LOQ of the low-concentration elements (Al, Fe, Mg, Si) in cement pore solutions were calculated respectively as three and ten times the standard deviation [236] of the mean element concentrations of ten independently prepared blanks [266] containing 200 mg/L of Na, K and S and 80 mg/L of Ca – as interferences – in HNO_3 2% (w/w) in UPW. The calibration solution for such determination contained: 20 µg/L of Al, 10 µg/L of Fe and Mg, 200.2 µg/L of Si and, again, 200 mg/L of Na, K and S and 80 mg/L of Ca – as interferences – in HNO_3 2% (w/w) in UPW. The method yielded the LOD and LOQ values for the different lines reported in Table 4.6.

Table 4.6: LOD and LOQ (reported in µg/L and in µmol/L) obtained with our method for the low concentration elements. The plasma viewing for all the lines is axial. n_{blanks} = 10, for all the proposed systems. Deviant values were discarded according to the ISO-recommended Grubbs' test with P = 0.05 [236].

Element	Selected spectral line (nm)	LOD		LOQ	
		(µg/L)	(µmol/L)	(µg/L)	(µmol/L)
Al	167.079	3.2	0.12	10.7	0.40
	396.152	3.7	0.14	12.2	0.45
Fe	259.940	0.6	0.011	1.9	0.034
Mg	279.079	2.6	0.11	8.6	0.35
	279.553	0.15	0.0082	0.51	0.0208
Si	251.611	8.7	0.31	29.0	1.03
	288.158	9.4	0.33	31.2	1.11

4.4.2 Composition of cement pore solutions

The composition of the pore solutions (filtered with 0.45 µm syringe filters) obtained from C1 and C2 cements, containing SP 0.2% active bwc and filtered with 0.45-µm and 0.1-µm syringe filters for high- and low-concentration elements is shown in Table 4.7.

Table 4.7: Composition of the cement pore solutions from C1 and C2 cements without SP and filtered with 0.45-μm syringe filters, with SP 0.2% active bwc filtered with 0.45-μm syringe filters and with SP 0.2% active bwc filtered with 0.1-μm syringe filters for high- (Ca, K, Na, S) and low- (Al, Fe, Mg, Si) concentration elements. The results are expressed as the mean value and the standard error of the mean at the 95% confidence limit. $n_{samples}$ = 5, for all the proposed systems. Deviant values were discarded according to the ISO-recommended Grubbs' test with P = 0.05 [236]. The concentration values are those obtained with the lines with the best trueness. For the potassium lines (same closeness of agreement), the one with the lower percentage standard deviation was chosen. The * indicates that the value in the diluted solution was below the LOQ of the method, but above the LOD.

	C1	C1+SP	C1+SP .1	C2	C2+SP	C2+SP .1
c_{Ca} (mg/L)	18.2 ± 0.9	20.8 ± 0.4	20.2 ± 0.8	19.1 ± 0.3	20.3 ± 0.2	20.4 ± 0.6
c_K (mg/L)	406 ± 4	381 ± 6	386 ± 14	443 ± 11	424 ± 5	439 ± 12
c_{Na} (mg/L)	57.8 ± 0.9	55.9 ± 0.5	55.4 ± 0.8	114 ± 3	112 ± 2	114 ± 2
c_S (mg/L)	184 ± 4	173 ± 4	173 ± 2	206 ± 4	197 ± 2	204 ± 4
c_{Al} (μg/L)	1.7*	212 ± 18	166 ± 19	< LOD	2.2*	2.2*
c_{Fe} (μg/L)	16 ± 1	151 ± 6	138 ± 10	5 ± 2	7.3 ± 0.9	9 ± 2
c_{Mg} (μg/L)	1.2 ± 0.2	481 ± 39	367 ± 43	1.2 ± 0.2	0.7 ± 0.3	0.6 ± 0.3
c_{Si} (μg/L)	70 ± 3	452 ± 50	346 ± 33	56 ± 5	66 ± 3	66 ± 1

Table 4.7 shows a small increase in calcium concentration upon the direct addition of SP to both cements. Interestingly, the ratio between the concentration values of the high-concentration elements in the pore solutions from cement pastes with the direct addition of SP and the concentration values of the same elements from cement pastes without SP is the same for both cements. Table 4.7 also shows a dramatic increase of the concentration values of the low-concentration elements upon the direct addition of SP to the C1 cement, when they are compared with the values from the cement paste without SP. Such an increase is not visible when we look at the results for the C2 cement with SP 0.2% active bwc. A subsequent filtration of the pore solutions with a 0.1-μm syringe filter (after a first one with a 0.45-μm syringe filter) does not cause significant differences in the concentration of the high-concentration elements. On the contrary, the use of the smaller filter pore size leads to a systematic decrease of the low-concentration elements only for the C1 cement. However, aluminium concentration remains substantially higher than in the non-admixed C1 cement paste.

4.4.3 Effect of dosage and time of addition of SP on pore solution composition

As shown in Figure 4.3, the addition of SP 0.2% active bwc to C2 cement pastes – in both direct and delayed modes – does not affect the composition of the pore solution with respect to the non-admixed samples. However, the addition of SP 0.4% active bwc dramatically increases the concentration of the low-concentration elements, showing a significant effect after the direct addition of SP. As before, a small increase in calcium concentration can also be observed with these polymer dosages.

Figure 4.4 shows the presence of nanoparticles in the filtered solutions from C2 pastes containing SP 0.4% active bwc. Their concentration is remarkably higher when SP is added directly with the mixing UPW, as evidenced by the higher intensity of the scattered light.

In the case of direct addition of SP (Figure 4.4a), nanoparticles with a size of around 190 nm were detected. High-speed centrifugation dramatically reduces the amount of these particles and nanoparticles of around 9 nm are then also observed. In the case of delayed addition of SP, the pore solutions contain particles of around 9 and 140 nm (Figure 4.4b). However, after centrifugation, only the smaller nanoparticles, corresponding to the free polymer, could be identified. The broad peak at 120 nm in the pattern of the synthetic pore solution is caused by possible external interferences during the DLS measurement. However, this does not contribute significantly on the intensity of the scattered light.

The chemical composition of the pore solutions shows that the concentrations of calcium, potassium, sodium and sulfur remain the same even after centrifugation in both direct and delayed addition mode (Figure 4.5a). In contrast, high-speed centrifugation decreases the concentration of the low-concentration elements by a factor between 1.5 and 10, as shown in Figure 4.5b. This decrease is more pronounced in the case of direct addition.

When SP is directly added to the cement paste, the removal of these nanoparticles after centrifugation does not show a statistically significant decrease of the amount of organic carbon in solution (Figure 4.6). In addition, the organic carbon content in

the pore solution is not affected by centrifugation when the SP is added in delayed mode.
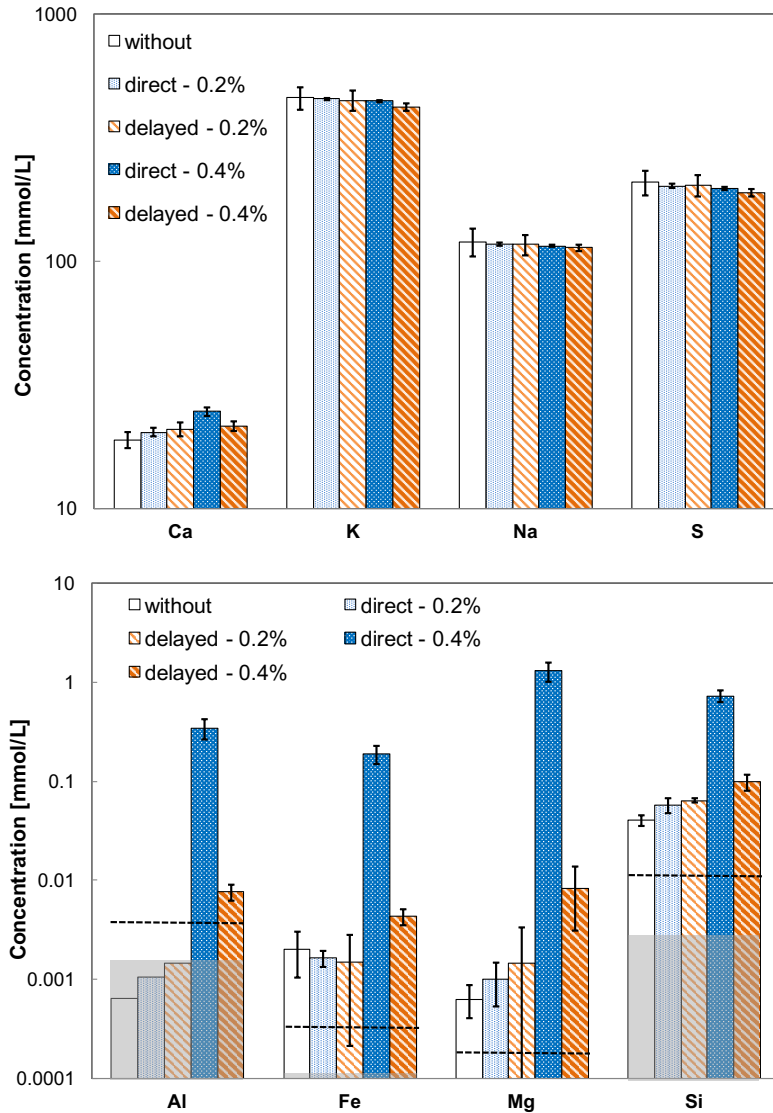
Figure 4.3: Composition of pore solutions from C2 cement with SP at different concentrations (0.2% active bwc and 0.4% active bwc) and at different addition times for the high- (Ca, K, Na, S) and low-concentration (Al, Fe, Mg, Si) elements. The results are shown as the mean values and the standard errors of the mean at the 95% confidence limit. The grey-shaded bands in the figure on the right indicate 10×LODs for the different elements, whereas the dashed segments indicate 10×LOQs for the different elements. The standard errors are shown when the values were above 10×LOQs. The 10× results from the dilution of the sample solutions for the quantification of the low-concentration elements (aluminium, iron, magnesium, silicon). The grey-shaded band for the 10×LOD of magnesium is not visible with the used scale. $n_{samples}$ = 4, for the samples without SP; $n_{samples}$ = 5, for the samples treated with SP 0.2% active bwc and 0.4% active bwc and direct addition; $n_{samples}$ = 3, for the samples treated with SP 0.2% active bwc and delayed addition; $n_{samples}$ = 6, for the samples treated with SP 0.4% active bwc and delayed addition.
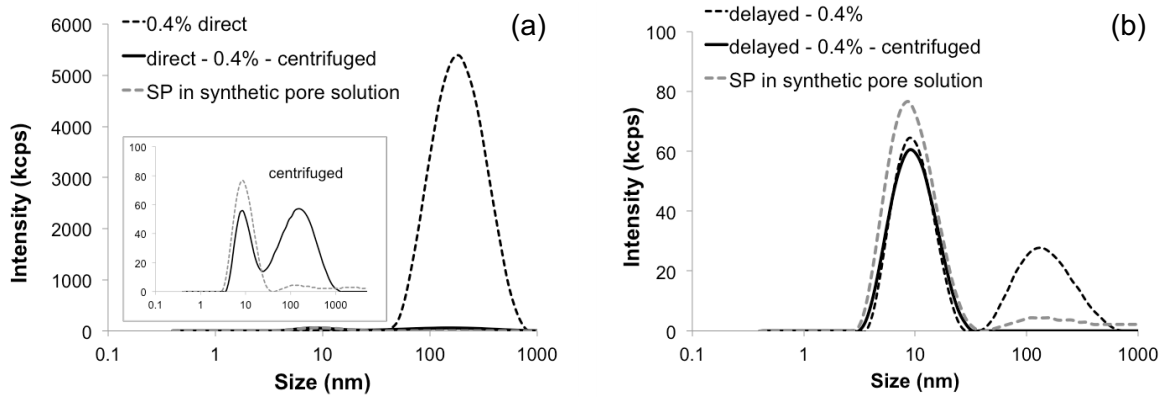
Figure 4.4: Intensity size distribution of pore solutions from C2 cement containing SP 0.4% active bwc, before and after 1 h high-speed centrifugation, at different addition times: (a) direct addition and (b) delayed addition.
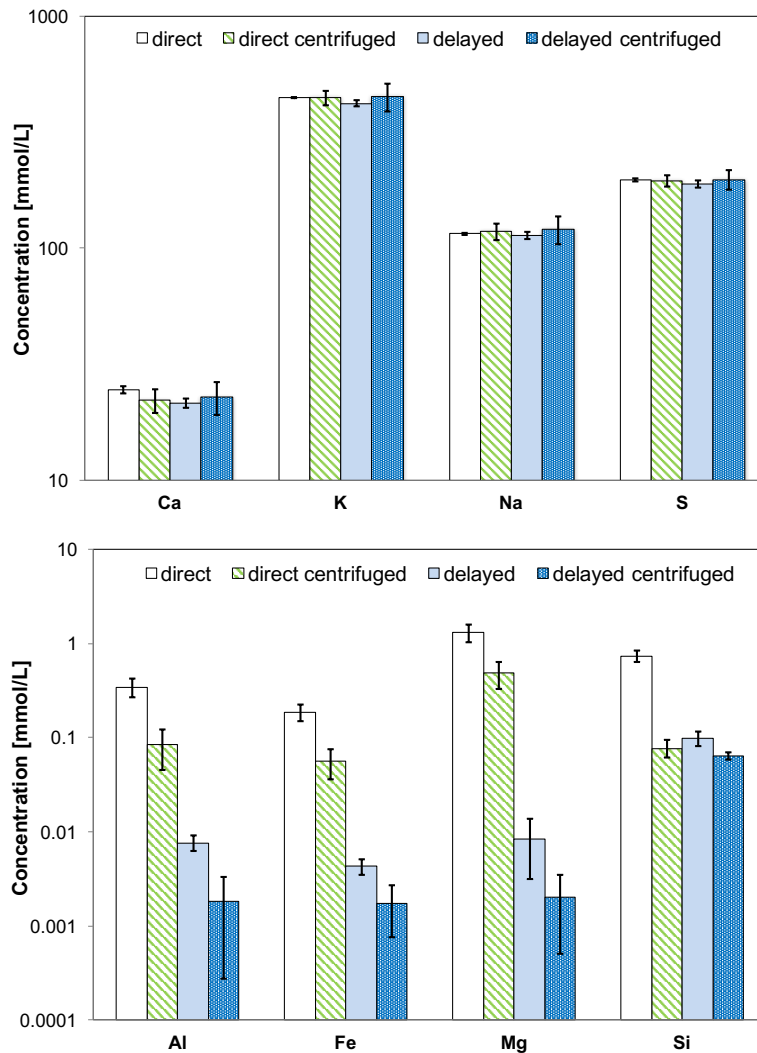
Figure 4.5: Composition of pore solutions from C2 cement containing SP 0.4% active bwc, at different addition times, before and after 1-hour high-speed centrifugation for high- (Ca, K, Na, S) and low-concentration (Al, Fe, Mg, Si) elements. The results are shown as the mean values and the standard errors of the mean at the 95% confidence limit. $n_{samples}$ = 4. Deviant values were discarded according to the ISO-recommended Grubbs' test with P = 0.05 [236].
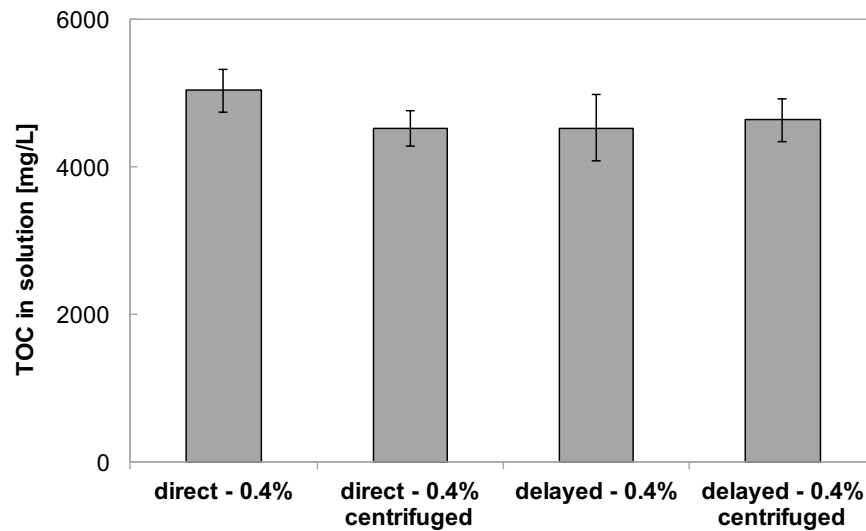
Figure 4.6: Total organic carbon in solution from C2 pastes containing SP 0.4% active bwc, direct and delayed addition modes, before and after high-speed centrifugation. The results are shown as the mean values and the standard errors of the mean at the 95% confidence limit. $n_{samples}$ = 4, for the samples with direct addition of SP; $n_{samples}$ = 5, for the samples with delayed addition of SP; $n_{samples}$ = 4, for the samples with delayed addition of SP and centrifuged.

4.5 Discussion

4.5.1 Relevance of the method

The presented method shows a good trueness. From Table 4.5, we can in particular highlight the importance of the proper choice of a spectral line. Overall, the measures of closeness reported for our method in Table 4.5 are much better (lower) than the 25% for an ICP-OES method that would feature a calibration not specifically designed for the matrix of interest [273].

Our LOD values for silicon and aluminium in cement pore solutions are 12 and 34 times lower, respectively, when compared with the ones reported by the most recent reference that to the best of our knowledge explicitly provides such values (0.004 mmol/L for both elements) for pore solutions (Table 4.6) [256]. The same values are 12 and 31 times lower, when compared with the ones obtained by ion chromatography in another study [262]. Our LOD value for magnesium in cement pore solutions is 162 times lower when compared to the most recent one (0.001 mmol/L, corresponding to slightly less than 25 μg/L) available in literature [265].

When compared with the estimated LOD values for aluminium, iron and magnesium, reported by the ASTM standard test method for the analysis of elements of water by ICP-OES [282], our values are 14, 12 and 200 times lower, respectively, despite using a much more complicated matrix.

However, all the authors of the above-mentioned studies fail to describe the procedure, the dilution and the blanks employed to determine the LOD values. Our approach keeps into account the interferences possibly arising from the high concentration values of calcium, potassium, sodium and sulfur. It should be noted that if the determination of the LOD values is carried out in simpler matrices (but not relevant for cement), much lower values are expected [266]. In addition, the lines we suggest here were chosen to avoid spectral and matrix interferences noticed with other lines, to ensure linearity in the range of the measured concentrations and to have the best possible trueness. As a result, the presented method offers very much enhanced reliability and sensitivity in solution analysis of cement pore solutions by ICP-OES.

4.5.2 Impact of SP on pore solution composition

In the particular case of aluminium, concentrations obtained for both cements and in absence of polymer are below the LOQ, while this is not the case for the other low-concentration elements (Figure 4.3 and Table 4.7). The addition of a polycarboxylate-based SP dramatically increases the amount of all low-concentration elements, going up in some situations by a factor of 500 and 2000 for aluminium and magnesium, respectively (Figure 4.3 bottom). The magnitude of this increase depends on the type of cement, dosage and mode of addition of the polymer. A more accurate accounting of the role of these factors is however beyond the scope of this paper.

The observed increase of the low-concentration elements when SP is added in direct mode could be partially explained by the presence of nanoparticles (around 190 nm, Figure 4.4a), in the pore solution and going through the 0.45-μm filter used. Indeed, when using a 0.1-μm filter, a partial reduction of the low-concentration elements is

observed for cement C1 (Table 4.7). This probably indicates that the amount of these nanoparticles is also reduced, confirming experimental observations reported in other studies [9,176]. However, a more radical reduction of the amount of these nanoparticles was obtained after high-speed centrifugation. For direct addition of SP, this reduced the amount of nanoparticles (Figure 4.4a) and decreased the concentration of the low-concentration elements (Al, Fe, Mg, Si) by a factor between 1.5 and 10 (Figure 4.5 bottom). The delayed addition of the SP always produces substantially fewer nanoparticles (Figure 4.4b) and correspondingly much lower values of the low-concentration elements (Figure 4.5 bottom).

We discard a priori the option of ultrafine and very reactive particles from the anhydrous cement, not reacting upon direct addition of SPs. The dissolution of such particles (mainly composed of silicates) before the ICP analysis (treatment with nitric acid) would, in fact, not explain the dramatic increase of magnesium, aluminium and iron, which are minority elements in anhydrous cement. In this section, we examine three hypotheses concerning the nature of these nanoparticles:

1. They are nano-ettringite, nano-AFm and/or nano-C-S-H particles, whose growth is inhibited by adsorbed SPs that additionally keep them dispersed [9,176,283]. These stabilized nanoparticles would not agglomerate or precipitate onto clinker particles, remaining in the pore solution and passing through even very fine filters [9];

2. They are comb copolymers that form intramolecular complexes with aluminium, iron and/or magnesium, similarly to what is reported in literature for PEO with other cations [170–172];

3. In agreement with recent developments in the alternative theory of crystallization [284–286], they could result from a miscibility gap causing a liquid-liquid separation. The nanoparticles observed would be droplets in an immiscible liquid rich in complexes of polymers and polyvalent cations [287].

On the basis of the present results, it is not trivial to discriminate between the above-mentioned hypotheses. The major changes in the system occur in the case of

direct addition of the SP, indicating a perturbation of the initial dissolution of the anhydrous clinker phases, mainly tricalcium aluminate, and/or nucleation of initial hydrates. When the SP is directly added with the UPW, the decrease of the amount of aluminium after centrifugation could be attributed to the removal of nano-ettringite and/or nano-AFm particles stabilized by the adsorbed SP. Based on the particle size measured by DLS, the calculation of the specific surface of this ettringite leads to a value of 18.6 m^2/g. Using the adsorption conformation model proposed by Flatt et al. [65], we can estimate that the plateau adsorption for our polymer is about 8 mg/g of ettringite. Therefore, since centrifugation reduced aluminium by about 0.26 mmol/L (corresponding to 162 mg of ettringite/L), we estimate that the PCE concentration would change by about 1.3 mg/L if the particles are indeed ettringite. This amount is unfortunately below the one that can be resolved from our TOC measurements.

At the same time, we cannot exclude the possibility that either polymeric aggregates or a liquid-liquid separation is at stake. In both cases, the formation of aluminium-, iron- and magnesium-polymer complexes would be involved, which is compatible with the observed increase of the concentration of these elements in solution. DLS measurements of the pore solution obtained from samples after the direct addition of SP confirmed that the free polymer (9 nm) is only observable after centrifugation. Additionally, the nanoparticle peak is substantially reduced (Figure 4.4a) by the centrifugation, but the TOC value is not changed (Figure 4.6). This suggests that the polymer might initially be contained in aggregates or droplets that are decomposed during the centrifugation, releasing free polymer in solution. However, more careful TOC experiments will be needed to support (or exclude) the first of the three proposed hypotheses in the case of direct addition.

The delayed addition of SP reduces the effect of the polymer on the concentration of aluminium in the pore solution (Figure 4.3 bottom), as the hydration of tricalcium aluminate has substantially slowed down before the addition of the polymer. In this case, the free polymer has been identified in the DLS curves together with a lower number of particles around 140 nm than in the case of direct addition. As for the particles of similar size identified in direct addition, these particles disappear upon

centrifugation, indicating that they decompose under the same forces and are probably of similar nature.

While it is clear that the formation of solid nanoparticles (namely, nano-hydrates of the aluminates) and/or aqueous intramolecular complexes can potentially have major implications in the early stages of hydration of admixed cementitious systems, defining the exact nature and impact still requires additional research.

4.6 Conclusions

Although ICP-OES is broadly used in the cement community for characterizing pore solutions, its potential seems to have been largely underused. Indeed, levels of detection and quantification reported in the literature are substantially worse than those reported in this study. The reason seems to lie in a sub-optimal (whenever) accounting of matrix effects that has almost never been reported in the corresponding literature. With the proposed method, it is possible to characterize such a complex matrix, containing elements at very high concentration and other ones at very low concentration, pushing the limits for detecting aluminium. This is of great importance in the hydration of chemically admixed systems or in the ones containing aluminosilicate SCMs.

In terms of changes in solution composition in the presence of polycarboxylate-based SPs, we showed that very substantial increases of aluminium, iron and magnesium take place. However, these occur in case of direct addition, indicating that changes arise from perturbing the initial dissolution of tricalcium aluminate and/or nucleation of ettringite.

It is suspected that nano-hydrates of the aluminates and/or a phase composed of polymer aggregates (possibly, intramolecular complexes between polymers and multivalent cations) form. The exact nature of this phase must still be elucidated, but its formation opens new keys to interpreting the impact of organic admixtures on the initial hydration kinetics of cement.

Chapter 5

Impact of PCEs on flow loss

The content of this chapter is presently not included in any publication or draft publication. However, in combination with the content of Chapter 6, these will be the main topic of a peer-reviewed ISI journal paper.

5.1 Introduction

It is widely known that the loss of fluidity might be affected by a number of factors, such as cement hydration, mixing procedure as well as type, dosage and addition mode of superplasticizers [8,12,13,158–160,288]. The fact that all of these parameters can act simultaneously makes it very challenging to account for flow loss in quantitative terms. This is why – over the past two decades – fluidity loss in superplasticized systems has been mainly explained in qualitative terms and only on a comparative basis [11–13,288]. As a consequence, the mechanism responsible for the flow loss in superplasticized cementitious systems and the role of the polymer molecular structure remain unexplained in the literature.

This chapter presents results that fill that missing gap. In particular, we establish a relationship occurring between flow loss and hydration kinetics. More importantly, we show that all the data can be rationalized with a master curve that allows predicting the effect of the molecular structure and dosage of PCEs on flow loss.

5.2 Materials and methods

5.2.1 Materials

Five 25-kg bags of fresh commercial CEM I 52.5R OPC (Holcim Group Services Ltd./Holcim Technology Ltd., Zurich, Switzerland) were used in the present work. The content of the cement bags was mixed and transferred into three PE screw cap barrels to limit possible changes in composition due to hydration and carbonation reactions.

Table 5.1 shows the mineralogical composition of the used cement, as determined by Rietveld analysis of the X-ray diffraction (Bruker AXS D8 ADVANCE with metal target of Cobalt anode) patterns and expressed in values normalized to 100% of crystalline phases.

Table 5.1: Mineralogical composition of the used cement. The mineralogical composition was obtained by X-ray diffraction and Rietveld refinement.

Minerals	Cement % (w/w)
C_3S	72.1
C_2S	4.8
C_3A	5.2
C_4AF	10.9
Calcite	0.1
Periclase	0.8
Gypsum	3.2
Hemihydrate	2.3
Anhydrite	0.6

One sample was taken from each of the three barrels used. Table 5.2 reports the mean value and the corresponding standard deviation of the characteristic particle diameter (volume based) of this cement, measured (in isopropanol suspensions) by laser diffraction with a Malvern Mastersizer 5 instrument (Malvern Instruments Ltd., Malvern, UK). The same table also shows its specific surface area (SSA_{BET}) determined by nitrogen adsorption with a Tristar II instrument by Micromeritics (Micromeritics GmbH, Aachen, Germany). Anhydrous samples were degassed in an external degassing station (VacPrep 061, also by Micromeritics) at 40 °C under nitrogen flow for 16 h as reported in Chapter 3.

Table 5.2: Characteristic particle diameters (volume based) and SSA_{BET} of Cement I 52.5R Normo 5R. The results of the SSA are expressed as the mean value and the standard deviation of the mean ($n_{samples}$ = 3).

Cement	D_{v10} (µm)	D_{v50} (µm)	D_{v90} (µm)	SSA_{BET} (m²/g)
Normo 5R	2.6 ± 0.1	18.1 ± 0.6	46 ± 1	1.04 ± 0.01

Five non-commercial polycarboxylate ether-based comb polymer were used as superplasticizers (SPs) in the present study. The structural parameters are described in Table 5.3. They were synthesized by copolymerization and ultrafiltered afterwards (Labscale TFF System, Merck Millipore) to remove residual monomers, side chains and salts. More details about the synthesis pathway and the quantification of charges are presented in section II.1.

Table 5.3: Characteristic molecular parameters of the used comb-shaped copolymers. n is the number of units or the number of side chains for a single molecule. C/E is the number of monomers in the backbone for a single side chain that contains *P* monomers of ethylene oxide (*P* simply representing the length of one side chain). S_{PCE} is the surface occupied by a single adsorbed molecule calculated with Equation (2.7). *K* is the adsorption equilibrium constant (Equation (2.4)). #COO⁻ is the content of carboxylate groups in mmol per g of dry polymer. The asterisk indicates the Mw determined by SEC calibrated with PEO/PEG molar mass standards.

PCE type	Mw [kDa]	C/E ratio	P	n	S_{PCE} [nm²/molecule]	K×10⁵	#COO- [mmol/g PCE]
2.5PMA1000	31.9	2.70	23	24	123	52	2.111
4.0PMA1000	25.4	4.13	23	18	101	126	2.87
2.5PMA2000	64.0	2.75	46	28	262	13	1.18
4.0PMA2000	45.7	4.36	46	19	198	39	1.77
2.5PMA5000	106.0*	1.89	115	20	399	2	0.36

The molar masses of these polymers were determined by Size Exclusion Chromatography (SEC) with an Agilent 1260 Infinity system (Agilent Technologies, Santa Clara, CA, USA) equipped with a refractive index detector and a multi-angle laser light scattering detector (MALLS). The molar mass determination was generally done by using by SEC-MALLS. However, for the polymer 2.5PMA5000, the molar mass determination was done by using a calibration based on PEO/PEG standards since about 11% of residual chains still remained in solution even after the ultrafiltration. Under these conditions, the absolute method cannot be adopted for the quantification of the molar mass, as the uncertainty on the initial concentration would be too high. In Table 5.3, the Mw of the polymer 2.5PMA5000 is differentiated from the ones of the other polymers with an asterisk. The carboxylate-to-ester ratio (C/E) indicates the grafting density of the side chains and was calculated knowing the number of charges quantified by titration (section II.1). The used ultrapure water (UPW, ρ = 18.2 MΩ·cm, TOC around 1–2 ppb) was dispensed by a Milli-Q A+ water purification system from MilliPore (Merck & Cie, Schaffhausen, Switzerland).

5.2.2 Methods

5.2.2.1   Cement paste preparation

2 kg of OPC were sampled from different heights of PE barrel to prepare a cement paste with UPW with a constant water to cement ratio (w/c) of 0.3 using a Hobart mixer (N50 5-Quart Mixer). PCEs were dosed directly with the mixing water (direct addition). The mixing procedure was started after pouring the cement in the solution. This consists of 30 seconds at low mixing speed (139 rpm), 30 seconds at high speed 2 (285 rpm), 30 seconds of stop were necessary to scrape the paste off from the bowl surface, then, 4 minutes at speed 2 for the final mixing.

Just after the mixing, the cement paste was poured in 10 plastic beakers containing each 250 g of paste, then covered with Parafilm to avoid water evaporation and uptake of carbon dioxide over time. At the chosen time of rest, each small batch of paste was mixed for 3 minutes at 800 rpm with a vertical mixer (Eurostar power control visc with a 4-bladed propeller stirrer, IKA) to study the evolution of the cement paste properties, namely fluidity, pore solution compositions, and specific surface area over time.

In absence of PCEs, the procedure for the preparation of the cement pastes involved the delayed addition of UPW to reach a sufficiently large initial spread diameter to reliably evaluate the evolution of the yield stress and the specific surface area. The initial procedure as well as the partition of the paste are the same as presented in the above paragraph. It is known that a change of the initial w/c ratio can strongly affect the dissolution/precipitation processes. Therefore, additional water was added 10 minutes after the first contact with water and mixed with the original paste at 800 rpm for 2 minutes to range final w/c ratios between 0.494 and 0.55. Calorimetric tests were started just after the end of the mixing. Using this procedure, we could demonstrate that a delayed addition of water, keeping the same w/c ratio at the beginning of the hydration and consequently the same supersaturation of the pore solution, does not affect significantly the dissolution process in the first hours of hydration (as shown by the similar initial part of the calorimetric curves in Figure

5.1b), whereas the main differences are noticed in the intensity of the silicate peak at later times (Figure 5.1a).
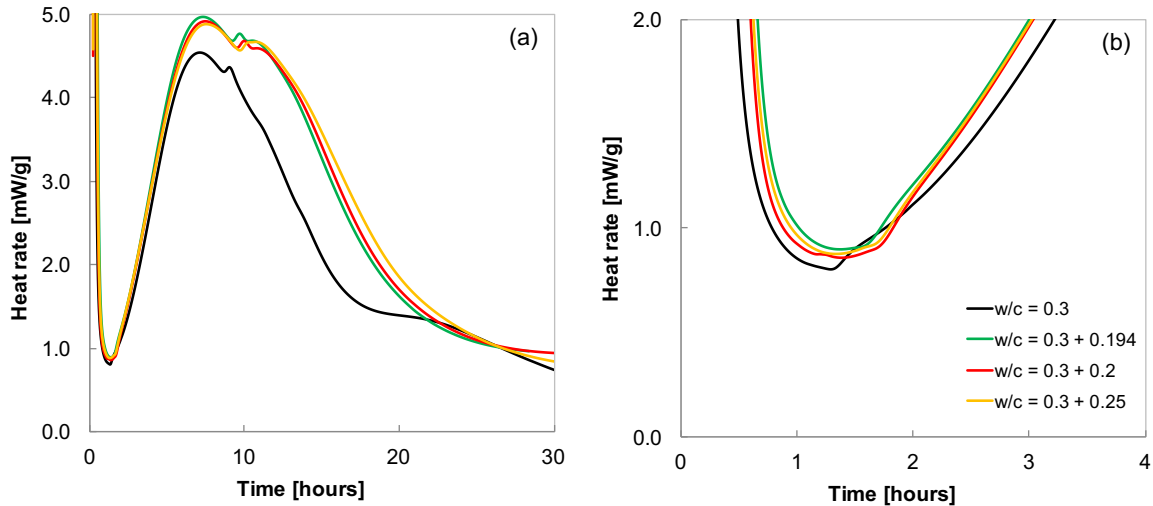
Figure 5.1: Calorimetric tests shown as heat rate over time for cement pastes without PCE at different delayed additions of water. (b) shows an expansion of (a) of the first 4 hours. This shows better the induction and the take-off of the acceleration period.

5.2.2.2   Yield stress from spread flow measurements

After a predetermined resting time, each cement paste sample is remixed for 3 minutes at 800 rpm with a vertical mixer (Eurostar power control visc with a 4-bladed propeller stirrer, IKA) before the spread flow test. This breaks down the bonds formed by thixotropic build-up while the cement was left at rest and puts samples in a comparable shear history state before being measured.

The flow spread test is performed by using a plastic cylindrical mould, having both diameter and height of 5 cm. It is placed on a flat horizontal glass plate with a smooth and wet surface and is filled with the cement paste one minute after mixing. The cylinder is slowly lifted one minute later to let the paste flow. Two perpendicular diameters of the spread at the base of the sample are then measured. The glass plate and the cylinder with the remaining paste are weighed to calculate the density of the cement paste.

The shape of cementitious materials at stoppage is well accepted to be related to the yield stress [115,116,289,290].

Over the past years, a greater attention has been taken to quantitatively obtain reliable relations between yield stress values and either spread flow or slump tests. Roussel and Coussot demonstrated that high yield stresses lead to deformation involving extensional flow (Equation (5.1)) [132]. For very low spreads, they express yield stress by the following equation:

$$\tau_0 = \frac{\rho V g}{\sqrt{3}\ \pi R^2} \qquad\qquad (5.1)$$

where ρ and V are the density and the volume of the sample, respectively, R is the radius of the spread and g the standard gravity.

As expressed elsewhere [154], the spread flow depends on the sample volume and the mould geometry in addition to the yield stress, which is a material property.

Roussel et al. [291] demonstrated that samples with low yield stress are subject to pure shear flow at very large diameters. The proposed model relates the characteristics of the cement paste, namely either height or radius, to the variation of the pressure in the sample. The yield stress is then calculated as:

$$\tau_0 = \frac{225}{128\pi^2} g V^2 R^{-5} - \lambda \frac{R^2}{V} \qquad\qquad (5.2)$$

where surface tension effect is taken into account by the last term for which the coefficient λ of 0.005 is proposed as a reasonable value for most cases.

Flatt et al. [154] proposed to combine both expressions above, Equations (5.1) and (5.2), using an exponential function of the spread diameter:

$$\tau_0 = \exp(b - a \cdot D) \qquad\qquad (5.3)$$

where D is the spread diameter (cm), a and b are fitting parameters corresponding to 0.3506 and 8.1505, respectively.

In the context of this thesis, the fitting parameters a and b were slightly changed to 0.3480 and 7.9473, respectively, considering that the averaged density of the

produced cement pastes is 2.00 g/m³ and used cylinder. In the following plots, the updated version of this model is referred to as "Flatt et al. (2006) – adapted".

Some years later, Equations (5.1) and (5.2) were merged in a different way, using an analytical solution that covers the limits of both high and low deformations [93]. An advantage over the previous interpolation is that the volume and the sample density dependence are explicitly included:

$$\tau_0 = \frac{225\rho g V^2}{\left[128\pi^2 R^5 \left(1 + \frac{225}{128\pi} \cdot \sqrt{3}VR^{-3}\right)\right]} - \lambda \frac{R^2}{V}$$

(5.4)

More recently, Pierre et al. [118] intended to rationalize the previous equations and to develop an *ex novo* model valid for intermediate flow regimes. Their objective is to account for the shape of the sample at the stoppage. Because of this, they consider that the upper part of the sample keeps the shape of the original mould, while the spreading sample around the central part is considered almost unsheared.

Equation (5.5) enables the reliable quantification of the yield stress regardless of the flow regime, sample volume or mould shape. However, the calculation of the yield stress is quite elaborate and is only presented for cylindrical moulds. This leads to the following solution:

$$\tau_0 = \left(\frac{-b - \sqrt{b^2 - 4ac}}{2a}\right)^2$$

(5.5)

$$\boldsymbol{a} = \frac{\pi R_0^2 \sqrt{3}}{\rho g}, \boldsymbol{b} = \left[\frac{8\pi}{15}(R\text{-}R_0)^{\frac{5}{2}} + \frac{4\pi}{3}R_0(R\text{-}R_0)^{\frac{3}{2}} + \pi R_0^2(R\text{-}R_0)^{\frac{1}{2}}\right]\sqrt{\frac{2}{\rho g}} \text{ and } \boldsymbol{c} = \text{-}V$$

where V is the volume of the sample, R and R_0 are the radius of the spread and the radius of the cylinder, respectively.

In two independent works, it was demonstrated that the surface tension effect cannot be neglected for high spread values corresponding to about 1-2 Pa [154,291]. The model proposed by Pierre et al. [118] does not include the contribution of the surface tension effect. However, it can be easily included in the same way as Roussel

et al. did. We have done this and refer to the resulting equation as "Pierre et al. (2013) – adapted" using:

$$\tau_0 = \left(\frac{-b - \sqrt{b^2 - 4ac}}{2a}\right)^2 - \lambda \frac{R^2}{V} \qquad \textbf{(5.6)}$$

This upgraded version of the equation proposed by Pierre et al. is considered as the benchmark model because it holds throughout the range of spread values and does not involve any fitting parameters.

A closer look at the relative value of the different models with respect to the benchmark is given in Figure 5.2.
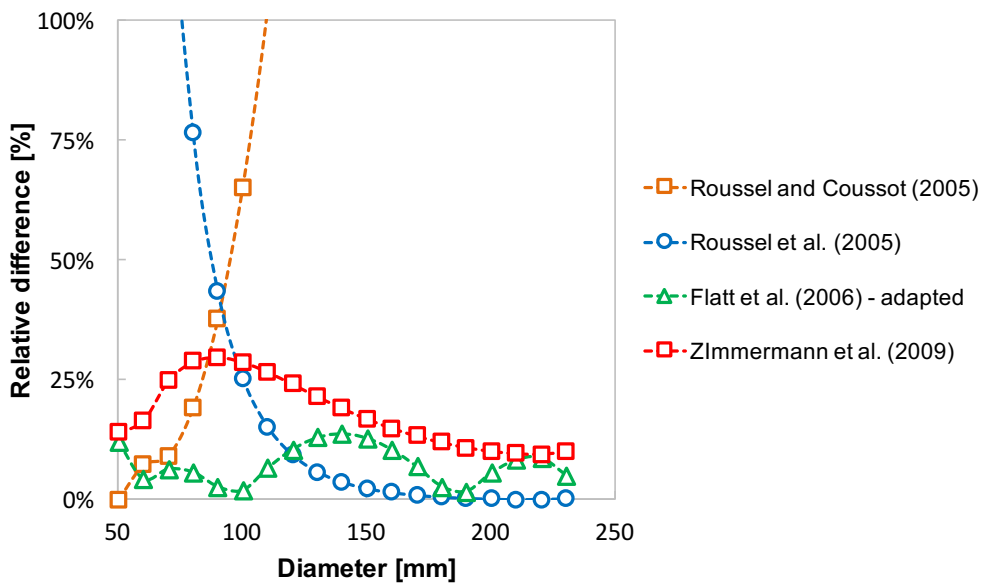
Figure 5.2: Comparison between different models for the calculation of the yield stress and the adapted model proposed by Pierre et al. [118], expressed as absolute relative error in percentage, by varying the spread diameter. The sample density is 2.00 g/cm³ and the cylinder has a volume of 98 cm³.

This shows major deviations for those models that can be reliably applied only for either very low or very high diameters, respectively. The empirical equation proposed by Zimmermann et al. [93] suffers at the intermediate range of spread values, reaching a relative difference higher than 25%. However, the simple interpolation using an exponential function (Flatt at al. (2006) – adapted) offers a very good match to the benchmark over the whole range of spreads. For this reason and because of the simplicity of its mathematical expression, we have used this relation to analyse flow spread tests through this thesis. We note, however, that

yield stress predictions at very low spreads are inherently questionable. Therefore, while data is reported, flow values lower than 6.5 cm are not used in quantitative analysis of flow loss.

5.2.2.3   Isothermal calorimetry

Calorimetric measurements were performed on about 5 g of the final paste in an isothermal calorimeter TAM Air (Waters GmbH, UB TA Instruments, Eschborn, Germany) at 23 °C. The calorimetric test is started just after the mixing and performing the spread flow at 10 minutes. The exact starting time of the measurement was taken into account to guarantee the right calculation of both heat rate, expressed in mW/g_{cement}, and cumulative heat, expressed in J/g_{cement}, at the time corresponding to the spread flow tests.

Owing to both instrumental and operative limitations, calorimetric data can only be considered reliable 30-40 minutes after the start of the experiment. This time is indeed necessary to let the sample reach the set temperature. By doing this, information relating to the aluminate dissolution (that makes its most significant contribution to cumulated heat released in the first minutes of hydration) is partially omitted.

5.2.2.4   Adsorption tests by TOC measurements

The content of organic carbon in pore solution from admixed pastes is typically quantified by the TOC (Total Organic Carbon) analyser (TOC-V CSH Shimadzu Schweiz GmbH, Reinach, Switzerland). Pore solutions were filtered from about 50 g of cement paste poured in the barrel (V_{max} = 200 mL) of a stainless-steel pressure filter holder previously mounted with a nylon 0.45 μm membrane filter (Sartorius Stedim Biotech) connected to a high-pressure air circuit (4 bar) for 10 minutes. The pore solution was, then, filtered in a plastic syringe through a disposable syringe 0.45 μm filter (CHROMAFIL Xtra H-PTFE-45/35, Macherey-Nagel).

The instrument was calibrated by suitably diluting a 1000 mg/L TOC standard (by Sigma-Aldrich, produced according to ISO/CEN EN1484) in UPW to have a calibration curve ranging 0-100 ppm and 0-250 ppm. Freshly spilled UPW was the

blank used for the analyses. The reference material had a concentration of 50 ppm of TOC, also prepared by diluting the above-mentioned TOC standard solution.

The percentage deviation (a measurement of the trueness of the method) referring to the measured and the expected concentrations of the above-mentioned reference material (four samples from the same reference solution were spilled) is 1.7%. The obtained Limit of Detection (LOD) and Limit of Quantification (LOQ) (n_{blanks} = 3) are 0.10 mg/L, and 0.35 mg/L, respectively.

For TOC measurements, a part of the filtered solution was diluted at least 20 times with a 0.05 M HCl (Sigma-Aldrich, TraceSELECT, fuming, ≥ 37%) in UPW to fit in the above-mentioned calibration range of the TOC analyser. The acidification causes the dissolution of hydrates that may have passed through the 0.45 µm filters, while the dilution decreases the salt concentration. This protocol is beneficial for a longer service life of the catalyst of the TOC analyser.

The so-called "depletion method" was used to quantify the amount of adsorbed PCE. The TOC content of the reference paste without polymer was measured and subtracted from the analysis of the samples with polymer. This is a way of correcting for possible organic compounds in the cement paste, such as grinding aids.

5.2.2.5   Stopping cement hydration

Solvent exchange was adopted to efficiently stop cement hydration by the removal of the capillary water. In this work, hydration had to be stopped on numerous samples for their characterization over the first few hours of hydration. The protocol proposed in Chapter 3, involving the mixing of cold isopropanol at 5 °C with the cement paste at the ratio cement paste/solvent ratio of 10 and the proposed double-step filtration, was optimized for this purpose.

5.2.2.6   SSA$_{BET}$ measurements

The BET surface area measurements (SSA$_{BET}$) were carried out on the previously dried samples using a BET multi-point nitrogen physisorption apparatus (Micromeritics Tristar II 3020). The nitrogen adsorption was measured from an 11-

points isotherm at a relative pressure *P/P₀* range of 0.05 to 0.30 at 77 K. The SSA determinations were repeated three times for each sample. The samples were degassed in an external degassing station (VacPrep 061 from Micromeritics) at 40 °C under N_2 flow (with a maximum flux of about 3×10^{-3} m³/h) for 16 hours as reported in Chapter 3.

5.2.2.7   Shifting factor (dosage dependence of yield stress)

One of the problems when studying the effect of superplasticizers on the yield stress of cement pastes is that high dosages will lead to segregation, while low dosages will lead to pastes whose yield stress cannot be easily measured. A resulting problem is that it is difficult to characterize the effect of volume fraction, because for a given superplasticizer dosage, the volume fraction can only be changed within a small range without running into one of the two problems above. Some relations have been proposed in section 2.4.3.1, but they lack abroad experimental validations for cement suspensions.

In this section, we propose an approach based on the assumption that yield stress is proportional to the product between a function of the volume fraction and another function of the degree of dispersion, the latter depending on superplasticizer type and dosage. This is expressed by Equation (5.7):

$$\tau_{0,t} \propto f(\phi) \cdot g(PCE, c) \tag{5.7}$$

Considering Equation (5.7), we decided to measure the yield stress of cement pastes at different dosages, using the possible range of volume fraction allowed by each of those dosages. This means – for example – that for a high dosage, the volume fractions tested would be high, whereas, for a low dosage, the volume fraction would be low. Based on Equation (5.3), it should then be possible to multiply each data series by a factor to build a master curve of yield stress versus volume fraction. Such a plot would then provide with the expression of the volume fraction dependence, as explained in section 5.3.6.

In addition, the shifting factors needed for pastes prepared without superplasticizer are expected to give the ratio of interparticle forces of the dispersed pastes with respect to the plain cement. Plotting these factors versus dosage would then provide the dependence of yield stress on polymer dosage, as shown in section 5.3.6.

For this set of experiments, 2 kg of OPC were sampled from the PE barrel at different heights to prepare a cement paste with UPW with a constant water-to-cement ratio (w/c) of 0.3 using a Hobart mixer (N50 5-Quart Mixer). PCEs were dosed in direct addition mode as described in section 5.2.2.1. The resulting cement paste is then split into 10 small batches whose masses have been carefully measured. The hydration kinetics is monitored by isothermal calorimetry. The additional water is weighed and added 10 minutes after the initial mixing in the paste over the induction period when a low activity in the dissolution process is observed and the yield stress of the paste remains unchanged. Right after each water addition, the cement paste was mixed for 3 minutes at 800 rpm with a vertical mixer (Eurostar power control visc with a 4-bladed propeller stirrer, IKA).

5.3 Experimental results

5.3.1 Yield stress evolution

Figure 5.3 shows the evolution of the fluidity in relation to the polymers structure. Different concentrations were selected to cover a broad range of spread diameters for each polymer at the beginning of hydration.

The initial fluidity, expressed as yield stress (Pa) and calculated by the Equation (5.3), depends on the polymer dosage and structure. Specifically, the yield stress increases when the dosage decreases. Generally, it is however noticed that all polymers lead to a yield stress that rapidly stabilizes and then evolves only very slowly during a period that we define as open time. This is followed by a rapid increase of yield stress, which we have tried to correlate to polymer structure and dosage.
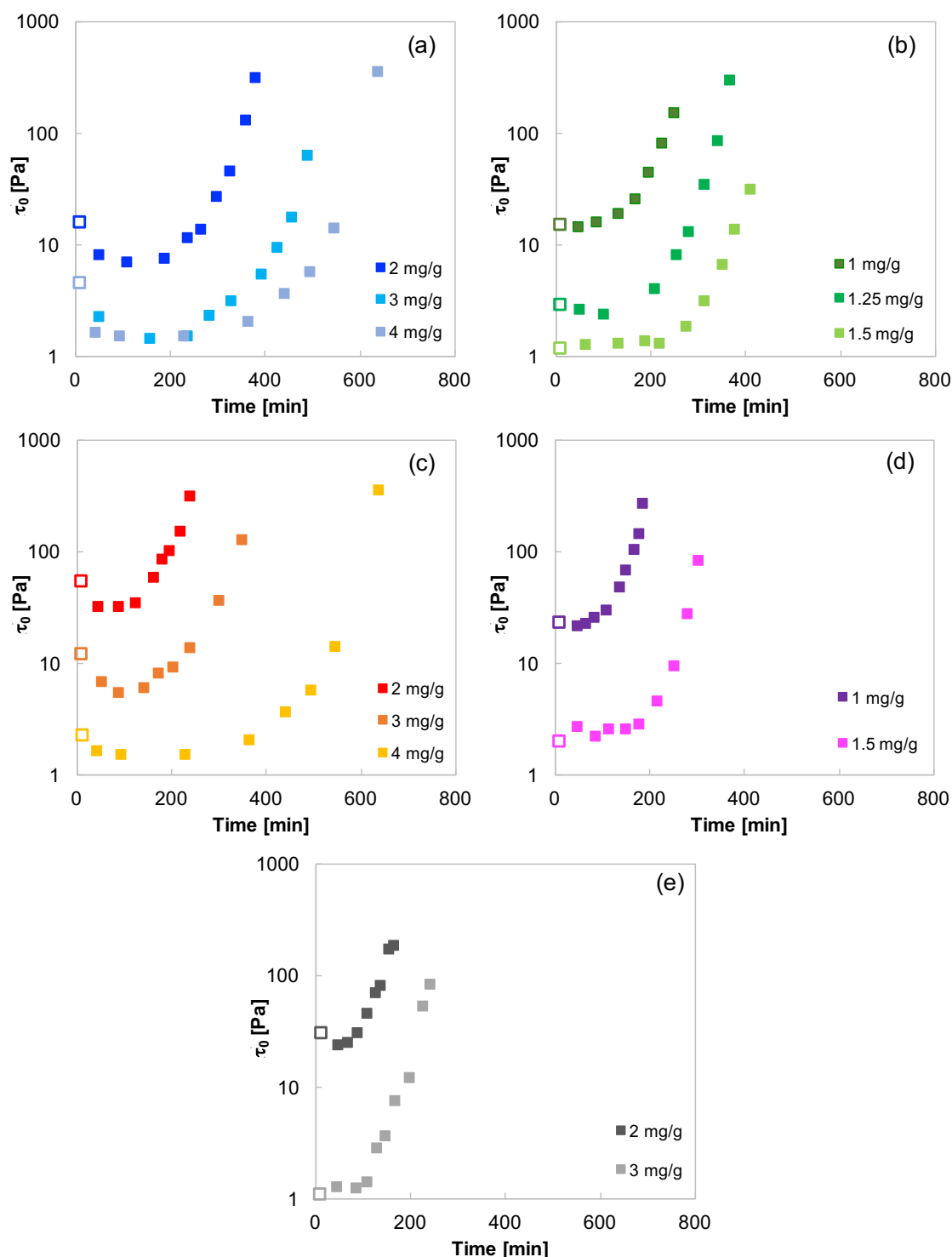
Figure 5.3: Evolution of yield stress over time in presence of different polymers: (a) 2.5PMA1000, (b) 4.0PMA1000, (c) 2.5PMA2000, (d) 4.0PMA2000 and (e) 2.5PMA5000. Each graph shows data series for different dosages. The empty symbols indicate the first data that cannot be related to isothermal calorimetry measurements.

It should be noted that the first data points after the mixing are collected before the start of the isothermal calorimetry measurements. Therefore, they cannot be related

to the first steps of hydration kinetics and are not included in our subsequent data analysis.

Refludification, evidenced as an increase of the spread diameter after some minutes after mixing, is most clearly observed with the polymers having a C/E ratio of 2.5. However, this effect is less evident or even absent with polymers with higher C/E ratio. Such effects depend on the sulfate content of cement and the molecular structure of the polymer [91]. In essence, it relates to a possible sulfate competition as explained in section 2.3.4. Therefore, polymers having high sensitivity to sulfates should be most susceptible to refluidication [93,292].

Refludification is also an example of how mixing affects properties. Other examples include the so-called "irreversible structural breakdown" [104]. In the context of this thesis, it was noticed that a too short mixing time would lead to an underestimation of the polymer dispersion ability. As a consequence, the polymer could be overdosed, causing some pastes to segregate even after few hours. For this reason, the impact of mixing duration was carefully studied and it was found that a mixing time between 4 and 6 minutes could limit such problems.

The developed protocol involved the preparation of large quantities of cement pastes by using the Hobart mixer. Since this is a rotation rate controlled mixer we could only set the mixing speed and time, so that the mixing energy changed from case to case depending on the cohesion of the paste. To the best of our knowledge, there is no alternative approach to overcome this issue when using rotation rate controlled mixers.

5.3.2 Adsorption evolution

The evolution of adsorption for 2.5PMA2000 and 4.0PMA1000 is presented over time and for different dosages in Figure 5.4. This evolution is clearly influenced by the polymer structure. For 4.0PMA1000 at the reported dosages, the initial adsorption does not increase much with dosage and only increases moderately with time. The polymer 2.5PMA2000 maintains a roughly constant adsorption until a

critical moment after which its adsorbed amount drastically increases. In contrast, the polymer 4.0PMA1000 is adsorbed and only slightly more consumed over time, regardless of its dosage.
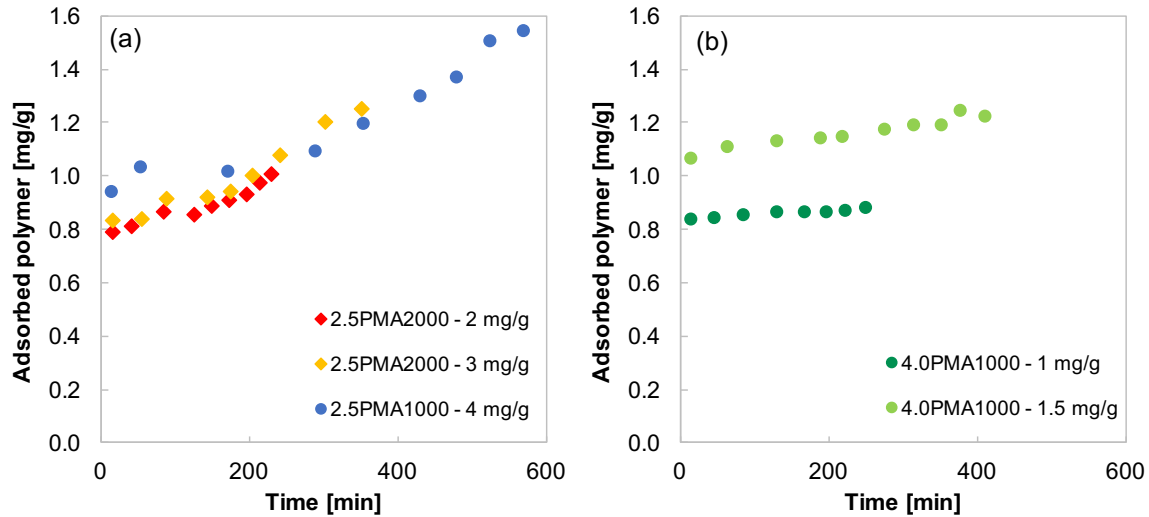
Figure 5.4: Adsorption evolution by varying the polymer concentration for the polymers: (a) 2.5PMA1000 and 2.5PMA2000, and (b) 4.0PMA1000.

5.3.3 SSA$_{BET}$ evolution

The SSA$_{BET}$ of the anhydrous cement is around 1 m^2/g. Because of this reason, Figure 5.5 emphasizes the SSA$_{BET}$ changes after the mixing of cement with water and polymer. As a general observation, the SSA$_{BET}$ increase ranges approximately from 2 to 3.5 m^2/g in the studied timeframe.

The changes in SSA$_{BET}$ are lowest for the polymers with higher C/E, as exemplified in Figure 5.5c, for 4.0PMA1000. For polymers with a lower C/E, the SSA$_{BET}$ increases more (Figure 5.5a and b)). Also, in all cases, it appears to be a period of slight change followed by one of more substantial increase. These trends are consistent with those observed for adsorption in Figure 5.4.

As shown in Figure 5.6, no significant changes can be observed by varying the w/c ratio in absence of PCE in agreement with the evolution of the heat rate (Figure 5.1). This confirms that the delayed addition of the water dos not modify the hydration of cement in the early stages.
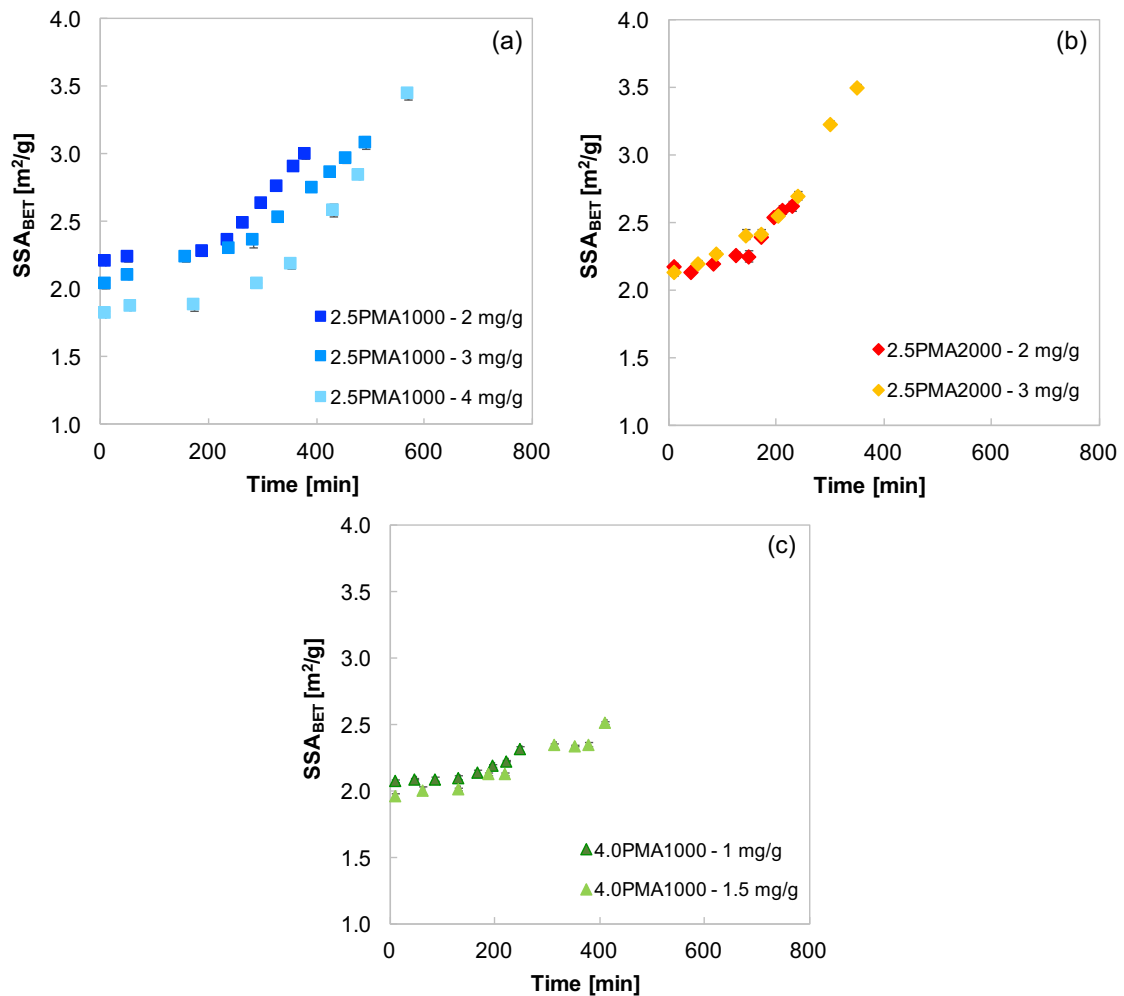
Figure 5.5: SSA$_{BET}$ evolution by varying the polymer concentration for the polymers: (a) 2.5PMA1000, (b) 2.5PMA2000, and (c) 4.0PMA1000. The results are shown as the mean values and the standard deviation of the mean for $n_{samples}$ = 3. The error bars are included, but often not visible because they are smaller than the data markers.
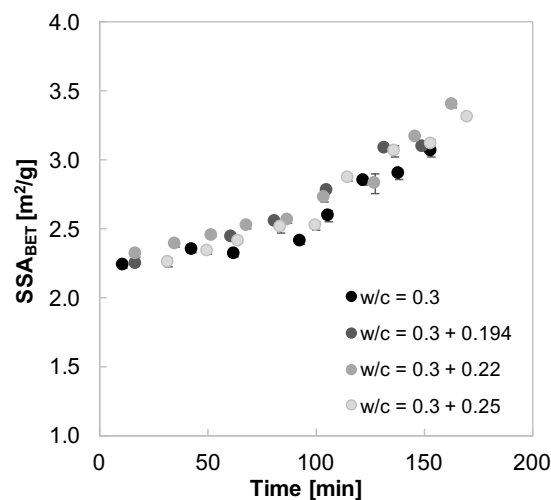
Figure 5.6: SSA$_{BET}$ evolution of reference pastes at different final w/c ratios. The results are shown as the mean values and the standard deviation of the mean for $n_{samples}$ = 3. The error bars are included, but often not visible because they are smaller than the data markers.

The initial mixing is very important since it is during that period that cement undergoes a first substantial increase in SSA_{BET}, mainly due to the precipitation of ettringite [9]. In this work, the initial SSA_{BET} typically increases from 1 m^2/g to about 2 m^2/g, with minor differences of SSA_{BET} values depending on the polymer dosage. A similar trend has been recently presented in literature when studying the hydration of a model cement. However, the absolute values were much larger [15,16]. This might be due to the massive dosage of the C_3A in the model cement used by those authors (20%) in contrast with the moderate amount in the industrial cement used here (about 6%).

We also note that, for a given polymer, the initial SSA_{BET} (measured after around 10 minutes from the beginning of hydration) decreases when the number of charges introduced in the system is increased. This is evidenced in Figure 5.7 and confirms the results obtained using small batches of cement paste (Chapter 3). It suggests that the carboxylate groups have a blocking effect on hydration, either on the formation of hydrates or on the opening of dissolution pits, or both.
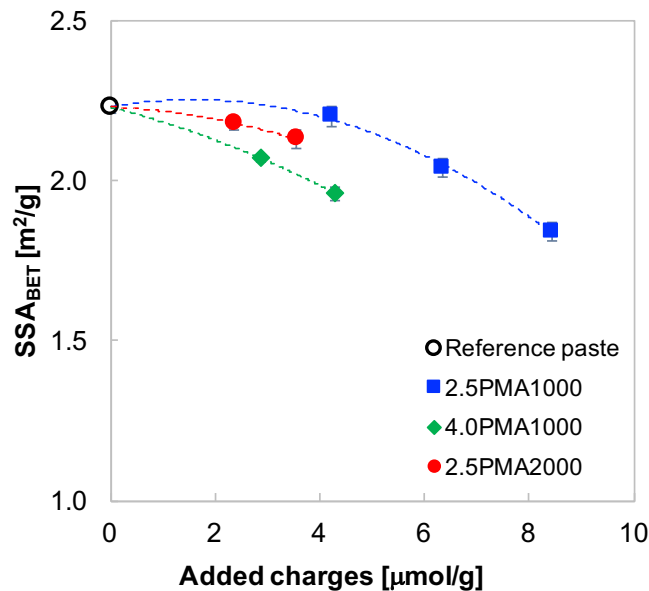
Figure 5.7: Relation between the number of charges introduced and the initial SSA_{BET}. The results are shown as the mean values and the standard deviation of the mean with $n_{samples}$ = 3. The error bars are included, but often not visible because they are smaller than the data markers. The discontinuous lines are polynomial fits serving as guide for the eye.

5.3.4 Surface coverage

The surface coverage is a key parameter to take into account for the understanding of the fluidity loss [123]. In fact, by decreasing this coverage, the number of contact points among bare surfaces increases, leading to much higher cohesion forces.

In our case, the surface coverage is expected to change with time because of new surfaces produced by hydration. As long as admixtures can adsorb on these surfaces, the yield stress should barely change. In contrast, once polymer is no more available, newly created surfaces should cause high increases in yield stress.

The surface coverage, θ_{SP}, represents the fraction of the surface covered by adsorbed polymers with respect to the total surface. It can be calculated using the adsorbed conformation model proposed by Flatt et al. [65] and an adsorption measurement:

$$\theta_{SP} = m_{adsorbed} \cdot N_A \cdot \frac{S_{SP}}{M_w} \tag{5.8}$$

where $m_{adsorbed}$ is the polymer adsorption expressed mg/m^2 of dry cement, N_A the Avogadro constant, S_{SP} the surface occupied by an adsorbed molecule expressed as nm^2/mol (Equation (2.7)), and M_w the molar mass in g/mol. The mass of the adsorbed polymer, generally given in mg/g$_{cement}$, is divided by SSA$_{BET}$ to get $m_{adsorbed}$ in units of mg/m^2.

Literature data occasionally report adsorption measurements over time, but not specific surface area of hydrating cements [69,293]. This might be due to the numerous inconveniences coming from the sample preparation. In contrast to those works, and using the methods developed in this thesis, Figure 5.8 shows the true evolution of surface coverages.

It shows that, for the three studied polymers, the average surface coverage does not significantly change over time. Also, for a given polymer, the initial surface coverage increases by increasing the polymer dosage. This results mainly from an excess of available polymer coupled with a decrease of the surface formed when the polymer dosage is high (Figure 5.7).
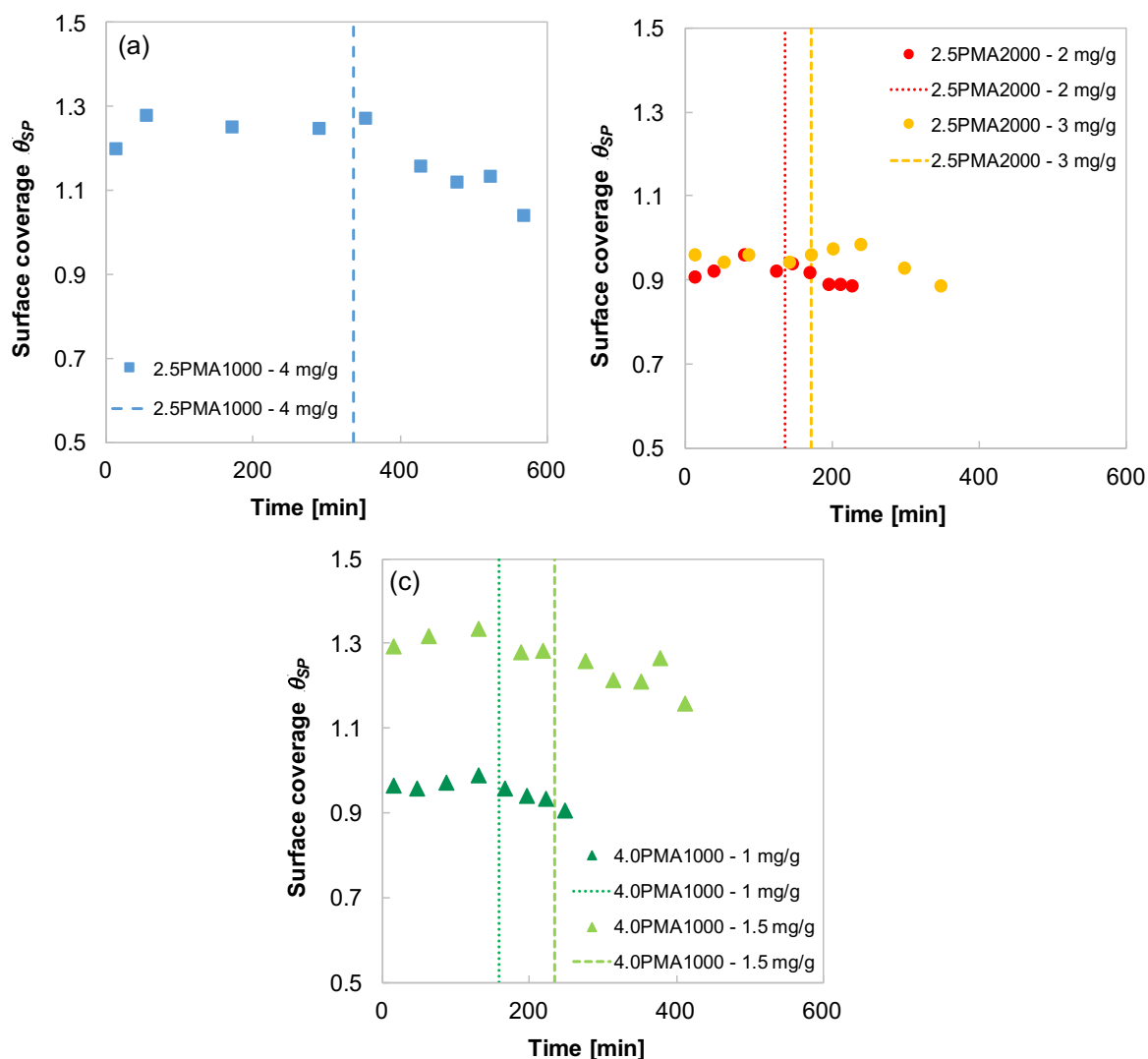
Figure 5.8: Surface coverage evolution for (a) 2.5PMA1000, (b) 2.5PMA2000 and (c) 4.0PMA1000 at different dosages. The mass of adsorbed polymer is divided by the total SSA$_{BET}$ measured at a given time. The dashed lines correspond to the onset time (t$_{OS}$) for a given polymer and dosage.

As shown in Figure 5.8, the calculated surface coverages seem to be overestimated since, at the highest dosage, they reach values up to 1.3 (30% excess). Therefore, it appears that the model proposed to calculate the surface coverage (Equation (5.8)) does not fully describe the system. However, this only affects the absolute value of surface coverage and not the conclusion concerning the low evolution of this parameter over time.

5.3.5 Relation between heat rate and SSA$_{BET}$

An important contribution of this thesis is to study flow loss in relation to changes in specific surface area. Since the latter are driven by hydration, it makes sense to study their quantitative relationship. As shown in Figure 5.9, we find that there is a linear relation between the specific surface and the heat rate with and without PCEs.
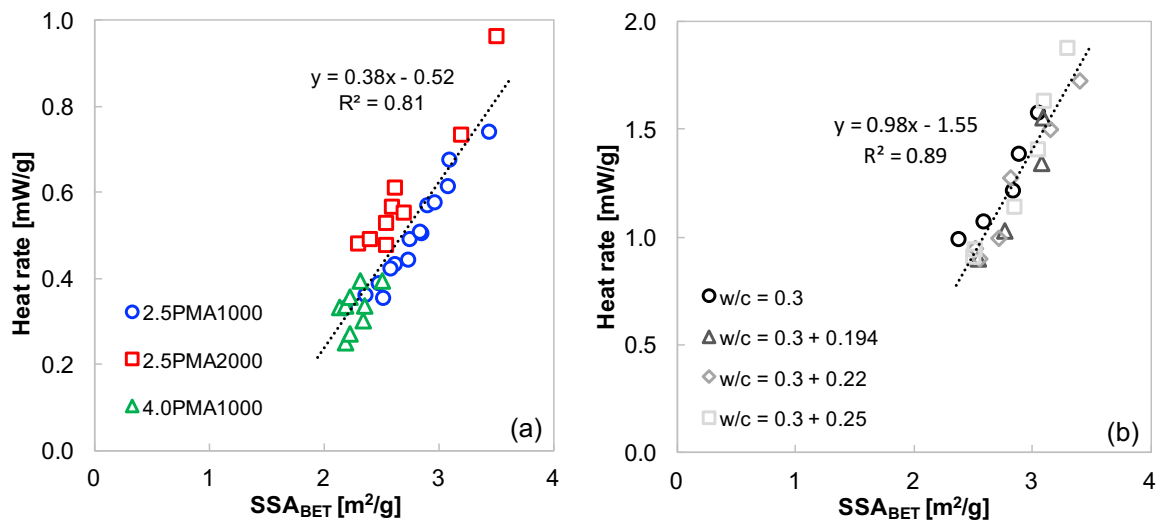
Figure 5.9: Relation between heat rate and SSA$_{BET}$ after the onset: (a) with PCEs and (b) without PCEs by varying the w/c ratio with a delayed addition of water.

The data reported in that figure are taken in the acceleration period after the onset (a detailed determination of this onset is given in sections 5.4.4 and 5.5). In addition to the linear relation, we note that the heat rate would be zero for a specific surface area of about 1.46 m^2/g and 1.58 m^2/g with and without PCEs, respectively. These values are higher than that of the dry cement ($\sim$1 m^2/g) and lower than one of the hydrated cement in the first minutes after contact with water ($\sim$2 m^2/g). This means that the extrapolated values are globally consistent with the formation process of the initial hydrates.

5.3.6 Effect of volume fraction on yield stress

Hydration causes a change of the volume fraction of solids in cement paste, which could affect the yield stress. For this we need a reliable description of how volume fraction affects yield stress, as explained in section 5.2.2.7. This is difficult to achieve

experimentally because of running either to segregation or pastes too thick to measure. As explained in section 5.2.2.7, we dealt with this problem by measuring spread diameter of a series of pastes, with each series having a different polymer dosage. For each of these dosages, the volume fraction of cement was varied. Each data series showed similar volume fraction dependencies.

Therefore, we could shift all yield stress data onto a master curve at the yield stress level of cement paste without PCE. In accordance to Equation (5.9), the shifting factors needed describe the yield stress ratio of each polymer and dosage to the reference without PCE. This result is used in section 6.3.1.
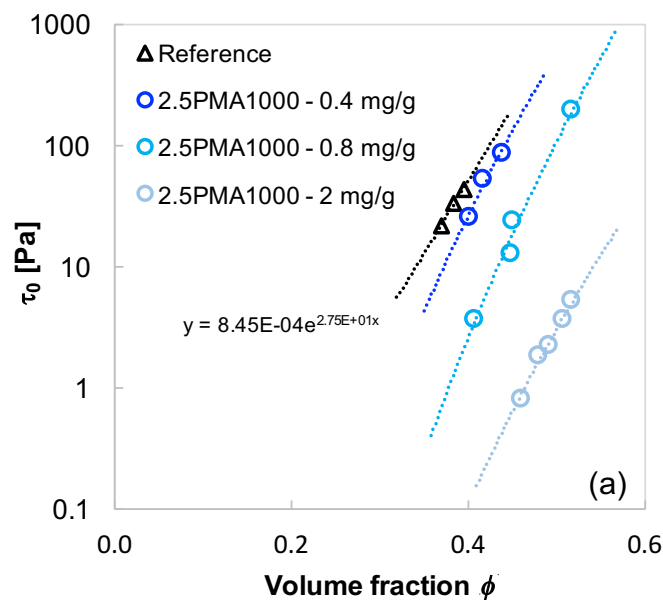
Figure 5.10: Relation between yield stress and volume fraction with the polymer 2.5PMA1000 initially dosed at 0.4, 0.8 and 2 mg/g. The exponential equation refers to the fit obtained for the references pastes.

To illustrate this, we can see in Figure 5.10 that the dependence on volume fraction is very similar for all dosages used. This is also valid for the other two polymers, 4.0PMA1000 and 2.5PMA2000. This supports the idea that the yield stress is a separable function of volume fraction and interparticle forces.

After shifting all data onto the trend of the paste without PCE, we obtained Figure 5.11. This leads to a master curve suggesting that yield stress can be well fitted by an exponential function of volume fraction:

$$\tau_{0,t} = a_\phi exp(b_\phi \phi) \tag{5.9}$$

where a_ϕ and b_ϕ are 4.22 × 10⁻⁴ and 29.2820, respectively.
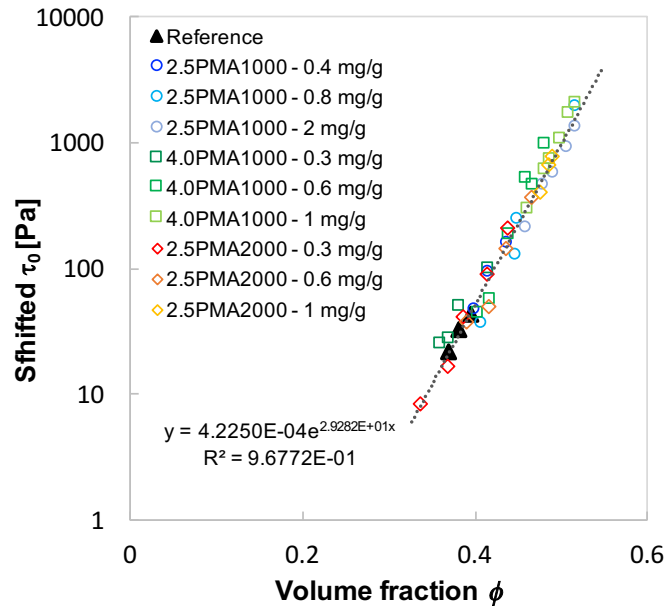
Figure 5.11: Relation between yield stress and volume fraction after the shifting used to align all yield stress data (*n* = 43), as shown in Figure 5.10, with the trend of the paste without PCE, indicated as reference.

5.3.7 Effect of dosage on interparticle forces

From the above analysis, we take the multiplication factors used for each dosage to create the master curve in Figure 5.11. Based on Equation (5.9), these "shifting factors" should correspond to the ratio between the interparticle forces of the cement pastes without and with PCE. We therefore refer to this as an "interparticle force ratio".

In Figure 5.12a and c, the interparticle force ratio values obtained from the factors in Figure 5.11 are reported versus the dosage with filled symbols respectively for 2.5PM1000 and 4.0PMA1000. In both cases, the data are well fit by an exponential function of dosage. However, this function does not have an intercept equal to one, suggesting that some amount of polymer is lost by either a competition with other ions present in the pore solution or a possible sequestration by aluminates hydrates [5–8].

The dosages used in these experiments are, however, very low due to the dilutions used for the "shifting factor" experiments. We therefore decided to report additional data points obtained at higher concentrations and at the volume fraction of 0.52 used for flow loss experiments for w/c = 0.3. For this, we used Equation (5.9) to get the yield stress of the paste without PCE at that volume fraction. By dividing this by the measured yield stresses with higher PCE dosages, we calculated additional interparticle force ratios indicated as open symbols in Figure 5.12.

These additional data well align with the trends of 4.0PMA1000 (Figure 5.12c) when plotted versus the initial dosage, but not for 2.5PMA1000 and 2.5PMA2000 (Figure 5.12a, e). This is because the higher dosages of 2.5PMA1000 and 2.5PMA2000 are already at the saturation plateau. Therefore, we reported the interparticle force ratios in terms of adsorbed polymer (expressed as mg/m^2 of cement) at the time when adsorption was measured. When reported in this way, an exponential function fits very well all the data. We choose to express adsorption with respect to the cement surface rather than its mass, because the surface will be changing over time during hydration. Also, when reported in this way, data can be extremely well fit with an exponential function, which is very convenient. However, here again the intercepts are not 1, as shown in Figure 5.12b, d and f.

The exponential function can be then rewritten as follows:

$$\tau_{0,t} = a_\theta exp(b_\theta \theta) \qquad\qquad\qquad\qquad \textbf{(5.10)}$$

where a_θ and b_θ are obtained from Figure 5.12 and reported in Table 5.4 for the three studied polymers.

Table 5.4: Fitting parameters a_θ and b_θ from shifting factor experiments expressed in mg/m^2.

PCE type	a_θ	b_θ $[m^2/mg]$
2.5PMA1000	0.037	23.436
4.0PMA1000	0.210	15.669
2.5PMA2000	0.236	13.282
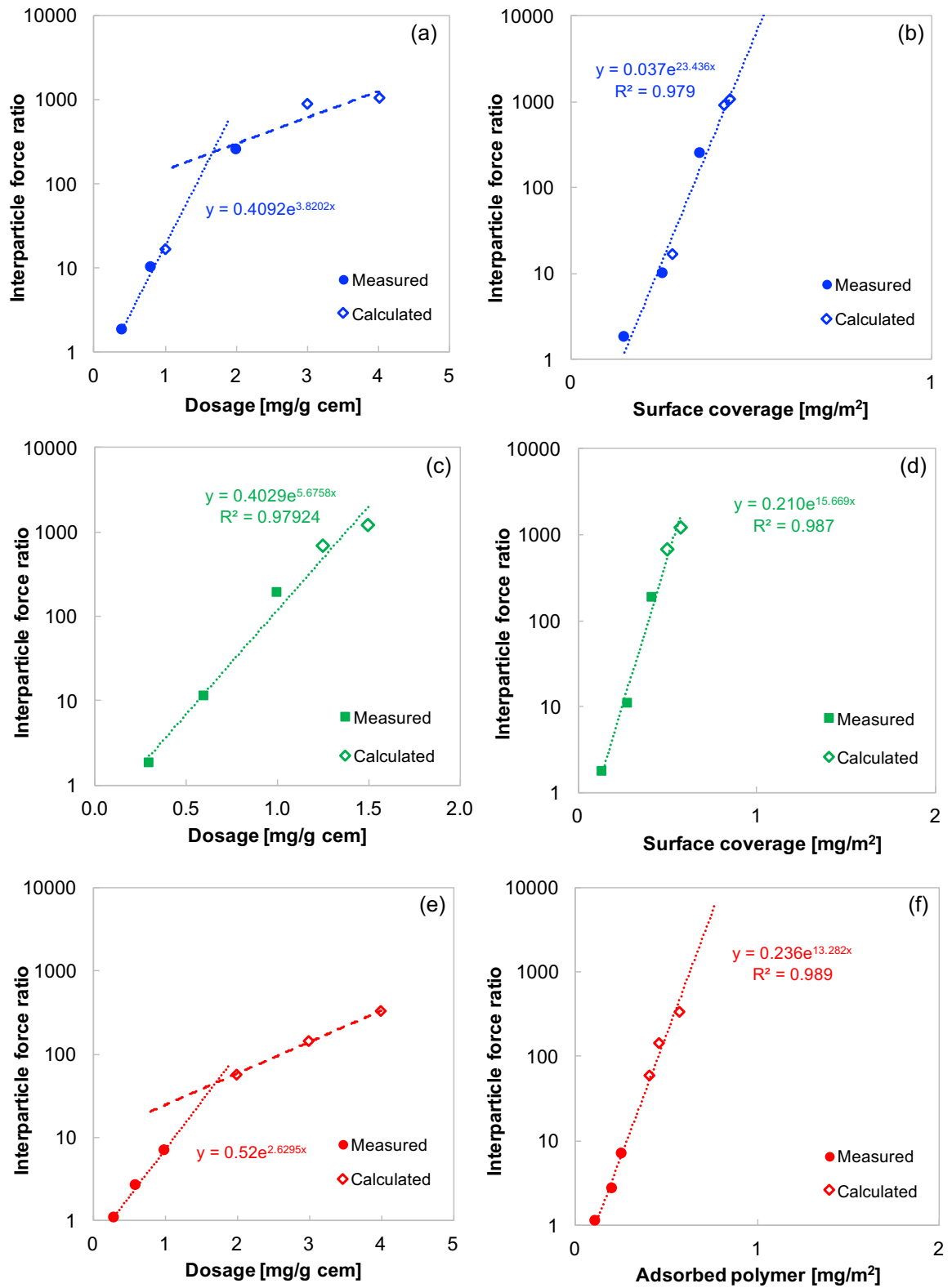
Figure 5.12: Interparticle force ratio in relation to polymer dosage or adsorbed polymer for the polymer (a, b) 2.5PMA1000, (c, d) 4.0PMA1000 and (e, f) 2.5PMA2000.

5.4 Master curve of yield stress and heat rate

5.4.1 Basic observations

Experiments indicate that hydration kinetics measured by isothermal calorimetry and the yield stress evolution are strongly correlated, as shown in Figure 5.13.
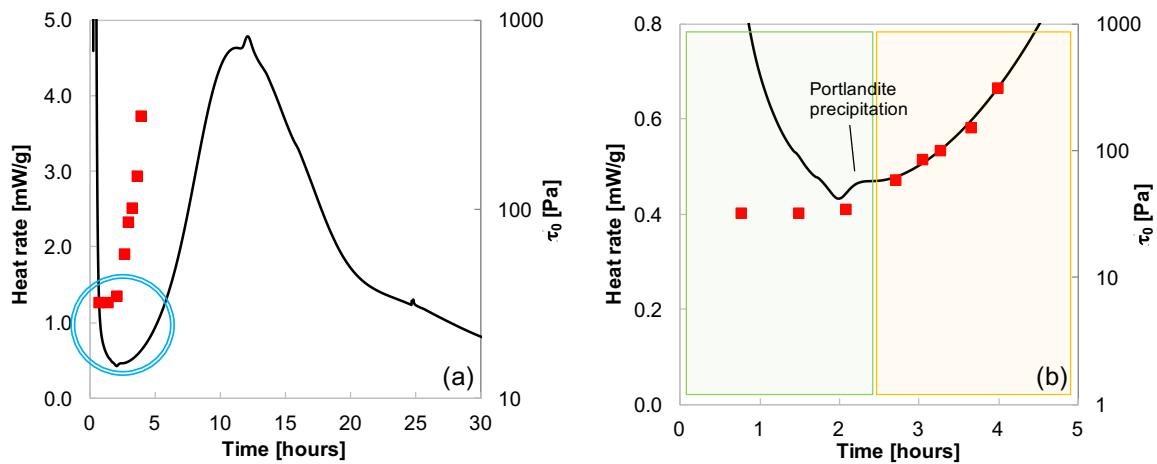
Figure 5.13: Heat rate and yield stress evolution for an OPC paste with 2.5PMA2000 dosed at 2 mg/g: (a) Overall view, (b) zoom over the first 5 hours. The green-shaded area corresponds to the period when the yield stress is roughly constant, whereas the orange-shaded area shows the yield stress increasing exponentially with the heat rate.

This is most apparent when plotting the yield stress versus either the heat rate or versus the cumulative heat released, as in Figure 5.14. Both representations show two zones: in the first one, the yield stress is roughly constant (horizontal in the green-shaded zone in Figure 5.13b), whereas it increases exponentially with both heat rate or cumulated heat released in the second zone.

The point at which the two regimes intersect is defined as *onset* and the time when this occurs is defined as t_{OS}. Beyond this, the fluidity is lost at a substantial rate. The two arrows in Figure 5.14 a and b indicate the direction of increasing time for each zone. They both go from left to right for cumulative heat (Figure 5.14a), but have opposite directions in the plot of heat rate (Figure 5.14b). This is because the heat rate first decreases and then increases (Figure 5.13a).

A more careful analysis of the data shows that the best exponential fits are obtained with the heat rate rather than the cumulative one. Therefore, in what follows, we will mostly report yield stress versus heat rate.
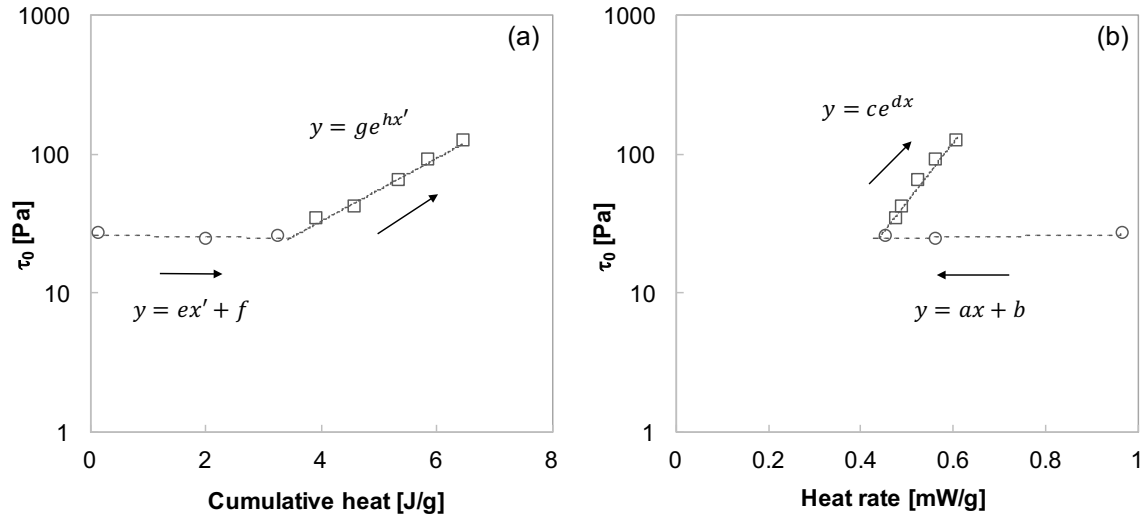
Figure 5.14: Graphical representation of the relation of yield stress versus (a) cumulative heat and (b) heat rate. The used polymer is 2.5PMA2000 dosed at 2 mg/g. The arrows indicate the time evolution.

5.4.2 From yield stress back to spread diameters

As explained above, we generally find that the exponential function of the heat rate fits very well the yield stress:

$$\tau_{0,t} = \tau_{0,0} \cdot \exp\left(u \cdot \frac{dH}{dt}\right) \qquad \textbf{(5.11)}$$

where u represents is the yield stress gain coefficient and $\tau_{0,0}$ is the yield stress extrapolated to $dH/dt = 0$.

As explained in section 5.2.2.2, we obtain yield stress from spread flow test using an exponential function of the spread flow diameter D (5.3):

$$\tau_0 = \exp(b - aD) \qquad \textbf{(5.3)}$$

where a and b are constant values corresponding to 0.3480 and 7.9473, respectively.

Therefore, we write $\tau_{0,0}$ as:

$$\tau_{0,0} = \exp\big(b - aD_{0,0}\big) \tag{5.12}$$

Equations (5.3), (5.11) and (5.12) can be combined to give the yield stress $\tau_{0,t}$ at time t:

$$\exp(b - a \cdot D_t) = \exp\big(b - a \cdot D_{0,0}\big) \cdot \exp\left(u \cdot \frac{dH_t}{dt}\right) \tag{5.13}$$

where $D_{0,0}$ is the spread diameter corresponding to the extrapolated yield stress $\tau_{0,0}$.

This gives the spread diameter D_t at time t as:

$$D_t = D_{0,0} - v \cdot \frac{dH_t}{dt} \tag{5.14}$$

with v being the rate of flow loss coefficient given by:

$$v = \frac{u}{a} \tag{5.15}$$

Equation (5.14) expresses the fact that, since the yield stress is an exponential function of both the spread diameter and the heat rate, then a linear relation should subsist between spread diameter and heat rate, as illustrated in Figure 5.15.

As shown in Figure 5.15, both $D_{0,0}$, and therefore $\tau_{0,0}$, are just extrapolated values, which by themselves do not have a physical meaning, but are useful fitting parameters to determine. In doing so, data points of spread diameters smaller than 6.5 cm – corresponding to high yield stresses – were generally excluded as they tended to depart from the exponential fit. This may have a physical origin, but is rather attributed to the lower accuracy of yield stress prediction for low spread measurements. Additionally, for very large spreads, the contribution from the surface tension to flow spreads is only the result of an approximation. Therefore, here also the accuracy of the exponential relation between flow spread and yield stress can be questioned. For transparency, the plot in Figure 5.15 and those ones in

section II.3 show the data points used for the fits with filled symbols and the excluded ones with open symbols.
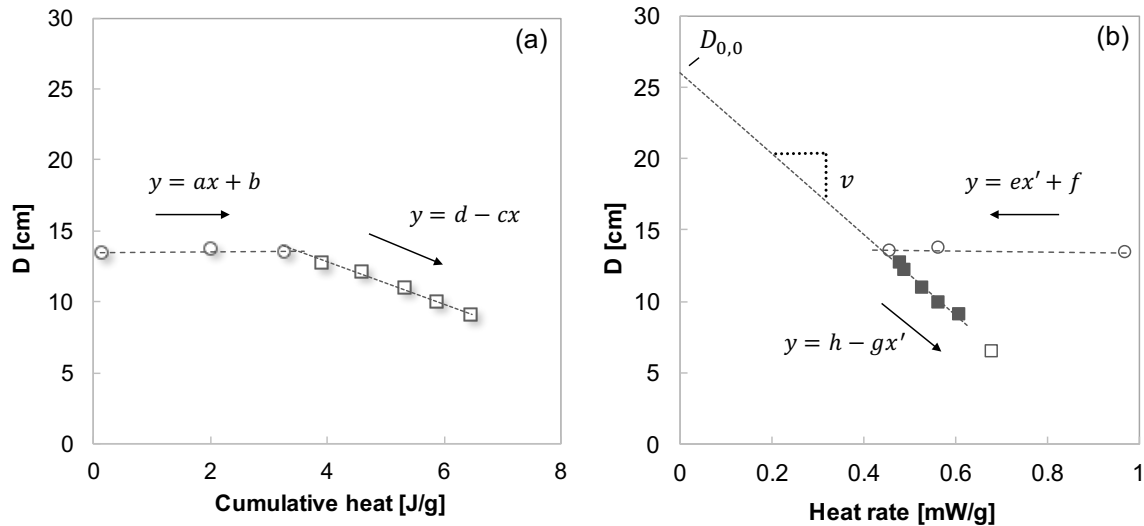
Figure 5.15: Graphical representation of spread diameters with respect to (a) cumulative heat released or (b) heat rate. The polymer is 2.5PMA200 dosage at 2 mg/g. The intercept $D_{0,0}$ and the slope v of the linear regression of D versus heat rate in the acceleration period are shown. The arrows indicate the time evolution.

5.4.3 Parametric dependence of flow loss

In this section, we exploit Equation (5.14) to determine how flow loss is related to the type and dosage of superplasticizers. Starting with $D_{0,0}$, in Figure 5.16a, we see that values are roughly gathered into two groups according to the C/E ratio of the polymers. However, there is no dependence of $D_{0,0}$ on the side chain length or on dosage Figure 5.16b. Therefore, in what follows, we use the notation $D_{0,0}^{C/E}$ rather than $D_{0,0}$ to indicate that we use a value of $D_{0,0}$ that depends on C/E.

Based on Figure 5.16, the most appropriate data analysis of flow spread diameters versus $\frac{dH}{dt}$ is to force each linear regression through the corresponding average intercept value $D_{0,0}^{C/E}$ (26.8 for C/E = 2.5 and 36.9 for C/E =4.0). This leads us to revised values of v^* in the following calculations.
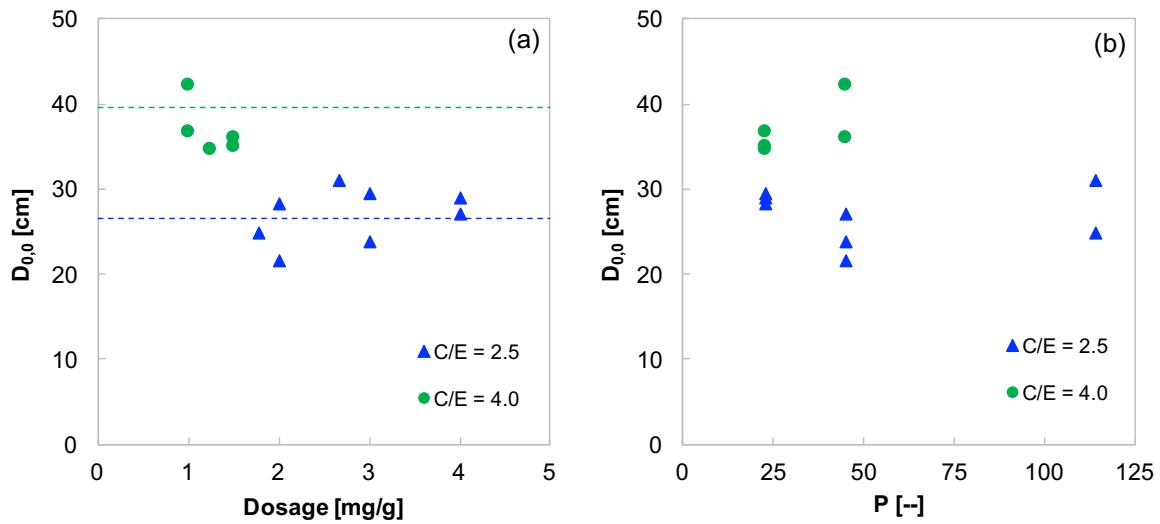
Figure 5.16: Correlation between $D_{0,0}$ and (a) the polymer dosage, expressed as mg/g cement for polymers with C/E ratios of 2.5 and 4.0. The dashed lines indicate the averaged $D_{0,0}$ values for the two series of data. Figure (b) shows the non-dependence of $D_{0,0}$ on P.

Figure 5.17 shows that $1/v^*$ increases linearly with polymer dosage and there is a clear separation between polymers according to their C/E ratios. Very importantly also, both lines share the intercept, $1/v_0^*$, which makes physical sense since this would correspond to the value of $1/v^*$ in absence of polymer.
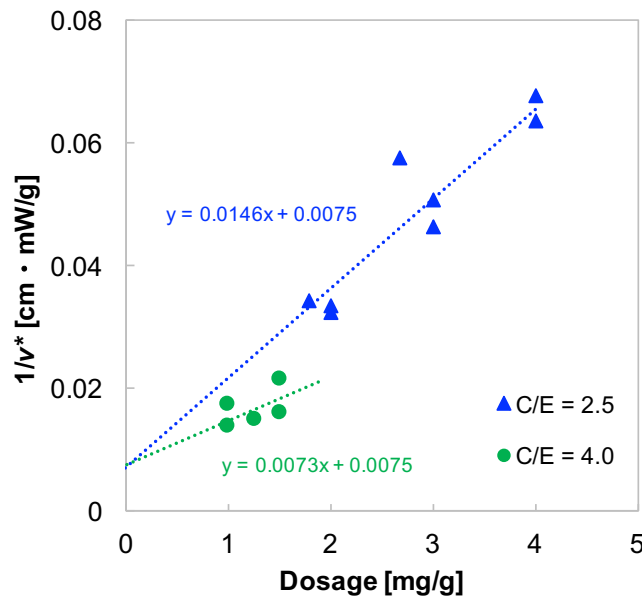
Figure 5.17: Relation between the modified rate of flow loss and the polymer dosage

An additional important observation from Figure 5.18 is that the slope of both regressions is proportional to c/N where $N = (C/E + 1)$, as indicated by Equation (5.16):

$$\frac{1}{v^*} = \left(\frac{1}{v_0^*} + \varepsilon_{TOT} \cdot \frac{c}{N}\right)$$ **(5.16)**

where c is the dosage in mg/g of cement, ε_{TOT} is a fitting parameter and v_0^* would express the rate of flow loss coefficient in absence of polymer.

Based on the above equation, $1/v^*$ can be replotted versus c/N to give the master curve shown in Figure 5.18.
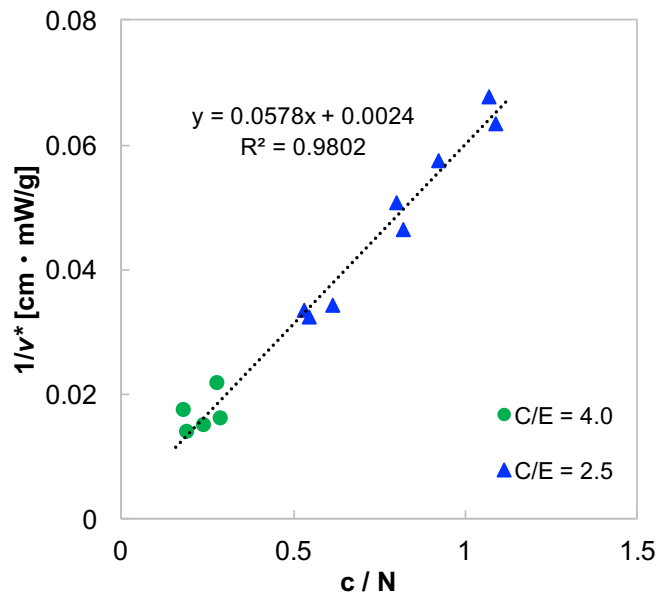
Figure 5.18: Relation between the modified rate of flow loss and N monomers in the backbone for repeat unit and dosage.

Using Equations (5.15) and (5.16), the yield stress can be rewritten as follows:

$$\tau_{0,t} = \tau_{0,0} \cdot exp\left(\frac{a}{\frac{1}{v_0^*} + \varepsilon_{TOT}\frac{c}{N}} \cdot \frac{dH_t}{dt}\right)$$ **(5.17)**

where a is the fitting parameter (from the adapted Equation (5.3)) equal to 0.3480, $1/v_0^*$ and ε_{TOT} are 0.0024 and 0.0578, respectively, from Figure 5.18.

5.4.4 Determination of the parameters at the *onset*

Our data clearly show that there must be a moment during hydration when a real change of regime occurs, probably caused by a critical event that leads to an

acceleration of the hydration. We refer such a moment as onset and use the subscript OS to refer to it.

At the onset, the yield stress can be expressed as follows:

$$\tau_{0,OS} = \tau_{0,0} \cdot exp\left(\frac{a}{\frac{1}{v_0^*} + \varepsilon_{TOT}\frac{c}{N}} \cdot \frac{dH_{OS}}{dt}\right)$$
(5.18)

The ratio between Equations (5.17) and (5.18) gives:

$$\frac{\tau_{0,t}}{\tau_{0,OS}} = exp\left(\frac{a}{\frac{1}{v_0^*} + \varepsilon_{TOT}\frac{c}{N}}\left(\frac{dH_t}{dt} - \frac{dH_{OS}}{dt}\right)\right)$$
(5.19)

where $\left(\frac{dH_t}{dt} - \frac{dH_{OS}}{dt}\right)$ is the increase of the heat rate after the onset.

In order to assess the validity of this equation, we need to estimate the yield stress $\tau_{0,OS}$ and the heat rate $\frac{dH_{OS}}{dt}$ at the onset. We determine these parameters from the values of D_{OS} and $\frac{dH_{OS}}{dt}$ using the intersections between both regimes on the plots of spread diameters versus heat rate (Figure 5.19).

In addition to the heat rate and the yield stress at the onset, we wish to determine the exact time of the onset (t_{OS}), which is a more delicate step. Indeed, it would *a priori* be useful to use the continuous calorimetric measurement to identify that time when the value of $\frac{dH_{OS}}{dt}$ occurs. Unfortunately, around the onset, portlandite may nucleate causing a non-monotonic evaluation of the heat rate as shown in Figure 5.13b. This means that the value of $\frac{dH_{OS}}{dt}$ may occur at different times over a short period, but only one of these times corresponds to the real onset. We resolved this issue using linear fits of the spread diameter versus time to extrapolate t_{OS} in correspondence to D_{OS} obtained from Figure 5.19b.

The combination of values of D_{OS}, $\tau_{0,OS}$, $\frac{dH_{OS}}{dt}$, and $t_{0,OS}$ obtained are summarized in Table 5.5.
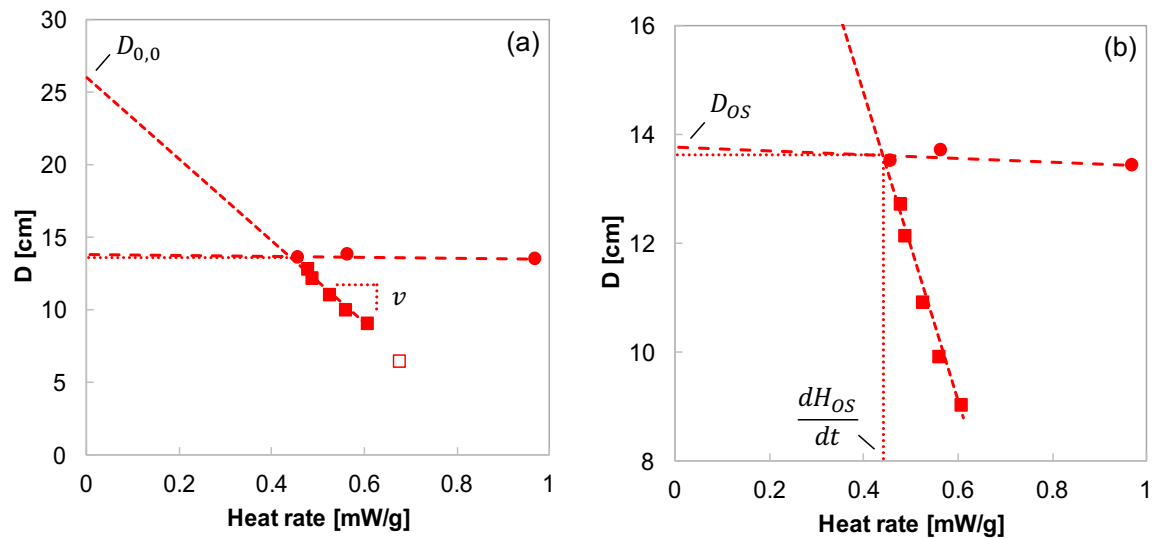
Figure 5.19: Relation between the spread diameter and the heat rate for an OPC paste with the polymer 2.5PMA2000 initially dosed at 2 mg/g of cement. The zoomed area in (b) shows the diameter (D_{OS}) and (dH_{OS}/dt) at the onset, both obtained at the intersection of the two regime curves. The empty symbol in (a) at very small spread flow was excluded from the fit calculation

Table 5.5: Summary of the main parameters at the onset point. The heat rate and the diameter at the onset were extrapolated at the intersection of the two regime curves, as shown in Figure 5.19. The yield stress was calculated by using the updated version of the Equation (5.3). t_{os} is extrapolated by the linear fit of spread diameter versus time in correspondence of D_{os}.

PCE		dH_{os}/dt	D_{os}	τ_0	t_{os}
Type	Dosage [mg/g]	[mW/g cement]	[cm]	[Pa]	[min]
	2	0.32	17.2	7.1	183
2.5PMA1000	3	0.31	21.3	1.7	265
	4	0.30	22.7	1.1	337
	2	0.44	13.7	24.9	135
2.5PMA2000	3	0.41	18.0	5.4	171
	4	0.39	21.0	1.9	222
2.5PMA5000	1.78	0.45	13.1	29.6	88
	2.67	0.38	22.0	1.3	106
	1	0.31	14.3	19.4	159
4.0PMA1000	1.25	0.23	20.5	2.2	175
	1.5	0.23	22.0	1.3	235
4.0PMA2000	1	0.41	13.5	26.0	105
	1.5	0.35	20.3	2.4	172

5.4.5 Master curve

From Equation (5.19), we expect a linear relation between the normalized yield stress and the increase of heat rate after the onset. This relation is verified as shown in Figure 5.20. Also, we can see that the slopes in these semi-logarithmic plots depend both on polymer structure and type. Equation (5.19) predicts that this slope should be $\left(\frac{1}{v_0^*} + \varepsilon_{\mathrm{TOT}}\frac{c}{N}\right)$.

To verify this, we report the normalized yield stress versus its value as predicted by Equation (5.19). To distribute relative errors equally over the large range of values, Figure 5.21 reports the natural logarithm of each of these expressions of yield stress. This shows that the 61 data points are very well correlated, with R^2 of 0.88 and a slope of 0.99 (discontinuous line).

This very good correlation shows that Equation (5.19) well captures the dependence of yield stress increase in relation to polymer structure and dosage. More specifically, it takes into account the change of the yield stress normalized with respect to its value at the onset. Values at the onset are therefore needed if absolute changes need to be determined. However, for relative changes, Equation (5.19) is sufficient.

5.4.6 Relation between hydration kinetics and surface area evolution

The relation between yield stress and heat rate is not necessarily intuitive. Rather, a relation to specific surface might appear more natural for yield stress that depends on cohesion forces between particles. Therefore, we examine whether there is a relation between heat rate and specific surface.
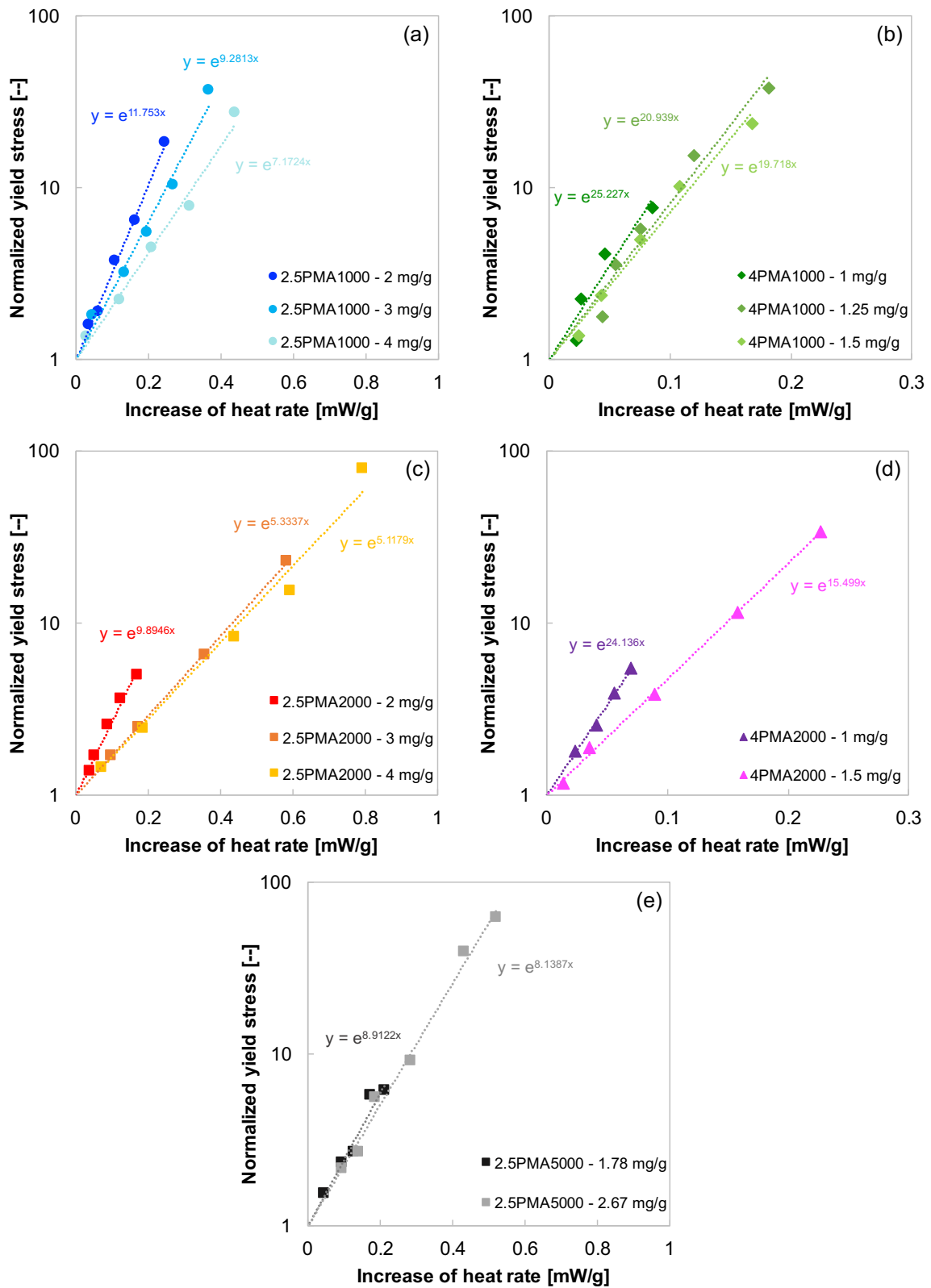
Figure 5.20: Correlation between normalized yield stress and the increase of heat rate after the onset for the polymers (a) 2.5PMA1000, (b) 4.0PMA1000, (c) 2.5PMA2000, (d) 4.0PMA2000 and (e) 2.5PMA5000 by varying the polymer dosage.
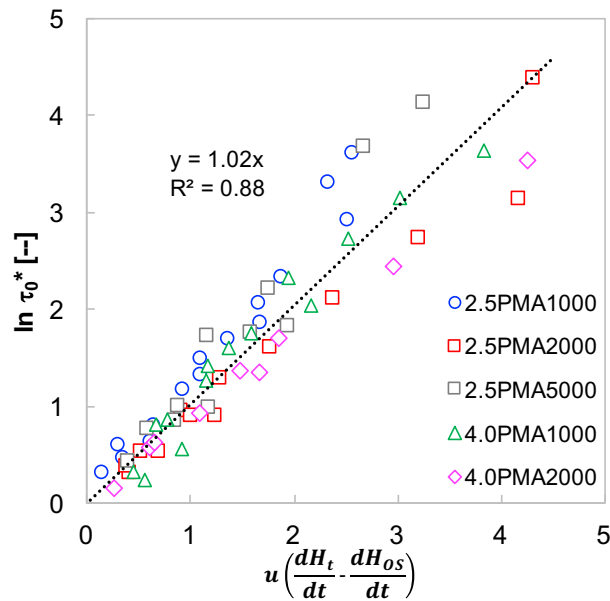
Figure 5.21: Master curve showing the dependence of the normalized yield stress and the increase of heat rate according to Equation (5.19).
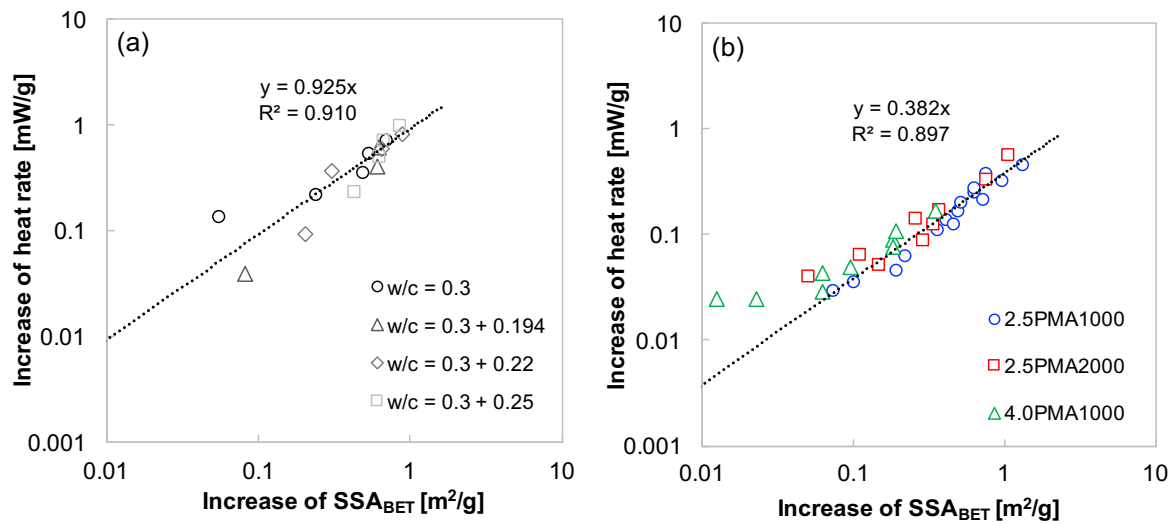
Figure 5.22: Increase of the heat rate in relation to the increase of the SSA_{BET} after the onset: (a) for plain mixes and (b) with PCEs.

As shown in Figure 5.22, there is indeed such a relation with and without PCE. This is shown for three polymers, for a total of seven dosages, and four mixes without PCE.

The data points look more scattered at low values. However, in those cases the estimation of the parameters of the onset were more delicate. In particular, at low

dosages of PCE and in absence of polymer both $\frac{dH_{OS}}{dt}$ and SSA_{OS} have been extrapolated taking the same t_{OS} from Figure 5.24b.

The slope of this linear relation with PCE is almost half of that obtained from the reference mixes, showing how PCEs slow down the dissolution, which, in turn, leads to an inhibition of the growth of the specific surface.

Importantly, Figure 5.22b also shows that this relation does not depend on polymer type or dosage. This observation could be accounted for both by boundary nucleation and growth or dissolution [38–40,45,46]. In any of these cases, we will however consider that we have the following general relation:

$$\frac{dH_t}{dt} - \frac{dH_{OS}}{dt} = \gamma_{SP}(SSA_t - SSA_{OS}) \qquad \textbf{(5.20)}$$

where $(SSA_t - SSA_{OS})$ is the increase of SSA$_{\text{BET}}$ after the onset, γ_{SP} (in mW/m²) is the slope from Figure 5.22b (0.382 mW/m² from our experiments). Therefore, Equation (5.19) can be rewritten as:

$$\frac{\tau_{0,t}}{\tau_{0,OS}} = \exp\left(\frac{a}{\frac{1}{v_0} + \varepsilon_{TOT}\frac{c}{N}}\gamma_{SP}(SSA_t - SSA_{OS})\right) \qquad \textbf{(5.21)}$$

The proportionality between the change of heat rate and of specific surface area means that Equations (5.19) and (5.21) should fit the data in a similar manner. By looking at the two plots in Figure 5.23, in which the same original data points are taken, the fits are indeed of comparable quality.

The slightly larger scatter for specific surface data points and deviation from the origin can be attributed to experimental errors. However, this does not indicate whether increases in both heat rate or specific surface area trigger the change in yield stress. In our opinion, it is rather the specific surface area that should be considered and, therefore, this is the case we will discuss from here on from a theoretical point of view.
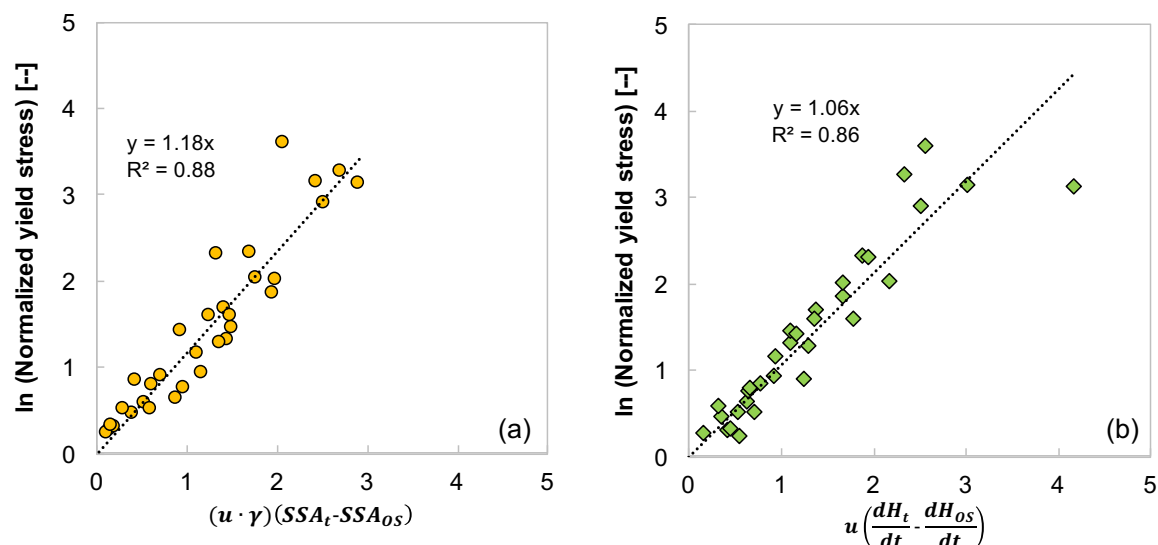
Figure 5.23: Relation between yield stress and (a) increase of surface area and (b) increase of heat rate accounting for the dependency of the parameter u on the polymer dosage and structure.

5.5 Time of onset (start of rapid flow loss)

We defined as onset the moment when the yield stress starts to increase exponentially with the heat rate (Figure 5.14). This corresponds to the take-off of the acceleration period and would indicate *de facto* the duration of the induction period shown in the calorimetric curve.

In section 5.4.4, we explained how the time of the onset was determined. As shown in Figure 5.24, this time linearly increases with the number of charges introduced in the system.

This linearity resembles the case of delayed addition recently reported for a model cement by Marchon et al. [15,16]. However, here the slope of this regression is the same for all polymers and does not show a dependence on C/E. This difference may be due to the fact that the polymers used in the present work were produced by copolymerization rather than grafting. Alternatively, it could be due to the fact that experiments were carried out in direct rather than indirect addition. The fact that there is no apparent "lost polymer", as in the case of direct addition by Marchon et al, suggests that the amount of polymer "consumed" by aluminates is very low, when compared to the used dosages.
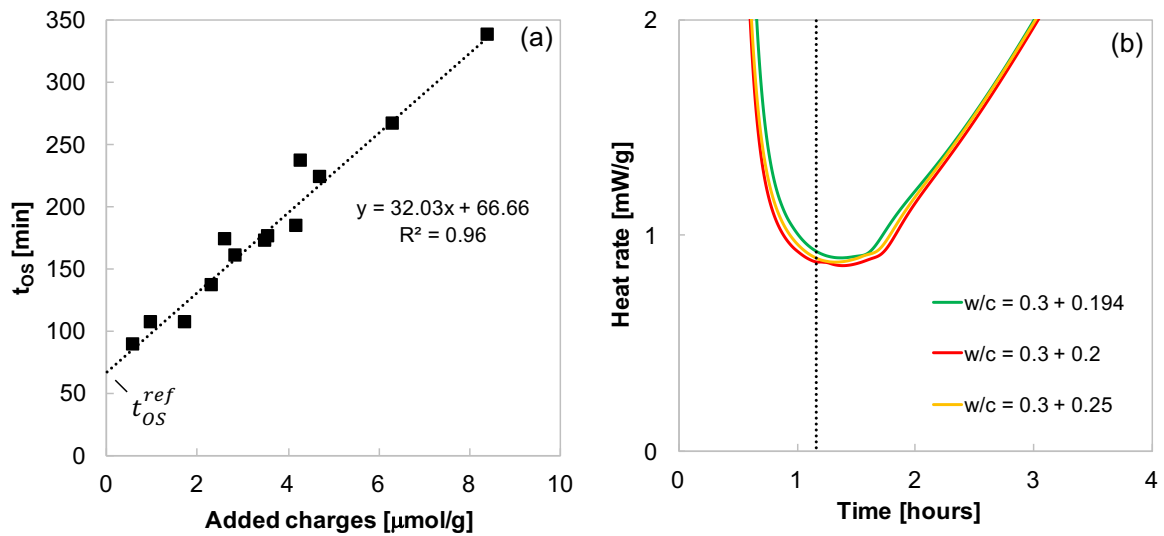
Figure 5.24: (a) Linear correlation between t_{os} and number of charges added. The extrapolation of the time at the intercept corresponds to the time at the onset in absence of PCEs; (b) calorimetric test for plain mixes in the first hours of hydration in which the discontinuous line represents the estimated t_{os}^{ref}.

The intercept from the linear regression corresponds to the time at the onset in absence of polymer, t_{OS}^{ref}. As shown from the calorimetric curve in Figure 5.24b, this value is considered a good estimation because it occurs when portlandite precipitates, at the transition between the induction and the acceleration period.
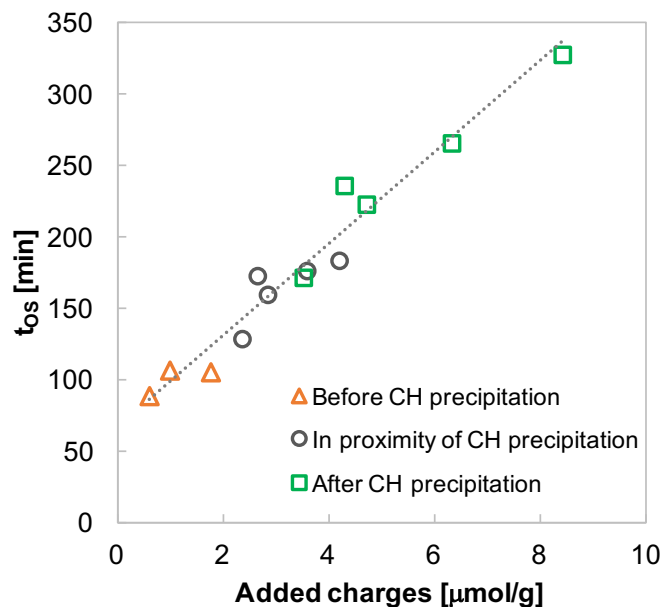
Figure 5.25: Time at the onset in relation to the portlandite (CH) precipitation, as identified by isothermal calorimetry by varying the number of added charges.

Very interestingly, the occurrence of the onset seems to be independent of the time when the portlandite precipitates. Indeed, Figure 5.25 shows that, for a low amount of charges, the onset occurs before the portlandite precipitation, whereas for a large number of charges the onset starts after portlandite precipitation.

5.6 Behaviour without PCE

Because of the clear change of regime at the onset, it makes sense to compare our data with respect to characteristic parameters of this onset, namely D_{OS} and $\frac{dH_{OS}}{dt}$. We use D_{OS} to determine the yield stress at the onset, τ_{OS}. Afterwards, we normalize the yield stresses with respect to it. Those values are then reported with respect to the increase of heat rate after the onset, $\frac{dH_t}{dt} - \frac{dH_{OS}}{dt}$. Figure 5.26 shows that this leads to an exponential relation that is virtually identical for the three cement pastes considered.
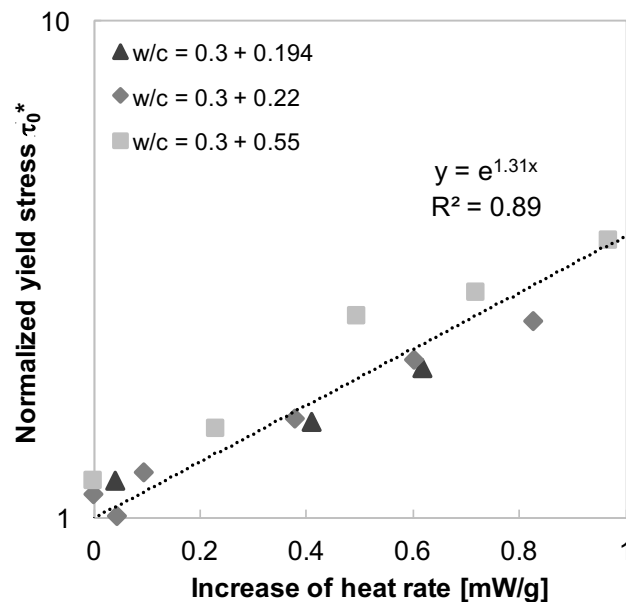
Figure 5.26: Normalized yield stress in relation to the increase of the heat rate after the onset without PCEs for three plain mixes having different final w/c ratio.

As a reminder, these three pastes were prepared by delaying addition of the extra water. The cement pastes were first prepared at the same w/c ratio, so that the initial dissolution of cementitious phases, surface roughening and opening of etch

pits would be identical. Adding water later leads to pastes that should have very similar hydration kinetics, which must contribute to the results in Figure 5.26.The factor of the exponential function corresponds to what we defined in section 5.4.2 as $u = v \cdot a$. More specifically, v is the rate of flow loss coefficient, which Figure 5.26 suggests to be 3.74 in absence of polymer. This is more than 100 times smaller than the value of 416 found for v_0^* from Figure 5.18 by extrapolation from experiments in presence of PCEs at w/c of 0.3. This big difference in the flow loss coefficient in "true absence of polymer" and in "extrapolated absence of polymer" means that the presence of the PCE is somehow making the cement pastes substantially more susceptible to the forming hydrates. As it will be discussed in the next chapter, this could be due to polymers promoting homogeneous rather than heterogeneous nucleation.

5.7 Conclusions

The main objective of this thesis is to explain and quantify the reasons of the fluidity loss of superplasticized cement pastes in relation to the dosage and molecular structure of PCEs. This issue is comparatively much less studied in the literature than effects of PCEs on the initial dispersion.

In this chapter, we quantitatively established a strong correlation between yield stress evolution and hydration kinetics. In contrast to the present theories by which flow loss is linked to the increased number of formed hydrates, we demonstrated that it is rather the heat rate that appears to modulate the fluidity after the onset (Figure 5.21). In fact, this probably hides the fact that it is the surface of hydrates that controls this evolution (Figure 5.23), since we also proved that – after the onset – hydration rate and specific surface change are proportional one to the other (Figure 5.22).

Our results show a rather minor evolution of yield stress during an "induction period", of which the duration depends on the number of charged functional groups from the dosed polymer (Figure 5.26). We could identify and quantify a clear

transition from this "induction" period to an "acceleration" period taking place at a time we defined as "onset". This marks the start of a completely new process, characterized by an exponential growth of the yield stress with the heat rate (and the specific surface).

Besides, we were able to rationalize our data with a master curve showing a linear relation between the normalized yield stress and the increase of heat rate after the onset, $\frac{dH_t}{dt} - \frac{dH_{OS}}{dt}$. This master curve is obtained by multiplying that heat rate change (and the specific surface area, $SSA_t - SSA_{OS}$) by a factor that depends both on polymer structure and dosage, $\left(\frac{1}{v_0^*} + \varepsilon_{\text{TOT}} \frac{c}{N}\right)$. Such a curve works well in presence of PCEs. However, it seems to fail in absence of PCEs. A more comprehensive analysis of these results is developed in the next chapter, with the main focus of explaining the meaning of the master curves presented in Figure 5.21 and Figure 5.23.

Chapter 6

Physical interpretation of the origin of flow loss and its master curve

The content of this chapter is presently not included in any publication or draft publication. However, in combination with the content of Chapter 5, these will be the main topic of a peer-reviewed ISI journal paper.

6.1 Introduction

The aim of this chapter is to explain the master curve shown in the previous chapter (Figure 5.22 and Figure 5.24). In doing so, we systematically analyse the effect of different factors that might be at the origin of the yield stress increase after the onset.

Firstly, it is worth recalling that two different languages are found, when talking about fluidity of cementitious materials. The first one is based on industrial and engineering practice. It derived from pragmatic tests, mainly comparative, for example, slump, slump flow and setting time. The second perspective has a physical basis and uses a vocabulary based on the intrinsic properties of the material, such as yield stress, plastic viscosity and apparent viscosity.

As explained in section 5.2.2.2, there are cases when the outcome of a pragmatic test can be converted to a physical property using analytical solutions and assessing its physical conditions of the test. This is the case for spread flow tests that have been used in the previous chapter to determine the yield stress of our cement pastes and are further analysed in this chapter. It is worth to underline that our analysis does not consider variations of plastic viscosity or other properties such as thixotropy. Such properties would have indeed required other types of measurements.

Our focus is on the yield stress and its evolution. The latter is, in fact, the parameter of major interest when comparing the performances of PCE polymers in cement pastes. It has recently been demonstrated that the addition of PCEs can also influence the plastic viscosity (more precisely, the residual viscosity) of cement mixes by the modification of the interstitial fluidity due to the presence of non-adsorbed polymers [137]. However, its macroscopic impact on the global fluidity of hydrating cementitious systems is less obvious and, therefore, we do not take it into consideration. Therefore, in the present work, the terms of fluidity and fluidity loss exclusively refer to the yield stress and its evolution.

6.2 Relation between increase in yield stress and hydration

Hydration is believed to be at the origin of the fluidity loss when the mixing energy becomes insufficient to break the interparticle connections [107,149,150]. However, the relationship between hydration kinetics and fluidity loss has not yet been systematically investigated, even less in presence of PCEs.

The results presented in the previous chapter identify two distinct periods of yield stress evolution in presence of PCEs and a clear transition between them defined as onset. The first period consists of a low and roughly linear evolution of yield stress, while the second period shows a strong and exponential growth of yield stress with heat rate. Both periods and the onset are separately discussed in the following sections.

6.1.1 Induction period or constant regime

Yield stress has been considered to increase linearly with time due to a constant formation of C-S-H bridges during the induction period [104,107,117,152,294]. Roussel [117,294] defined the constant rate for increase of yield stress τ_0 during a resting time t_{rest} as flocculation rate, A_{thix}:

$$\frac{\tau_{0,t}}{\tau_{0,0}} = 1 + \frac{A_{thix}}{\tau_{0,0}} t_{rest} \tag{6.1}$$

While this equation describes an evolution of the yield stress at rest, the procedure in our experiments "refreshes" the cement paste, by remixing it with an equivalent intensity (at least the same mixing rate and duration for all the samples) before spread measurements. Because of this, we neglect the thixotropic effects and only look at the impact of hydration reactions.

Figure 6.1 shows the evolution of the normalized yield stress according to Equation (6.1) and with respect to both heat rate and cumulative heat before the onset for seven mixes using three different PCEs.
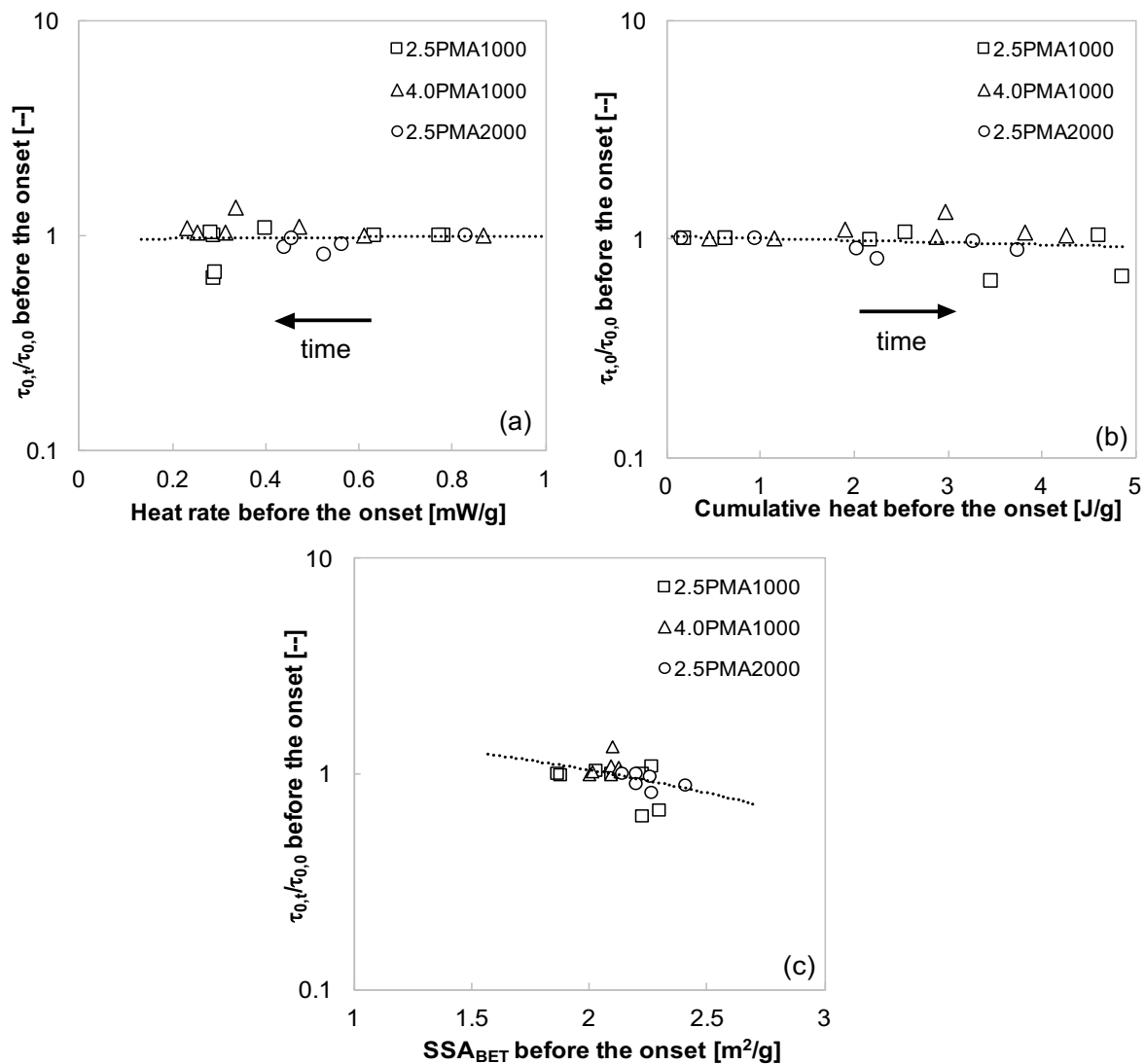
Figure 6.1: Relation between normalized yield stress and (a) heat rate, (b) cumulative heat, and (c) specific surface area before the onset. The cumulative heat is calculated subtracting the heat of the first 40 minutes during which the system needs to equilibrate. Arrows show the direction of time in the upper two plots. The discontinuous lines are drawn as a guide for the eye.

In any event, it is questionable how a reversible process (thixotropy of the system) might be related to an irreversible one (hydration reactions). At best, one could argue that the formation of nuclei compensates for the lack of Brownian motion of large cement particles and helps creating interparticle bonds that would otherwise take much longer to form. Any data showing a dependence of A_{thix} on the progress of hydration should therefore be critically evaluated before the onset. This topic is worth further investigation, but is outside of the scope of this work.

During the induction period, various factors affect the yield stress, such as particle

size distribution, polymer type and dosage. Specific surface area also plays a role, but as shown in Figure 6.1c, it cannot account alone for the effect of different polymer structures and dosages on the yield stress of a given cement. Also, we note that in the induction period the specific surface area remains rather constant and is not dependent on heat rate as shown in Figure 6.2. However, its evolution becomes relevant after the onset.
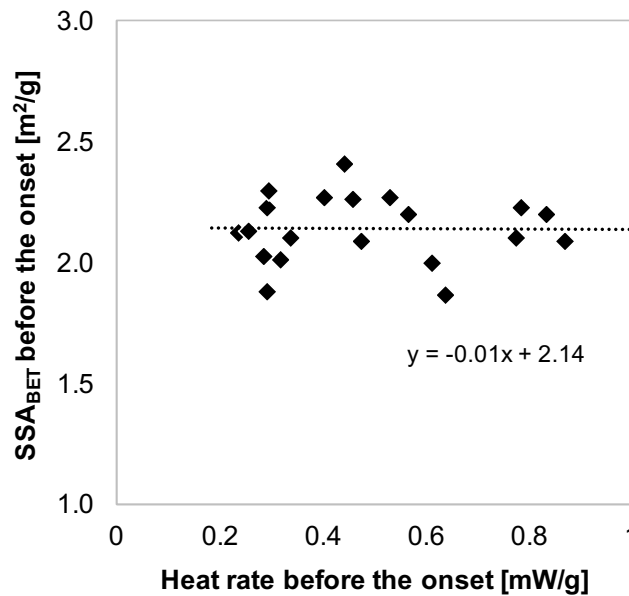
Figure 6.2: Relation between SSA$_{BET}$ and heat rate before the onset, both before the onset, for 13 mixes prepared using five PCEs having different molecular structure.

6.1.2 Onset or transition point

We defined the point after which the yield stress deviates from the linearity and starts to increase exponentially with the heat rate in an irreversible way as *onset*. This corresponds to the take-off of the acceleration period and would *de facto* indicate the duration of the induction period shown in the calorimetric curve.

The timing of the occurrence of the onset is linked to the retarding effect of PCEs. In this context, it was recently reported that in direct addition, a critical PCE concentration can be derived, after which the retardation, Δt, increases linearly with the dosed charges [15,16]. In contrast, the onset time is purely proportional to the dosed charges, something that the Marchon et al. had only observed in delayed

addition.

Portlandite nucleation and precipitation have been suggested as a possible trigger for the accelerated hydration rate [48,49]. It is very often observed as a small bump in calorimetric curves at the end of the induction period [47,48], However, while portlandite precipitation might be conceivable to explain the beginning of the acceleration period in plain mixes where the induction period is extremely short, this seems to be unrelated from the onset in presence of PCEs. Indeed, we evidence that the onset point can appear even several hours after the portlandite precipitation when high polymer dosages are used (as shown in Figure 5.26 in terms of dosed ionic groups). We infer therefore that the transition between the induction and the acceleration periods might be controlled by the initiation of nucleation and growth control or by the ending dissolution inhibition (see section 6.4.2).

6.1.3 Acceleration period or exponential regime

Various authors have reported an exponential increase of the yield stress over time [152–156]. In many cases, there is no clear distinction between the induction period and the acceleration period, but an attempt to describe the overall evolution by a single expression. For example, Perrot et al. [295] recently proposed the following expression for the normalized yield stress as:

$$\frac{\tau_{0,t}}{\tau_{0,0}} = \frac{A_{thix}}{\tau_{0,0}} t_c(e^{t/t_c} - 1) + 1 \qquad\qquad (6.2)$$

where t_c is a fitting parameter defined as characteristic time.

Linearization of the above equation for short times (typically in the range of few seconds [107]) leads to Equation (6.1). In the induction period, we evidence that hydration does not lead to irreversible changes and, therefore, the above equation must relate to thixotropy. However, after the onset, the exponential increase of the yield stress with respect to the heat rate describes an irreversible change. The

intermixing of these two phenomena (reversible and irreversible ones) in a single equation, therefore, may fit data well, but cannot provide physical insight.

Most of the data analysis reported in the literature attempts to directly express yield stress as a function of time. In this work, we try to relate the yield stress evolution to changes in physical properties of interest, such as specific surface area or adsorption. In doing so, we do not have to make a hypothesis about the effect of PCEs on hydration kinetics, but rather to characterize the consequence it has.

Also, our data analysis specifically focuses on changes at the take-off of the acceleration period. The advantage in studying superplasticized pastes is that a very clear transition from one regime to another can be detected. An important observation is that data in the acceleration period cannot be adequately fit by superposing two processes that would both take place over the whole course of hydration. Rather, after the onset, the yield stress seems to be amplified by hydration in a way and to an extent that does not occur before. From this perspective, it only makes sense to discuss our data by including the notion of onset. This marks a very clear difference with the existing literature and highlights the originality of the present work.

6.2 Effect of PCEs on hydration and SSA$_{BET}$ at the onset

As recently demonstrated by several authors [15,61,177], PCEs preferentially block highly reactive surfaces, characterized by defects in form of kinks and etch pits, limiting the step retreat process. We confirm this theory on the basis of two independent considerations.

Firstly, from Table 5.5 we notice that, for a given polymer, the heat rate at the onset decreases by increasing the number of charges. This confirms that PCEs slow down the dissolution of cement phases in relation to their molecular structure [15].

Secondly, the initial SSA$_{BET}$ decreases when the polymer dosage is increased, as

shown in Figure 5.7. This suggests that PCEs block the opening of etch pits and roughening of the cement grains more than promoting the nucleation of ettringite. Therefore, it seems that our PCEs adsorb both on ettringite and silicates from the beginning of the hydration. This contrasts with the study by Marchon et al., who found, in a model cement and direct addition, that at low dosages polymers are fully mobilized on ettringite [15,16]. On that basis, they considered the specific surface of hydrates formed as the surface on which polymers adsorb. In our case, however, it is more appropriate to consider that adsorption takes place on all cement phases.

6.3 Factors of influence in the increase of the yield stress

We present a general expression postulating that yield stress is a separable function of volume fraction, $g(\phi)$, particle size, $f(a)$, and interparticle forces, F. Here, we use the interparticle force parameter, G, which is independent of particle size. It is an interparticle force normalized by the particle size. The particle size dependence of F is included in $f(a)$, along with other particle size effects on yield stress [126,127]:

$$\tau \propto G \cdot f(a) \cdot g(\phi) \qquad \textbf{(6.3)}$$

Taking the ratio of values at time t and at the onset, we get:

$$\frac{\tau_{0,t}}{\tau_{0,os}} = \frac{G_t}{G_{os}} \cdot \frac{f(a_t)}{f(a_{os})} \cdot \frac{g(\phi_t)}{g(\phi_{os})} \qquad \textbf{(6.4)}$$

So, the normalized yield stress changes as a product of three ratios that we can try to determine separately.

6.3.1 Role of volume fraction

Based on what already described in section 5.3.6, we consider that yield stress is an exponential function of volume fraction as defined in Equation (5.9). Substitution

into Equation (6.4), for otherwise constant interparticle forces and particle sizes gives:

$$\frac{\tau_{0,t}}{\tau_{0,OS}} = exp\big[b_\phi(\phi_t - \phi_{OS})\big]$$ (6.5)

where ϕ_t and ϕ_{OS} are the volume fractions of solid at time t and at the onset, respectively.

This equation predicts the change of yield stress that would result only from a change in the degree of hydration. To check whether such an effect can explain our experimental observation, we need to estimate the dependency of the solid volume fraction on the degree of hydration. For simplicity, we consider that from each unit volume of cement reacted, two volumes of hydrates are produced. Under these conditions, the solid volume at a given point in time, $V_{S,t}$, depends on the initial volume of solids, $V_{S,OS}$, and on the increase in degree of hydration after the onset, $\Delta\alpha$:

$$V_{S,t} \cong V_{S,OS}(1 + \Delta\alpha)$$ (6.6)

Also, if shrinkage is neglected, the total volume at any time, $V_{T,t}$, remains equal to the total volume at the onset $V_{T,OS}$. So, the volume fraction of solid at any time t is given by:

$$\phi_t \cong \frac{V_{S,t}}{V_{T,t}} = \frac{V_{S,OS}}{V_{T,OS}}(1 + \Delta\alpha) = \phi_{OS}(1 + \Delta\alpha)$$ (6.7)

The change in volume fraction with respect to the onset needed for (6.5) is then:

$$\phi_t - \phi_{OS} \cong \phi_{OS}\Delta\alpha$$ (6.8)

Therefore, substituting Equation (6.8) in (6.5), the normalized yield stress should have the following relation to changes in volume fraction due to hydration:

$$\frac{\tau_{0,t}}{\tau_{0,OS}} = exp(b_\phi \phi_{OS} \Delta\alpha) \tag{6.9}$$

To verify Equation (6.9), for a given polymer and dosage, we take the parameters at time t at constant spread diameter of 10 cm, corresponding to a yield stress of 87.1 Pa. The incremental degree of hydration is estimated from the cumulative heat, Q, curve as:

$$\Delta\alpha = \frac{Q_t - Q_{OS}}{Q_{final}} \tag{6.10}$$

with Q_{final} being the cumulative heat measured after seven days corresponding to 320 J/g cement.

The degree of hydration, calculated as $\alpha_{OS} = \frac{Q_{OS}}{Q_{final}}$, is independent of the addition of PCEs with one point out linearity (Figure 6.3a). However, this suspected value is omitted from the linear regression, according to the estimation for each point of Cook's distance [236]. This roughly constant degree of hydration increases after the onset depending on the dosed charges as shown in (Figure 6.3b).
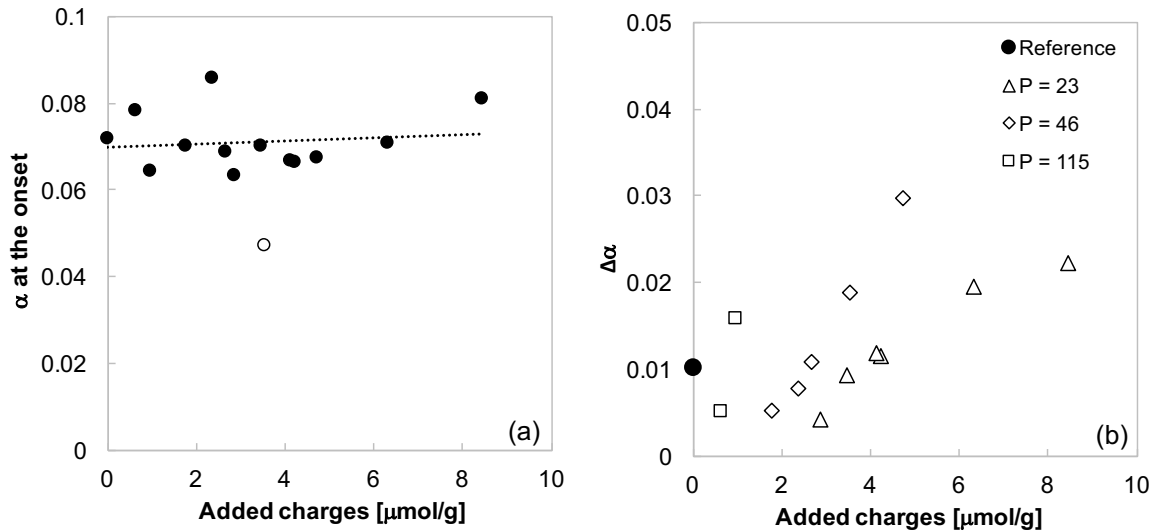
Figure 6.3: Effect of the added charges: a) on the degree of hydration α_{OS} and b) on the increase of the degree of hydration, $\Delta\alpha$, considering the side chain length expressed as P. The empty symbol in Figure (a) represents the outlier in the linear regression.

Considering an incremental degree of hydration of about 1% after the onset (Figure 6.3b), b_ϕ of 29.2820 from Figure 5.11, and ϕ_{OS} the volume fraction of 0.52 for w/c =

0.3, we can show that the volume fraction contributes to less than 5% in the change of yield stress after the onset. This is completely negligible when one considers the change of the yield stress measured experimentally. However, the contribution of the volume fraction can account for to 40% of the increase of yield stress by drastically decreasing the polymer dosage.

6.3.2 Role of surface coverage

As described in Equation (6.3), the yield stress is a function of the interparticle forces between cement particles. The average maximum attractive force between two particles can be estimated by assuming a statistical distribution of contact points between bare cement and polymer-coated particles [128]. The maximum value of the interparticle force parameter is then:

$$G_{max} \propto \frac{\theta^2}{\delta_P^2} + 8\frac{\theta(1-\theta)}{(\delta_P + \delta_0)^2} + \frac{(1-\theta)^2}{\delta_0^2} \tag{6.11}$$

where θ is the surface coverage, δ_P is the adsorbed layer thickness at full coverage and δ_0 is the semi-minimum separation distance between bare cement particles. The first term describes contacts between surfaces that are both coated with superplasticizers. The second relates to contacts in which one surface is coated and the other not. Finally, the last term refers to the force between two bare surfaces.

In the limit of full surface coverage, changes in G_{max} are dominated by the first term according to:

$$\lim_{\theta \to 1} G_\theta \propto \frac{\theta^2}{\delta_P^2} \tag{6.12}$$

Assuming that the onset occurs at a high surface coverage, then there is a period of time during which the relative yield stress change due to modifications of surface coverage would be written from Equation (6.4) as:

$$\frac{\tau_{0,t}}{\tau_{0,OS}} \cong \frac{G_t}{G_{OS}} \cong \left(\frac{\theta_t}{\theta_{OS}}\right)^2 \qquad (6.13)$$

We note that the above assumption of full surface coverage is only strictly valid for the highest dosages for 2.5PMA1000 and 4.0PMA1000. Otherwise, at lowest dosages, the contribution of the partially uncoated particles (second and third terms of Equation (6.11)) cannot be neglected. In such cases, we have:

$$G_t \propto \frac{1}{\delta_P^2}\left[\theta_t^2 + 8\frac{\theta_t(1-\theta_t)}{(1+\frac{\delta_0}{\delta_P})^2} + \frac{(1-\theta_t)^2}{\left(\frac{\delta_0}{\delta_P}\right)^2}\right] \qquad (6.14)$$

For those cases in which the onset occurs at a high surface coverage, Equation (6.12) gives:

$$G_{OS} \propto \frac{\theta_{OS}^2}{\delta_P^2} \qquad (6.15)$$

Taking the ratio of the two above equations, we get an improved expression of the impact of surface coverage change on yield stress with respect to the one in Equation (6.13):

$$\frac{G_t}{G_{OS}} \propto \frac{1}{\theta_{OS}^2}\left[\theta_t^2 + 8\frac{\theta_t(1-\theta_t)}{(1+\frac{\delta_0}{\delta_P})^2} + \frac{(1-\theta_t)^2}{\left(\frac{\delta_0}{\delta_P}\right)^2}\right] \qquad (6.16)$$

To evaluate this expression, we used δ_0 equal to 0.8 nm [296] and δ_P of 2.86, 2.78 and 4.58 nm for 2.5PMA1000, 4.0PMA1000 and 2.5PMA2000, respectively, as calculated from Equation (2.6) [65].

The more delicate part concerns the determination of θ, the fraction of the surface covered by the polymer. Unfortunately, there are not fully satisfying solutions for this. One approach relies on the adsorption conformation model, used in Equation (5.8), where the covered surface is calculated from the adsorbed mass on the surface occupied by an adsorbed polymer. While this model seems to catch the effect of the molecular structure parameter on the adsorbed conformation, its inaccuracies are problematic in the present case. In fact, in some cases, it leads to surface coverages

higher than one (for high polymer dosages corresponding to the plateau in the adsorption isotherms, see section II.2). Consequently, the second and third terms of Equation (6.16) give negative values and contributes to inaccurate predictions. In those specific cases, for which adsorption data were available, we use the highest adsorption concentration to calculate the maximum possible surface coverage and, then, rescale all the data for that polymer. In essence, this means that θ values calculated by Equation (5.8) are divided by the θ_{max} obtained for each polymer.

A similar rescaling could be done in a more reliable way if the highest dosage reaches the adsorption plateau. However, even the surface coverage is not necessarily well estimated. Indeed, the adsorption of PCEs can be perturbed by the competition with sulfate ions present in solution [76,93]. In addition, the plateau might not be even reached – as for the studied polymer 4.0PMA1000 – due to a possible precipitation of organo-mineral phases [6,96]. A separate issue can occur with polymers reaching the plateau, but giving surface coverages lower than one because of inaccuracies of the model. In such cases, the adsorption isotherms may help to correct for this with similar limitations as mentioned above.

An alternative way to express the dependency of yield stress on surface coverage is based on the shifting factor approach presented in section 5.3.7. There, we reported an exponential decrease of yield stress in relation to adsorption at the beginning of hydration (Figure 5.12). More specifically, this relation is best used if adsorption is expressed with respect to the surface of hydrating cement rather than to its mass:

$$A = {m_{SP}^{ads}} \Big/ {SSA_{cement}} \tag{6.17}$$

When trying to predict flow loss, this parameter will vary in relation to changes in the specific surface. Therefore, it is necessary to predict the amount of polymer adsorbed for a given dosage and a changing surface.

To do this, we have examined closer the adsorption isotherms of these polymers. In particular, we find that that these can be fitted considering that there is a first step of complete adsorption. In this regime, the polymer concentration in solution remains zero, but adsorption increases with dosage. Beyond a certain adsorption

level, defined as A_0, some polymer remains in solution. From this point on and until the plateau, the increased adsorption can be fitted by a Langmuir isotherm:

$$\Delta A = \frac{ax}{1 + bx} \tag{6.18}$$

where x the polymer concentration in solution. ΔA is the increased adsorption expressed as:

$$\Delta A = A - A_0 \tag{6.19}$$

To determine A_0, a and b, we linearize the Langmuir adsorption model as follows:

$$\frac{1}{\Delta A} = \frac{1}{a} \cdot \frac{1}{x} + \frac{b}{a} \tag{6.20}$$

We plot $\frac{1}{\Delta A}$ against $\frac{1}{x}$ and look for the best linear fit by adjusting A_0.

Based on the relation between adsorption at different times with changes in SSA_{BET}, the increase of the yield stress from Equation (5.10) can be estimated as:

$$\frac{\tau_{0,t}}{\tau_{0,OS}} = exp\left[-b_\theta\left(A_{t,calc} - A_{OS,calc}\right)\right] \tag{6.21}$$

This relation works at its best when experimental data for adsorption are not available either at time t or at the onset, or in neither. In cases when adsorption data is available, predictions from Equation (6.21) can be compared to those obtained using experimental values of A:

$$\frac{\tau_{0,t}}{\tau_{0,OS}} = exp\left[-b_\theta\left(A_{t,exp} - A_{OS,exp}\right)\right] \tag{6.22}$$

Figure 6.4 shows the individual contribution of the surface coverage change calculated according to Equations (6.16), (6.21), and (6.22). The dashed line represents a 1:1 relation between the calculated and the experimental normalized yield stress.

A first comment on Figure 6.4 is that predictions based on Equation (6.16) evolve rather independently of the experimental values. This is because the surface

coverage does not change more than 5-15% after the onset (see Figure 5.8) and that Equation (6.16) has a too low dependence on this to account for the very important associated yield stress changes.

This inconvenience could be overcome by using the principle of the shifting factor experiment. In fact, this showed that an exponential dependence of yield stress on surface coverage should be expected. Also, results from Equation (6.22) seem to capture better the trend of yield stress changes. Similar results are obtained when Equation (6.21) is used and calculated rather than measured adsorption values are used. The major deviation is noticed for the highest dosage of the polymer 4.0PMA1000, as indicated by the arrow in Figure 6.4.
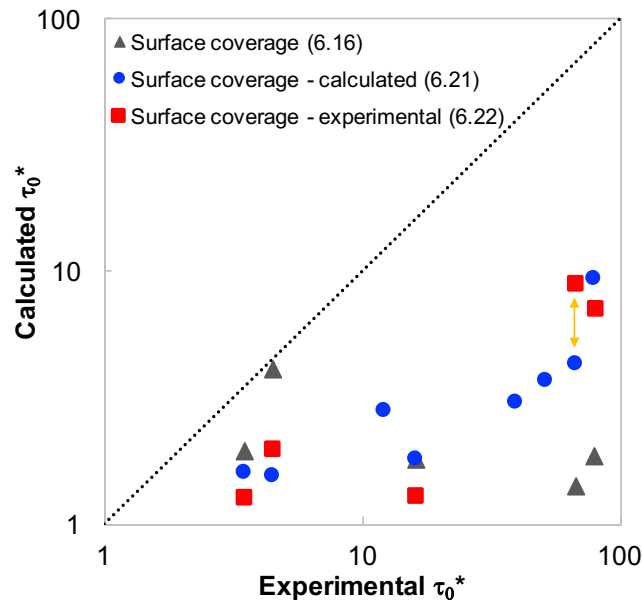
Figure 6.4: Individual contribution of the surface coverage to the change in yield stress after the onset calculated according to Equations (6.16) based on forces calculation (grey triangles), Equations (6.21) (blue circles) and (6.22) (red squares) based on the shifting factor experiments. The arrow indicates the difference between the calculated and experimental surface coverage contributions from Equations (6.21) and (6.22) for the 4.0PMA1000 dosed at 1.5 mg/g.

6.3.3 Role of change in particle size and SSA

The next topic to analyse is the dependence of the normalized yield stress on particle size. This relates both to the number of contacts points between particles

and the interparticle force. As a reminder, the combined dependence of yield stress on particle size is included in $f(a)$ (see first paragraph in section 6.3).

To estimate $f(a)$, we use the relation by Zhou et al. [124] that claims that the yield stress scales as the inverse square of the surface average diameter. In the Yodel model [126,127], the problem is more complex because the contact curvature and contact points among particles would also change. Therefore, for simplicity we consider the approach by Zhou et al. and need to express how the surface average particle size changes as cement hydrates. The surface average diameter, d_s, is given by:

$$d_s = \frac{1}{\Sigma\left(\frac{x_{vi}}{d_i}\right)} \tag{6.23}$$

where $x_{vi} = {v_i}/{\Sigma v_i}$ is the volume fraction ratio of particles of diameter d_i.

Let us consider that after the onset we have a mixture of two type of particles. The first ones are anhydrous cement particles and their size is not supposed to change in the extend of hydration considered. The second type are hydrates, mainly C-S-H, that are much smaller. The amount of both particles changes in the course of hydration. We note the respective diameters of these particles as d_1 and d_2 to rewrite the above equation as:

$$d_S = \frac{1}{\frac{x_{v1}}{d_1} + \frac{1 - x_{v1}}{d_2}} = \frac{d_1 d_2}{d_2 x_{v1} + d_1(1 - x_{v1})} = \frac{d_1}{\frac{d_1}{d_2} + x_{v1}\left(1 - \frac{d_1}{d_2}\right)} \tag{6.24}$$

where x_{v1} is the volume fraction of large particles among all particles and $(1 - x_{v1})$ the volume fraction of hydrates, also taken with respect to all particles.

Since $d_1 \gg d_2$,

$$d_S \cong \frac{d_1}{\frac{d_1}{d_2}(1 - x_{v1})} \cong \frac{d_2}{(1 - x_{v1})} \tag{6.25}$$

The volume fraction of large particles x_{v1} can be expressed as:

$$x_{v1} = \frac{V_1}{V_1 + V_2} \cong \frac{V_{OS}(1 - \Delta\alpha)}{V_{OS}(1 + \Delta\alpha)} = \frac{1 - \Delta\alpha}{1 + \Delta\alpha} \qquad (6.26)$$

where $\Delta\alpha$ is the incremental degree of hydration after the onset at time t, V_{OS} the volume of the anhydrous particles at the onset, V_1 the volume of anhydrous particles after a given t of hydration, and V_2 the volume of hydrates. In Equation (6.6), it is assumed that for one unit volume of reacted cement, there are two unit volumes of hydrates produced.

The substitution of Equation (6.26) in (6.25) would give:

$$d_S \cong d_2 \cdot \frac{(1 + \Delta\alpha)}{2\Delta\alpha} \qquad (6.27)$$

A more general expression is obtained by substituting (6.26) in (6.24) gives:

$$\frac{d_S}{d_1} = \frac{1}{\frac{d_1}{d_2} + \left(\frac{1 - \Delta\alpha}{1 + \Delta\alpha}\right)\left(1 - \frac{d_1}{d_2}\right)} \qquad (6.28)$$

As presented in the Yodel model [126,127] and by Zhou et al. [124], yield stress goes as the inverse second power of the average particle size. So, it makes sense to first report the inverse of the above equation:

$$\frac{d_1}{d_S} = \frac{d_1}{d_2} + \left(\frac{1 - \Delta\alpha}{1 + \Delta\alpha}\right)\left(1 - \frac{d_1}{d_2}\right) \qquad (6.29)$$

What we measure in our experiments is specific surface areas, that can be related to a change in the relative population of two particles of different sizes. Specifically, the specific surface of a mixture of two types of spherical particles (anhydrous and hydrates) is given by:

$$SSA = \frac{n_1 \pi d_1{}^2 + n_2 \pi d_2{}^2}{m_1 + m_2} \qquad (6.30)$$

The number of particles n is given by the ratio between the total volume of particles of a given size by the volume of a single particle of that size. With this, SSA is:

$$SSA = \frac{\frac{V_{OS}(1-\Delta\alpha)}{\frac{\pi}{6}d_1{}^3}\pi d_1{}^2 + \frac{2\,V_{OS}\Delta\alpha}{\frac{\pi}{6}d_2{}^3}\pi d_2{}^2}{V_{os}\rho_1(1-\Delta\alpha) + V_{os}\rho_2(2\Delta\alpha)} \cong 6\,\frac{\frac{(1-\Delta\alpha)}{d_1} + \frac{2\,\Delta\alpha}{d_2}}{\rho_1\left(1 - \Delta\alpha + 2\frac{\rho_2}{\rho_1}\Delta\alpha\right)} \qquad \textbf{(6.31)}$$

where ρ_1 is density of anhydrous cement and ρ_2 the density of C-S-H, corresponding to 3.15 g/cm³ and 1.91 g/cm³, respectively [297]. Rearranging the above equation, we get:

$$SSA = \frac{6}{\rho_1 d_1}\left(\frac{1 - \Delta\alpha + 2\frac{d_1}{d_2}\Delta\alpha}{1 - \Delta\alpha + 2\frac{\rho_2}{\rho_1}\Delta\alpha}\right) \qquad \textbf{(6.32)}$$

Considering that at the onset, $\Delta\alpha$ is close to zero, SSA_{OS} can be approximated as:

$$SSA_{OS} = \frac{6}{\rho_1 d_1} \qquad \textbf{(6.33)}$$

This means that a change in specific surface area with $0 < \Delta\alpha \ll 1$ gives:

$$\Delta SSA = \frac{6}{d_1\rho_1}\left(\frac{1 - \Delta\alpha + 2\Delta\alpha\frac{d_1}{d_2}}{1 - \Delta\alpha + 2\Delta\alpha\frac{\rho_2}{\rho_1}} - 1\right) \qquad \textbf{(6.34)}$$

with $\Delta SSA = SSA_t - SSA_{OS}$.

This can be rewritten as:

$$\Delta SSA = \frac{12\,\Delta\alpha}{d_1\rho_1}\left(\frac{\frac{d_1}{d_2} - \frac{\rho_2}{\rho_1}}{1 - \Delta\alpha + 2\Delta\alpha\frac{\rho_2}{\rho_1}}\right) \qquad \textbf{(6.35)}$$

Taking the ratio of Equations (6.35) and (6.33), we have:

$$\frac{\Delta SSA}{SSA_{OS}} = 2\Delta\alpha\left(\frac{\frac{d_1}{d_2} - \frac{\rho_2}{\rho_1}}{1 - \Delta\alpha + 2\Delta\alpha\frac{\rho_2}{\rho_1}}\right) \qquad \textbf{(6.36)}$$

Since $\alpha \ll 1$:

$$\frac{d_1}{d_2} = \frac{\frac{\Delta SSA}{SSA_{OS}}\left(1 - \Delta\alpha + 2\Delta\alpha\frac{\rho_2}{\rho_1}\right)}{2\Delta\alpha} + \frac{\rho_2}{\rho_1} \cong \frac{\frac{\Delta SSA}{SSA_{OS}}}{2\Delta\alpha} + \frac{\rho_2}{\rho_1} \qquad \textbf{(6.37)}$$

We note that the calculated ratio d_1/d_2 depends on the presence of the polymer, as shown in Figure 6.5. More specifically, it linearly relates to the number of added polymer charges, although data mainly show a cloud of points with d_1/d_2 between 8 and 16, with one point a bit further away. It is worth specifying that the point at the highest added charges has been confirmed by an additional repetition of the test.

To evaluate a possible impact of the polymer on the hydrate size, we must first get the value of d_1 as a BET particle size. We calculated that the SSA_{BET} particle size for the unreacted cement, d_1, from Equation (6.33), is 0.84 ± 0.05 μm (n_{mixes} = 10). This is an averaged value obtained from a broad range of polymer type and dosage. It also includes the data from the tests without PCE at final w/c ratios of 0.52 and 0.55.

Based on the d_1/d_2 values reported in Figure 6.5, we find that the average hydrate particle size, d_2, would range between 59 and 110 nm (n_{mixes} = 8). This suspect value is omitted from the linear regression, according to the estimation for each point of Cook's distance [236].

To evaluate this size in absence of PCEs, we tentatively use the ordinate at the origin of the linear regression in Figure 6.5. This suggests that in absence of polymer, the average particle diameter of the hydrates would be 128 nm. This value is slightly lower than the one obtained from two independent tests performed without PCE and for which we obtained a size of 139 nm as BET particle size for the hydrates from Equation (6.33).

The calculated d_2 represents an average between CH and C-S-H. The stoichiometry of the C_3S hydration reaction [298] is reported in Equation (6.38):

$$C_3S + 3.1H_2O = C_{1.7}SH_{1.8} + 1.3CH \qquad \textbf{(6.38)}$$
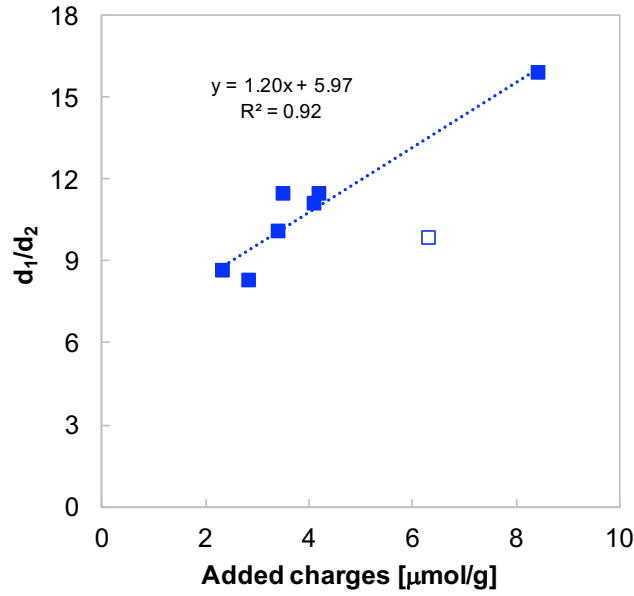
Figure 6.5: Influence of the added charges on the particle size of hydrates with respect to the unreacted cement expressed as d_1/d_2. The empty symbol represents the outlier in the linear regression.

Since C-S-H is much smaller than CH, almost all the surface is due to C-S-H, while the mass is contributed by both phases. Therefore, the average size of C-S-H is better estimated taking into account the mass ratio between C-S-H and CH. Specifically, since the amount of C-S-H is about 3.4 times greater than CH, d_2 should be close to $^4/_3$ that of C-S-H. We define it as d_{CSH} and write it as:

$$d_{CSH} = d_2 \cdot \frac{m_1}{m_1 + m_2} \tag{6.39}$$

where d_2 are the average particle size of hydrates, m_1 and m_2 the mass of C-S-H and CH, respectively. Our d_{CSH} is therefore estimated to range between 45 and 85 nm. In absence of polymer, therefore, d_{CSH}^{ref} is estimated to be 107 nm.

Similarly, to Equation (6.33), we could also express the surface area of C-S-H as:

$$SSA_{CSH} = \frac{6}{\rho_{CSH} d_{CSH}} \tag{6.40}$$

with SSA_{CSH} expressed as m²/g of C-S-H and ρ_{CSH} = 2.604 g/cm³ [298].

This gives values of SSA_{CSH} between 27 and 51 m²/g, that are comparable to that obtained by Allen et al. corresponding to 42 m²/g of C-S-H [298].

Let us now return to evaluating the change in the surface average particle size in relation to the degree of hydration. For this, we substitute the expression for d_1/d_2 from Equation (6.37) into (6.29), to obtain:

$$\frac{d_1}{d_S} = \frac{\frac{\Delta SSA}{SSA_{OS}}}{2\Delta\alpha} + \frac{\rho_2}{\rho_1} + \left(\frac{1-\Delta\alpha}{1+\Delta\alpha}\right)\left(1 - \frac{\frac{\Delta SSA}{SSA_{OS}}}{2\Delta\alpha} + \frac{\rho_2}{\rho_1}\right) \qquad \textbf{(6.41)}$$

This equation gives the ratio between the particle size at the onset and the one at some time t after it for which the specific surface and degree of hydration have been measured. Based on the work of Zhou et al. [124], it is expected that the second power of the ratio d_1/d_s, would correspond to the relative change in yield. Considering an average degree of hydration of 1% would give d_1/d_s of about 2.4 ± 0.2, that corresponds to a calculated normalized yield stress of 6.0 ± 0.8. Therefore, this estimation remains much smaller than what we measured, as shown in Figure 6.6.

6.3.4 Combination of surface effects

Figure 6.6 graphically summarizes the effect of the three individual contributions that might account for changes in yield stress, namely surface coverage, particle size, and volume fraction, as expressed in Equation (6.4). The dashed line represents a 1:1 relation between the calculated and the experimental normalized yield stress. None of these factors alone properly accounts for the experimental results. However, it can be noted that the effect of changes in particle size generally has a more significant impact than the other two factors.

Let us focus on the open symbols representing samples containing PCEs. For the points reported, the ones to the left of the figure correspond to the lowest dosages. In those cases, we observe that particle size changes have a greater impact than surface coverage changes. In contrast, points more to the right of this figure, corresponding to higher PCE dosages, suggest similar contributions from both

effects to the increase of the yield stress. The volume fraction is numerically the least important contribution.
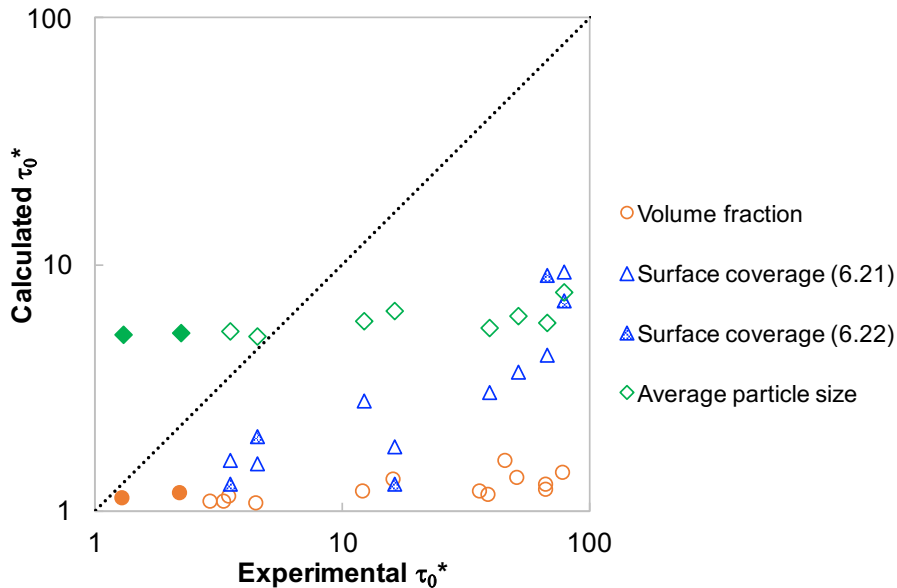
Figure 6.6: Graphical representation of the individual contribution of the volume fraction, average particle size and surface coverage on the increase of the yield stress after the onset. The filled markers correspond to values obtained from pastes without PCEs.

The combination of these three factors gives an acceptable data prediction of measured yield stress changes as shown in Figure 6.7. This combination, as indicated in Equation (6.4), is obtained by multiplying the normalized values of the three individual contributions examined in the previous sections. Importantly, Figure 6.7 shows that in almost all cases where adsorption data is available (filled symbols) the yield stress is better predicted than when it is estimated from adsorption isotherms (open symbols). It should be also reminded that the calculated surface coverage values are based on polymer-dependent parameters that are obtained from shifting factor experiments and that these have been carried out for only three polymers (out of five). This limits the number of samples for which all needed data is available to fully determine the combination of factors and explains the reduction of data points from 13, corresponding to the number of studied dosages with 5 polymers, to a maximum of 8 (open symbols in Figure 6.7).

Although this comparison can only be done for this limited number of data points, this conclusion is expected to be quite general. It emphasizes that the concepts used

to analyse yield stress changes must be correct, but that their proper quantification is delicate. Very specifically, this underlines the importance of having developed the experimental protocols needed to reliably determine the specific surface of cement. Additionally, it also emphasizes the importance of the result from the shifting factor experiments that give a much stronger dependence of yield stress on surface coverage than previously proposed in the literature.
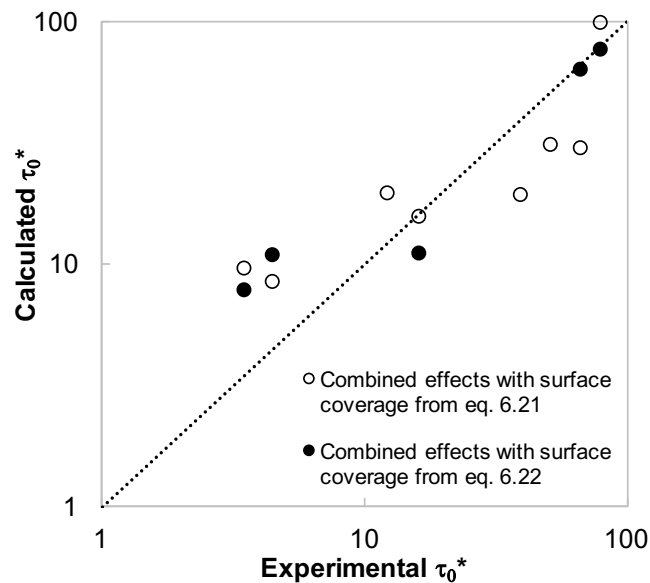
Figure 6.7: Graphical representation of the combined contribution of the volume fraction, average particle size and surface coverage on the increase of the yield stress after the onset.

6.3.5 Role of ionic composition

C-S-H particle surfaces are ionized in an alkaline environment due to the dissociation of the silanol groups. These charges are surrounded by counterions, typically Ca ions, whose concentration is higher close to the surface than in the bulk. As two identically charged surfaces approach, the ion concentration between the surface increases, in particular at mid-plane and a repulsive osmotic pressure is felt between the surfaces. However, this repulsive force decreases with the ionic strength and it becomes negligible for cement suspensions, having ionic strength values in the order of 100-300 mM [299,300].

Attractive forces can also develop in presence of divalent ions and for highly charged surfaces solution [301]. In the past years, several works evidenced that the pH and

the ionic concentration are the main parameters governing such short-range cohesion forces among C-S-H nanoparticles [301–304]. Indeed, calcium preferentially adsorb on charged C-S-H surfaces rather than sodium or, more generally, monovalent cations. These researchers agreed that the cohesion forces are not affected much by the variation of the ionic strength in the bulk solution, but rather by the pH. Therefore, increasing the charge density of the silanol groups should increase the concentration of calcium near the surface and, in turn, the strength of ion-correlation forces.

Figure 6.8 shows the bulk concentration of Ca and Na measured by ICP-OES in the pore solution filtered over time from the cement paste with the polymer 2.5PMA1000 dosed at 3 mg/g. Detailed information about sample preparation and ICP protocol are reported in the Appendix I. pH values were calculated as output of the simulations carried out on GEMS, according to the default thermodynamic database expanded with the cement specific CEMDATA 14.01 database [305–307]. The elemental composition of the pore solutions, experimentally determined by ICP-OES, provided the input data for such simulations. The electroneutrality was reached by floating the concentration of OH^- ions. The ionic strength calculated for studied pore solutions with and without PCE was calculated by GEMS to be around 500 mM.

Considering the timeframe studied for the admixed paste Figure 6.8b, we show that the Ca bulk concentration is about 20 mM until the onset point, after which it decreases slightly. In contrast, the Na bulk concentration is almost constant around the onset point at 70 mM and then increases. The pH remains roughly constant at a value of about 13. Similar ionic evolutions for Ca and pH are observed for the pore solution filtered from the reference paste Figure 6.8a.

Even if these data concern bulk concentrations of calcium, rather than surface ones, their marginal evolution suggests that their surface concentration also remains largely unchanged during hydration. Therefore, it appears unlikely that a change in the magnitude of ion-correlation forces can be put forward to rationalise yield stress changes due to hydration.
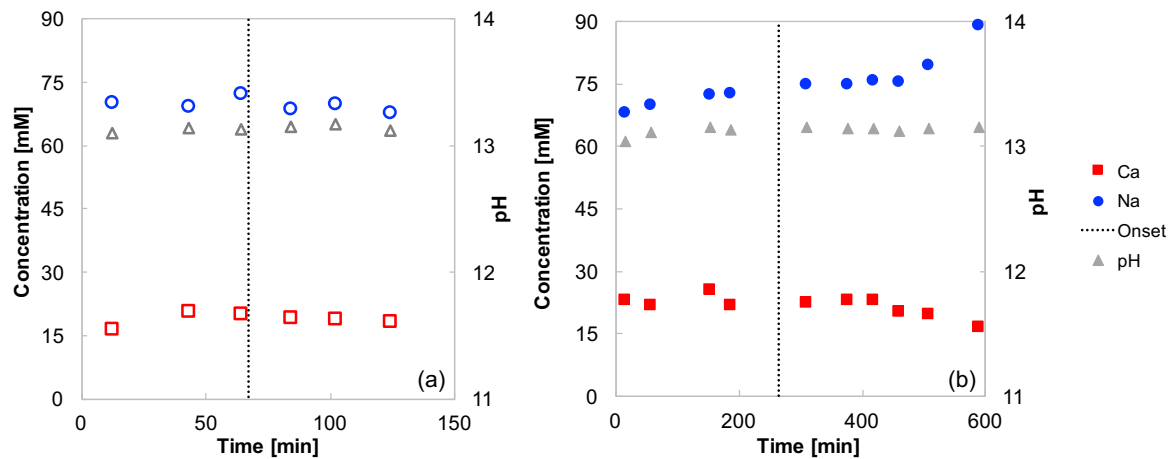
Figure 6.8: Evolution of the concentration of Ca, Na and pH in the pore solution from (a) the plain cement paste (empty symbols) and (b) with 2.5PMA1000 dosed at 3 mg/g (filled symbol). The dashed lines indicate the time at which the onset occurs.

In contrast, we noticed main changes for the low-concentration elements, such as Al, Fe, Mg, and Si, over time Figure 6.9. In absence of PCE (Figure 6.9a), the concentration of these elements is extremely low, suggesting that either particles are too big to pass through the filter or strongly agglomerate, precipitating on the cement surface [169,308].
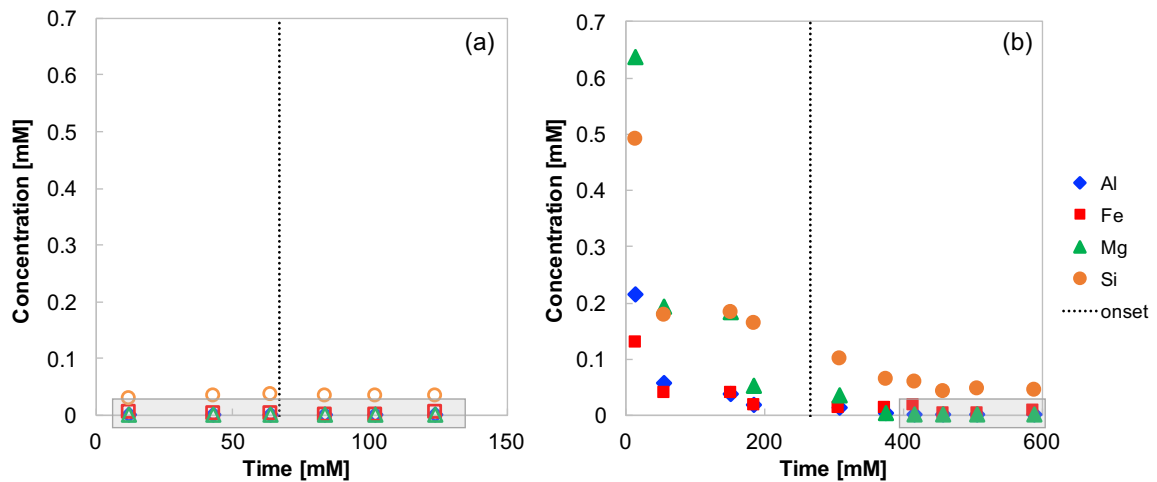
Figure 6.9: Evolution of the concentration of Al, Fe, Mg, and Si in the pore solution from (a) the plain cement paste (empty symbols) and (b) with 2.5PMA1000 dosed at 3 mg/g (filled symbol). The dashed line indicates the time at which the onset occurs. The grey-shaded areas correspond to concentration values of Al values below the LOQ in the diluted solution.

In presence of PCEs, their concentration is initially very high with respect to the plain cement paste. However, until the onset point is reached, their concentration steeply drops and Al can barely be quantified. This might suggest that hydrates, initially dispersed in the interstitial fluid [169,308,309], afterwards likely start to

precipitate on the cement surface or become large enough not to pass through the filter. In any case, new surfaces covered with layers of hydrates might affect the short-range forces among particles.

6.4 Discussion

6.4.1 Main observations

6.4.1.1   Induction period

During the induction period the yield stress may increase at rest due to thixotropy. However, values measured after remixing only show minor, if any, evolution. No irreversible structural build-up, therefore, takes place during the induction period, though the evidence from isothermal calorimetry shows that some reactions take place.

When reported with respect to the SSA_{BET}, adsorption does not evolve much during the induction period (Figure 5.4). This results from a proportional increase of both the amount of adsorbed polymer and the SSA_{BET}. The surface coverage is therefore relatively constant (Figure 5.7), which is consistent with a roughly constant yield stress.

6.4.1.2   Onset point

Our experiments clearly identify the existence of an onset that marks the start of a new process leading to an exponential increase of yield stress. This onset is not caused by the precipitation of calcium hydroxide, something that can be clearly seen in isothermal calorimetry at high PCE dosages.

For the onset to occur, the fraction of surface covered by a polymer should decrease with respect to its value at the beginning of the induction period. This decrease can start substantially before the onset, but never after. A reduction of surface coverage seems to be therefore a necessary, but not a sufficient condition for the onset to occur.

Interestingly, the occurrence of the onset directly depends on the number of polymer functional groups introduced in the system (Figure 5.25). This result is very relevant to practice, because it can greatly contribute to determine the open time of superplasticized concrete in relation to polymer type and dosage.

6.4.1.3 Acceleration period

In the acceleration period, the increase of the heat rate after the onset, $\left(\frac{dH_t}{dt} - \frac{dH_{OS}}{dt}\right)$, is proportional to the increase of the specific surface area, $(SSA_t - SSA_{OS})$, as shown in Figure 5.22. It is consistent with the acceleration period being controlled by a process of nucleation and growth. This is supported by the fact that our initial observation shows the exponential relation (5.21).

$$\frac{\tau_{0,t}}{\tau_{0,OS}} = \exp\left(\frac{a}{\frac{1}{v_0^*} + \varepsilon_{TOT}\frac{c}{N}}\left(\frac{dH_t}{dt} - \frac{dH_{OS}}{dt}\right)\right) \qquad (5.19)$$

$$\frac{\tau_{0,t}}{\tau_{0,OS}} = \exp\left(\frac{a}{\frac{1}{v_0^*} + \varepsilon_{TOT}\frac{c}{N}}\gamma_{SP}(SSA_t - SSA_{OS})\right) \qquad (5.21)$$

The above equations describe a master curve that accounts for the increase of yield stress in the acceleration period. This is a very important result for practice, in particular in digital fabrication where the initial yield stress growth plays an important role [310,311].

Very importantly, all contributions, namely volume fraction, particle size and interparticle forces, examined in the previous sections have been estimated individually with separate experiments from which the obtained parameters are disconnected from the data that we interpret in the master curve. We demonstrated that the yield stress growth could not be quantitatively accounted for changes in either volume fraction, particle size or surface coverage. However, the combination of these, in particular of particle size and surface coverage was encouraging, giving a good agreement for the studied dosages and polymers.

Unchanged particle shape is the main assumption made in our proposed calculations in section 6.3.3. Indeed, spherical particles, for both anhydrous cement and hydrates, were considered for the estimation of the SSA over the studied hydration timeframe. Around the onset, in correspondence with the take-off of the acceleration period in calorimetric curves, the forming C-S-H particles are mainly present as small nuclei for which a spherical shape is considered reasonable enough. Besides, the presence of PCEs is known to influence the morphological evolution of cement hydrates. Indeed, this topic has been already examined for ettringite [9, 103, 168] and C-S-H [309], but still at preliminary stages and they remain an open subject of research. Therefore, to the best of our knowledge and based on current scientific discussions, this assumption seems still admissible.

In what follows, we examine other factors that can either explain some of the observations or potentially contribute to better describing the obtained master curve.

6.4.2 Role of C-S-H nucleation balance

We identified that the combination of changes in particle size and surface coverage accounts relatively well for changes in yield stress. However, the master curve fails to describe the increase of the yield stress in absence of PCE. In our opinion, this is because the balance between heterogeneous and homogeneous nucleation is altered in presence of PCEs and this modifies the microstructure at contact points, leading to different characteristics of yield stress growth.

Different authors have reported that PCEs enhance homogeneous rather than heterogeneous nucleation of C-S-H, with probably the most direct evidence coming from Artioli et al. [312]. More recently, Valentini et al. [309] fitted hydration kinetics of C_3S pastes to a nucleation and growth model, from which they extracted numbers of nuclei formed homogeneously and heterogeneously. The model neglects the possibility of PCEs to inhibit dissolution, something shown experimentally to take place [15]. The results of the model of Artioli et al. [312] may therefore reflect an

indirect impact of PCEs on nucleation. With these limitations in mind, we discuss their results further.

In absence of PCEs, about 10^5 times more nuclei are claimed to be formed heterogeneously [309]. This confirms claims by other authors on the role of heterogeneous nucleation in absence of PCEs [309,312–314]. Also, when PCEs are included in delayed addition, no change in nucleation is observed. However, when directly added, PCEs completely change this balance. The total number of nuclei per unit volume remains similar, but this time there are about 10 times more nuclei formed homogenously than heterogeneously [309].

With respect to our experiments, this indicates that hydration with directly added PCEs cannot be easily compared to hydration in their absence. More specifically, using a PCE concentration dependence to extrapolate a behaviour in absence of PCEs cannot truly represent a cement without PCE. This probably explains why it is not possible to rationalise the behaviour of cement pastes without admixture based on the behaviour of pastes with PCEs (see section 5.6).

Concerning the effect of admixture type and dosage in direct addition, the limited data reported by Valentini et al. [309] show that the number of nuclei formed homogenously remains roughly constant. In contrast, they find large differences in those formed heterogeneously. Additional findings about this would be of high interest for the present work.

The question is how to rationalise the dependence on polymer type and dosage. In the work of Valentini et al. [309], there were no clear trends about how these factors affect nucleation balance. As mentioned before, these values are extracted from a model and subject to the quality of its underlying hypothesis. However, they do underline the change from heterogeneous to homogeneous nucleation in presence of PCEs.

Getting back to our master curve, we can state that for a given change in specific surface, the yield stress increases less with a high dosage and a high grafting degree (low N). Relating this to nucleation, an increased dosage should favour homogeneous nucleation. Those hydrates will not be at contact points between

grains and are therefore not expected to play a role in the increase of the yield stress. A polymer with a high grafting degree (low N) has a lower affinity for the surface. Therefore, a greater part of such polymer should remain in solution rather than adsorb on cement grains. We expect that this will also lead to an enhancement of homogeneous nucleation and would consequently attenuate the increase of yield stress. From a qualitative point of view, these expectations appear realistic. They account for our master curve, but call for some quantification going beyond the data fitting in the study by Valentini et al.

It should be noted that a limitation in the approach proposed by Valentini et al. [309] is that polymers added in delayed mode do not alter the nucleation balance. Therefore, the above argument would suggest that yield stress growth in those cases would not depend on the polymer type or dosage. This is quite unlikely, but is something that deserves to be confirmed experimentally in future research.

6.5 Conclusions

We quantitatively demonstrated that the yield stress growth cannot be accounted by the individual changes in either volume fraction, particle size or surface coverage. However, the combination of these surface factors provides good agreement with the experimental results. We observed that the surface coverage becomes more relevant than the particle size and volume faction as the polymer dosage is increased. At lower PCEs dosages, the particle size effect plays the dominant role. Also, we identified a substantial difference between plain and admixed systems that accounts for the inaccurate prediction of the flow loss evolution from the master curve in absence of PCEs. This could be explained by the shift from heterogeneous nucleation of C-S-H in absence of PCEs to homogeneous nucleation in their presence.

The effect of particle size was introduced through the empirical observation made in rheology of ceramic suspensions that the yield stress scales with the inverse square of the surface average particle size [124]. The analysis proposed is therefore very rough and would overlook details of particle size distribution. It also does not

include any changes in curvature at contact points. Other analysis may be undertaken in the future to refine this prediction and back it up with more solid microstructural arguments.

The other essential part of this result was that data can only be fitted considering that yield stress evolves as an exponential function of the amount of polymer adsorbed, provided that the latter is expressed with respect to the cement surface at each time considered. The exponential function was obtained by the shifting factor experiments carried out at early age. The entire approach proposed in that case is completely new and seems to provide a reliable description of interparticle forces evolution during hydration in presence of PCEs. Another essential element is a proper assessment of the amount of adsorbed polymer. If that amount is determined experimentally, predictions are generally quite good. Otherwise, by using an adsorption isotherm it is possible to get a relatively decent estimation of yield stress changes. Here again, the importance of having quality experimental data is underlined.

For both contributions of particle size and surface coverage, the measurement of specific surface has turned out to be crucial. This valorises more than anything else the very important efforts that were put into developing reliable experimental protocols to determine this parameter.

It is only thanks to the combination of all the above points that it has been possible to rationalize the yield stress evolution.

Chapter 7
Conclusion and outlook

7.1 Achieved results

The present work aimed to define the parameters governing flow loss in presence of PCEs. The development of reliable analytical methods was needed to study fresh cement pastes in terms of specific surface and aqueous phase composition.

Firstly, it was quantitatively demonstrated how harsh sample preparations could compromise final SSA$_{BET}$ results. Gypsum is very sensitive to temperature and it is the limiting factor to consider for the choice of the operative conditions. Hence, we found that a mild degassing at 40 °C under nitrogen flow for 16 hours preserves the structure of both gypsum and ettringite. Additionally, we found that a significant change in SSA$_{BET}$ of AFt is observed when more than 12 molecules of water are lost from its structure, at temperature higher than 50 °C under nitrogen flow. Thus, contrary to what had been reported up to now in the literature, gypsum is the most sensitive compound in fresh pastes and the drying conditions must be optimized taking this into account. Another important experimental issue is how the stop hydration, which literature reports to be problematic with solvents because of their possible substitution or dehydration of hydrates. In this thesis, it was shown that this problem can be overcome by using by using cold isopropanol used to stop the hydration, coupled to a specially developed fast filtration methodology. By using this procedure, it possible to retain the crystallinity of ettringite, thus enabling quantitative phase analysis. The absence of adequate sample preparation protocols up to now means that there are barely any reliable data in the literature concerning

the specific surface of cement pastes at early ages. Therefore, up to now, it was simply not possible to critically examine the causes of flow loss in superplasticized pastes.

The elemental characterization of cement pore solutions is of paramount importance for the study of complex coupling of dissolution and precipitation reactions in presence of PCEs. An easy and robust ICP-OES method for characterizing cement pore solutions was developed considering the quantification of eight elements of major interest. For the first time, we obtained robust values of aluminium and magnesium concentrations in the order of nmol/L-µmol/L, despite of the complexity of the matrix. We also identified that PCEs promote the formation of nanoparticles that might be at the origin of the increased amount of the low-concentration elements in solution.

Thanks to these solid analytical bases, we could systematically investigate the effect of five polymers on flow loss. We quantitatively established a strong correlation between yield stress evolution and hydration kinetics expressed as heat rate after the onset. This time during hydration marks the clear transition from the induction to the acceleration period after which the yield stress grows exponentially. We proved that the onset is not caused by the precipitation of portlandite. More interestingly, two distinct processes are involved before and after the onset and for the first time we could examine them individually. In this way, we quantitatively demonstrated that, during the induction period, the linear evolution of the yield stress is independent of hydration reactions and, therefore, we refer to it as thixotropy. In contrast, after the onset, the exponential increase of the yield stress is proportional to the heat rate, describing an irreversible structural build-up.

7.2 Influence of PCEs on flow loss

For the first time, we establish a master curve showing how the rate of flow loss depends on the molecular structure and dosage of PCEs. Very interestingly, we proved that flow loss is related to the heat rate. Because calorimetry is a very

straight forward method, this could be done for all samples and was clearly established in all cases. For the large, but more limited number of cases in which specific surface was measured, we also found a direct relation of flow loss and specific surface. The key question is therefore whether the flow loss is more directly linked to changes in heat rate or specific surface. Because yield stress originates from interparticle contacts, it is our expectations that the true origin of flow loss lies in the formation of additional specific surface. In support of this, our results also show that, after the onset, hydration rate and specific surface changes are proportional one to the other. This is something expected in an initial stage of nucleation and growth. It is therefore normal that yield stress could be expressed as a function of either changes in heat rate or changes in specific surface, although the mechanistic relation would rather involve specific surface.

Yield stress can be defined by a product between a function of volume fraction and an average interparticle force [126]. In the specific case of superplasticized cementitious systems, we include also the contribution of the surface coverage. Based on this, we systematically analysed the contribution of these factors to assess whether they also affect the yield stress increase after the onset.

We reported that none of these surface factors accounts alone for the experimental results obtained. However, their combination provides a good correlation to experimental results. An important element here is to use an appropriate expression for the dependence of yield stress on surface coverage. This was only possible thanks to the novel experimental approach we devised to overcome the hurdles that are normally encountered when trying to do this with cement pastes. The approach in question involves the so-called shifting factor experiments and leads to an exponential dependence of yield stress on the amount of adsorbed polymer per unit surface of cement. Results showed that yield stress changes as a combination of a change in particle size and surface coverage, with both factors having a relative importance that changes with polymer dosage. At lower PCEs dosages, the particle size effect plays the dominant role. Based on this, we could account for the

exponential growth of the yield stress in function of the amount of adsorbed polymer.

Importantly, our analysis of flow loss focused on relating the change in yield stress to the change in other properties of cement paste, in particular specific surface and adsorption. We did not however deal with the question of how polymers modify the hydration kinetics in the flow loss. This would have represented a higher order problem and would probably have made it impossible to reach any tangible results, just as any other study on this subject. The question of how hydration kinetics are modified by PCEs is however an important issue and research on that question would deliver kinetic laws that could be coupled to our results to provide a kinetic prediction of flow loss.

We also identified a substantial difference between plain cement pastes and ones containing PCEs. Specifically, extrapolating the behaviour of admixed systems to zero dosage lead to predictions that do not match at all the behaviour of pastes prepared in absence of PCEs. This could be explained by the shift from heterogeneous nucleation of C-S-H in absence of PCEs to homogeneous nucleation in their presence.

7.3 Future developments

The present work presented how PCEs can influence the yield stress evolution when they are included in the mixing water (direct addition). This procedure is known to facilitate the strong interaction of PCEs with the aluminate hydrates forming immediately after contact with water, with a consequent reduction of polymer in solution needed for the dispersion.

It was recently demonstrated that the delayed addition of PCEs not only limits the loss of polymer in the first minutes of hydration, but also can affect the overall mechanism of hydration at later time [15,16]. Indeed, from some preliminary experiments (not reported in the manuscript), we found that the measured SSA_{BET} is greater when the delayed addition is adopted. As reported in Appendix I, after

direct PCE addition, the amount of low-concentration elements increases significantly, contrasting with solutions from pastes in which the PCE addition was delayed and for which concentrations were much lower. From isothermal calorimetry tests, we observed that the hydration reaction is accelerated compared to the paste prepared adding the PCE directly. These results led us to infer that both the macroscopic properties and their respective relations evolve differently with direct or delayed PCE addition. This translates into the impossibility of extrapolating flow loss data in presence of PCEs to infer the flow loss in their absence.

We showed that PCEs alter the dissolution and nucleation mechanisms in relation to both polymer architecture and dosage. The significant increase of the amount of low-concentration elements, mainly Al and Mg, is the main expression of this change at the beginning of the hydration. However, we observed that their concentration tends to decrease exponentially over time. In the first instance, we hypothesized that this might be due to the precipitation of the hydrates on the cement grains resulting in a reduced concentration in solution. In preliminary tests presented in Appendix I, we showed that the concentration decay is influenced by the polymer dosage and we support the idea that the polymeric molecular structure could also play a significant role.

The evolution of the elemental composition of superplasticized pore solution and its correlation to the yield stress change still deserves a deeper investigation. Indeed, if the rate of hydrates precipitation was linked to the yield stress growth, then the surface profile would also change affecting the cohesion interaction among hydrating participles. This stresses the importance of a detailed characterization of the forming superplasticized nanoparticles, whose size and chemical composition can modify the surface roughness. The complexity in characterizing hydrating cementitious systems at nanoscale level renders this future study very challenging. For this purpose, cryo-ESEM analysis seems to be promising to investigate the evolution of the surface morphology in hydrating cementitious systems [84,315,316].

Also, the analysis proposed to explain particle size changes in Chapter 6 overlooks details of particle size distribution and it does not include any changes in curvature at contact points. The application of a less empirical model, such as YoDEL, would mean that the effect of changes in particle size could be dealt with on a more fundamental basis.

Pore solution changes and microstructure evolution would represent important elements to include when addressing the kinetics of cement hydration. As explained above, this problem can in principle be decoupled from the question of flow loss which simplifies the question. Progress is needed in predicting how hydration kinetics are affected by PCEs in the acceleration period in order to reach a quantitative prediction of flow loss kinetics.

7.4 Outlooks

In this thesis, we obtained very important results showing that the onset time increases linearly with the added charges at a given w/c ratio. The onset time has a special significance in practice marking the duration of the open time, but it is also paradoxically difficult to determine reliably with simple tests. In order to have a larger applicability, this parameter obtained from a fundamental analysis would need to be converted to an outcome from pragmatic tests. Setting time measured by Vicat test [317] and force measurements by penetrometers [318] are generally carried out to verify the change in consistency of cementitious systems. Besides, Ultrasonic Pulse Velocity (UPV) [319,320] and Electrical Resistivity [321] tests are proposed to estimate the setting time in concrete. However, it is well known that these empirical tests are not always able to capture even major differences occurring in hydrating systems when they are conducted out of the range of standard procedures, mainly in presence of PCEs [14]. Also, it worth noting that the time at the onset might correspond – or not – to the setting time measured as proposed above.

The fundamental knowledge proposed in the present research might provide the right connection to the practice. This would pave the way for developing a model by which the correct onset time can be predicted by varying more than one parameter. In this way, initial dispersion and open time might be tuned by varying the polymer parameters – dosage, grafting degree, side chain length – and w/c ratios. This would possibly allow controlling the properties of concretes designed for different applications.

The subject that would most directly benefit from this involved digital fabrication with concrete, for which the initial increase in yield stress governs the success or failure of shaping [310,311]. In this context, it would be worth expanding the scope of this thesis to other admixtures, in particular combinations of retarders and accelerators that are used in digital fabrication.

A major objective for the future on the topic of flow loss is to couple the results of this thesis with hydration kinetics and how these are affected by PCEs. Although we demonstrated that the onset time increases with the added charges, it is however unclear how broadly valid this result is. For example, it shows a certain contrast with the study by Marchon et al. [15]. A possible reason is that this thesis used copolymerized PCEs, while Marchon et al. used grafted ones. It would be therefore important to examine whether this has an effect, but also to determine the role of changes in cement composition, in particular alkali and aluminates.

In addition, we proposed a master curve that relates the increase of yield stress to the increase of surface area. This relation is dependent on the molecular structure and dosage of PCEs through the factor c/N. However, a physical insight for this factor could not yet be given.

The above points highlight the importance to understand in detail the chemical reactions involved during cement hydration in presence of PCEs, to better predict the kinetics of flow loss in the acceleration period. This is a very complex subject that will require a lot of work. Methods developed in this thesis, in particular reliable measurements of the pore solution can be used in this endeavour.

In our experiments, we focused our attention on flow measurements after at least 30 minutes from the beginning of the hydration. During this timeframe, we could not observe major changes in the system's properties for the studied PCE dosages. Nevertheless, we cannot exclude that, at lower dosages, flow loss might occur earlier. Also, we often evidenced refluidication of the pastes at early stages, something that has been explained only in qualitative way. Such effects underline the importance of also investigating the hydration reactions during and shortly after mixing (up to 30 minutes), when the interaction between ettringite and PCEs can significantly impact the initial dispersion of cement grains. This requires a detailed study the effect of PCEs on the nucleation of hydrates as well as on the dissolution of anhydrous phase. For this, the characterization methods developed in this thesis, ICP and SSA in particular, could be very valuable. In addition to experimental approaches, the use of molecular modelling would provide very useful information in understanding how different organic compounds interact with the surface of the different phases present in cement paste. Recent developments on this front suggest that reliable chemical insight into these questions is now becoming available.

REFERENCES

[1]   S. Mantellato, R.J. Flatt, 15 – Formulation of commercial products, in: P.-C. Aitcin, R.J. Flatt (Eds.), Sci. Technol. Concr. Admix., Woodhead Publishing (2016) 219–256.

[2]   G. Gelardi, S. Mantellato, D. Marchon, M. Palacios, A.B. Eberhardt, R.J. Flatt, 9 – Chemistry of chemical admixtures, in: P.-C. Aïtcin, R.J. Flatt (Eds.), Sci. Technol. Concr. Admix., Woodhead Publishing (2016) 149–218.

[3]   H. Uchikawa, S. Hanehara, D. Sawaki, The role of steric repulsive force in the dispersion of cement particles in fresh paste prepared with organic admixture, Cem. Concr. Res. 27 (1997) 37–50. doi:10.1016/S0008-8846(96)00207-4.

[4]   Q. Ran, P. Somasundaran, C. Miao, J. Liu, S. Wu, J. Shen, Effect of the length of the side chains of comb-like copolymer dispersants on dispersion and rheological properties of concentrated cement suspensions, J. Colloid Interface Sci. 336 (2009) 624–633. doi:10.1016/j.jcis.2009.04.057.

[5]   R.J. Flatt, Y.F. Houst, A simplified view on chemical effects perturbing the action of superplasticizers, Cem. Concr. Res. 31 (2001) 1169–1176. doi:10.1016/S0008-8846(01)00534-8.

[6]   C. Giraudeau, J.-B. D'Espinose De Lacaillerie, Z. Souguir, A. Nonat, R.J. Flatt, Surface and Intercalation Chemistry of Polycarboxylate Copolymers in Cementitious Systems, J. Am. Ceram. Soc. 92 (2009) 2471–2488. doi:10.1111/j.1551-2916.2009.03413.x.

[7]   D. Marchon, U. Sulser, A. Eberhardt, R.J. Flatt, Molecular design of comb-shaped polycarboxylate dispersants for environmentally friendly concrete, Soft Matter. 9 (2013) 10719–10728. doi:10.1039/C3SM51030A.

[8]   R.J. Flatt, Towards a prediction of superplasticized concrete rheology, Mater. Struct. 37 (2004) 289–300. doi:10.1007/BF02481674.

[9]   F. Dalas, S. Pourchet, D. Rinaldi, A. Nonat, S. Sabio, M. Mosquet, Modification of the rate of formation and surface area of ettringite by polycarboxylate ether superplasticizers during early C_3A–$CaSO_4$ hydration, Cem. Concr. Res. 69 (2015) 105–113. doi:10.1016/j.cemconres.2014.12.007.

[10]   D. Marchon, S. Mantellato, A. Eberhardt, R.J. Flatt, 10 – Adsorption of chemical admixtures, in: P.-C. Aitcin, R.J. Flatt (Eds.), Sci. Technol. Concr. Admix., Woodhead Publishing, 2016, 219–256.

[11]   I. Schober, R.J. Flatt, Optimizing Polycaboxylate Polymers, in: Proc. 8th CANMETACI Int. Conf. Superplast. Chem. Admix. Concr. Sorrento (2006). ACI SP-239, 169-184.

[12]   K. Yamada, T. Takahashi, S. Hanehara, M. Matsuhisa, Effects of the chemical structure on the properties of polycarboxylate-type superplasticizer, Cem. Concr. Res. 30 (2000) 197–207. doi:10.1016/S0008-8846(99)00230-6.

[13]   T.M. Vickers Jr., S.A. Farrington, J.R. Bury, L.E. Brower, Influence of dispersant structure and mixing speed on concrete slump retention, Cem. Concr. Res. 35 (2005) 1882–1890. doi:10.1016/j.cemconres.2005.04.013.

[14]   P.-C. Nkinamubanzi, S. Mantellato, R.J. Flatt, 16 – Superplasticizers in practice, in: P.-C. Aïtcin, R.J. Flatt (Eds.), Sci. Technol. Concr. Admix., Woodhead Publishing, 2016, 353–377.

[15]   D. Marchon, Controlling cement hydration though the molecular structure of comb copolymer superplasticizers, Doctoral dissertation, ETH, 2016.

[16]   D. Marchon, P. Juilland, E. Gallucci, L. Frunz, R.J. Flatt, Molecular and submolecular scale effects of comb-copolymers on tri-calcium silicate reactivity: Toward molecular design, J. Am. Ceram. Soc. 100 (2017) 817-841. doi:10.1111/jace.14695.

[17]   A. Yahia, S. Mantellato, R.J. Flatt, 7 – Concrete rheology: A basis for understanding chemical admixtures, in: P.-C. Aïtcin, R.J. Flatt (Eds.), Sci. Technol. Concr. Admix., Woodhead Publishing, (2016) 97–127.

[18]   S. Mantellato, M. Palacios, R.J. Flatt, Reliable specific surface area measurements of fresh cement pastes, in: Monographie Bd. 45, (2012) 29–34 Dübendorf (Switzerland).

[19]   S. Mantellato, M. Palacios, R.J. Flatt, Reliable specific surface area measurements on anhydrous cements, Cem. Concr. Res. 67 (2015) 286–291. doi:10.1016/j.cemconres.2014.10.009.

[20]   S. Mantellato, M. Palacios, R.J. Flatt, Impact of sample preparation on the specific surface area of synthetic ettringite, Cem. Concr. Res. 86 (2016) 20–28. doi:10.1016/j.cemconres.2016.04.005.

[21]   F. Caruso, S. Mantellato, M. Palacios, R.J. Flatt, ICP-OES method for the characterization of cement pore solutions and their modification by polycarboxylate-based superplasticizers, Cem. Concr. Res. 91 (2017) 52–60. doi:10.1016/j.cemconres.2016.10.007.

[22]   F. Caruso, S. Mantellato, M. Palacios, R.J. Flatt, A Powerful Tool to Better Understand Cement Hydration, Chim. – Highlights Anal. Sci. Switz. – Div. Anal. Sci. 71 (2017).

[23]   H F W Taylor, Cement Chemistry, Thomas Telford Ltd, 1997.

[24]   N. Tenoutasse, The hydration mechanism of C_3A and C_3S in the presence of calcium chloride and calcium sulfate, in: Proc. 5th Int. Symp. Chem. Cem., Tokyo (Japan) (1968) 372–378.

[25]   P. Meredith, A.M. Donald, N. Meller, C. Hall, Tricalcium aluminate hydration: Microstructural observations by in-situ electron microscopy, J. Mater. Sci. 39 (2004) 997–1005. doi:10.1023/B:JMSC.0000012933.74548.36.

[26]   H. Minard, S. Garrault, L. Regnaud, A. Nonat, Mechanisms and parameters controlling the tricalcium aluminate reactivity in the presence of gypsum, Cem. Concr. Res. 37 (2007) 1418–1426. doi:10.1016/j.cemconres.2007.06.001.

[27]   A. Quennoz, K.L. Scrivener, Hydration of C_3A–gypsum systems, Cem. Concr. Res. 42 (2012) 1032–1041. doi:10.1016/j.cemconres.2012.04.005.

[28]   K.L. Scrivener, P.L. Pratt, Microstructural studies of the hydration of C_3A and C_4AF independently and in cement paste, in: Proc Br Ceram Soc. (1984) 207.

[29]   A. Quennoz, Hydration of C_3A with Calcium Sulfate Alone and in the Presence of Calcium Silicate, Doctoral thesis, EPFL (2011).

[30]   S. Pourchet, L. Regnaud, J.P. Perez, A. Nonat, Early C_3A hydration in the presence of different kinds of calcium sulfate, Cem. Concr. Res. 39 (2009) 989–996. doi:10.1016/j.cemconres.2009.07.019.

[31]   E.M. Gartner, J.F. Young, D. Damidot, Jawed, Chapter 3: Hydration of Portland Cement, in: Struct. Perform. Cem., J. Bensted, P. Barnes, CRC Press (2001) 57–113.

[32]   K.L. Scrivener, P. Juilland, P.J.M. Monteiro, Advances in understanding hydration of Portland cement, Cem. Concr. Res. 78, Part A (2015) 38–56. doi:10.1016/j.cemconres.2015.05.025.

[33]   E.M. Gartner, H.M. Jennings, Thermodynamics of Calcium Silicate Hydrates and Their Solutions, J. Am. Ceram. Soc. 70 (1987) 743–749. doi:10.1111/j.1151-2916.1987.tb04874.x.

[34]   H.N. Stein, J.M. Stevels, Influence of silica on the hydration of $3CaO,SiO_2$, J. Appl. Chem. 14 (1964) 338–346. doi:10.1002/jctb.5010140805.

[35]   D.D. Double, N.L. Thomas, D.A. Jameson, The hydration of Portland cement. Evidence for an osmotic mechanism, in: Proc. 7th Int. Symp. Chem. Cem., Paris (1980) 256–260.

[36]   F. Bellmann, D. Damidot, B. Möser, J. Skibsted, Improved evidence for the existence of an intermediate phase during hydration of tricalcium silicate, Cem. Concr. Res. 40 (2010) 875–884. doi:10.1016/j.cemconres.2010.02.007.

[37]   F. Bellmann, T. Sowoidnich, H.-M. Ludwig, D. Damidot, Analysis of the surface of tricalcium silicate during the induction period by X-ray photoelectron spectroscopy, Cem. Concr. Res. 42 (2012) 1189–1198. doi:10.1016/j.cemconres.2012.05.011.

[38]   P. Juilland, E. Gallucci, R. Flatt, K. Scrivener, Dissolution theory applied to the induction period in alite hydration, Cem. Concr. Res. 40 (2010) 831–844. doi:10.1016/j.cemconres.2010.01.012.

[39]   L. Nicoleau, A. Nonat, D. Perrey, The di- and tricalcium silicate dissolutions, Cem. Concr. Res. 47 (2013) 14–30. doi:10.1016/j.cemconres.2013.01.017.

[40]   J.W. Bullard, G.W. Scherer, J.J. Thomas, Time dependent driving forces and the kinetics of tricalcium silicate hydration, Cem. Concr. Res. 74 (2015) 26–34. doi:10.1016/j.cemconres.2015.03.016.

[41]   P. Juilland, E. Gallucci, Morpho-topological investigation of the mechanisms and kinetic regimes of alite dissolution, Cem. Concr. Res. 76 (2015) 180–191. doi:10.1016/j.cemconres.2015.06.001.

[42]   E. Pustovgar, R.P. Sangodkar, A.S. Andreev, M. Palacios, B.F. Chmelka, R.J. Flatt, J.-B. d'Espinose de Lacaillerie, Understanding silicate hydration from quantitative analyses of hydrating tricalcium silicates, Nat. Commun. 7 (2016) 10952. doi:10.1038/ncomms10952.

[43] S. Garrault, E. Finot, E. Lesniewska, A. Nonat, Study of C-S-H growth on C$_3$S surface during its early hydration, Mater. Struct. 38 (2005) 435–442. doi:10.1007/BF02482139.

[44] S. Garrault, T. Behr, A. Nonat, Formation of the C–S–H Layer during Early Hydration of Tricalcium Silicate Grains with Different Sizes, J. Phys. Chem. B. 110 (2006) 270–275. doi:10.1021/jp0547212.

[45] S. Garrault, A. Nonat, Hydrated Layer Formation on Tricalcium and Dicalcium Silicate Surfaces: Experimental Study and Numerical Simulations, Langmuir. 17 (2001) 8131–8138. doi:10.1021/la011201z.

[46] J.J. Thomas, H.M. Jennings, J.J. Chen, Influence of Nucleation Seeding on the Hydration Mechanisms of Tricalcium Silicate and Cement, J. Phys. Chem. C. 113 (2009) 4327–4334. doi:10.1021/jp809811w.

[47] A. Kumar, S. Bishnoi, K.L. Scrivener, Modelling early age hydration kinetics of alite, Cem. Concr. Res. 42 (2012) 903–918. doi:10.1016/j.cemconres.2012.03.003.

[48] J.F. Young, H.S. Tong, R.L. Berger, Compositions of Solutions in Contact with Hydrating Tricalcium Silicate Pastes, J. Am. Ceram. Soc. 60 (1977) 193–198. doi:10.1111/j.1151-2916.1977.tb14104.x.

[49] J.W. Bullard, R.J. Flatt, New Insights Into the Effect of Calcium Hydroxide Precipitation on the Kinetics of Tricalcium Silicate Hydration, J. Am. Ceram. Soc. 93 (2010) 1894–1903. doi:10.1111/j.1551-2916.2010.03656.x.

[50] L. Nicoleau, A. Nonat, A new view on the kinetics of tricalcium silicate hydration, Cem. Concr. Res. 86 (2016) 1–11. doi:10.1016/j.cemconres.2016.04.009.

[51] H.M. Jennings, A model for the microstructure of calcium silicate hydrate in cement paste, Cem. Concr. Res. 30 (2000) 101–116. doi:10.1016/S0008-8846(99)00209-4.

[52] A.J. Allen, R.C. Oberthur, D. Pearson, P. Schofield, C.R. Wilding, Development of the fine porosity and gel structure of hydrating cement systems, Philos. Mag. Part B. 56 (1987) 263–288. doi:10.1080/13642818708221317.

[53] A.J. Allen, J.J. Thomas, H.M. Jennings, Composition and density of nanoscale calcium–silicate–hydrate in cement, Nat. Mater. 6 (2007) 311–316. doi:10.1038/nmat1871.

[54] H.M. Jennings, J.W. Bullard, J.J. Thomas, J.E. Andrade, J.J. Chen, G.W. Scherer, Characterization and Modeling of Pores and Surfaces in Cement Paste, J. Adv. Concr. Technol. 6 (2008) 5–29. doi:10.3151/jact.6.5.

[55] E.M. Gartner, A proposed mechanism for the growth of C–S–H during the hydration of tricalcium silicate, Cem. Concr. Res. 27 (1997) 665–672. doi:10.1016/S0008-8846(97)00049-5.

[56] E.M. Gartner, K.E. Kurtis, P.J.M. Monteiro, Proposed mechanism of C-S-H growth tested by soft X-ray microscopy, Cem. Concr. Res. 30 (2000) 817–822. doi:10.1016/S0008-8846(00)00235-0.

[57] A. Bazzoni, Study of early hydration mechanisms of cement by means of electron microscopy, EPFL (2014).

[58] S. Bishnoi, K.L. Scrivener, Studying nucleation and growth kinetics of alite hydration using μic, Cem. Concr. Res. 39 (2009) 849–860. doi:10.1016/j.cemconres.2009.07.004.

[59] D.M. Kirby, J.J. Biernacki, The effect of water-to-cement ratio on the hydration kinetics of tricalcium silicate cements: Testing the two-step hydration hypothesis, Cem. Concr. Res. 42 (2012) 1147–1156. doi:10.1016/j.cemconres.2012.05.009.

[60] F. Begarin, S. Garrault, A. Nonat, L. Nicoleau, Hydration of alite containing aluminium, Adv. Appl. Ceram. 110 (2011) 127–130. doi:10.1179/1743676110Y.0000000007.

[61] P. Suraneni, R.J. Flatt, Use of micro-reactors to obtain new insights into the factors influencing tricalcium silicate dissolution, Cem. Concr. Res. 78, Part B (2015) 208–215. doi:10.1016/j.cemconres.2015.07.011.

[62] E. Pustovgar, R.K. Mishra, M. Palacios, J.-B. D'Espinose De Lacaillerie, T. Matschei, A.S. Andreev, H. Heinz, R. Verel, R.J. Flatt, Influence of aluminates on the hydration kinetics of tricalcium silicate, Cem. Concr. Res. 100 (2017) 245-262.

[63] A. Quennoz, K.L. Scrivener, Interactions between alite and C$_3$A-gypsum hydrations in model cements, Cem. Concr. Res. 44 (2013) 46–54. doi:10.1016/j.cemconres.2012.10.018.

[64] L. Nicoleau, E. Schreiner, A. Nonat, Ion-specific effects influencing the dissolution of tricalcium silicate, Cem. Concr. Res. 59 (2014) 118–138. doi:10.1016/j.cemconres.2014.02.006.

[65]   R.J. Flatt, I. Schober, E. Raphael, C. Plassard, E. Lesniewska, Conformation of Adsorbed Comb Copolymer Dispersants, Langmuir. 25 (2009) 845–855. doi:10.1021/la801410e.

[66]   T. Nawa, H. Ichiboji, M. Kinoshita, Influence of Temperature on Fluidity of Cement Paste Containing Superplasticizer with Polyethylene Oxide Graft Chains, Spec. Publ. 195 (2000) 181–194.

[67]   D. Rinaldi, T. Hamaide, C. Graillat, F. D'Agosto, R. Spitz, S. Georges, M. Mosquet, P. Maitrasse, RAFT copolymerization of methacrylic acid and poly(ethylene glycol) methyl ether methacrylate in the presence of a hydrophobic chain transfer agent in organic solution and in water, J. Polym. Sci. Part Polym. Chem. 47 (2009) 3045–3055. doi:10.1002/pola.23374.

[68]   .Gelardi, N. Sanson, G. Nagy, R.J. Flatt, Characterization of Comb-Shaped Copolymers by Multidetection SEC, DLS and SANS, Polymers. 9 (2017) 61. doi:10.3390/polym9020061.

[69]   F. Winnefeld, S. Becker, J. Pakusch, T. Götz, Effects of the molecular architecture of comb-shaped superplasticizers on their performance in cementitious systems, Cem. Concr. Compos. 29 (2007) 251–262. doi:10.1016/j.cemconcomp.2006.12.006.

[70]   A. Papo, L. Piani, Effect of various superplasticizers on the rheological properties of Portland cement pastes, Cem. Concr. Res. 34 (2004) 2097–2101. doi:10.1016/j.cemconres.2004.03.017.

[71]   X. Peng, C. Yi, X. Qiu, Y. Deng, Effect of Molecular Weight of Polycarboxylate-type Superplasticizer on the Rheological Properties of Cement Pastes, Polym. Polym. Compos. 20 (2012) 725–736.

[72]   G.H. Kirby, J.A. Lewis, Comb Polymer Architecture Effects on the Rheological Property Evolution of Concentrated Cement Suspensions, J. Am. Ceram. Soc. 87 (2004) 1643–1652. doi:10.1111/j.1551-2916.2004.01643.x.

[73]   C.-Z. Li, N.-Q. Feng, Y.-D. Li, R.-J. Chen, Effects of polyethlene oxide chains on the performance of polycarboxylate-type water-reducers, Cem. Concr. Res. 35 (2005) 867–873. doi:10.1016/j.cemconres.2004.04.031.

[74]   S. Hanehara, K. Yamada, Rheology and early age properties of cement systems, Cem. Concr. Res. 38 (2008) 175–195. doi:10.1016/j.cemconres.2007.09.006.

[75]   D. Platel, Impact of Polymer Architecture on Superplasticizer Efficiency, in: 9th ACI Int. Conf. Superplast. Chem. Admixtures American Concr. Inst., (2009).

[76]   K. Yamada, S. Ogawa, S. Hanehara, Controlling of the adsorption and dispersing force of polycarboxylate-type superplasticizer by sulfate ion concentration in aqueous phase, Cem. Concr. Res. 31 (2001) 375–383. doi:10.1016/S0008-8846(00)00503-2.

[77]   Y.F. Houst, P. Bowen, F. Perche, A. Kauppi, P. Borget, L. Galmiche, J.-F. Le Meins, F. Lafuma, R.J. Flatt, I. Schober, P.F.G. Banfill, D.S. Swift, B.O. Myrvold, B.G. Petersen, K. Reknes, Design and function of novel superplasticizers for more durable high performance concrete (superplast project), Cem. Concr. Res. 38 (2008) 1197–1209. doi:10.1016/j.cemconres.2008.04.007.

[78]   F. Perche, Y.F. Houst, P. Bowen, H. Hofmann, Adsorption of Lignosulfonates and Polycarboxylates – Depletion and Electroacoustic Methods, in: Proc. 7th CANMETACI Int. Conf. Superplast. Chem. Admix. Concr. VM Malhotra Berl. Ger. (2003) 1-15.

[79]   R.J. Flatt, Y.F. Houst, R. Oesch, P. Bowen, H. Hofmann, J. Widmer, U. Sulser, U. Mäder, T.A. Burge, Analysis of superplasticizers used in concrete, Analusis. 26 (1998) 28–34. doi:10.1051/analusis:199826020028.

[80]   P.G.D. Gennes, Scaling theory of polymer adsorption, J. Phys. 37 (1976) 1445–1452. doi:10.1051/jphys:0197600370120144500.

[81]   E. Bouchaud, M. Daoud, Polymer adsorption: concentration effects, J. Phys. 48 (1987) 1991–2000. doi:10.1051/jphys:0198700480110199100.

[82]   K. Yoshioka, E. Tazawa, K. Kawai, T. Enohata, Adsorption characteristics of superplasticizers on cement component minerals, Cem. Concr. Res. 32 (2002) 1507–1513. doi:10.1016/S0008-8846(02)00782-2.

[83]   J. Plank, C. Hirsch, Impact of zeta potential of early cement hydration phases on superplasticizer adsorption, Cem. Concr. Res. 37 (2007) 537–542. doi:10.1016/j.cemconres.2007.01.007.

[84]   A. Zingg, F. Winnefeld, L. Holzer, J. Pakusch, S. Becker, L. Gauckler, Adsorption of polyelectrolytes and its influence on the rheology, zeta potential, and microstructure of various cement and hydrate phases, J. Colloid Interface Sci. 323 (2008) 301–312. doi:10.1016/j.jcis.2008.04.052.

[85]   C. Gay, E. Raphaël, Comb-like polymers inside nanoscale pores, Adv. Colloid Interface Sci. 94 (2001) 229–236. doi:10.1016/S0001-8686(01)00062-8.

[86]   G. Gelardi, N. Sanson, G. Nagy, R.J. Flatt, Characterization of Comb-Shaped Copolymers by Multidetection SEC, DLS and SANS, Polymers. 9 (2017) 61. doi:10.3390/polym9020061.

[87]   M. Piotte, Charactérisation du poly(naphtalènesulfonate) – Influence de son concentration et de sa mass moléculaire sur son interaction avec le ciment, University of Sherbrooke (1993).

[88]   K. Reknes, J. Gustafsson, Effect of Modifications of Lignosulfonate on Adsorption on Cement and Fresh Concrete Properties, in: Proc. 6th CANMETACI Int. Conf. Superplast. Chem. Admix. Concr. Nice (2000) ACI SP-195, 127-141.

[89]   K. Reknes, B.G. Peterson, Novel lignosulfonate with superplasticizer performance, in: Proc. 7th CANMET/ACI Int. Conf. Superplast. Chem. Admix. Concr. Berl (2003). ACI Suppl. Pap. 285 – 299.

[90]   R. Magarotto, I. Torresan, N. Zeminian, Influence of the Molecular Weight of Polycarboxylate Ether Superplasticizers on the Rheological Properties of Fresh Cement Pastes, Mortar and Concrete, in: Proc. 11th Int. Congr. Chem. Cem. Durb. South Afr. Vol 2 11–16 May (2003) 514–26.

[91]   L. Regnaud, A. Nonat, S. Pourchet, B. Pellerin, P. Maitrasse, J.-P. Perez, S. Georges, Changes in Cement Paste and Mortar Fluidity after mixing induced by PCP: A parametric study, in: Proc. 8th CANMET/ACI Int. Conf. Superplast. Chem. Admix. Concr. Sorrento Oct. 20-23 (2006) 389–408.

[92]   R. Flatt, I. Schober, 7 – Superplasticizers and the rheology of concrete A2 – Roussel, Nicolas, in: Underst. Rheol. Concr., Woodhead Publishing (2012) 144–208.

[93]   J. Zimmermann, C. Hampel, C. Kurz, L. Frunz, R.J. Flatt, Effect of Polymer Structure on the Sulfate-Polycarboxylate Competition, in: 9th CANMET/ACI Int. Conf. Superplast. Chem. Admix. Concr Seville (2009) 165-176.

[94]   R.J. Flatt, Y.F. Houst, P. Bowen, H. Hofmann, J. Widmer, U. Sulser, U. Mäder, T.A. Bürge, Effect of Superplasticizers in Highly Alkaline Model Suspensions Containing Silica Fume, Proc 6th CANMET/ACI Intern Conf. Fly-Ash Silica Fume Slag Nat. Pozzolans Concr. 2 (1998) 911–930.

[95]   J. Plank, C. Winter, Competitive adsorption between superplasticizer and retarder molecules on mineral binder surface, Cem. Concr. Res. 38 (2008) 599–605. doi:10.1016/j.cemconres.2007.12.003.

[96]   J. Plank, H. Keller, P.R. Andres, Z. Dai, Novel organo-mineral phases obtained by intercalation of maleic anhydride–allyl ether copolymers into layered calcium aluminium hydrates, Inorganica Chim. Acta. 359 (2006) 4901–4908. doi:10.1016/j.ica.2006.08.038.

[97]   L. Lei, J. Plank, A study on the impact of different clay minerals on the dispersing force of conventional and modified vinyl ether based polycarboxylate superplasticizers, Cem. Concr. Res. 60 (2014) 1–10. doi:10.1016/j.cemconres.2014.02.009.

[98]   J.L. Suter, P.V. Coveney, Computer simulation study of the materials properties of intercalated and exfoliated poly(ethylene)glycol clay nanocomposites, Soft Matter. 5 (2009) 2239–2251. doi:10.1039/B822666K.

[99]   P.D. Svensson, S. Hansen, Intercalation of smectite with liquid ethylene glycol — Resolved in time and space by synchrotron X-ray diffraction, Appl. Clay Sci. 48 (2010) 358–367. doi:10.1016/j.clay.2010.01.006.

[100] S. Ng, J. Plank, Interaction mechanisms between Na montmorillonite clay and MPEG-based polycarboxylate superplasticizers, Cem. Concr. Res. 42 (2012) 847–854. doi:10.1016/j.cemconres.2012.03.005.

[101] K. Yamada, Basics of analytical methods used for the investigation of interaction mechanism between cements and superplasticizers, Cem. Concr. Res. 41 (2011) 793–798. doi:10.1016/j.cemconres.2011.03.007.

[102] W. Prince, M. Espagne, P.-C. Aïtcin, Ettringite formation: A crucial step in cement superplasticizer compatibility, Cem. Concr. Res. 33 (2003) 635–641. doi:10.1016/S0008-8846(02)01042-6.

[103] M.R. Meier, A. Rinkenburger, J. Plank, Impact of different types of polycarboxylate superplasticisers on spontaneous crystallisation of ettringite, Adv. Cem. Res. 28 (2016) 310–319. doi:10.1680/jadcr.15.00114.

[104] G.H. Tattersall, P.F.G. Banfill, The rheology of fresh concrete, Pitman Advanced Publishing Program (1983).

[105] H.A. Barnes, A handbook of elementary rheology, University of Wales, Institute of Non-Newtonian Fluid Mechanics (2000).

[106] H.A. Barnes, Thixotropy – a review, J. Non-Newton. Fluid Mech. 70 (1997) 1–33. doi:10.1016/S0377-0257(97)00004-9.

[107] N. Roussel, G. Ovarlez, S. Garrault, C. Brumaud, The origins of thixotropy of fresh cement pastes, Cem. Concr. Res. 42 (2012) 148–157. doi:10.1016/j.cemconres.2011.09.004.

[108] H.A. Barnes, K. Walters, The yield stress myth?, Rheol. Acta. 24 (1985) 323–326. doi:10.1007/BF01333960.

[109] A. Yahia, K.H. Khayat, Analytical models for estimating yield stress of high-performance pseudoplastic grout, Cem. Concr. Res. 31 (2001) 731–738. doi:10.1016/S0008-8846(01)00476-8.

[110] P. Moller, A. Fall, V. Chikkadi, D. Derks, D. Bonn, An attempt to categorize yield stress fluid behaviour, Philos. Trans. R. Soc. Math. Phys. Eng. Sci. 367 (2009) 5139–5155. doi:10.1098/rsta.2009.0194.

[111] R. Lapasin, A. Papo, S. Rajgelj, Flow behavior of fresh cement pastes. A comparison of different rheological instruments and techniques, Cem. Concr. Res. 13 (1983) 349–356. doi:10.1016/0008-8846(83)90034-0.

[112] M. Nehdi, M.-A. Rahman, Estimating rheological properties of cement pastes using various rheological models for different test geometry, gap and surface friction, Cem. Concr. Res. 34 (2004) 1993–2007. doi:10.1016/j.cemconres.2004.02.020.

[113] N. Roussel, Understanding the Rheology of Concrete, Elsevier, 2011.

[114] N. Roussel, Rheology of fresh concrete: from measurements to predictions of casting processes, Mater. Struct. 40 (2007) 1001–1012. doi:10.1617/s11527-007-9313-2.

[115] A.W. Saak, H.M. Jennings, S.P. Shah, A generalized approach for the determination of yield stress by slump and slump flow, Cem. Concr. Res. 34 (2004) 363–371. doi:10.1016/j.cemconres.2003.08.005.

[116] J. Murata, Flow and deformation of fresh concrete, Matér. Constr. 17 (1984) 117–129. doi:10.1007/BF02473663.

[117] N. Roussel, A thixotropy model for fresh fluid concretes: Theory, validation and applications, Cem. Concr. Res. 36 (2006) 1797–1806. doi:10.1016/j.cemconres.2006.05.025.

[118] A. Pierre, C. Lanos, P. Estellé, Extension of Spread-Slump Formulae for Yield Stress Evaluation, Appl. Rheol. 23 (2013) 63849.

[119] N. Roussel, Correlation between Yield Stress and Slump: Comparison between Numerical Simulations and Concrete Rheometers Results, Mater. Struct. 39 (2006) 501–509. doi:10.1617/s11527-005-9035-2.

[120] D.B. Genovese, J.E. Lozano, M.A. Rao, The rheology of colloidal and noncolloidal food dispersions, J. Food Sci. 72 (2007) R11-20. doi:10.1111/j.1750-3841.2006.00253.x.

[121] J.N. Israelachvili, Intermolecular and Surface Forces (Third Edition) (2011).

[122] R.J. Flatt, Interparticle forces and superplasticizers in cement suspensions, EPFL (1999).

[123] G. Gelardi, R.J. Flatt, 11 – Working mechanisms of water reducers and superplasticizers, in: P.-C. Aïtcin, R.J. Flatt (Eds.), Sci. Technol. Concr. Admix., Woodhead Publishing (2016) 257–278.

[124] Z. Zhou, M.J. Solomon, P.J. Scales, D.V. Boger, The yield stress of concentrated flocculated suspensions of size distributed particles, J. Rheol. 1978-Present. 43 (1999) 651–671. doi:10.1122/1.551029.

[125] Z. Zhou, P.J. Scales, D.V. Boger, Chemical and physical control of the rheology of concentrated metal oxide suspensions, Chem. Eng. Sci. 56 (2001) 2901–2920. doi:10.1016/S0009-2509(00)00473-5.

[126] R.J. Flatt, P. Bowen, Yodel: A Yield Stress Model for Suspensions, J. Am. Ceram. Soc. 89 (2006) 1244–1256. doi:10.1111/j.1551-2916.2005.00888.x.

[127] R.J. Flatt, P. Bowen, Yield Stress of Multimodal Powder Suspensions: An Extension of the YODEL (Yield Stress mODEL), J. Am. Ceram. Soc. 90 (2007) 1038–1044. doi:10.1111/j.1551-2916.2007.01595.x.

[128] A.M. Kjeldsen, R.J. Flatt, L. Bergström, Relating the molecular structure of comb-type superplasticizers to the compression rheology of MgO suspensions, Cem. Concr. Res. 36 (2006) 1231–1239. doi:10.1016/j.cemconres.2006.03.019.

[129] L. Bergström, C.H. Schilling, I.A. Aksay, Consolidation Behavior of Flocculated Alumina Suspensions, J. Am. Ceram. Soc. 75 (1992) 3305–3314. doi:10.1111/j.1151-2916.1992.tb04426.x.

[130] F. Winnefeld, S. Becker, J. Pakusch, T. Götz, Polymer structure/concrete property relations of HRWR, in: Proc. 8th CANMET/ACI Int. Conf. Superplast. Chem. Admix. Concr. Sorrento (2006) ACI Suppl. Pap. 159-177.

[131] R.L. Roy, N. Roussel, The marsh cone as a viscometer: Theoretical analysis and practical limits, Mater. Struct. 38 (2005) 25–30. doi:10.1007/BF02480571.

[132] N. Roussel, P. Coussot, "Fifty-cent rheometer" for yield stress measurements: From slump to spreading flow, J. Rheol. 1978-Present. 49 (2005) 705–718. doi:10.1122/1.1879041.

[133] L. Struble, G.-K. Sun, Viscosity of Portland cement paste as a function of concentration, Adv. Cem. Based Mater. 2 (1995) 62–69. doi:10.1016/1065-7355(95)90026-8.

[134] K. Asaga, D.M. Roy, Rheological properties of cement mixes: IV. Effects of superplasticizers on viscosity and yield stress, Cem. Concr. Res. 10 (1980) 287–295. doi:10.1016/0008-8846(80)90085-X.

[135] J. Björnström, S. Chandra, Effect of superplasticizers on the rheological properties of cements, Mater. Struct. 36 (2003) 685–692. doi:10.1007/BF02479503.

[136] J. Hot, H. Bessaies-Bey, C. Brumaud, M. Duc, C. Castella, N. Roussel, Adsorbing polymers and viscosity of cement pastes, Cem. Concr. Res. 63 (2014) 12–19. doi:10.1016/j.cemconres.2014.04.005.

[137] N. Roussel, H. Bessaies-Bey, Steady state flows of fresh cement pastes and concretes: simplified underlying physics, Adv. Appl. Ceram. 114 (2015) 402–405. doi:10.1179/1743676115Y.0000000024.

[138] N. Roussel, A. Lemaître, R.J. Flatt, P. Coussot, Steady state flow of cement suspensions: A micromechanical state of the art, Cem. Concr. Res. 40 (2010) 77–84. doi:10.1016/j.cemconres.2009.08.026.

[139] C.M. Neubauer, M. Yang, H.M. Jennings, Interparticle Potential and Sedimentation Behavior of Cement Suspensions: Effects of Admixtures, Adv. Cem. Based Mater. 8 (1998) 17–27. doi:10.1016/S1065-7355(98)00005-4.

[140] D. Feys, R. Verhoeven, G. De Schutter, Why is fresh self-compacting concrete shear thickening?, Cem. Concr. Res. 39 (2009) 510–523. doi:10.1016/j.cemconres.2009.03.004.

[141] F. Rosquoët, A. Alexis, A. Khelidj, A. Phelipot, Experimental study of cement grout: Rheological behavior and sedimentation, Cem. Concr. Res. 33 (2003) 713–722. doi:10.1016/S0008-8846(02)01036-0.

[142] D. Lootens, H. Van Damme, P. Hébraud, Giant Stress Fluctuations at the Jamming Transition, Phys. Rev. Lett. 90 (2003) 178301. doi:10.1103/PhysRevLett.90.178301.

[143] T.H. Phan, M. Chaouche, M. Moranville, Influence of organic admixtures on the rheological behaviour of cement pastes, Cem. Concr. Res. 36 (2006) 1807–1813. doi:10.1016/j.cemconres.2006.05.028.

[144] M. Cyr, C. Legrand, M. Mouret, Study of the shear thickening effect of superplasticizers on the rheological behaviour of cement pastes containing or not mineral additives, Cem. Concr. Res. 30 (2000) 1477–1483. doi:10.1016/S0008-8846(00)00330-6.

[145] N. Fernandez, From Tribology to Rheology: Impact of interparticle friction in the shear thickening of non-Brownian suspensions, ETH Zurich (2014).

[146] N. Fernandez, R. Mani, D. Rinaldi, D. Kadau, M. Mosquet, H. Lombois-Burger, J. Cayer-Barrioz, H.J. Herrmann, N.D. Spencer, L. Isa, Microscopic Mechanism for Shear Thickening of Non-Brownian Suspensions, Phys. Rev. Lett. 111 (2013) 108301. doi:10.1103/PhysRevLett.111.108301.

[147] R. Lapasin, V. Longo, S. Rajgelj, Thixotropic behaviour of cement pastes, Cem. Concr. Res. 9 (1979) 309–318. doi:10.1016/0008-8846(79)90123-6.

[148] K. Kovler, N. Roussel, Properties of fresh and hardened concrete, Cem. Concr. Res. 41 (2011) 775–792. doi:10.1016/j.cemconres.2011.03.009.

[149] S.P. Jiang, J.C. Mutin, A. Nonat, Studies on mechanism and physico-chemical parameters at the origin of the cement setting. I. The fundamental processes involved during the cement setting, Cem. Concr. Res. 25 (1995) 779–789. doi:10.1016/0008-8846(95)00068-N.

[150] S.P. Jiang, J.C. Mutin, A. Nonat, Studies on mechanism and physico-chemical parameters at the origin of the cement setting II. Physico-chemical parameters determining the coagulation process, Cem. Concr. Res. 26 (1996) 491–500. doi:10.1016/S0008-8846(96)85036-8.

[151] W.-G. Lei, L.J. Struble, Microstructure and Flow Behavior of Fresh Cement Paste, J. Am. Ceram. Soc. 80 (1997) 2021–2028. doi:10.1111/j.1151-2916.1997.tb03086.x.

[152] D. Lootens, P. Jousset, L. Martinie, N. Roussel, R.J. Flatt, Yield stress during setting of cement pastes from penetration tests, Cem. Concr. Res. 39 (2009) 401–408. doi:10.1016/j.cemconres.2009.01.012.

[153] K.V. Subramaniam, X. Wang, An investigation of microstructure evolution in cement paste through setting using ultrasonic and rheological measurements, Cem. Concr. Res. 40 (2010) 33–44. doi:10.1016/j.cemconres.2009.09.018.

[154] R.J. Flatt, D. Larosa, N. Roussel, Linking yield stress measurements: Spread test versus Viskomat, Cem. Concr. Res. 36 (2006) 99–109. doi:10.1016/j.cemconres.2005.08.001.

[155] T. Lecompte, A. Perrot, Non-linear modeling of yield stress increase due to SCC structural build-up at rest, Cem. Concr. Res. 92 (2017) 92–97. doi:10.1016/j.cemconres.2016.11.020.

[156] M. Bellotto, Cement paste prior to setting: A rheological approach, Cem. Concr. Res. 52 (2013) 161–168. doi:10.1016/j.cemconres.2013.07.002.

[157] J. Plank, Z. Dai, P.R. Andres, Preparation and characterization of new Ca–Al–polycarboxylate layered double hydroxides, Mater. Lett. 60 (2006) 3614–3617. doi:10.1016/j.matlet.2006.03.070.

[158] H. Uchikawa, D. Sawaki, S. Hanehara, Influence of kind and added timing of organic admixture on the composition, structure and property of fresh cement paste, Cem. Concr. Res. 25 (1995) 353–364. doi:10.1016/0008-8846(95)00021-6.

[159] I. Aiad, Influence of time addition of superplasticizers on the rheological properties of fresh cement pastes, Cem. Concr. Res. 33 (2003) 1229–1234. doi:10.1016/S0008-8846(03)00037-1.

[160] D. Han, R.D. Ferron, Influence of high mixing intensity on rheology, hydration, and microstructure of fresh state cement paste, Cem. Concr. Res. 84 (2016) 95–106. doi:10.1016/j.cemconres.2016.03.004.

[161] P. Juilland, A. Kumar, E. Gallucci, R.J. Flatt, K.L. Scrivener, Effect of mixing on the early hydration of alite and OPC systems, Cem. Concr. Res. 42 (2012) 1175–1188. doi:10.1016/j.cemconres.2011.06.011.

[162] N. Robeyst, G. De Schutter, C. Grosse, N. De Belie, Monitoring the effect of admixtures on early-age concrete behaviour by ultrasonic, calorimetric, strength and rheometer measurements, Mag. Concr. Res. 63 (2011) 707–721. doi:10.1680/macr.2011.63.10.707.

[163] F. Kreppelt, M. Weibel, D. Zampini, M. Romer, Influence of solution chemistry on the hydration of polished clinker surfaces – a study of different types of polycarboxylic acid-based admixtures, Cem. Concr. Res. 32 (2002) 187–198. doi:10.1016/S0008-8846(01)00654-8.

[164] A. Zingg, L. Holzer, A. Kaech, F. Winnefeld, J. Pakusch, S. Becker, L. Gauckler, The microstructure of dispersed and non-dispersed fresh cement pastes — New insight by cryo-microscopy, Cem. Concr. Res. 38 (2008) 522–529. doi:10.1016/j.cemconres.2007.11.007.

[165] C. Shi, G. Zhang, T. He, Y. Li, Effects of superplasticizers on the stability and morphology of ettringite, Constr. Build. Mater. 112 (2016) 261–266. doi:10.1016/j.conbuildmat.2016.02.198.

[166] V.T. Yilmaz, F.P. Glasser, Influence of sulphonated melamine formaldehyde superplasticizer on cement hydration and microstructure, Adv. Cem. Res. 2 (1989) 111–119. doi:10.1680/adcr.1989.2.7.111.

[167] W. Prince, M. Edwards-Lajnef, P.-C. Aïtcin, Interaction between ettringite and a polynaphthalene sulfonate superplasticizer in a cementitious paste, Cem. Concr. Res. 32 (2002) 79–85. doi:10.1016/S0008-8846(01)00632-9.

[168] S. Pourchet, C. Comparet, A. Nonat, P. Maitrasse, Influence of three types of superplasticizers on tricalciumaluminate hydration in presence of gypsum., in: 8th CANMET/ACI Int. Conf. Superplast. Chem. Admix. Concr., Sorrento (2006) 151–158.

[169] L. Holzer, P. Gasser, A. Kaech, M. Wegmann, A. Zingg, R. Wepf, B. Muench, Cryo-FIB-nanotomography for quantitative analysis of particle structures in cement suspensions, J. Microsc. 227 (2007) 216–228. doi:10.1111/j.1365-2818.2007.01804.x.

[170] R. Heeb, S. Lee, N.V. Venkataraman, N.D. Spencer, Influence of salt on the aqueous lubrication properties of end-grafted, ethylene glycol-based self-assembled monolayers, ACS Appl. Mater. Interfaces. 1 (2009) 1105–1112. doi:10.1021/am900062h.

[171] K. Tasaki, Poly(oxyethylene)–cation interactions in aqueous solution: a molecular dynamics study, Comput. Theor. Polym. Sci. 9 (1999) 271–284. doi:10.1016/S1089-3156(99)00015-X.

[172] Y. Masuda, T. Nakanishi, Ion-specific swelling behaviour of poly(ethylene oxide) gel and the correlation to the intrinsic viscosity of the polymer in salt solutions, Colloid Polym. Sci. 280 547–553. doi:10.1007/s00396-002-0651-x.

[173] J. Plank, B. Sachsenhauser, Experimental determination of the effective anionic charge density of polycarboxylate superplasticizers in cement pore solution, Cem. Concr. Res. 39 (2009) 1–5. doi:10.1016/j.cemconres.2008.09.001.

[174] A. Picker, Influence of Polymers on Nucleation and Assembly of Calcium Silicate Hydrates, Doctoral dissertation, University of Konstanz (2013).

[175] N.L. Thomas, J.D. Birchall, The retarding action of sugars on cement hydration, Cem. Concr. Res. 13 (1983) 830–842. doi:10.1016/0008-8846(83)90084-4.

[176] C. Comparet, Etude des interactions entre les phases modèles représentatives d'un ciment Portland et des superplastifiants du béton, Université de Bourgogne (2004).

[177] L. Nicoleau, M.A. Bertolim, Analytical Model for the Alite (C_3S) Dissolution Topography, J. Am. Ceram. Soc. 99 (2016) 773–786. doi:10.1111/jace.13647.

[178] D. Marchon, P. Juilland, E. Gallucci, L. Frunz, R.J. Flatt, Molecular and submolecular scale effects of comb-copolymers on tri-calcium silicate reactivity: Toward molecular design, J. Am. Ceram. Soc. 100 (2017) 817-841. doi:10.1111/jace.14695.

[179] S. Pourchet, C. Comparet, L. Nicoleau, A. Nonat, Influence of PC Superplasticizers on Tricalcium Silicate Hydration, in: Proc. 12th Int. Congr. Chem. Cem., Montreal (Canada), 2007.

[180] M.C. Garci Juenger, H.M. Jennings, New insights into the effects of sugar on the hydration and microstructure of cement pastes, Cem. Concr. Res. 32 (2002) 393–399. doi:10.1016/S0008-8846(01)00689-5.

[181] G. Falini, S. Manara, S. Fermani, N. Roveri, M. Goisis, G. Manganelli, L. Cassar, Polymeric admixtures effects on calcium carbonate crystallization: relevance to cement industries and biomineralization, CrystEngComm. 9 (2007) 1162–1170. doi:10.1039/B707492A.

[182] J. Rieger, J. Thieme, C. Schmidt, Study of Precipitation Reactions by X-ray Microscopy: $CaCO_3$ Precipitation and the Effect of Polycarboxylates, Langmuir. 16 (2000) 8300–8305. doi:10.1021/la0004193.

[183] H. Keller, J. Plank, Mineralisation of $CaCO_3$ in the presence of polycarboxylate comb polymers, Cem. Concr. Res. 54 (2013) 1–11. doi:10.1016/j.cemconres.2013.06.017.

[184] C.-T. Chen, L.J. Struble, Cement–Dispersant Incompatibility due to Ettringite Bridging, J. Am. Ceram. Soc. 94 (2011) 200–208. doi:10.1111/j.1551-2916.2010.04030.x.

[185] A. Zingg, F. Winnefeld, L. Holzer, J. Pakusch, S. Becker, R. Figi, L. Gauckler, Interaction of polycarboxylate-based superplasticizers with cements containing different C_3A amounts, Cem. Concr. Compos. 31 (2009) 153–162. doi:10.1016/j.cemconcomp.2009.01.005.

[186] C. Rößler, B. Möser, J. Stark, Influence of superplasticizers on C_3A hydration and ettringite growth in cement paste, in: Proc. 12th Int. Congr. Chem. Cem., Montreal (Canada), 2007.

[187] F. Winnefeld, L. Holzer, R. Figi, J. Pakusch, S. Becker, Interaction of Polycarboxylate-Based Superplasticizers and Cements: Influence of Polymer Structure and C_3A-Content of Cement, in: Proc. 12th Int. Congr. Chem. Cem., Montreal (Canada), 2007.

[188] L. Regnaud, C. Rossino, R. Alfari, A. Vichot, Effect of Comb Type Superplasticizers on Hydration Kinetics of Industrial Portland Cements, in: Proc. 13th Inter- Natl. Conf. Cem. Chem., Madrid (Spain), 2011.

[189] M. Palacios, H. Kazemi-Kamyab, S. Mantellato, P. Bowen, Laser Diffraction and Gas Adsorption Techniques, in: Pract. Guide Microstruct. Anal. Cem. Mater., Taylor & Francis (2016).

[190] M.M. Costoya Fernández, Effect of particle size on the hydration kinetics and microstructural development of tricalcium silicate, EPFL (2008).

[191] S. Bishnoi, Vector modelling of hydrating cement microstructure and kinetics, EPFL (2008).

[192] Lea's Chemistry of Cement and Concrete (Fourth Edition), Butterworth-Heinemann, Oxford (2003).

[193] D. Marchon, R.J. Flatt, 12 – Impact of chemical admixtures on cement hydration, in: P.-C. Aïtcin, R.J. Flatt (Eds.), Sci. Technol. Concr. Admix., Woodhead Publishing (2016) 279–304.

[194] H.M.J. Jeffrey J. Thomas, The Surface Area of Hardened Cement Paste as Measured by Various Techniques, Concr. Sci. Eng. 1 (1999) 45–64.

[195] M.C. Garci Juenger, H.M. Jennings, The use of nitrogen adsorption to assess the microstructure of cement paste, Cem. Concr. Res. 31 (2001) 883–892. doi:10.1016/S0008-8846(01)00493-8.

[196] I. Odler, The BET-specific surface area of hydrated Portland cement and related materials, Cem. Concr. Res. 33 (2003) 2049–2056. doi:10.1016/S0008-8846(03)00225-4.

[197] R.L. Blaine, A simplified air-permeability fineness apparatus, Bull. Am. Soc. Test. Mater. (1943) 51–55.

[198] J. Kozeny, Über kapillare Leitung des Wassers im Boden, Akad Wiss Wien. 136 (1927) 271–306.

[199] P.C. Carman, Fluid flow through granular beds, Chem. Eng. Res. Des. 75, Supplement (1937) S32–S48. doi:10.1016/S0263-8762(97)80003-2.

[200] P.C. Carman, Flow of gases through porous media, Butterworths Sci. Publ. Lond. 1 (1956) 124–125. doi:10.1016/0010-2180(57)90038-X.

[201] ASTM C204, Test Methods for Fineness of Hydraulic Cement by Air-Permeability Apparatus, ASTM International (2011).

[202] L. Holzer, B. Muench, M. Wegmann, P. Gasser, R.J. Flatt, FIB-Nanotomography of Particulate Systems—Part I: Particle Shape and Topology of Interfaces, J. Am. Ceram. Soc. 89 (2006) 2577–2585. doi:10.1111/j.1551-2916.2006.00974.x.

[203] B. Münch, P. Gasser, L. Holzer, R. Flatt, FIB-Nanotomography of Particulate Systems—Part II: Particle Recognition and Effect of Boundary Truncation, J. Am. Ceram. Soc. 89 (2006) 2586–2595. doi:10.1111/j.1551-2916.2006.01121.x.

[204] L. Holzer, R.J. Flatt, S.T. Erdoğan, J.W. Bullard, E.J. Garboczi, Shape Comparison between 0.4–2.0 and 20–60 μm Cement Particles, J. Am. Ceram. Soc. 93 (2010) 1626–1633. doi:10.1111/j.1551-2916.2010.03654.x.

[205] S.T. Erdogan, X. Nie, P.E. Stutzman, E.J. Garboczi, Micrometer-scale 3-D shape characterization of eight cements: Particle shape and cement chemistry, and the effect of particle shape on laser diffraction particle size measurement, Cem. Concr. Res. 40 (2010) 731–739. doi:10.1016/j.cemconres.2009.12.006.

[206] C.F. Ferraris, E. Garboczi, MEASURING CEMENT PARTICLE SIZE AND SURfACE AREA BY LASER DIFFRACTION, Res. Results Dig. (2013).

[207] S. Brunauer, P.H. Emmett, E. Teller, Adsorption of Gases in Multimolecular Layers, J. Am. Chem. Soc. 60 (1938) 309–319. doi:10.1021/ja01269a023.

[208] A.E. Hill, The Transition Temperature of Gypsum to Anhydrite, J. Am. Chem. Soc. 59 (1937) 2242–2244. doi:10.1021/ja01290a039.

[209] E. Posnjak, The system, $CaSO_4 \cdot H_2O$, Am. J. Sci. 35 (1938) 247–272.

[210] A.E. Charola, J. Pühringer, M. Steiger, Gypsum: a review of its role in the deterioration of building materials, Environ. Geol. 52 (2007) 339–352. doi:10.1007/s00254-006-0566-9.

[211] M.C. Ball, L.S. Norwood, Studies in the system calcium sulphate/water. Part 5 –Surface area and porosity changes in the dehydration of calcium sulphate dihydrate, J. Chem. Soc. Faraday Trans. 1 Phys. Chem. Condens. Phases. 73 (1977) 932–941. doi:10.1039/F19777300932.

[212] M.C. Ball, L.S. Norwood, Studies in the system $CaSO_4$-H_2O. Part 6 – Surface chemistry and porosity of the $CaSO_4$ hemihydrates, J. Chem. Soc. Faraday Trans. 1 Phys. Chem. Condens. Phases. 74 (1978) 1477–1487. doi:10.1039/F19787401477.

[213] J. Zhang, G.W. Scherer, Comparison of methods for arresting hydration of cement, Cem. Concr. Res. 41 (2011) 1024–1036. doi:10.1016/j.cemconres.2011.06.003.

[214] V. Kocaba, Development and evaluation of methods to follow microstructural development of cementitious systems including slags, Doctoral thesis, EPFL (2009).

[215] J.F. Young, Y. Shimada, Structural changes during thermal dehydration of ettringite, Adv. Cem. Res. 13 (2001) 77–81. doi:10.1680/adcr.2001.13.2.77.

[216] L.G. Baquerizo, T. Matschei, K.L. Scrivener, Impact of water activity on the stability of ettringite, Cem. Concr. Res. 79 (2016) 31–44. doi:10.1016/j.cemconres.2015.07.008.

[217] M.R. Hartman, S.K. Brady, R. Berliner, M.S. Conradi, The evolution of structural changes in ettringite during thermal decomposition, J. Solid State Chem. 179 (2006) 1259–1272. doi:10.1016/j.jssc.2006.01.038.

[218] Q. Zhou, F.P. Glasser, Thermal stability and decomposition mechanisms of ettringite at <120 °C, Cem. Concr. Res. 31 (2001) 1333–1339. doi:10.1016/S0008-8846(01)00558-0.

[219] N.N. Skoblinskaya, K.G. Krasilnikov, Changes in crystal structure of ettringite on dehydration. 1, Cem. Concr. Res. 5 (1975) 381–393. doi:10.1016/0008-8846(75)90093-9.

[220] N.N. Skoblinskaya, K.G. Krasilnikov, L.V. Nikitina, V.P. Varlamov, Changes in crystal structure of ettringite on dehydration. 2, Cem. Concr. Res. 5 (1975) 419–431. doi:10.1016/0008-8846(75)90017-4.

[221] G. Renaudin, Y. Filinchuk, J. Neubauer, F. Goetz-Neunhoeffer, A comparative structural study of wet and dried ettringite, Cem. Concr. Res. 40 (2010) 370–375. doi:10.1016/j.cemconres.2009.11.002.

[222] F. Deschner, B. Lothenbach, F. Winnefeld, J. Neubauer, Effect of temperature on the hydration of Portland cement blended with siliceous fly ash, Cem. Concr. Res. 52 (2013) 169–181. doi:10.1016/j.cemconres.2013.07.006.

[223] E. Dubina, L. Wadsö, J. Plank, A sorption balance study of water vapour sorption on anhydrous cement minerals and cement constituents, Cem. Concr. Res. 41 (2011) 1196–1204. doi:10.1016/j.cemconres.2011.07.009.

[224] O.M. Jensen, P.F. Hansen, E.E. Lachowski, F.P. Glasser, Clinker mineral hydration at reduced relative humidities, Cem. Concr. Res. 29 (1999) 1505–1512. doi:10.1016/S0008-8846(99)00132-5.

[225] M.C. Ball, L.S. Norwood, Studies in the system calcium sulphate–water. Part I. Kinetics of dehydration of calcium sulphate dihydrate, J. Chem. Soc. Inorg. Phys. Theor. (1969) 1633–1637. doi:10.1039/J19690001633.

[226] E. Badens, P. Llewellyn, J.M. Fulconis, C. Jourdan, S. Veesler, R. Boistelle, F. Rouquerol, Study of Gypsum Dehydration by Controlled Transformation Rate Thermal Analysis (CRTA), J. Solid State Chem. 139 (1998) 37–44. doi:10.1006/jssc.1998.7797.

[227] M. Carbone, P. Ballirano, R. Caminiti, Kinetics of gypsum dehydration at reduced pressure: an energy dispersive X-ray diffraction study, Eur. J. Mineral. 20 (2008) 621–627.

[228] M. Triollier, B. Guilhot, The hydration of calcium sulphate hemihydrate, Cem. Concr. Res. 6 (1976) 507–514. doi:10.1016/0008-8846(76)90079-X.

[229] C.H. Chio, S.K. Sharma, D.W. Muenow, Micro-Raman studies of gypsum in the temperature range between 9 K and 373 K, Am. Mineral. 89 (2004) 390–395.

[230] S. Seufert, C. Hesse, F. Goetz-Neunhoeffer, J. Neubauer, Quantitative determination of anhydrite III from dehydrated gypsum by XRD, Cem. Concr. Res. 39 (2009) 936–941. doi:10.1016/j.cemconres.2009.06.018.

[231] M. Ball, Effects of Dehydration and Rehydration on Porosity in Calcium-Sulfate and Its Hydrates, Br. Ceram. Trans. J. 88 (1989) 79–82.

[232] S. Novak, Alterung von Calciumsulfatphasen : Physiko-chemisch bedingte Feuchteaufnahmen und Einfluss auf die Reaktivität, Doctoral thesis, Bauhaus-Universität Weimar (2013).

[233] C. Bezou, A. Nonat, J.-C. Mutin, A.N. Christensen, M.S. Lehmann, Investigation of the Crystal Structure of γ-$CaSO_4$, $CaSO_4 \cdot 0.5\ H_2O$, and $CaSO_4 \cdot 0.6H_2O$ by Powder Diffraction Methods, J. Solid State Chem. 117 (1995) 165–176. doi:10.1006/jssc.1995.1260.

[234] H.-B. Fischer, S. Nowak, M. Hartmann, C. Riechert, About the reactivity of calcium sulphate binders, Univ. Politeh. Buchar. Sci. Bull. Ser. B Chem. Mater. Sci. 74 (2012) 3–24.

[235] F. Goetz-Neunhoeffer, J. Neubauer, Refined ettringite ($Ca_6Al_2(SO_4)_3(OH)_{12} \cdot 26H_2O$) structure for quantitative X-ray diffraction analysis, Powder Diffr. 21 (2006) 4–11. doi:10.1154/1.2146207.

[236] J.N. Miller, J.C. Miller, Statistics and Chemometrics for Analytical Chemistry, Pearson Education (2010).

[237] F. Dalas, Influence des paramètres structuraux de superplastifiants sur l'hydratation, la création de surfaces initiales et la fluidité de systèmes cimentaires modèles, Doctoral thesis, Université de Bourgogne (2014).

[238] A.E. Moore, H.F.W. Taylor, Crystal structure of ettringite, Acta Crystallogr. B. 26 (1970) 386–393. doi:10.1107/S0567740870002443.

[239] Q. Zhou, E.E. Lachowski, F.P. Glasser, Metaettringite, a decomposition product of ettringite, Cem. Concr. Res. 34 (2004) 703–710. doi:10.1016/j.cemconres.2003.10.027.

[240] H. Poellmann, S. Auer, H.-J. Kuzel, R. Wenda, Solid solution of ettringites, Cem. Concr. Res. 23 (1993) 422–430. doi:10.1016/0008-8846(93)90107-K.

[241] H. Poellmann, H.-J. Kuzel, R. Wenda, Solid solution of ettringites part I: incorporation of OH^- and CO_3^{2-} in $3CaO \cdot Al_2O_3 \cdot 32H_2O$, Cem. Concr. Res. 20 (1990) 941–947. doi:10.1016/0008-8846(90)90057-5.

[242] K. Wieczorek-Ciurowa, K. Fela, A. Kozak, Chromium(III)-Ettringite Formation and its Thermal Stability, J. Therm. Anal. Calorim. 65 (2001) 655–660. doi:10.1023/A:1017978414203.

[243] G. Möschner, B. Lothenbach, J. Rose, A. Ulrich, R. Figi, R. Kretzschmar, Solubility of Fe–ettringite $(Ca_6[Fe(OH)_6]_2(SO_4)_3 \cdot 26H_2O)$, Geochim. Cosmochim. Acta. 72 (2008) 1–18. doi:10.1016/j.gca.2007.09.035.

[244] A. Martucci, G. Cruciani, In situ time resolved synchrotron powder diffraction study of thaumasite, Phys. Chem. Miner. 33 (2006) 723–731. doi:10.1007/s00269-006-0124-8.

[245] E.E. Lachowski, S.J. Barnett, D.E. Macphee, Transmission electron optical study of ettringite and thaumasite, Cem. Concr. Compos. 25 (2003) 819–822. doi:10.1016/S0958-9465(03)00107-0.

[246] S. Pourchet, C. Comparet, A. Nonat, P. Maitrasse, Influence of Three Types of Superplasticizers on Tricalciumaluminate Hydration in Presence of Gypsum, in: Proc. 8th CANMETACI Int. Conf. Superplast. Chem. Admix. Concr. Sorrento ACI SP-239 Pp 151-168, 2006: pp. 151–168.

[247] N.C. Collier, J.H. Sharp, N.B. Milestone, J. Hill, I.H. Godfrey, The influence of water removal techniques on the composition and microstructure of hardened cement pastes, Cem. Concr. Res. 38 (2008) 737–744. doi:10.1016/j.cemconres.2008.02.012.

[248] J.M. Makar, T. Sato, The effect of drying method on ordinary Portland cement surfaces during the early stages of hydration, Mater. Struct. 46 (2013) 1–12. doi:10.1617/s11527-012-9878-2.

[249] E. Knapen, O. Cizer, K. Van Balen, D. Van Gemert, Effect of free water removal from early-age hydrated cement pastes on thermal analysis, Constr. Build. Mater. 23 (2009) 3431–3438. doi:10.1016/j.conbuildmat.2009.06.004.

[250] R. Khoshnazar, L. Raki, J. Beaudoin, R. Alizadeh, Solvent exchange in sulphoaluminate phases. Part I: ettringite, Adv. Cem. Res. 25 (2013) 314–321. doi:10.1680/adcr.12.00042.

[251] R. Snellings, Chapter 4 – X-ray powder diffraction applied to cement, in: Pract. Guide Microstruct. Anal. Cem. Mater., Ed. Scrivener, K., Lothenbach, B., Snellings, R., Taylor and Francis (2016).

[252] D. Rothstein, J.J. Thomas, B.J. Christensen, H.M. Jennings, Solubility behaviour of Ca-, S-, Al-, and Si-bearing solid phases in Portland cement pore solutions as a function of hydration time, Cem. Concr. Res. 32 (2002) 1663–1671. doi:10.1016/S0008-8846(02)00855-4.

[253] B. Lothenbach, F. Winnefeld, Thermodynamic modelling of the hydration of Portland cement, Cem. Concr. Res. 36 (2006) 209–226. doi:10.1016/j.cemconres.2005.03.001.

[254] R. d. Hooton, M. d. a. Thomas, T. Ramlochan, Use of pore solution analysis in design for concrete durability, Adv. Cem. Res. 22 (2010) 203–210. doi:10.1680/adcr.2010.22.4.203.

[255] D. Marchon, R.J. Flatt, 8 - Mechanisms of cement hydration, in: Sci. Technol. Concr. Admix., Woodhead Publishing (2016) 129–145.

[256] A. Vollpracht, B. Lothenbach, R. Snellings, J. Haufe, The pore solution of blended cements: a review, Mater. Struct. 49 (2015) 3341–3367. doi:10.1617/s11527-015-0724-1.

[257] A. Leemann, B. Lothenbach, C. Thalmann, Influence of superplasticizers on pore solution composition and on expansion of concrete due to alkali-silica reaction, Constr. Build. Mater. 25 (2011) 344–350. doi:10.1016/j.conbuildmat.2010.06.019.

[258] S. Mantellato, Q. Mehmeti, L. Ceni, M. Palacios, R.J. Flatt, Mastering Flow Loss in Superplasticized Cementitious Systems, in: Proc. 11th CANMETACI Int. Conf. Superplast. Chem. Admix. Concr. Ott. ACI SP-302-10 Pp 133-144, Ottawa, Canada, 2015: pp. 133–144.

[259] X. Hou, R.S. Amais, B.T. Jones, G.L. Donati, Inductively Coupled Plasma Optical Emission Spectrometry, in: Encycl. Anal. Chem., John Wiley & Sons, Ltd (2006).

[260] R.S. Barneyback Jr., S. Diamond, Expression and analysis of pore fluids from hardened cement pastes and mortars, Cem. Concr. Res. 11 (1981) 279–285. doi:10.1016/0008-8846(81)90069-7.

[261] F. Schmidt, F.S. Rostásy, A method for the calculation of the chemical composition of the concrete pore solution, Cem. Concr. Res. 23 (1993) 1159–1168. doi:10.1016/0008-8846(93)90176-A.

[262] F. Winnefeld, B. Lothenbach, Hydration of calcium sulfoaluminate cements — Experimental findings and thermodynamic modelling, Cem. Concr. Res. 40 (2010) 1239–1247. doi:10.1016/j.cemconres.2009.08.014.

[263] W. Yao, M.J. Wu, Solubility Behaviour of the Hydration Products in the Pore Solution of Hydrated Cement Pastes, Key Eng. Mater. 539 (2013) 189–194. doi:10.4028/www.scientific.net/KEM.539.189.

[264] C. Nalet, A. Nonat, Effect of the Stereochemistry of Polyols on the Hydration of Cement: Influence of Aluminate and Sulfate Phases, Spec. Publ. 302 (2015) 349–358.

[265] B. Lothenbach, E. Wieland, A thermodynamic approach to the hydration of sulphate-resisting Portland cement, Waste Manag. 26 (2006) 706–719. doi:10.1016/j.wasman.2006.01.023.

[266] S.J. Hill, A. Fisher, M. Foulkes, Basic Concepts and Instrumentation for Plasma Spectrometry, in: S.J. Hill (Ed.), Inductively Coupled Plasma Spectrom. Its Appl., Blackwell Publishing Ltd (2006) 61–97.

[267] D. Harvey, Modern analytical chemistry, McGraw-Hill Higher Education, Boston (2000).

[268] D. Harris, Quantitative Chemical Analysis, Eight edition, W.H. Freeman and Company, New York (2010).

[269] T.J. Manning, W.R. Grow, Inductively Coupled Plasma – Atomic Emission Spectrometry, Chem. Educ. 2 (n.d.) 1–19. doi:10.1007/s00897970103a.

[270] C. Dubuisson, E. Poussel, J.-M. Mermet, Comparison of Axially and Radially Viewed Inductively CoupledPlasma Atomic Emission Spectrometry in Terms of Signal-to-Background Ratioand Matrix Effects, J. Anal. At. Spectrom. 12 (1997) 281–286. doi:10.1039/A606445K.

[271] F.V. Silva, L.C. Trevizan, C.S. Silva, A.R.A. Nogueira, J.A. Nóbrega, Evaluation of inductively coupled plasma optical emission spectrometers with axially and radially viewed configurations, Spectrochim. Acta Part B At. Spectrosc. 57 (2002) 1905–1913. doi:10.1016/S0584-8547(02)00176-3.

[272] J. Dean, Practical Inductively Coupled Plasma Spectroscopy. Analytical techniques in the sciences (2005).

[273] C.B. Boss, K.J. Fredeen, Concepts, instrumentation and techniques in inductively coupled plasma optical emission spectrometry, Perkin Elmer Norwalk (2004).

[274] G.M. Hieftje, Introduction – A Forward-Looking Perspective, in: S.J. Hill (Ed.), Inductively Coupled Plasma Spectrom. Its Appl., Blackwell Publishing Ltd (2006) 1–26.

[275] ISO 5725-1:1994(en), Accuracy (trueness and precision) of measurement methods and results – Part 1: General principles and definitions, (n.d.).

[276] Bureau International des Poids et Mesures, JCGM 200:2012 — International Vocabulary of Metrology — Basic and General Concepts and Associated Terms (VIM), 3rd edition JCGM, 2012.

[277] M. Nič, J. Jirát, B. Košata, A. Jenkins, A. McNaught, Precision, in: IUPAC Compend. Chem. Terminol., 2.1.0, IUPAC, Research Triangle Park, NC (2015).

[278] M. Nič, J. Jirát, B. Košata, A. Jenkins, A. McNaught, Limit of detection in analysis, in: IUPAC Compend. Chem. Terminol., 2.1.0, IUPAC, Research Triangle Park, NC (2009).

[279] J. Uhrovčík, Strategy for determination of LOD and LOQ values – Some basic aspects, Talanta. 119 (2014) 178–180. doi:10.1016/j.talanta.2013.10.061.

[280] BS EN 196-2:2005 - Methods of testing cement. Chemical analysis of cement – BSI British Standards, (n.d.).

[281] A. Kauppi, K.M. Andersson, L. Bergström, Probing the effect of superplasticizer adsorption on the surface forces using the colloidal probe AFM technique, Cem. Concr. Res. 35 (2005) 133–140. doi:10.1016/j.cemconres.2004.07.008.

[282] ASTM D1976, Standard Test Method for Elements in Water by Inductively-Coupled Argon Plasma Atomic Emission Spectroscopy, ASTM International (2012).

[283] C. Hirsch, Untersuchungen zur Wechselwirkung zwischen polymeren Fliessmitteln und Zementen bzw. Mineralphasen der frühen Zementhydratation, Technischen Universität München (2005).

[284] M. Niederberger, H. Cölfen, Oriented attachment and mesocrystals: Non-classical crystallization mechanisms based on nanoparticle assembly, Phys. Chem. Chem. Phys. 8 (2006) 3271–3287. doi:10.1039/B604589H.

[285] D. Gebauer, A. Völkel, H. Cölfen, Stable Prenucleation Calcium Carbonate Clusters, Science. 322 (2008) 1819–1822. doi:10.1126/science.1164271.

[286] F.C. Meldrum, R.P. Sear, Now You See Them, Science. 322 (2008) 1802–1803. doi:10.1126/science.1167221.

[287]   D. Gebauer, M. Kellermeier, J.D. Gale, L. Bergström, H. Cölfen, Pre-nucleation clusters as solute precursors in crystallisation, Chem. Soc. Rev. 43 (2014) 2348–2371. doi:10.1039/C3CS60451A.

[288]   M.-H. Zhang, K. Sisomphon, T.S. Ng, D.J. Sun, Effect of superplasticizers on workability retention and initial setting time of cement pastes, Constr. Build. Mater. 24 (2010) 1700–1707. doi:10.1016/j.conbuildmat.2010.02.021.

[289]   N. Pashias, D.V. Boger, J. Summers, D.J. Glenister, A fifty cent rheometer for yield stress measurement, J. Rheol. 40 (1996) 1179–1189. doi:10.1122/1.550780.

[290]   S. Clayton, T.G. Grice, D.V. Boger, Analysis of the slump test for on-site yield stress measurement of mineral suspensions, Int. J. Miner. Process. 70 (2003) 3–21. doi:10.1016/S0301-7516(02)00148-5.

[291]   N. Roussel, C. Stefani, R. Leroy, From mini-cone test to Abrams cone test: measurement of cement-based materials yield stress using slump tests, Cem. Concr. Res. 35 (2005) 817–822. doi:10.1016/j.cemconres.2004.07.032.

[292]   R.J. Flatt, J. Zimmermann, C. Hampel, C. Kurz, I. Schober, L. Frunz, C. Plassard, E. Lesniewska, The Role of Adsorption Energy in the Sulfate-Polycarboxylate Competition, Spec. Publ. 262 (2009) 153–164.

[293]   A. Colombo, M. Geiker, H. Justnes, R.A. Lauten, K. De Weerdt, On the mechanisms of consumption of calcium lignosulfonate by cement paste, Cem. Concr. Res. 98 (2017) 1–9. doi:10.1016/j.cemconres.2017.02.026.

[294]   N. Roussel, Steady and transient flow behaviour of fresh cement pastes, Cem. Concr. Res. 35 (2005) 1656–1664. doi:10.1016/j.cemconres.2004.08.001.

[295]   A. Perrot, A. Pierre, S. Vitaloni, V. Picandet, Prediction of lateral form pressure exerted by concrete at low casting rates, Mater. Struct. 48 (2014) 2315–2322. doi:10.1617/s11527-014-0313-8.

[296]   A. Perrot, T. Lecompte, H. Khelifi, C. Brumaud, J. Hot, N. Roussel, Yield stress and bleeding of fresh cement pastes, Cem. Concr. Res. 42 (2012) 937–944. doi:10.1016/j.cemconres.2012.03.015.

[297]   H.M. Jennings, P.D. Tennis, Model for the Developing Microstructure in Portland Cement Pastes, J. Am. Ceram. Soc. 77 (1994) 3161–3172. doi:10.1111/j.1151-2916.1994.tb04565.x.

[298]   A.J. Allen, J.J. Thomas, H.M. Jennings, Composition and density of nanoscale calcium–silicate–hydrate in cement, Nat. Mater. 6 (2007) 311–316. doi:10.1038/nmat1871.

[299]   R.J. Flatt, P. Bowen, Electrostatic repulsion between particles in cement suspensions: Domain of validity of linearized Poisson–Boltzmann equation for nonideal electrolytes, Cem. Concr. Res. 33 (2003) 781–791. doi:10.1016/S0008-8846(02)01059-1.

[300]   H.G. Pedersen, L. Bergström, Forces Measured between Zirconia Surfaces in Poly(acrylic acid) Solutions, J. Am. Ceram. Soc. 82 (1999) 1137–1145. doi:10.1111/j.1151-2916.1999.tb01887.x.

[301]   B. Jönsson, A. Nonat, C. Labbez, B. Cabane, H. Wennerström, Controlling the Cohesion of Cement Paste, Langmuir. 21 (2005) 9211–9221. doi:10.1021/la051048z.

[302]   S. Lesko, E. Lesniewska, A. Nonat, J.C. Mutin, J.P. Goudonnet, Investigation by atomic force microscopy of forces at the origin of cement cohesion, Ultramicroscopy. 86 (2001) 11–21.

[303]   B. Jönsson, H. Wennerström, A. Nonat, B. Cabane, Onset of cohesion in cement paste, Langmuir. 20 (2004) 6702–6709. doi:10.1021/la0498760.

[304]   C. Plassard, E. Lesniewska, I. Pochard, A. Nonat, Nanoscale experimental investigation of particle interactions at the origin of the cohesion of cement, Langmuir ACS J. Surf. Colloids. 21 (2005) 7263–7270. doi:10.1021/la050440+.

[305]   D. Kulik, GEMS-PSI 2.1, PSI-Villigen, Switzerland, 2007.

[306]   T. Thoenen, D. Kulik, Nagra/PSI Chemical Thermodynamic Data Base 01/01 for the GEM-Selektor (V.2-PSI) Geochemical Modeling Code, PSI-Villigen, Switzerland, 2003.

[307]   Various authours, CEMDATA14 – Database development, n.d.

[308]   T. Sowoidnich, T. Rachowski, C. Rößler, A. Völkel, H.-M. Ludwig, Calcium complexation and cluster formation as principal modes of action of polymers used as superplasticizer in cement systems, Cem. Concr. Res. 73 (2015) 42–50. doi:10.1016/j.cemconres.2015.01.016.

[309]   L. Valentini, M. Favero, M.C. Dalconi, V. Russo, G. Ferrari, G. Artioli, Kinetic Model of Calcium-Silicate Hydrate Nucleation and Growth in the Presence of PCE Superplasticizers, Cryst. Growth Des. 16 (2016) 646–654. doi:10.1021/acs.cgd.5b01127.

[310] E. Lloret, A.R. Shahab, M. Linus, R.J. Flatt, F. Gramazio, M. Kohler, S. Langenberg, Complex concrete structures, Comput.-Aided Des. 60 (2015) 40–49. doi:10.1016/j.cad.2014.02.011.

[311] T. Wangler, E. Lloret, L. Reiter, N. Hack, F. Gramazio, M. Kohler, M. Bernhard, B. Dillenburger, J. Buchli, N. Roussel, R. Flatt, Digital Concrete: Opportunities and Challenges, RILEM Tech. Lett. 1 (2016) 67–75. doi:10.21809/rilemtechlett.2016.16.

[312] G. Artioli, L. Valentini, M. Voltolini, M.C. Dalconi, G. Ferrari, V. Russo, Direct Imaging of Nucleation Mechanisms by Synchrotron Diffraction Micro-Tomography: Superplasticizer-Induced Change of C–S–H Nucleation in Cement, Cryst. Growth Des. 15 (2015) 20–23. doi:10.1021/cg501466z.

[313] S. Garrault-Gauffinet, A. Nonat, Experimental investigation of calcium silicate hydrate (C-S-H) nucleation, J. Cryst. Growth. 200 (1999) 565–574. doi:10.1016/S0022-0248(99)00051-2.

[314] J. Stark, B. Möser, F. Bellmann, Nucleation and growth of C-S-H phases on mineral admixtures, in: Adv. Constr. Mater. (2007) 531–538. doi:10.1007/978-3-540-72448-3_54.

[315] L. Holzer, Quantitative microstructure analysis of complex suspensions using Cryo-FIB-nanotomography, Microsc. Microanal. 13 (2007) 172–173. doi:10.1017/S1431927607074752.

[316] N. Ruffray, P. Gasser, A. Greet Bittermann, F. Lucas, D. Marchon, M. Palacios, R.J. Flatt, Challenges of cryo-FIB-ESEM tomography to study early hydration of cementitious materials, in: Les Diablerets, Switzerland (2017) 120–123.

[317] ASTM C191, Standard Test Methods for Time of Setting of Hydraulic Cement by Vicat Needle, ASTM International (2008).

[318] ASTM C403/C403M, Standard Test Method for Time of Setting of Concrete Mixtures by Penetration Resistance, ASTM International (2016).

[319] G. Trtnik, G. Turk, F. Kavčič, V.B. Bosiljkov, Possibilities of using the ultrasonic wave transmission method to estimate initial setting time of cement paste, Cem. Concr. Res. 38 (2008) 1336–1342. doi:10.1016/j.cemconres.2008.08.003.

[320] H.W. Reinhardt, C.U. Grosse, Continuous monitoring of setting and hardening of mortar and concrete, Constr. Build. Mater. 18 (2004) 145–154. doi:10.1016/j.conbuildmat.2003.10.002.

[321] Li Zongjin, Xiao Lianzhen, Wei Xiaosheng, Determination of Concrete Setting Time Using Electrical Resistivity Measurement, J. Mater. Civ. Eng. 19 (2007) 423–427. doi:10.1061/(ASCE)0899-1561(2007)19:5(423).

[322] D. Harvey, Modern Analytical Chemistry, McGraw Hill Higher Education, Boston (2000).

[323] T. Yuasa, T. Nishikawa, N. Sakamoto, T. Hirata, H. Izukashi, T. Ueta, H. Tanaka, Y. Onda, T. Uno, Polycarboxylic acid type copolymer, method for producing the same, cement additive and cement composition, EP2003154 A2 (2008).

[324] G. Gelardi, Characterization of comb compolymers superplsticizers by a multi-tecnique approach, Doctoral dissertation, ETH Zurich (2017).

[325] X. Huang, S. Bhattacharjee, E.M.V. Hoek, Is Surface Roughness a "Scapegoat" or a Primary Factor When Defining Particle−Substrate Interactions?, Langmuir. 26 (2010) 2528–2537. doi:10.1021/la9028113.

[326] Y.I. Rabinovich, J.J. Adler, A. Ata, R.K. Singh, B.M. Moudgil, Adhesion between Nanoscale Rough Surfaces, J. Colloid Interface Sci. 232 (2000) 10–16. doi:10.1006/jcis.2000.7167.

[327] A. Kumar, T. Staedler, X. Jiang, Role of relative size of asperities and adhering particles on the adhesion force, J. Colloid Interface Sci. 409 (2013) 211–218. doi:10.1016/j.jcis.2013.07.039.

[328] J. Katainen, M. Paajanen, E. Ahtola, V. Pore, J. Lahtinen, Adhesion as an interplay between particle size and surface roughness, J. Colloid Interface Sci. 304 (2006) 524–529. doi:10.1016/j.jcis.2006.09.015.

[329] W.A. Ducker, T.J. Senden, R.M. Pashley, Direct measurement of colloidal forces using an atomic force microscope, Nature. 353 (1991) 239–241. doi:10.1038/353239a0.

[330] Y. Zou, S. Jayasuriya, C.W. Manke, G. Mao, Influence of Nanoscale Surface Roughness on Colloidal Force Measurements, Langmuir. 31 (2015) 10341–10350. doi:10.1021/acs.langmuir.5b02672.

[331] R.F. Considine, C.J. Drummond, Surface Roughness and Surface Force Measurement: A Comparison of Electrostatic Potentials Derived from Atomic Force Microscopy and Electrophoretic Mobility Measurements, Langmuir. 17 (2001) 7777–7783. doi:10.1021/la0017227.

[332] E.M.V. Hoek, S. Bhattacharjee, M. Elimelech, Effect of Membrane Surface Roughness on Colloid–Membrane DLVO Interactions, Langmuir. 19 (2003) 4836–4847. doi:10.1021/la027083c.

Appendix I

Effect of PCEs on the cement pore solution composition

I.1 Introduction

The evolution of the ionic composition of cement pore solutions reflects the relative kinetics of dissolution and precipitation processes taking place during cement hydration [6]. During the first stage of hydration, PCEs can influence these processes leading to different nucleation and precipitation of cement hydrates [6,15,16]. Besides this, the accurate quantification of sulfates in the aqueous phase is of particular interest as they can modify the balance of the competitive adsorption with polycarboxylates [176] affecting the flow evolution over time [74,76,101]. If a system initially contains a large amount of sulfates, then only a small fraction of polymers can adsorb. However, as hydration reactions proceed, sulfates get consumed and the non-adsorbed polymers begin to adsorb, which leads to the so-called "delayed fluidification" [91].

ICP-OES is broadly used by the cement community for the characterization pore solutions. However, its potential seems to have been largely underused, Chapter 4 presents the first robust guidelines for the quantification of the eight main elements present in cement pore solutions. The main achievement was the reliable quantification of aluminium ions – at the level of μmol/L – taking into account the complexity of cement-paste matrices having an average concentration of about 40 g/L. Our results also show how PCEs increase the concentration of Al, Mg, Fe, and Si, keeping almost unchanged the concentration of the high-concentration elements

with respect to the solution from the plain paste. In support of this modification, the formation of either nanoparticles or complexes was proposed.

In all these measurements, a rate-determining step is the amount of time involved in separating the liquid from the solid phase. However, the importance of the sample preparation is often underestimated and the systematic effect of different procedures to extract cement pore solutions is barely reported in the literature where single measurements are typically presented. This limits the possibility to identify possible mistakes due to the sample preparation and/or instrumental issues.

The separation of the liquid phase from the solid in cement pastes is not a trivial task, especially in the case of highly dispersed systems with low water contents. Centrifugation is advisable for the separation of dilute suspensions, while pressure filtration is needed at higher volume fractions of solids. The latter is normally carried out by applying vacuum an under-pressure below the filter. Alternatively, pressure higher than the atmospheric one may be applied on top of the suspension. As filtration proceeds, the height of the particle bed on the filter increases. In highly dispersed systems, this leads to a very low permeability of the particle beds, increasing the filtration time substantially. A prolonged filtration may become problematic with respect to cement hydration, in particular when considering aluminate reactivity in the early stages, thus preventing a rigorous characterization of the pore solutions.

A further filtration is recommended before the analysis, mainly after centrifugation, to prevent possible coarse particles from clogging the hydraulic part of the ICP-OES. This is conveniently done with filters having a pore size of at least 0.45 μm. However, this step may be a limiting factor if nano-hydrates are formed and stabilized in the interstitial fluid with chemical admixtures. Comparet [176] claimed that filters with pore sizes as small as 0.1 μm are needed to retain ettringite crystals formed in the presence of SNFCs. However, we demonstrated that that PCEs lead to ettringite particles and/or aluminium containing agglomerates of PCEs even smaller than 0.1 μm (Chapter 4)[21]. In turn, Sowoïdnich et al. demonstrated that such small

particles forming in presence of PCEs can be separated by ultracentrifugation [308]. These experimental evidences raise the question of what the effects of admixtures adsorbed on nanoparticles can be for the rheological behaviour.

In this Appendix, the effect of five different PCEs on the composition of the aqueous phase of cement pastes is investigated. Also, some preliminary results on the evolution of the aqueous composition over time are presented when varying the polymer dosage.

I.2 Materials and methods

I.2.1 Materials

Five 25 kg-bags of fresh CEM I 52.5R OPC were provided by Holcim (Holcim Group Services Ltd/Holcim Technology Ltd, Zurich, Switzerland). After delivery, the content of the cement bags was transferred into two PE screw cap barrels to limit possible changes in composition due to hydration and carbonation reactions. Five non-commercial polycarboxylate ether-based comb polymers were used in the present study. For further details, see sections 5.2.1 and II.1.

I.2.2 Sample preparation

I.2.1.1   Small batches of cement pastes

Cement pastes were prepared in PP containers by mixing 200 g of cement and 60 g of UPW (w/c = 0.3) and the polymer is dosed directly with the mixing water (direct addition) as described in section 4.3.2.2. Three repetitions were carried out for each dosage for the polymer 2.5PMA1000, and only one for the other polymers.

The effect of the delayed addition of PCE was also investigated for the polymers 2.5PMA1000 and 2.5PMA2000. In this case, 85% of the total water, corresponding to 51 g of UPW for 200 g of OPC, was mixed to the cement following the same procedure as above. After 15 minutes from the first contact with water, the

polymeric solution and the remaining water were added and mixed at 800 rpm for two minutes. The remaining water was calculated subtracting the water content in the dosed polymeric solution. This procedure allows having the same dissolution process and, therefore the same solution supersaturation, within the first minutes of hydration, so that only the effect of the polymer can be appreciated after its addition.

Afterwards, 50 g of cement paste were put in the barrel (V_{max} = 200 mL) of a stainless-steel pressure filter holder previously mounted with a nylon 0.45 μm membrane filter, both by Sartorius. The stainless-steel pressure filter holder was then connected to a high-pressure air circuit (4 bar) to let the system filter the cement paste for 10 min.

I.2.1.2   Big batches of cement pastes

2 kg of OPC were sampled from the PE barrel at different heights to prepare a cement paste with UPW with a constant w/c of 0.3 using a Hobart mixer (N50 5-Quart Mixer) and the polymer is dosed directly with the mixing water (direct addition) as described in section 5.2.2.1.

Cement pore solution were extracted as described in the previous section. Part the filtered solutions from cement pastes with 2.5PMA1000 for the study of the performances over time was centrifuged for 1 h at 41000 g with a 3-30KS instrument from Sigma (SciQuip Ltd, Newtown, UK) and filtered with a 0.45-μm filter.

I.2.3 Spread flow measurements

Cement pastes were remixed for three minutes at 800 rpm with a vertical mixer (Eurostar power control visc with a 4-bladed propeller stirrer, IKA) before spread flow tests to break down the bonds forming between cement particles over time at rest, before spread flow tests. The yield stress from spread diameter measurements is calculated according to the protocol described in section 5.2.2.2.

I.2.4 ICP-OES

A Thermo Scientific iCAP 6300 Dual View ICP-OES (Thermo Fisher Scientific Inc., Waltham, MA, USA) with a CETAC ASX-260 autosampler (CETAC, Omaha, NE, USA) was used for the analyses. The composition of the calibration solutions used in this study is reported in Table I.1.

Table I.1: Composition of the calibration solutions used in this study. CS-SP-H refers to the calibration solution used for quantifying high-concentration elements in the cement pore solutions. CS-SP-L1 and CS-SP-L2 refer to the calibration solutions used for quantifying low-concentration elements, in which high concentrations of calcium, potassium, sodium and sulfur in CS-SP solutions provide matrix-matched standards.

Solvent/blank	CS-SP-L1 in 2% (w/w) HNO$_3$ in UPW	CS-SP-L2 in 2% (w/w) HNO$_3$ in UPW	CS-SP-H in 2% (w/w) HNO$_3$ in UPW
c_{Ca} (mg/L)	10	10	10
c_K (mg/L)	200	200	200
c_{Na} (mg/L)	20	20	20
c_S (mg/L)	100	100	100
c_{Al} (µg/L)	25	1000	---
c_{Fe} (µg/L)	25	1000	---
c_{Mg} (µg/L)	25	2000	---
c_{Si} (µg/L)	100.1	1001	---

The reference solutions were independently prepared so that the concentration of the elements lies at half of the calibration range of the method CS-SP-L and CS-SP-H. For the method CS-SP-L1, the concentration of the reference materials at very low-concentration elements with 15 µg/L of Al, 10 µg/L of Fe and Mg, 50.05 µg/L of Si and 10 mg/L of Ca, 20 mg/L of Na, 100 mg/L of S and 200 mg/L of K – as interferences – in HNO$_3$ 2% (w/w) in UPW. The contribution of the polymer content in the matrix is not taken into account and the blank was the solution HNO$_3$ 2% (w/w) in UPW.

I.2.5 Dynamic Light Scattering (DLS)

A Malvern Zetasizer Nano ZS was used to determine the presence of nanoparticles in the filtered pore solutions. Measurements were conducted at 25 °C. The wavelength

of the incident laser was 633 nm and the scattered light was detected at a constant angle of 173°. For reference purposes, DLS measurements were also carried out on the pure SP in a synthetic pore solution (prepared as in Houst et al.[77]).

I.3 Effect of PCEs during the initial hydration

In this section of the annex, the results about the effect of the sample preparation on the reproducibility of the solution composition are presented. Particular attention is devoted to results about the influence of polymer structure and dosage on the final composition of cement-paste aqueous phase at the beginning of hydration. The evolution of the pore solution composition is studied in cement pastes with the polymer 2.5PMA1000 at different dosages.

I.3.1 Effect of sample preparation on the pore solution composition

The amount of cement pastes to be filtered might be an additional issue to take into account when preparing the samples. A sufficiently large amount of paste is typically filtered to guarantee the right quantity of liquid for several analyses. This contributes to the packing of the solid on the filter, slowing down the filtration. However, a constant filtration time is recommended for a better comparison of the results.

The consistency of the two cement pastes after 10 minutes of filtration is shown in Figure I.1. A fluid paste is observed when the largest amount of cement paste is used (Figure I.1b), inferring that the filtration is not complete. It was noticed that a moist paste – as observed for small amount of paste (Figure I.1a) – is obtained only by filtering for, at least, 25 minutes. After the first 10 minutes of filtration, the amount of the filtered solution was double using less paste as a thinner consolidated bed is formed. The issue of the amount of filtered paste becomes less critical by decreasing the polymer content.

Figure I.1: Effect of the filtration for 10 minutes under pressure of 50 g (a) and 150 g (b) of a cement paste prepared with 4 mg/g active by weight of cement of 2.5PMA1000 at w/c ratio of 0.3.

Figure I.2 shows the effect of the amount of filtered paste on the composition of the interstitial pore solution. The main differences are observed at high polymer dosage where the packing of the solid on the filter is more pronounced, mainly for the low-concentration elements. The incomplete filtration noticed in Figure I.1 starting from 150 g of paste generally leads to a dramatic decrease of the content of the low-concentration elements. This might be due to the effect of a gradient of concentration through the packing paste over a relatively short filtration.

Figure I.2: Composition of pore solutions with the polymer 2.5PMA1000 at different dosages for the low-concentration (Al, Fe, Mg, Si) elements from the filtration of (a) 50 g and (b) 150 g of admixed cement paste. Each point corresponds to the averaged value with $n_{samples}$ = 3.

For the low-concentration elements, the average calculated relative standard errors are 38%, considering the quantification of 1-2 mg/L in the diluted solutions obtained from the filtration of 50 g of paste with the highest polymer dosages. At

dosages lower than 2 mg/g, the relative standard error decreases down to 22%, excluding the contribution of the Al, whose concentration was lower than its LOQ (Figure I.3a). In the worst case from 150 g of pastes, namely when 3 mg/g of PCE is added, the calculated relative standard errors for the same elements are on average greater than 300%.

Figure I.3: Composition of pore solutions with polymer 2.5PMA1000 at different dosages for the low-concentration (Al, Fe, Mg, Si) elements from the filtration of (a) 50 g and (b) 150 g of admixed cement paste. The results are shown as the mean values and the standard errors of the mean at the 95% confidence limit with $n_{samples}$ = 3.

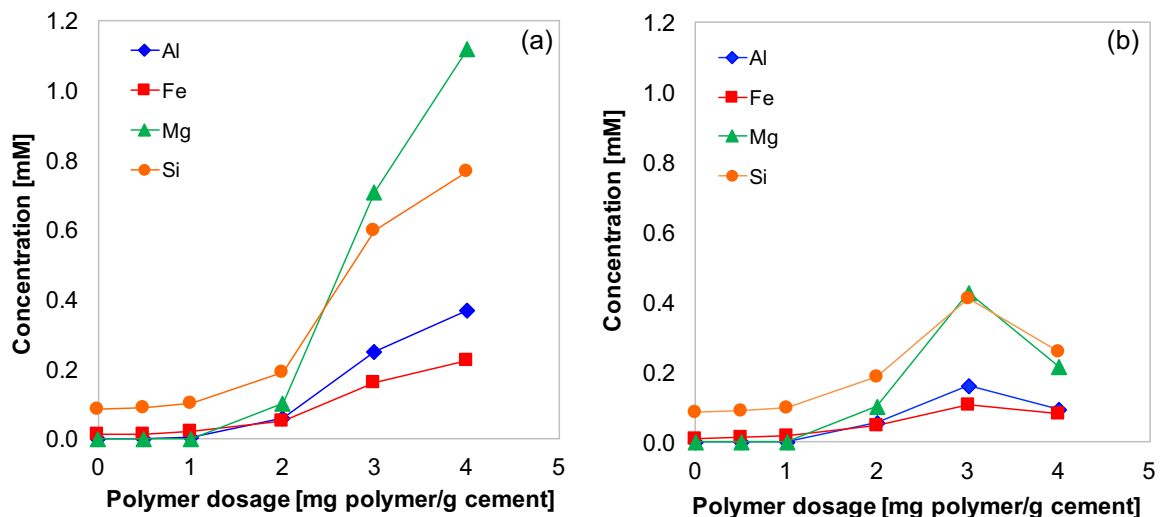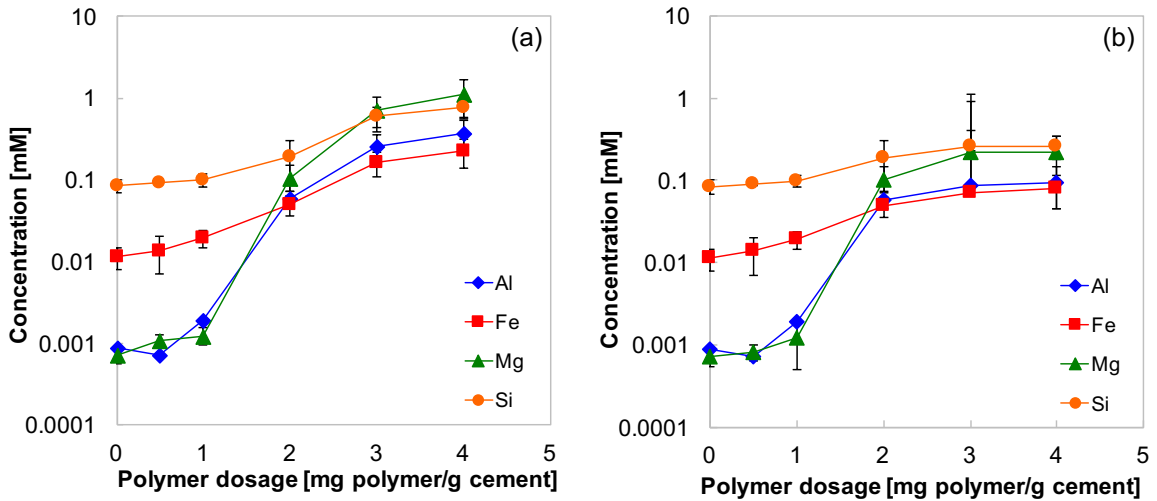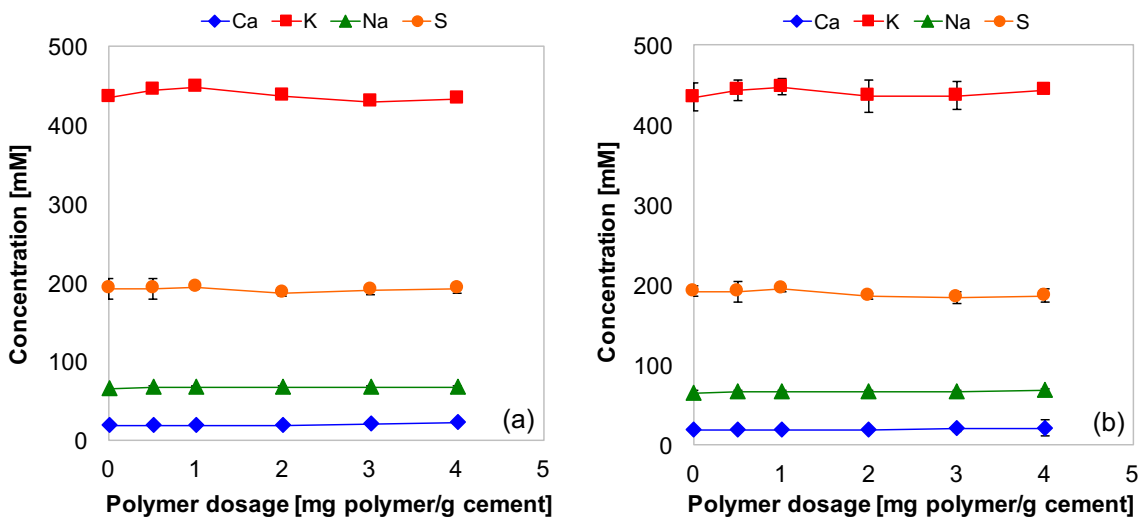**Figure I.4: Composition of pore solutions with polymer 2.5PMA1000 at different dosages for high-concentration elements (Ca, K, Na, S) from the filtration of (a) 50 g and (b) 150 g of admixed cement paste.** The results are shown as the mean values and the standard errors of the mean at the 95% confidence limit with $n_{samples}$ = 3.

In contrast, no significant differences between the two procedures were noticed using one or the other procedure with different amount of paste, for the high-concentration elements (Figure I.4). The relative standard errors are generally of 6% for Ca, and even lower (around 3%) for the other elements, S, K, and Na when the aqueous phases are obtained from 50 g of paste. The relative standard errors from solution filtered from higher amount of paste are slightly greater (namely, 15% for Ca and 4%, on average, for the other elements).

I.3.2 Effect of polymer dosage

Figure I.5 shows that the content of the low-concentration elements increases by increasing the polymer dosage. The maximum concentration of these elements in solution is also dependent on the polymer structure. As a general consideration, the contents of Mg and Si ions in solution are most affected by the presence of PCEs. Specifically, values of about 2.3 and 1.5 mM for Mg and Si, respectively, are reached at the highest dosage of the polymer 2.5PMA1000. For a better comparison among the studied polymers, the concentrations of the same elements were put in relation to the number of charges introduced in the system, as shown in Figure I.6. In addition, the measured yield stress values were also reported in the plots.

Figure I.6 evidences that, for a given polymer, the concentration of this set of elements follows a similar trend by increasing the number of dosed charges.

The evolution of the most concentrated elements obtained by varying the polymer charges cannot be generalized (Figure I.7). Indeed, Na concentration remains approximately constant for broad ranges of dosages and polymer type, whereas Ca concentration tends to increase with the dosed charges. In contrast, S and K concentrations decrease with the dosed charges differently according to the polymer structure.
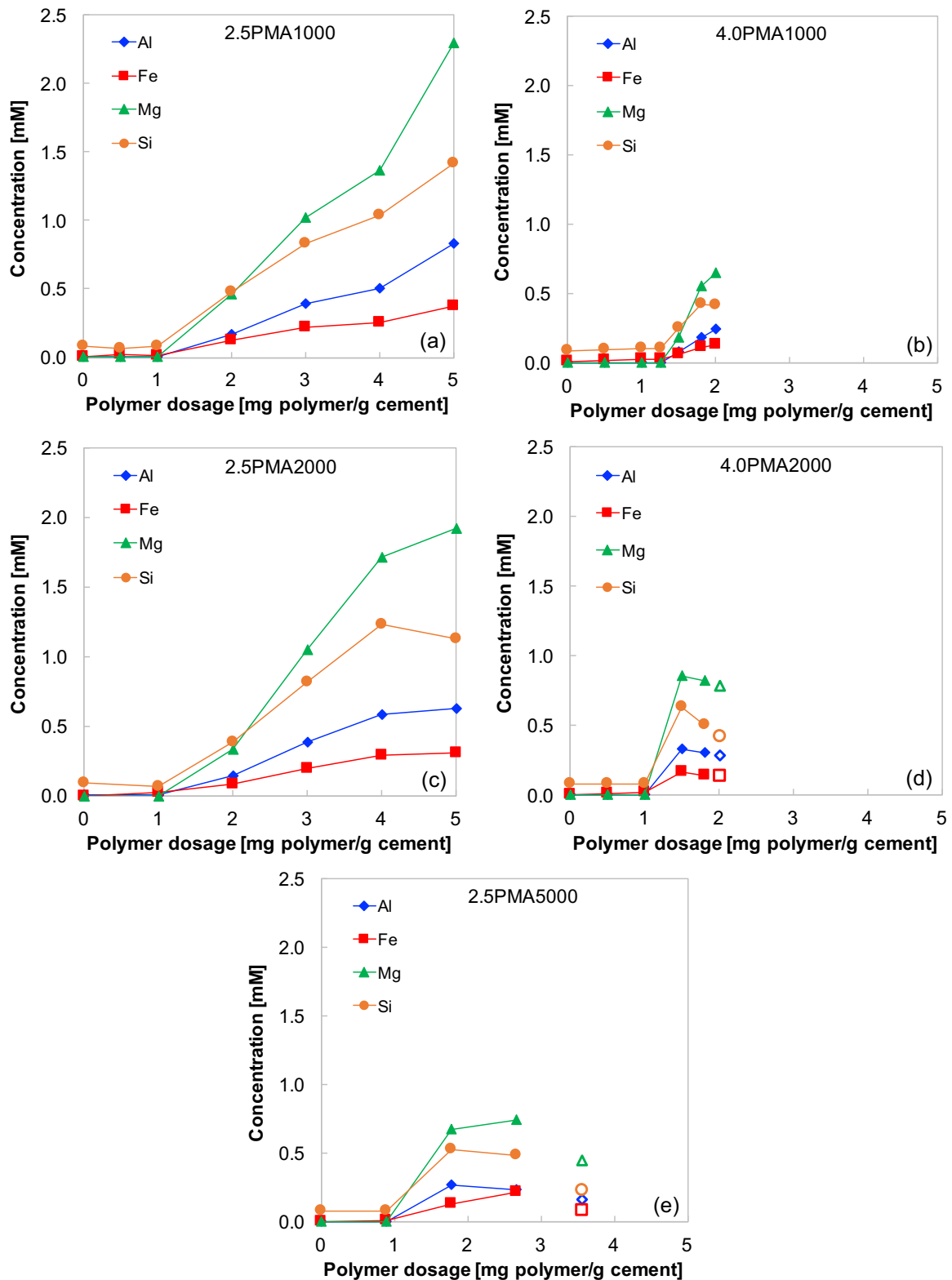
Figure I.5: Composition of pore solutions by increasing the dosages for low-concentration (Al, Fe, Mg, Si) elements with polymers: (a) 2.5PMA1000, (b) 4.0PMA1000, (c) 2.5PMA2000, (d) 4.0PMA2000 and (e) 2.5PMA5000 from the filtration of 50 g of admixed cement paste. The empty symbols represent the elemental composition of cement pastes that were close to the bleeding condition.
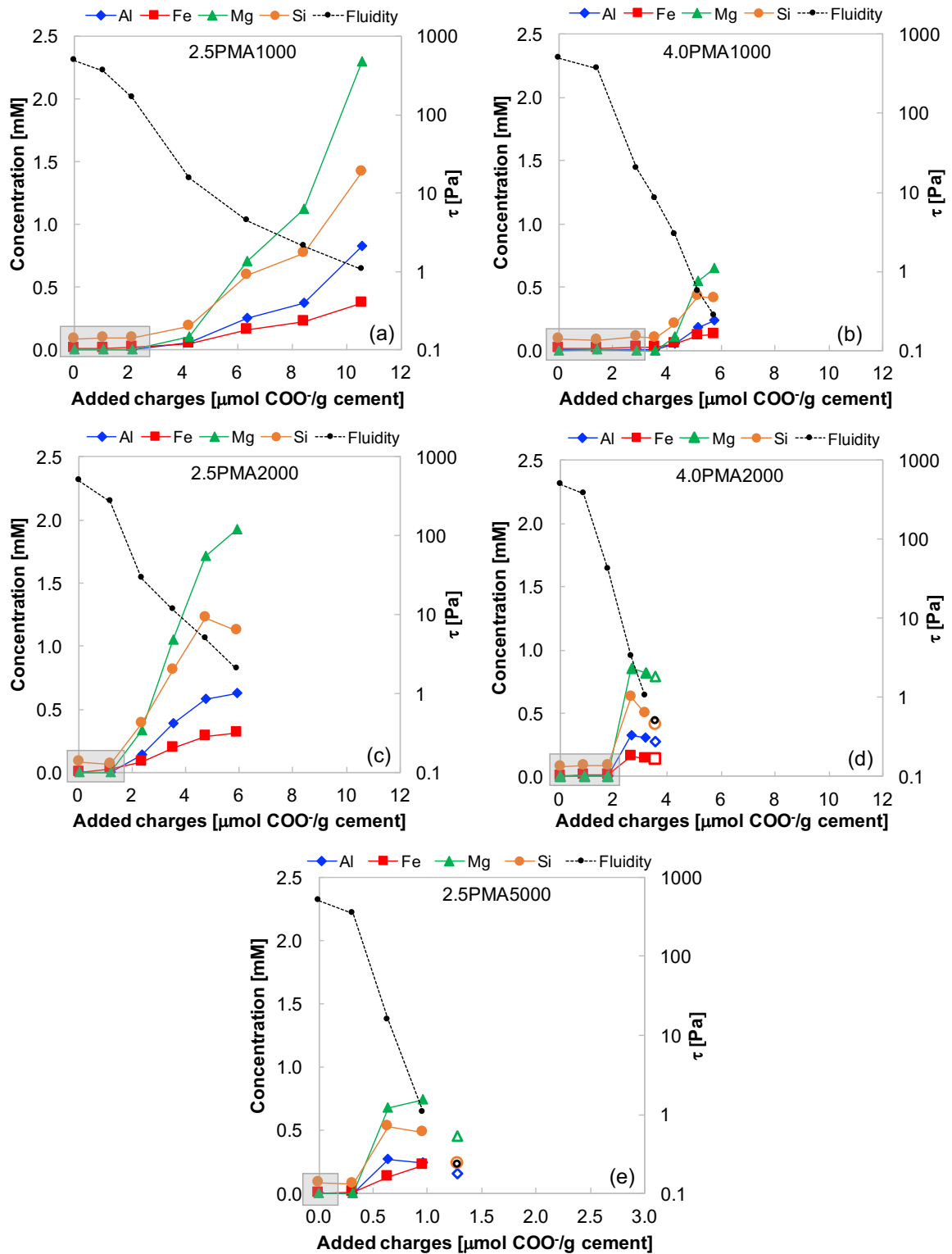
Figure I.6: Composition of pore solutions by increasing the added charges for low-concentration elements (Al, Fe, Mg, Si) with polymers: (a) 2.5PMA1000, (b) 4.0PMA1000, (c) 2.5PMA2000, (d) 4.0PMA2000 and (e) 2.5PMA5000 from the filtration of 50 g of admixed cement paste. Empty symbols represent the elemental composition of cement pastes that were close to the bleeding condition. The grey-shaded areas correspond to concentration values of Al below the LOQ in the diluted solution.
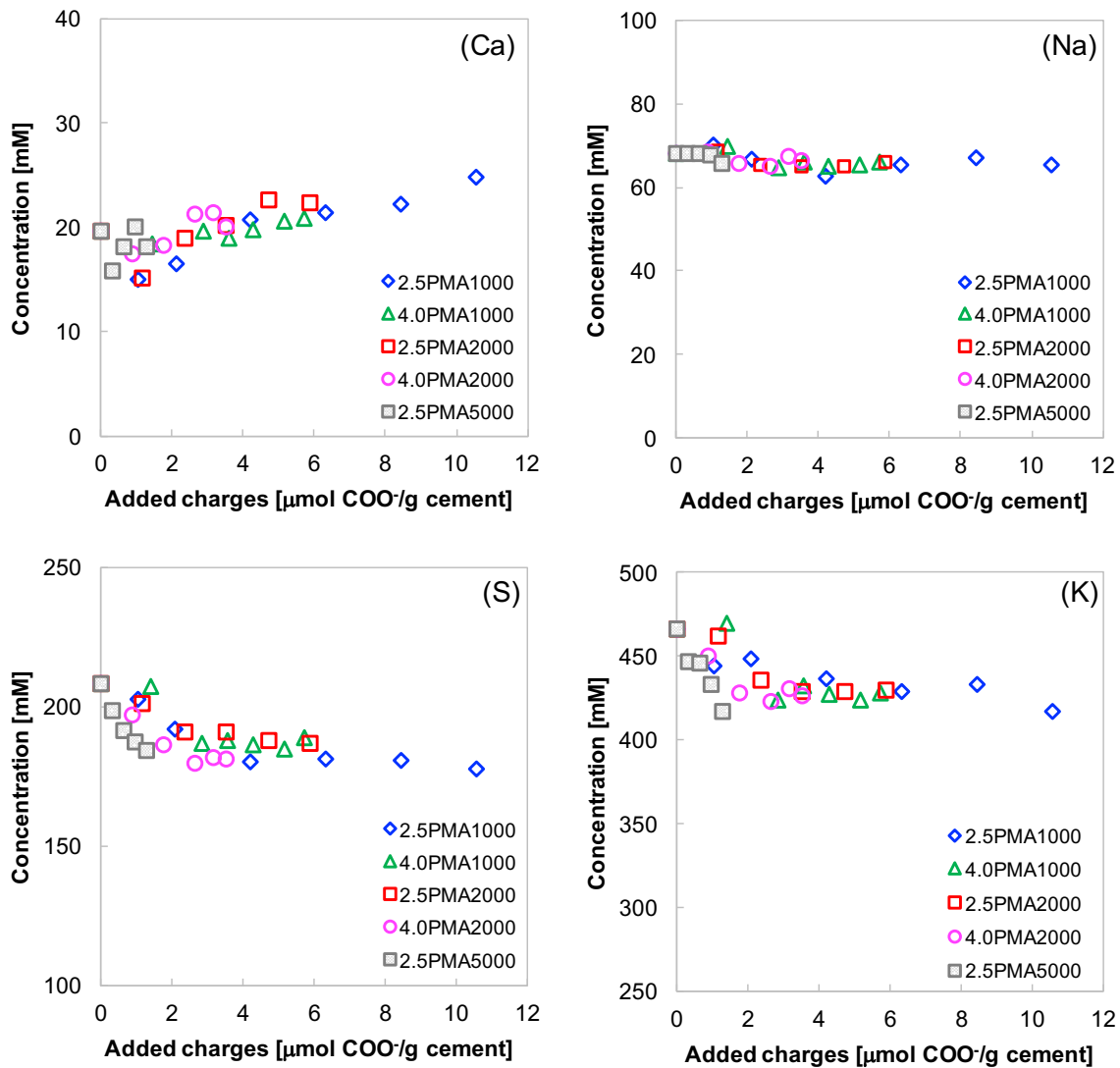
Figure I.7: Composition of pore solutions as a function of the dosages of polymers for low-concentration (Al, Fe, Mg, Si) elements for: (a) 2.5PMA1000, (b) 4.0PMA1000, (c) 2.5PMA2000, (d) 4.0PMA2000 and (e) 2.5PMA5000 from the filtration of 50 g of admixed cement paste. The empty symbols represent the elemental composition of cement pastes that were close to the bleeding condition.

I.3.3 Effect of addition mode of the polymer

The delayed addition of PCE significantly affects the ionic composition of cement pore solutions as well as the yield stress evolution, as shown in Figure I.8. For a given polymer, the amount of the low-concentration elements is drastically reduced by factors of 10 for Si and even 280 for Mg with the 2.5PMA1000 at the highest dosage when the polymer addition is delayed.

This drastic alteration of the concentration of these elements after delayed addition of the polymer corresponds to a greater dispersion even at low PCE added charges.
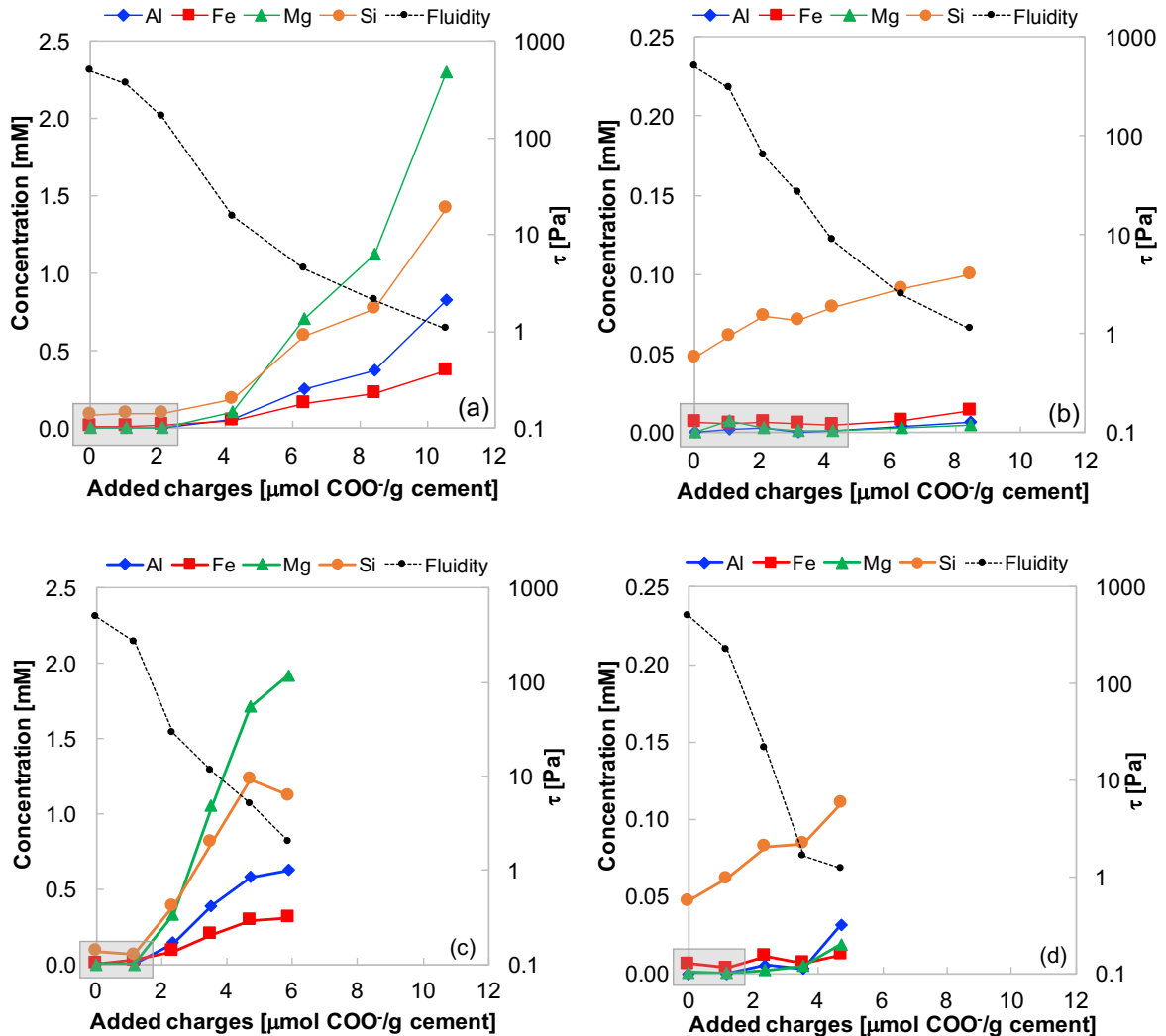
Figure I.8: Composition of pore solutions for low-concentration (Al, Fe, Mg, Si) elements by increasing the added charges using different addition modes with polymers: 2.5PMA1000 (a) direct addition, (b) delayed addition and 2.5PMA2000 (c) direct addition, (d) delayed addition from the filtration of 50 g of admixed cement paste. The grey-shaded areas correspond to the Al values below the LOQ in the diluted solution.

As shown in Figure I.9, the evolution of the concentration of Ca and K remains relatively insensitive to the addition mode of PCE with different structure and dosage. In contrast, the concentrations of Na and S slightly vary when the addition of PCE is delayed.
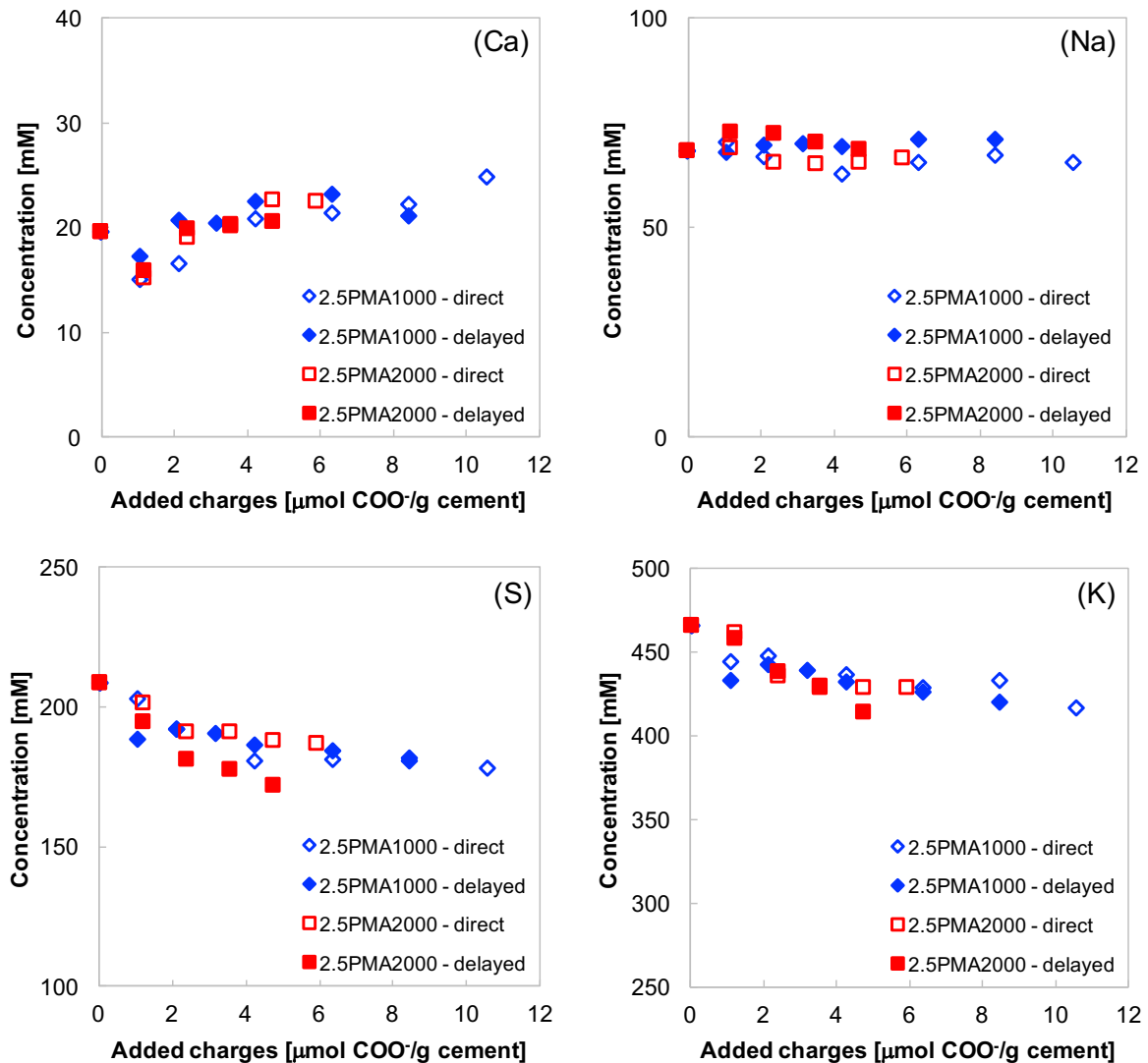
Figure I.9: Composition of pore solutions for high-concentration elements by increasing the added charges with polymers 2.5PMA1000 and 2.5PMA2000 at different addition, direct and delayed, from the filtration of 50 g of admixed cement paste. Ca (top, left), Na (top, right), S (bottom, left) and K (bottom, right).

I.4 Influence of PCEs over time

Figure I.10 shows the qualitative comparison of the evolution of the low-concentration elements over time for the polymer 2.5PMA1000 by varying its initial concentration from 2 to 4 mg/g. After few minutes from the direct addition of the PCE, the concentration of these elements decreases and the rate at which this occurs depends on the polymer dosage. Also, this decay may be fitted with an exponential function, but the meaning of this is unclear and would require further investigation.

The evolution of the high-concentration elements appears more homogeneous by varying the initial dosage (Figure I.11).
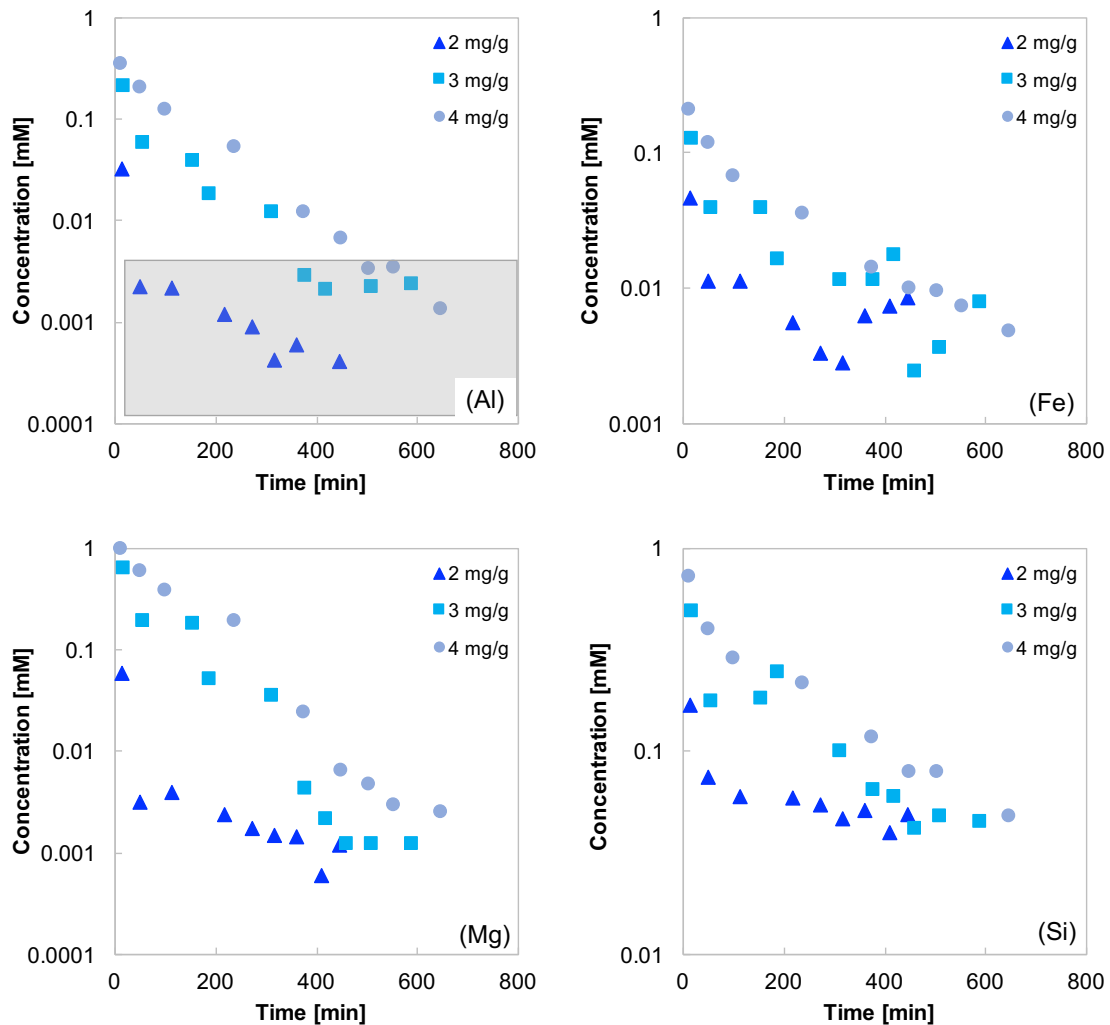
Figure I.10: Composition of pore solutions over time from cement pastes with 2.5PMA1000 at three different dosages for low-concentration elements: Al (top, left), Fe (top, right), Mg (bottom, left) and Si (bottom, right). The grey-shaded areas correspond to the Al values below the LOQ in the diluted solution. The filtration was carried out from 50 g of admixed cement paste.

After a small initial increase, Ca concentration tends to decrease over time. S shows the opposite trend characterized by an initial significant decrease. This is followed by an increase of its concentration over time with a dosage-dependent evolution. For Na and K we observe a common trend by normalizing the data by the value at the latest time. A common similar normalized concentration is quantified at the beginning with a gradual increase that depends on the dosage.
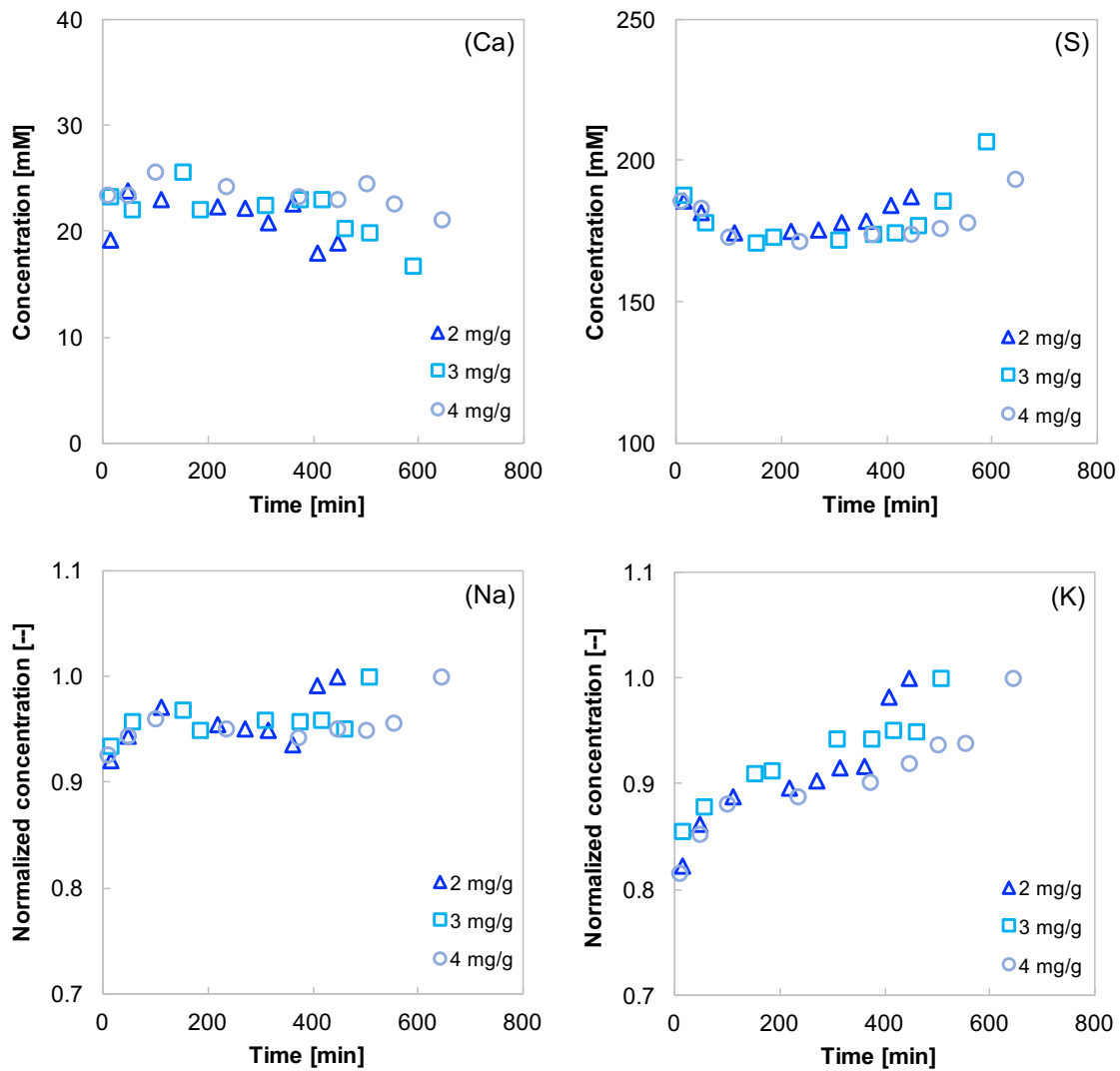
Figure I.11: Composition of pore solutions over time from cement pastes with 2.5PMA1000 at three different dosages for high-concentration elements: Ca (top, left), S (top, right), Na (bottom, left) and K (bottom, right). The filtration was carried out from 50 g of admixed cement paste.

I.5 Discussion

I.5.1 Presence of nanoparticles

As presented in Chapter 4, the observed increase of the low-concentration elements when PCE is added in direct mode could be explained by the formation of nanoparticles or agglomerates in the aqueous phase. DLS measurements of the aqueous phase shown in Figure I.12 evidence how the size of these species varies when increasing the polymer dosage. In particular, the main peak seems to shift towards lower sizes at high polymer dosages. A quantitative assessment of these

nanoparticles is not possible due to the lack of an appropriate calibration. The qualitative comparison of the intensities suggests that the number of the scattered nanoparticles increasing with the dosage of polymer initially added in the cement paste.
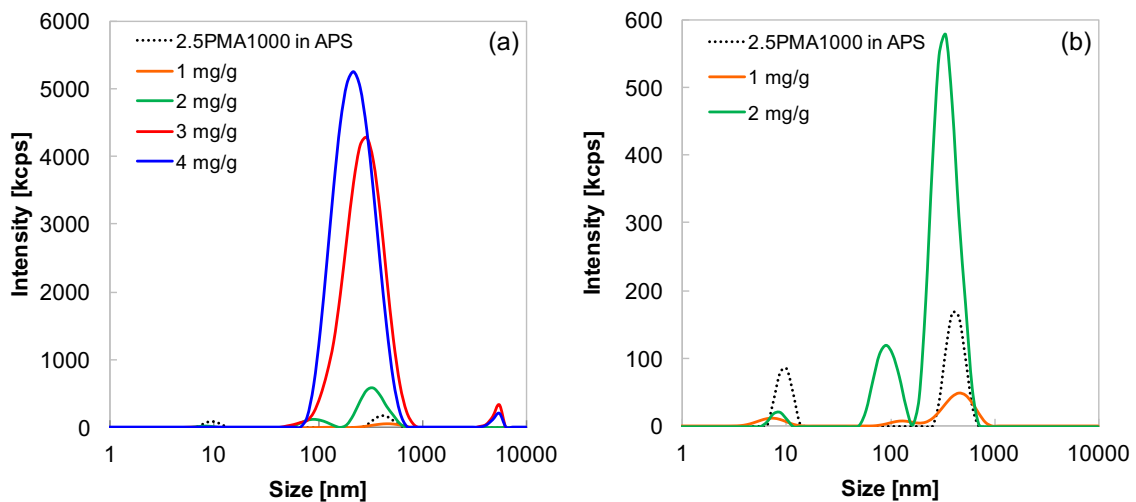
Figure I.12: Intensity size distribution of pore solutions from cement pastes containing different 2.5PMA1000 dosages in direct addition mode: (a) Overall view, (b) zoom of the Intensity size distribution for the pure polymer in artificial pore solution and the lowest PCE dosages.

In Chapter 4, we reported that a filtration of the pore solutions with a 0.1 μm syringe filter (after a first one with a 0.45 μm syringe filter) leads to a systematic decrease of the low-concentration elements. However, from DLS measurements, we showed that some particles can be smaller than 0.1 μm. It has been reported in literature that such nanoparticles can be separated by centrifugation [308]. Firstly, we noted that the centrifugation does induce a visible separation with a sediment at the bottom of the vial. Also, the nature of this sediment is different for solution filtered from pastes with 2 or 4 mg/g of polymer. At low dosage, the resulting pore solution after centrifugation within one hour of hydration appears opaque from the beginning and the sediment is white and spread at the bottom of the vial (Figure I.13b). In contrast, in (Figure I.13a) solutions from highly admixed pastes appear yellowish with a brown sediment at the bottom of the plastic vial. In both cases, these solutions became more transparent over time and the sediments disappeared. The ICP measurements were carried out on the solutions deprived of the solid.
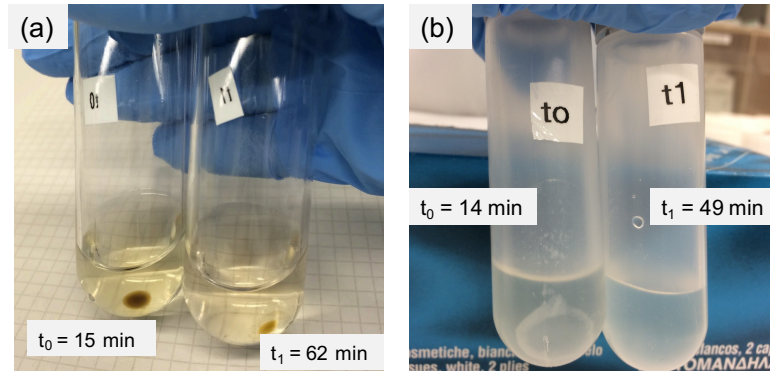
Figure I.13: Cement pore solution after filtration and subsequent centrifugation filtered from 50 g of paste plasticized with 2.5PMA1000 dosed at: (a) 4 mg/g and (b) 2 mg/g
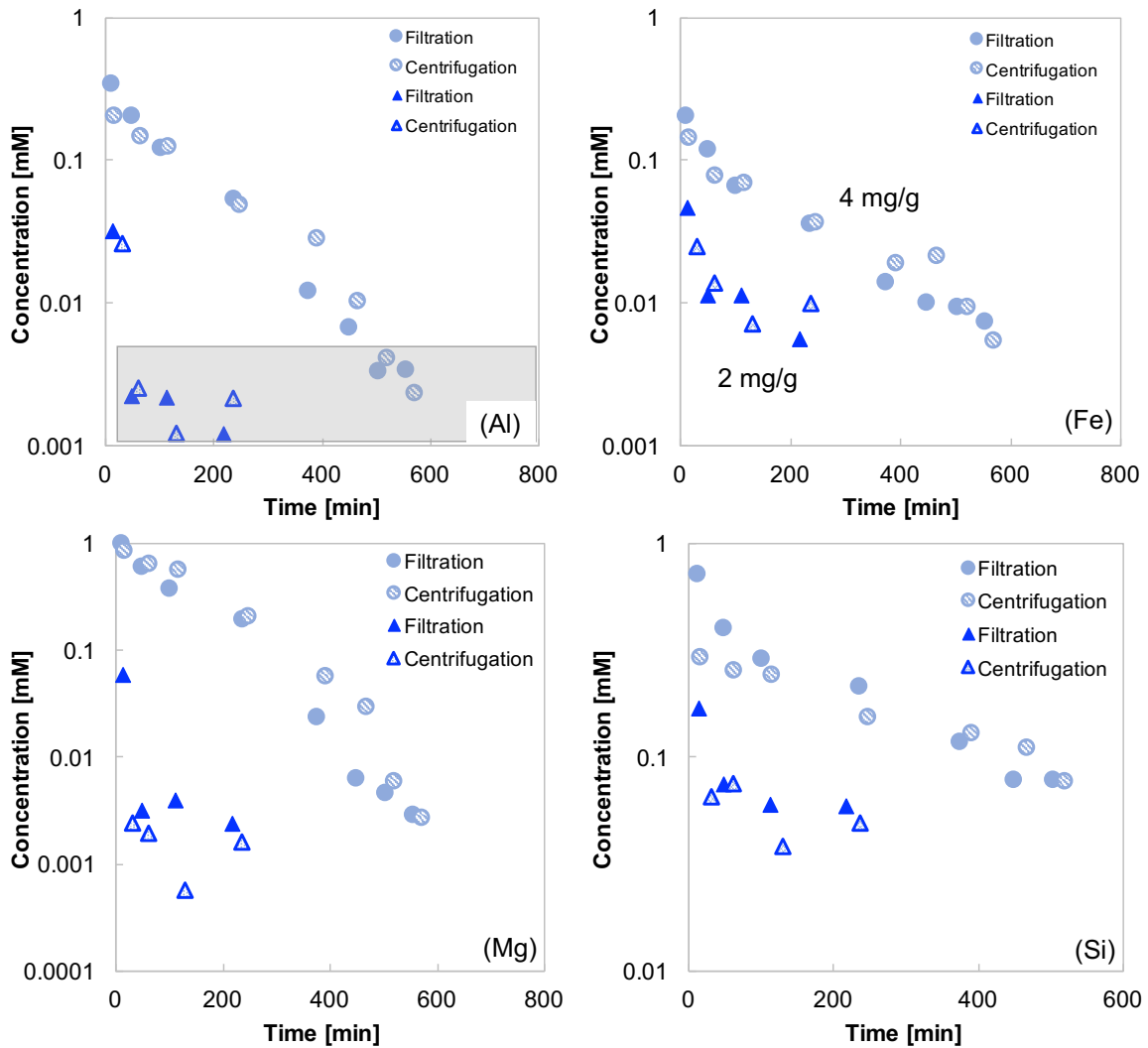
Figure I.14: Composition of pore solutions over time from cement pastes with 2.5PMA1000 dosed at 2 mg/g (triangles) and 4 mg/g (circles) for low-concentration elements after filtration and centrifugation: Al (top, left), Fe (top, right), Mg (bottom, left) and Si (bottom, right). The grey-shaded areas correspond to the Al values below the LOQ in the diluted solution. The filtration was carried out from 50 g of admixed cement paste.

As shown in Figure I.14, only small differences of the amount of low-concentration elements are quantified in pore solutions before and after the centrifugation. The Si represents the only exception, showing a decrease in the first 30 minute of hydration induced by the centrifugation. The amount of the high-concentration elements in solution is not affected by this additional treatment.
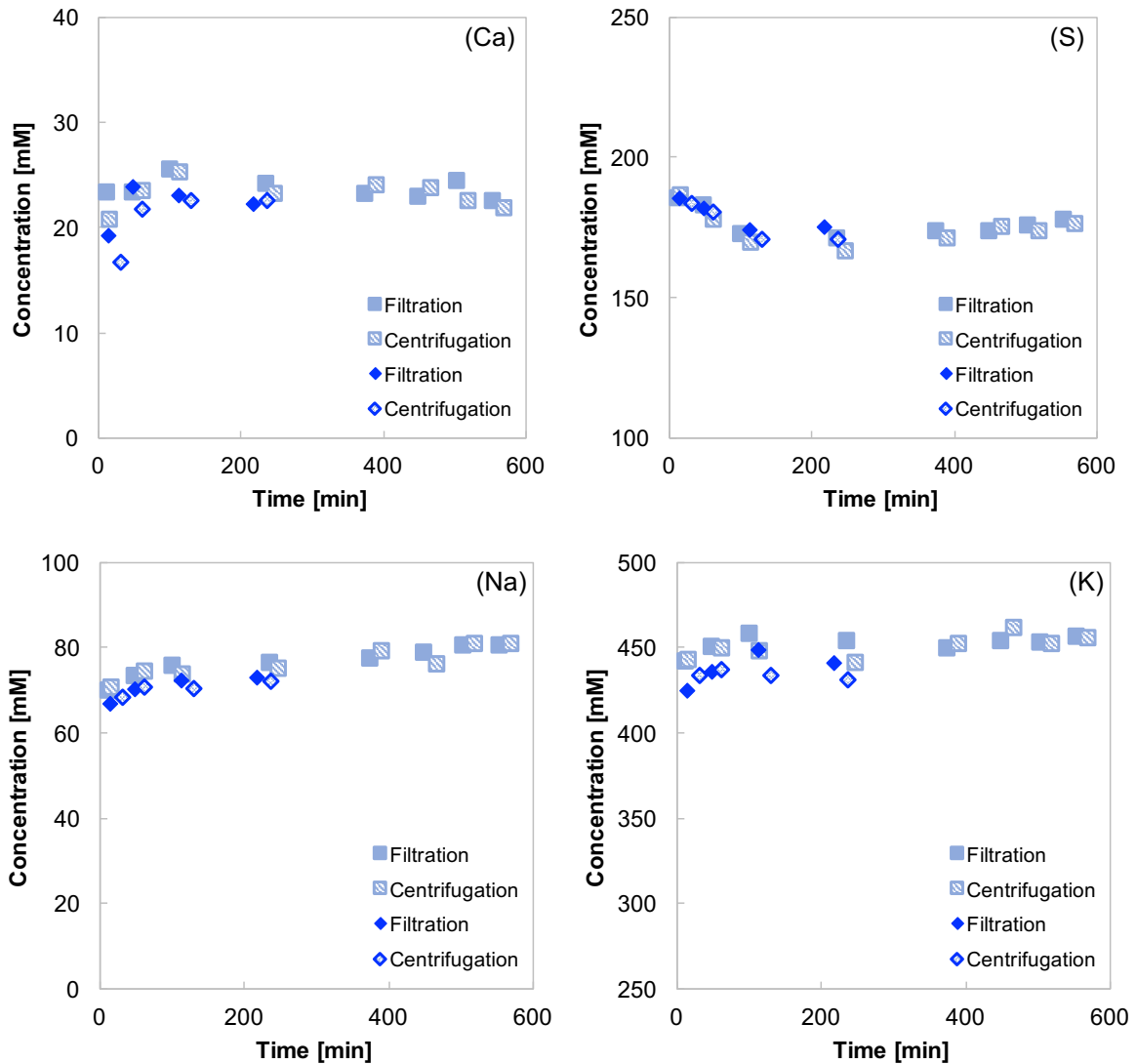
Figure I.15: Composition of pore solutions over time from cement pastes with 2.5PMA1000 dosed at 2 mg/g (diamond) and 4 mg/g (square) for high-concentration elements after filtration and centrifugation: Ca (top, left), S (top, right), Na (bottom, left) and K (bottom, right). The filtration was carried out from 50 g of admixed cement paste.

I.5.2 Influence of pore solution composition on rheology

We showed that PCEs alter the dissolution and nucleation of hydrates and the significant increase of the amount of low-concentration elements, mainly Al and Mg,

is the main expression of this change at the beginning of the hydration. This mechanism is dependent on both polymer architecture and dosage. Indeed, pore solutions filtered from cement pastes with polymers having high C/E ratio are generally less concentrated in Al, Mg, Fe, and Si with respect to pastes with polymer with C/E = 2.5. This is observed as a result of a better dispersion with polymers having high C/E ratio, at given dosed charges.

The amount of the low-concentration elements drastically increases when the polymer is added directly with the mixing water. This scenario is totally altered when the polymer is added few minutes after the mixing water, regardless of the type of used polymer.

The amount of the high-concentration elements does not seem to be affected by the structure of the polymer, but rather by the dosage. Also, the delayed addition of the polymer does not influence the overall composition of the cement pore solutions.

Interestingly, we observed that the amount of the low-concentration elements tends to decrease exponentially over time. However, the beginning of this decay cannot be directly related to the time at the onset, corresponding to 183, 265, 337 minutes for the 2.5PMA1000 dosed at 2, 3, and 4 mg/g, respectively. The same consideration is valid also for the high-concentration elements.

At the beginning of the hydration, small nuclei are stabilized in the interstitial fluid by the presence of the polymer, that influences also their size. Therefore, we hypothesize that this decay observed over time might be due to the growth and precipitation of the hydrates on the cement grains resulting in a reduced concentration in solution. Under such conditions, these hydrates cannot be then easily separated from the paste. The fact that the centrifugation did not show a significant and systematic changes in pore solution composition over time might be related to the sample preparation involving a first filtration with a 0.45 μm syringe filter. However, we show that the concentration decay is influenced by the polymer dosage and we support the idea that the polymer structure could also play a significant role. At this stage, based on the above-mentioned arguments, the

formation of complexes claimed in Chapter 4 to justify the increase of the low-concentration elements cannot be excluded.

I.6 Conclusions

A reliable procedure for preparing cement pore solution for ICP measurements is presented, underlining the detrimental effect caused by an incomplete filtration.

As shown in Chapter 4, the increase of the amount of the low-concentration element by increasing the PCE dosage is confirmed. It was also demonstrated that polymers with different structures affect the final concentrations differently. Also, the delayed addition of PCEs plays a role, decreasing the amount of the low-concentration elements at similar and very low levels found in solutions filtered out from plain mixes. In both addition modes, the amount of Ca, Na, S, and K does not vary significantly with PCEs dosages.

Interestingly, the amount of the low-concentration elements varies substantially over time. At the beginning of the hydration – generally within one hour –, their concentration is high and it depends on the initial PCE dosage used. Afterwards, their amount in solution drops exponentially. Unfortunately, it was not possible to correlate this evolution with the rheological properties (mainly the onset time).

Appendix II

Supplementary material for chapters 5 and 6

II.1 Quantification of PCE charges by acid-base titration

The characterization of the main characteristics of the polymers used in the present work is summarized in Chapter 5. Besides the molar mass, the number of charges on the backbone is a property of major interest. In fact, the latter affects the affinity and thus the adsorption mechanism of the polymer onto the cement particles [12,91].

Acid–base titration is a titrimetric method, in which an acidic or basic titrant reacts with the analyte that is present in solution. The signal is a volume. The equivalent point occurs when equivalent amounts of analyte and titrant react according to the stoichiometry of the reaction. The concentration of the analyte can be calculated considering the concentration of the titrant reacting with the analyte and the volume added at the endpoint (which should be as close as possible to the equivalent one) [322]. A specific acid-base titration in Ultrapure Water (UPW) was developed for PCEs and results are compared to the those obtained by High-Performance Liquid Chromatography.

II.1.1 Materials and methods

II.1.1.1   Materials

The characterization Five non-commercial polycarboxylate ether-based comb polymer, provided by SIKA AG, were used as superplasticizer (SP) in the present study. They were synthesized by copolymerization. The ester and methacrylic acid (MA, Sigma-Aldrich) were simultaneously put into the reactor filled with ultrapure water (UPW) for four hours, to favour a more uniform charge distribution along the backbone, and to limit the gradient of charges typical for copolymerization (Table 2.1). The used esters are Bisomer S10W and Bisomer S20W, both supplied by Geo Speciality Chemicals, and Bisomer 5000 from Evonik Plex 6965-O. The used initiator and the chain terminator were $Na_2S_2O_5$ (Sigma-Aldrich, puriss., ACS reagent, 98-100.5%) and $Na_2S_2O_8$ (Sigma-Aldrich, reagent grade, ≥98%), respectively.

The synthesis of these polymers is typically incomplete and residual monomers, side chains and salts remain in solution, as reported in Table II.1.

Table II.1: Content of the residual (w/w %) present in the original polymers and the ultrafiltered ones. The former residuals are obtained considering the yield of reactions provided by the manufacturer (SIKA AG, Switzerland). The latter ones are estimated by SEC measurements conducted in our laboratory.

	Residuals (%)	
	Original polymer	Filtered polymer
2.5PMA1000	10.2	--
2.5PMA2000	16	--
2.5PMA5000	15.5	11
4.0PMA1000	13.4	--
4.0PMA2000	18.1	--

However, for the present study, pure polymers are needed for a better quantification of their amount in cement pastes. Therefore, the polymers were ultrafiltered by a Labscale TFF System (Merck Millipore). The ultrafiltration system was equipped with a polyethersulfone (PES) membrane Pellicon XL Biomax 5kDa (Millipore Corporation) for polymers having side chain length of 1 and 2 kDa or a PES membrane Pellicon XL Biomax 10 kDa (Millipore Corporation) for those

polymers with side chain length of 5 kDa. As shown in Table II.1, the residuals in the polymer 2.5PMA5000 could not be efficiently removed, although a membrane with a bigger pore size was used.

The molar masses of these polymers were determined by size exclusion chromatography (SEC) with an Agilent 1260 Infinity system (Agilent Technologies, Santa Clara, CA, USA) equipped with refractive index (RI) and multi-angle laser light scattering (MALS) detectors. The eluent for SEC was Na_2HPO_4 0.067 mol/L at a flow rate of 1 mL/min. The molar masses of the studied polymers are reported in Table II.3.

Table II.2: Molar masses (Mw) of the studied PCEs, as obtained from SEC measurements with standard calibration with PEO/PEG standards based on RI and absolute method based on MALLS.

	Mw (Da)	
	Standard Calibration by RI	**Absolute method by MALS**
2.5PMA1000	32000	31900
2.5PMA2000	47000	64000
2.5PMA5000	106000	--
4.0PMA1000	28700	25400
4.0PMA2000	40000	45700

The molar mass determination was generally done by SEC-MALS. The refractive index increment value (dn/dc), needed for SEC-MALS, of each PCE was determined on-line. This protocol represents the best possible approximation of the molar mass of our polymers. However, this is effective only when the exact concentration of the pure polymer is known.

This was not the case for the polymer 2.5PMA5000, containing about 11% of residual chains (estimated by SEC) even after the ultrafiltration. The molar mass for this polymer, therefore, was determined with refractive index (RI) by a calibration based on PEO/PEG standards.

Importantly for this work, the properties of the adsorbed polymer as the layer thickness and the surface occupied per unit mass do not depend on n [65,68,92].

Therefore, inaccuracies on the molar mass determination are not critical in terms of interpreting polymer structure effects.

Table II.3: Molar masses (Mw) of the studied PCEs, as obtained from SEC measurements with standard calibration with PEO/PEG standards based on RI and absolute method based on MALLS.

	Mw (Da)	
	Standard Calibration by RI	**Absolute method by MALS**
2.5PMA1000	32000	31900
2.5PMA2000	47000	64000
2.5PMA5000	106000	--
4.0PMA1000	28700	25400
4.0PMA2000	40000	45700

II.1.1.2   Method for charges quantification in UPW

The titration system consists of an automatic titrator (EasyPro Titration, Mettler Toledo GmbH, Switzerland) equipped with a pH electrode suitable for aqueous solution (EG11-BNC) and a temperature sensor (NT1000), both by Mettler Toledo GmbH. The solution is constantly stirred during the measurement. The functionality and the calibration of the pH electrode are periodically checked with buffer solutions at pH 3 and 7 at 20 °C (Fluka).

The quantification of the charges is achieved by the titration of a polymeric solution, having a known mass of 1.5 g of active polymer with a KOH solution at a known concentration. The KOH solution used as titrant is standardized with the primary standard potassium hydrogen phthalate (KHPt, Fluka, for HPLC, $\geq$ 99.5%). The concentration of the titrant is 0.4275 M $\pm$ 0.004 M.

A reliable quantification of the polymer charges requires that all the carboxylic groups are protonated. This can be achieved by adding a concentrated solution of HCl (Fluka, TraceSELECT, fuming, $\geq$ 37%) drop by drop to reach pH 1.6. Therefore, the titration evolves with two equivalent points (EQPs). The first point at lower pH corresponds to the titration of the excess of HCl, the latter at around pH 9 to the titration of the carboxylic groups of the polymer. This titration system can detect

both EQPs, but it only reports the last one detected and does so giving the used volume to reach that EQP.

To overcome this inconvenience, the polymeric solution is split in two after the preliminary acidification with HCl. The first titration is necessary to identify the first EQP and this value can be considered as blank. This value is then subtracted from the one from the complete titration with two EQPs. The obtained values (expressed as mmol) need to be normalized by the amount of pure polymer in solution titrated, as follows:

$$\text{N}umber\ of\ carboxylic\ groups = \frac{n}{m_{polymer}} = \frac{n_{EQP2}}{(m_{polymer})_2} - \frac{n_{EQP1}}{(m_{polymer})_1} \qquad \textbf{(II.1)}$$

where n represents the moles expressed in mmol and $m_{polymer}$ the mass of the polymer in g.

In this way, it is only necessary to know the concentration of the initial solution and the amount of polymer in both solutions after acidification.

The number of charges can be expressed either as mmol carboxylate/g polymer or as mg KOH/g polymer, commonly indicated as TCAV (Total Carboxylic Acid Value) [323].

For PCEs, the number of charges can be expressed in mmol/g active polymer as:

$$x_0 = n_{RU}^{tot} \cdot {C}/{E} \cdot 1000 \qquad \textbf{(II.2)}$$

where $n_{RU}^{tot} = \frac{c_{PCE}}{M_{RU}}$ is the total number of repeating unit, c_{PCE} is PCE dosage by mass (mg/g cement) and M_{RU} is the molar mass (g/mol) of the repeat unit given by:

$$M_{RU} = P \cdot M_{SC} + ({C}/{E} + 1) \cdot M_{BB} \qquad \textbf{(II.3)}$$

with M_{SC} and M_{BB} the molar masses of the side chains and the backbone monomers, respectively, here ethylene oxide and methacrylic acid. From Equation (II.3), the C/E ratio can be derived as follows:

$$C/{E} = \frac{x_0(P \cdot M_{SC} + M_{BB})}{1000\ c_{PCE} - x_0 M_{BB}} \qquad \textbf{(II.4)}$$

II.1.2 Results and discussion

II.1.2.1   Charges quantification in UPW

Table II.4 reports the number of charges expressed in mmol/g of polymer from Equation (II.1) and as TCAV. C/E ratios calculated according to Equation (II.4) are also included. The measurements were repeated three times on three independent polymeric solutions in UPW. For the quantification of the charges of the polymer 2.5PMA5000, the content of residuals was taken into account in the final amount of dosed polymer used for the titration.

Table II.4: Charges quantification of filtered PCEs in UPW at 23 °C

	Number of charges		Calculated C/E ratio
	COO⁻ (mmol/g polymer)	TCAV (mg KOH/g polymer)	
2.5PMA1000	2.111 ± 0.009	118.4 ± 0.5	2.80 ± 0.02
2.5PMA2000	1.18 ± 0.07	66 ± 4	2.75 ± 0.08
2.5PMA5000	0.36 ± 0.01	20 ± 1	1.91 ± 0.03
4.0PMA1000	2.87 ± 0.02	161 ± 1	4.13 ± 0.04
4.0PMA2000	1.77 ± 0.01	99.5 ± 0.4	4.36 ± 0.02

II.1.2.2   Comparison with HPLC

The C/E ratios calculated after the titration are compared to the values provided by the manufacturer (SIKA AG, Switzerland) using a procedure based on HPLC analysis (Waters Acquity UHPLC System, equipped with Evaporative Light Scattering (ELS) and Photodiode Array (PDA) detector). The HPLC protocol involves the quantification of unreacted monomers (methacrylic acid and methacrylic-PEG ester) and hydrolysed side chain monomers (resulting in free PEG) by UHPLC. Knowing the amount of the reagents introduced, the amount of reacted monomers can then be calculated by subtracting the relative values. In this way, the composition of the final polymer is known and the charges per mass of polymer can be calculated (personal communication of Lukas Frunz, SIKA AG, Switzerland).

The comparison between the two methodologies used for the estimation of the polymer charges in Figure II.1 shows results in very good agreement. Furthermore, this similarity confirms that these polymers, synthesized a couple of years ago, did not hydrolyse over time in water solution with a concentration ranging between 20 and 40%.

The main advantages in adopting the HPLC protocol is that immediate results after the synthesis can be obtained and that only a tiny amount of sample is necessary. However, since a calibration with the original reagent used for the synthesis is needed, this would be in principle very difficult to apply at later times.
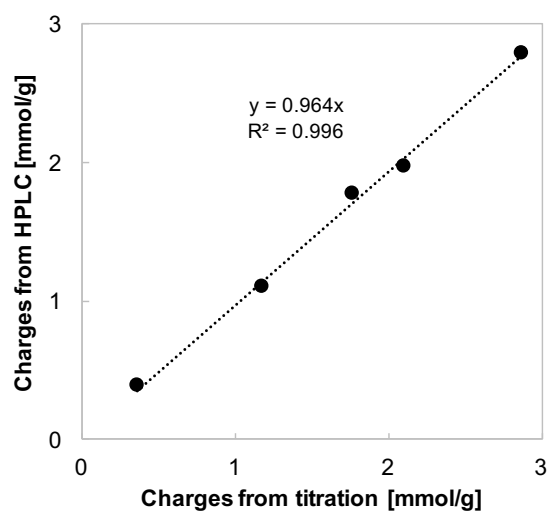
Figure II.1: Comparison between acid-base titration and HPLC method for the quantification of the charges of PCEs in UPW.

The acid-base titration is therefore more suitable for off-line and quality control measurements over time after synthesis. Also, possible hydrolysis reactions of PCEs in alkaline medium at different temperatures could be investigated [173]. However, a relatively high amount of sample for a single measurement is needed, as well as an accurate quantification of the amount of residuals. In case of ultrafiltered polymers, the residues should be removed, so that this issue is eliminated.

II.1.3 Conclusions

The amount of charges on the backbone of PCEs affects the initial interaction with cement grains. A reliable quantification is therefore useful for a better comparison of

the performance of different polymers. In this Annex, it was demonstrated that the titration acid-base protocol provides precise results in agreement with the ones obtained from a different technique, as HPLC. However, it is worth reminding here that these values, whatever methods is used, would be consistent with the performance in cement pastes only if the charges are randomly distributed on the backbone. This implies that different polymeric fractions would in principle have a proportional number of charges. It is generally claimed that copolymerization would lead to less homogeneous charge distribution. However, it is expected that the specific synthetic pathway adopted for the polymers used in this thesis should limit this. There are, however, no quantitative studies about such issues for PCEs formed by copolymerization. For grafted ones, the situation is not much better, with the thesis of Ms. Gelardi (ETHZ, this group) [324] being the first to address this question in a rigorous way.

II.2 Adsorption isotherms

The adsorption isotherms for the five studied polymers are shown in Figure II.2.
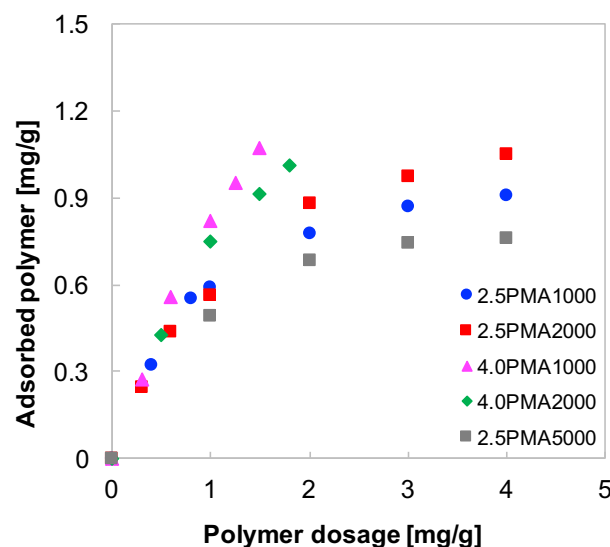
Figure II.2: Adsorption isotherm (at 23 °C) for the five studied polymers.

For the study of the adsorption isotherms, cement pastes were prepared in a small batch (200 g of cement) according to the procedure described in section 4.3.2.2 and

the solution preparation according to the procedure in section 5.2.2.4. The filtration of cement pore solution started after 6 minutes from the first contact with UPW.

II.3 Spread diameter in relation to heat rate

Relations between the spread diameter and the heat rate for the studied polymers at different dosages are presented from Figure II.3 to Figure II.7. Empty symbols at spread flow lower than 6.5 cm were excluded in the optimization of the fit as in Figure 5.15.

Table II.5 reports the values of $D_{0,0}$ and v obtained from Figure II.3 to Figure II.7 according to the procedure described in section 5.4.2.
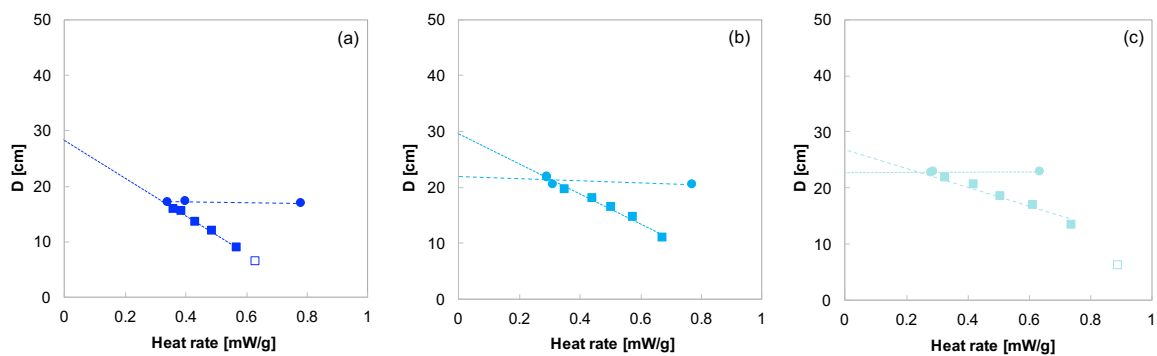
Figure II.3: Relation between spread diameter and heat rate for the polymer 2.5PMA1000 dosed at: (a) 2 mg/g, (b) 3 mg/g, and (c) 4 mg/g
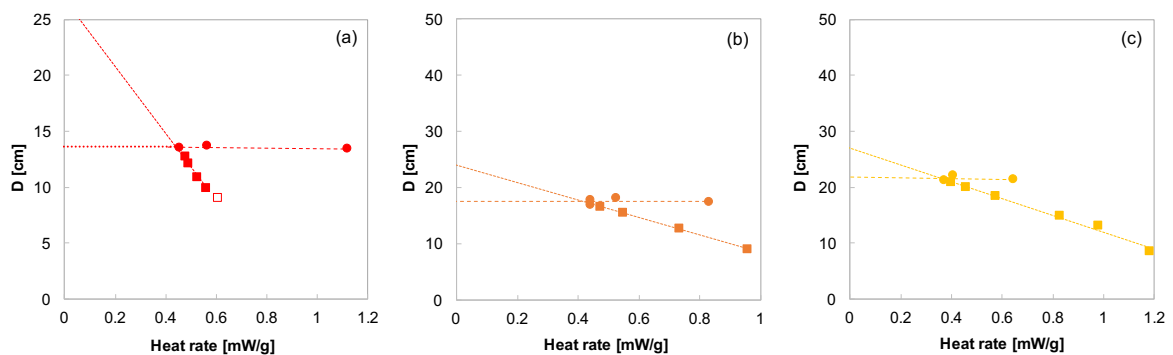
Figure II.4: Relation between spread diameter and heat rate for the polymer 2.5PMA2000 dosed at: (a) 2 mg/g, (b) 3 mg/g, and (c) 4 mg/g.
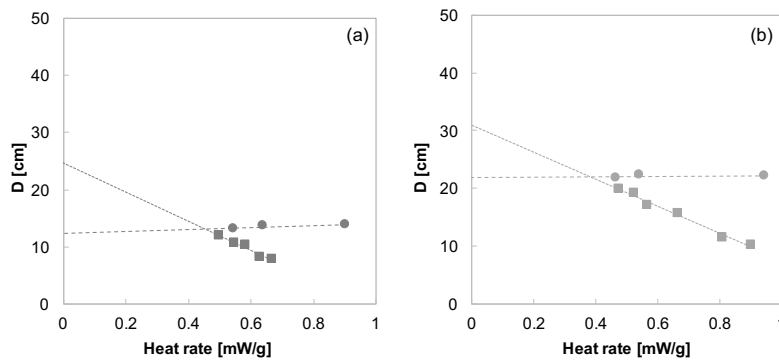
Figure II.5: Relation between spread diameter and heat rate for the polymer 2.5PMA5000 dosed at: (a) 2 mg/g and (b) 3 mg/g.
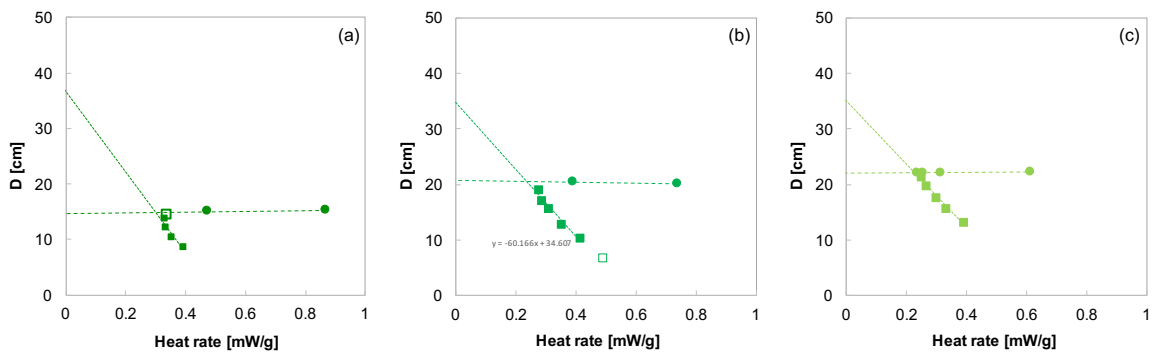
Figure II.6: Relation between spread diameter and heat rate for the polymer 4.0PMA1000 dosed at: (a) 1 mg/g, (b) 1.25 mg/g, and (c) 1.5 mg/g.
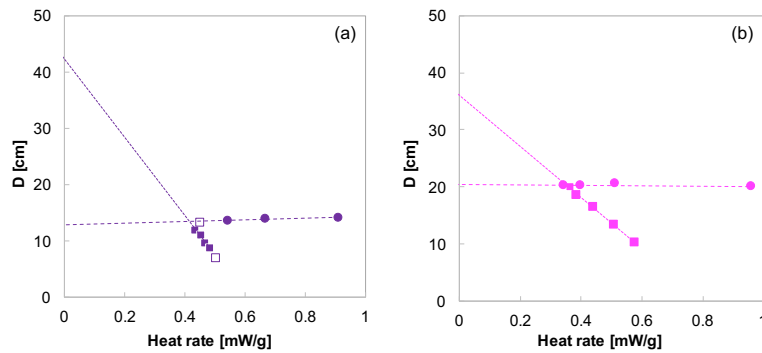
Figure II.7: Relation between spread diameter and heat rate for the polymer 4.0PMA2000 dosed at: (a) 1 mg/g and (b) 1.5 mg/g

Table II.5: Summary of the intercepts $D_{0,0}$ and the slope v for the studied polymer at different dosages from the linear regression of D versus heat rate in the acceleration period shown in Figure II.3-7.

Polymer	Dosage [mg/g]	$D_{0,0}$ [cm]	v [cm·mW/g]
2.5PMA1000	2	28.18	33.77
	3	29.52	26.67
	4	29.02	20.70
2.5PMA2000	2	21.53	21.94
	3	23.77	15.34
	4	27.02	15.02
2.5PMA5000	1.78	24.76	25.61
	2.67	30.95	23.39
4.0PMA1000	1	36.69	72.51
	1.25	34.61	60.17
	1.5	34.87	56.66
4.0PMA2000	1	42.16	69.36
	1.5	35.98	44.54

II.4 Considerations on possible role of roughness on flow loss

At one point in this thesis, changes in surface roughness of cement particles were considered as a possible alternative interpretation for yield stress changes. The explanation may have some value and might be in the background of the effects of particle size and or surface coverage discussed in Chapter 6. Therefore, it was decided to document the thoughts we had on this subject as an annex. The main idea is that the formation of C-S-H at contact points between grains plays a relevant role.

II.4.1 Yield stress amplification

The equation for our master curve indicates that, after the onset, the yield stress is amplified by an exponential function of the specific surface area (or heat rate). This means that the yield stress at a given dispersion at time t is equal to the yield stress

at the onset multiplied by an (exponential) function of the change in specific surface area (or heat rate) between the onset and that time t.

From the Chapter 6, it appears that the combined contribution of changes in particle size and surface coverage offers a quantitatively reasonable accounting of the experimental results. However, that interpretation involves a new relation between yield stress and adsorption that is empirically derived and for which a theoretical interpretation is still missing. This relation is, however, very important in explaining the exponential variation of yield stress with changes in specific surface.

Possibly that relation may be discussed in terms of an amplification factor expressed as exponential function of adsorption. To gain insight into this question, it is useful to rewrite Equation (5.21) as:

$$\ln\frac{\tau_{0,t}}{\tau_{0,OS}} = \frac{a}{\frac{1}{v_0^*} + \varepsilon\frac{c}{N}} \cdot (SSA_t - SSA_{OS}) \tag{II.5}$$

And take its derivative:

$$d ln\tau_{0,t} = \frac{a}{\frac{1}{v_0^*} + \varepsilon\frac{c}{N}} \cdot dSSA_t \tag{II.6}$$

Which is rewritten as:

$$d\tau_{0,t} = \tau_{0,t}\frac{a}{\frac{1}{v_0^*} + \varepsilon\frac{c}{N}} \cdot dSSA_t \tag{II.7}$$

Therefore, for a given change in specific surface, the change in yield stress will be greater if the yield stress is already large. Qualitatively, this behaviour can be understood as the consolidation of connections between particles. Doubling the number of C-S-H particles in a contact zone between two particles will more than double the strength of that connection.

Therefore, the adsorption of PCEs on cement particles directly influences this interaction by modifying nucleation and growth of hydrates, their size and precipitation rate on the cement surface as well as the number of interacting contact zones according to the surface coverage.

II.4.2 Surface roughness in cement science

In colloid science, surface roughness is reported to greatly amplify particle capture, accounting for some discrepancies from theoretical predictions based on DLVO considerations for smooth and chemically homogeneous particle surfaces [325]. However, the validation of theoretical description of such effects still remains challenging.

To some extent, the notion of roughness is analogous to using the radius at contact points among particles, rather than particle sizes, to describe interparticle forces, something done in the YODEL model to account for the yield stress of alumina suspensions [126]. Here, however, we are considering a lower length scale, one at which C-S-H plays a role in the acceleration period, probably in the range of nanometers. In this context, it is important to note that surface roughness covers several length scales, but that it is at the nanometric level that it plays an important role [325–328]. Also, effects of surface roughness are more accentuated for particles at separation distances smaller than 3 nm [329] immersed in highly concentrated salt solutions [330,331].

Recent experiments by colloidal probe AFM demonstrated that contact forces among opposing and similar particles are indeed enhanced by roughness [325,330]. Of particular interest in the context of this PhD is that an increase of the ionic strength reduces the length scale of the roughness. For our cement pastes with very high ionic strengths, this suggests that C-S-H nuclei forming at contact points might play an important role in the yield stress amplification.

Depending on the polymer concentration, and therefore, the layer thickness on the surface, the roughness can be masked [330,332]. In our pastes an even more important factor is the impact of polymers on dissolution, nucleation and growth. In particular, it is reported that PCEs inhibit the opening of etch pits, particularly when they are added in the mixing water [61,177,178]. Therefore, at the onset, the surface state of cement particles may be quite different depending on the polymer type and dosage, probably affecting the roughness development after the onset.

II.4.3 Role of surface roughness on flow loss

If roughness is the factor to consider, then the term $\frac{1}{a\,\gamma}\left(\frac{1}{v_0} + \varepsilon\frac{c}{N}\right)$ would be a multiple of a smooth surface area that would become roughened by the addition of C-S-H. This smooth area would increase in size as the polymer dosage is increased, which is compatible with the inhibition that PCEs have on C_3S dissolution [15]. The role of N is less straight forward to explain. It might require including an argument about the balance of homogeneous and heterogeneous nucleation.

Let us now consider the term $\frac{1}{v_0}$ that should relate to a smooth surface area in absence of polymer. This value is extrapolated from a concentration dependence and does not correspond to the value found in absence of polymer, something that can be explained by the change of nucleation balance in delayed addition (section 6.4.2). This reference surface can be estimated by polymer dosage for which:

$$\frac{1}{v_0} = \varepsilon\frac{c_0}{N} \qquad\qquad\qquad \textbf{(II.8)}$$

For a polymer with N = 4, the above equation is satisfied if c_0 = 0.2 mg/g. Considering that values of mass per unit surface of the studied polymers are roughly constant (Table II.6), we find that this dosage corresponds to an occupied surface of about 0.1 m^2/g.

Putting this in relation with the specific surface of about 2 m^2/g before the onset, we infer that only 5% of the total surface contributes to particle-particle contacts.

This value can be considered as reasonable based on the following argument. We consider two spherical cement grains with diameters d_1. If the cohesion between them is controlled by the diameter of C-S-H, d_{C-S-H}, then the effective contact surface would be $\pi\,d_1 d_{CSH}$ and the ratio to the surface of a single particle would be d_{C-S-H}/d_1. Because each particle has more than one contact, the fraction of surface accounting for contacts would be some multiple of d_{CSH}/d_1. From the respective values of d_1 and d_{CSH} calculated in section 6.3.3, the ratio d_{C-S-H}/d_1 is estimated to be between 1/10 and 1/20. Qualitatively, this is close enough to the 5% estimated above, that the surface roughness hypothesis could not be excluded.

Table II.6: Mass of polymer per unit surface of the studied polymers. This parameter is calculated as the ratio between the Mw reported in Table 5.3 and surface occupied by a single adsorbed molecule according to Equation (2.7).

PCE type	Mass per unit surface [mg/m^2]
2.5PMA1000	0.431
4.0PMA1000	0.418
2.5PMA2000	0.406
4.0PMA2000	0.384
2.5PMA5000	0.441

II.4.4 Conclusions

On a qualitative basis, it is possible to develop arguments according to which changes in surface roughness may explain yield stress changes, at least in part. However, in the present state of knowledge it is not possible to quantify these statements, which is why they are simply documented here as an annex.

Independently of this, yield stress changes can be well accounted for in quantitative terms by changes in particle size and surface coverage. Therefore, effects of surface roughness may be a second order effect or another way of explaining those same factors, but for which no quantification is possible.

CURRICULUM VITAE

SARA MANTELLATO

Sihlfeldstrasse 198
CH-8004 Zurich

Mobile: +41 76 245 59 69
sara.mantellato@gmail.com

Date of birth: 14.08.1982
Nationality: Italian

Stefano-Franscini-Platz 3
CH-8093 Zurich

Phone: +41 44 633 32 97
saraman@ethz.ch

EDUCATION

ETH Zurich – *Zurich, Switzerland*   *Aug. 2012 – Oct. 2017*

Ph.D. in the group of Physical Chemistry of Building Materials at the Institute for Building Materials.
Advisor: Prof. Dr. Robert J. Flatt
Dissertation: Flow loss in superplasticized cement pastes

University of Padova – *Padova, Italy*   *Oct. 2005 – Dec. 2007*

M.Sc. in Industrial Chemistry
Advisor: Prof. Gianni Cavinato. External supervisor: Ms. Francesca Moratti (BASF Construction Chemicals SPA Italia)
Awarded with graduating marks 110 out of 110
Dissertation: Effect of the presence of clay minerals in crushed sands on the performance of superplasticizers in concrete.

University of Padova – *Padova, Italy*   *Sep. 2001 – Sep. 2005*

B.Sc. in Industrial Chemistry
Advisor: Prof. Carla Marega.
Awarded with graduating marks 91 out of 110
Dissertation: Study on crystallization kinetics of isotactic polypropylene/organo-montmorillonite nanocomposites.

WORK EXPERIENCE

ETH Zurich – *Zurich, Switzerland*   *Nov. 2011 – Aug. 2012*

Research assistant
Advisor: Prof. Dr. Robert J. Flatt
Topic 1: Preliminary investigations on the project "formwork Free Concrete" in collaboration with Dr. Ena Lloret-Fritschi
Topic 2: Preliminary synthesis of ettringite and its characterization

BASF Construction Chemicals Europe AG – *Zurich, Switzerland*   *Mar. 2011 – Aug. 2011*

Research chemist at Research & Development
Delegation at the Business Unit MEYCO Global Underground Construction
Topic 1: Synthesis, scale-up and process development of a new inorganic accelerator for sprayed concrete applications
Topic 2: Evaluation of a sprayed concrete admixtures performance by isothermal calorimetry and rheological tests

BASF Construction Chemicals Spa Italia – *Treviso, Italy*   *Feb. 2008 – Oct. 2011*

Research chemist at Research & Development
Topic 1: Evaluation of the interaction between superplasticizers, cement and fine aggregates by means of adsorption tests (TOC) and X-Ray Diffraction
Topic 2: Formulation development and technical support for the Italian and European Ready-Mix market
Topic 3: Characterization of the properties of polymeric fibers to use in concrete
Topic 4: Supervision of field tests at customers' concrete production sites for the development of new products

BASF Construction Chemicals Spa Italia – *Treviso, Italy*   *Oct. 2006 – Jun. 2007*

Master degree internship
Topic 1: Study on the effect of clay minerals on the mechanism of action of superplasticizers in concrete

SKILLS

- Developments of new methods, use, and maintenance for a broad range of analytical techniques;
- Supervision of health and safety issues, with particular attention to the chemistry ones;
- Supervision of students and technical personnel;
- Supervision of chemical laboratories

EDUCATIONAL EXPERIENCE

Teaching Assistent – ETH Zurich, *Switzerland*   *Fall semesters 2011 – 2015*

Materials III for Civil Engineering B.Sc
- Microstructure, Mineral binder and Durability in reinforced concrete

Supervision of students – ETH Zurich, *Switzerland*   *2012 – 2014*

Civil Engineering B.Sc students
- Bachelor project on "Flow loss in superplasticized cementitious binders" – Mr. Lindrit Ceni and Qendrim Mehmeti – 2014
- Summer internship on "mastering flow loss of cementitious materials" – Ms. Soujanya Mandadi – 2013
- Bachelor project (in co-supervision with Mr. Amir Shahab and Dr. Ena Lloret-Fritschi) on "Formwork Free Concrete" – Mr. Adriano Alberti, Mr Lukas Ambühl and Ms. Daniela Christen – 2012

PROFESSIONAL QUALIFICATION

Dec. 2008

Chemist professional qualification exam obtained at the University of Padova

LANGUAGES

Italian: native
English: Advanced knowledge of written and spoken English
German: Intermediate knowledge

IT SKILLS

Very good knowledge of the following software bundles: Microsoft Word, Microsoft Excel, Microsoft PowerPOint, Microsoft Publisher, OpenOffice.Org, Microcal Origin, ChemDraw. Fair knowledge of macOS. Medium knowledge of Ubuntu and Linux/UNIX. Basic knowledge of GEMS and PHREEQC chemical speciation program.

SELECTED ADVANCED COURSES ATTENDED

- Workshop on ICP-OES analysis of precious metals, organized by ThermoFicher, Reinach (Switzerland), 2016
- 4th Gibbs Energy Minimization Software (GEMS) workshop on thermodynamic modeling of cementitious systems, organized by EMPA, Dübendorf (Switzerland), 2014
- Introduction to GEMS, organized by PSI, Villigen (Switzerland), 2013

PUBLICATIONS IN PEER-REVIEWED INTERNATIONAL JOURNALS

4. F. Caruso, **S. Mantellato**, M. Palacios, R.J. Flatt, A Powerful Tool to Better Understand Cement Hydration, CHIMIA – Highlights Anal. Sci. Switzerland – Div. Anal. Sci – 71(3) (2017)

3. F. Caruso, **S. Mantellato**, M. Palacios, R.J. Flatt, ICP-OES method for the characterization of cement pore solutions and their modification by polycarboxylate-based superplasticizers, Cem. Concr. Res. 91 (2017) 52–60. doi:10.1016/j.cemconres.2016.10.007.

2. **S. Mantellato**, M. Palacios, R.J. Flatt, Impact of sample preparation on the specific surface area of synthetic ettringite, Cem. Concr. Res. 86 (2016) 20–28. doi:10.1016/j.cemconres.2016.04.005.

1. **S. Mantellato**, M. Palacios, R.J. Flatt, Reliable specific surface area measurements on anhydrous cements, Cem. Concr. Res. 67 (2015) 286–291. doi:10.1016/j.cemconres.2014.10.009.

PUBLICATIONS IN PEER-REVIEWED BOOKS

6. A. Yahia, **S. Mantellato**, R.J. Flatt, 7 – Concrete rheology: A basis for understanding chemical admixtures, P.-C. Aïtcin, R.J. Flatt (Eds.) in *Science and Technology of Concrete Admixtures*, Woodhead Publishing, (2016) 97–127. ISBN: 978-0-08-100693-1.

5. G. Gelardi, **S. Mantellato**, D. Marchon, M. Palacios, A.B. Eberhardt, R.J. Flatt, 9 – Chemistry of chemical admixtures, P.-C. Aïtcin, R.J. Flatt (Eds.) in *Science and Technology of Concrete Admixtures*, Woodhead Publishing (2016) 149–218. ISBN: 978-0-08-100693-1.

4. D. Marchon, **S. Mantellato**, A. Eberhardt, R.J. Flatt, 10 – Adsorption of chemical admixtures, P.-C. Aitcin, R.J. Flatt (Eds.) in *Science and Technology of Concrete Admixtures*, Woodhead Publishing, 2016, 219-256. ISBN: 978-0-08-100693-1.

3. **S. Mantellato**, A.B. Eberhardt, R.J. Flatt, 15 – Formulation of commercial products, P.-C. Aitcin, R.J. Flatt (Eds.) in *Science and Technology of Concrete Admixtures*, Woodhead Publishing (2016) 343-349. ISBN: 978-0-08-100693-1.

2. P.-C.Nkinamubanzi, **S. Mantellato**, R.J. Flatt, 16 – Superplasticizers in practice, P.-C. Aitcin, R.J. Flatt (Eds.) in *Science and Technology of Concrete Admixtures*, Woodhead Publishing (2016) 353-377. ISBN: 978-0-08-100693-1.

1. M. Palacios, H. Kazemi-Kamyab, **S. Mantellato**, P. Bowen, 10 – Laser diffraction and gas adsorption techniques, K. Scrivener, R. Snellings, B. Lothenbach in *A Practical Guide to Microstructural Analysis of Cementitious Materials*. Taylor & Francis (2016) 445-483. ISBN: 978-1-4987-38675.

PUBLICATIONS IN PROCEEDINGS OF INTERNATIONAL CONFERENCES

1. **S. Mantellato**, Q. Mehmeti, L. Ceni, M. Palacios, and R.J. Flatt. Mastering Flow Loss in Superplasticized Cementitious Systems, in *Proceedings 11th CANMET/ACI International Conference on Superplasticizers and Other Chemical Admixtures in Concrete,* Ottawa, Canada (2015) *SP-302-10,* 133–44. ISBN: 978-1-942727-22-4.

SELECTED PRESENTATIONS

- Mastering flow loss in superplasticized cementitious systems, *11th CANMET/ACI International Conference on Superplasticizers and Other Chemical Admixtures,* Ottawa, Canada, July 2015.

- Fresh cement pastes – A systematic study on their specific surface area, *1st International Conference on the Chemistry of Construction Materials*, Berlin, Germany, October 2013

- Reliable specific surface area measurements of fresh cement pastes, GDCh – Tagung Bauchemie, Dübendorf, Switzerland, October 2012